AC ELECTROSTATIC PRECIPITATION

by

RICHARD M. EHRLICH

S.B., Massachusetts Institute of Technology
(1977)

S.M., Massachusetts Institute of Technology
(1979)

Submitted in Partial Fulfillment

of the Requirements for the

Degree of

Doctor of Science

at the

Massachusetts Institute of Technology

March, 1984

Signature of Author.....
Department of Electrical Engineering and Computer Science,
March 21, 1984

Certified by.....
James R. Melcher
Thesis Supervisor

Accepted By.....
Arthur C. Smith
Chairman, Department Committee

Table of Contents

Abstract

Quantitative observations of the charging, transport, and precipitation processes in a laboratory-scale electrostatic precipitator, excited either by a DC or AC voltage source, are reported. The dimensions and experimental parameters used were: plate-spacing, $2H \approx 3$ cm, corona wire diameter, $D \approx 0.015$ cm, precipitator length, $L \approx 1.5$ m, axial air flow velocity, $U = 1.5 - 8.9$ m/sec, characteristic applied voltage magnitude, $V_o \approx 8$ kV RMS, electric field strength, $E_o \sim 3 \times 10^5$ v/m, corona current density, $J_o \sim 1$ μa/cm^2, and excitation frequency, $f = 20 - 500$ Hz (along with DC). AC excitations were biased so as to supply zero time-average corona current to the ground plates. An aerosol of DOP (Dioctyl Phthalate) particles of diameter, $2R \approx 1$ μm, was used.

With the corona wires aligned in the axial (ie., air-flow) direction, particles charged in positive or negative DC coronas attained mobilities, $|b_p| \sim 3 \times 10^{-7}$ m^2/v·sec. The mobility spectra of particles that were charged in a low-frequency ($f < 50$ Hz) AC corona of the same RMS voltage were characterized by an RMS spread in mobility of similar magnitude, and a small mean mobility. The RMS spread in mobility decreased with rising frequency, and the magnitude of the mean mobility increased. The particle charge (and hence, mobility) bias was shown to be influenced strongly by the spatial distributions of the positive and negative coronas.

Measurements are presented of the corona wind, induced by electric field forces on the corona ions. Velocities of the order of 1 m/sec were measured with both DC and AC excitations. The induced transverse flow velocity decreased with increasing frequency, for a fixed value of the RMS excitation voltage, falling to a low level for frequencies above roughly 300 Hz.

A new technique for measuring the effective flow diffusivity was developed, making use of the longitudinal mixing of a stream of particles charged in a sinusoidal corona electric field. Values of the diffusion coefficient, D_t, inferred from the experiments, ranged from $1 - 17 \times 10^{-3}$ m^2/sec, for flow velocities of 2.5 - 7.5 m/sec, respectively.

The overall collection efficiency of the precipitator was measured. With positive and negative DC voltages of magnitude, $V_o \sim 8$ kV, the measured effective precipitation velocities, $w_{eff} \equiv (UH/L) \ln(1-\eta)$, where η is the collection efficiency, were 5.6 and 12.5 cm/sec, respectively. With an 8 kV RMS 60 Hz AC excitation, the effective precipitation velocity was about 3.5 cm/sec. The performance of the device with AC excitations was not significantly affected by the addition of a thin insulating coating over the collection plates.

A model was developed for the charging, migration, turbulent mixing, and precipitation of particles in a time-varying corona. It is shown that the complete-mixing limit of this model (which accounts for the finite particle charging rate due to ion impaction, but not for effects of non-uniform electric fields, finite ion migration rates, or non-uniform ion fluxes) is able to predict the overall precipitation efficiency with AC excitations in terms of the measured results with positive DC coronas. It is also able to predict some of the particle charging statistics for low-frequency excitations (< 150 Hz). The predictions deviate significantly from the observed results of the charging experiments for higher frequencies.

Acknowledgements

The completion of this thesis was made possible by the efforts of many people besides myself. Given the limited space available [I've already numbered the rest of the pages, and only page 7 is left], I will try to mention the most important contributors.

I am about as much a product of Professor James Melcher as a student can possibly be. In the nine years that I have known him, he has supervised not only all three of my theses, but also my development as a scientist and an engineer. He is truly an educator, providing both training and inspiration to those around him.

The rest of my thesis committee, Professors Louis Smullin, Marcus Zahn, and Joseph Haritonidis, were extremely helpful, and took an active role in guiding the progress of my research. Professor Haritonidis did his best to make the fluid mechanics of an electrical engineer presentable to the world

This project was funded by Combustion Engineering, Inc.. Our contract supervisor, Gerald Driggers, was particularly helpful in achieving a balance between the need for practical results and our desire to understand electrostatic precipitation. The company is to be commended for its support of basic scientific research. The contract was administered by the MIT Energy Lab, from which I received a Cabot Solar Energy fellowship for one year. That fellowship allowed the Continuum Electromechanics Group to purchase the laser-Doppler-anemometer which produced most of the data in this thesis.

Professors Alan Grodzinsky and Raphael Lee provided the computer resources that were necessary to utilize the anemometer's capabilities. I repaid them by crashing the system on a weekly basis. Professor Jeffery Lang advised me in the design and construction of a digital interface between the anemometer and computers. Paul Warren managed to keep the laboratory running relatively smoothly, in spite of my presence there.

Several undergraduate students worked on the project. Amongst them were Julian Joseph, who took much of the precipitation data of chapter 4, and Lama Mouayad, who did some of the initial theoretical work on the uniform-field charging model of chapter 3.

I owe thanks to the rest of the students in the Continuum Electromechanics Group, both for arguing with me constantly about nuances of my experimental and theoretical results, and for providing moral support during difficult periods. Eliot Frank deserves special recognition for the many times that he saved me from the brink of digital destruction, and for the excellent text editor that he developed. Without it, this thesis, would never have been fi[illegible]shed f[illegible]nis[illegible] done.

List of Commonly-Used Symbols

Symbol	Comments	Ref. Page
A	Effective precipitator area	66
A_{LDV}	LDV observation volume cross-sectional area	226
A_n	N'th coeff., series rep. of particle concentration	347
b_i	Ion mobility	44
b_o	Ion mobility	188
b_p	Particle mobility	36
b_{sat}	Particle saturation mobility	20
d	Pipe diameter	130
d_h	Hydraulic diameter of channel	131
D	1) Corona wire diameter	2
	2) Molecular diffusivity	130
	3) Precipitator plate width	330
D_t	Effective turbulent diffusivity	22
$\overline{E}$	Electric field vector	60
E_a	Electric field intensity outside particulate layer	33
E_B	Value of E_ℓ which results in electrical breakdown	26
E_o	Charging/collection electric field intensity	20
E_ℓ	Electric field intensity in collected particulate layer	26
f	1) Fanning friction factor	130
	2) Excitation frequency	74
$F(f)$	Fourier transform of particle velocity function	146
g	Dimensionless parameter	342
G	Dimensionless parameter	232
H	Precipitator wire-plate separation	21
i	Corona current	44
I_{eff}	Effective corona current	82
I_P	Peak charging current	80
$I_\pm$	Characteristic particle charging currents	66
$\overline{J_o}$	Corona current density	20
k	Dimensionless parameter	342
$\tilde{k}$	Complex decay exponent for particle charge density	231
L	Precipitator Length	21
LDV	Laser-Doppler Velocimeter	51
n	Particle concentration	114
n_o	Particle concentration at precipitator inlet	114
n_∞	Particle concentration at outer edge of boundary layer	130
N	Number of particle velocity measurements in a set	145
$\dot{N}$	LDV data rate	226
q	Particle charge	63
$q_{c\pm}$	Particle saturation charges	66
q_o	Characteristic particle saturation charge	82
$q_{o\pm}$	Particle initial charges	67
$q_{particle}$	Particle charge	224
q_∞	Steady-state peak particle charge	70
Q_o	Amplitude of particle charging source	224

R	Particle Radius	20
R_E	Reynolds number	43
R_i	Inner cylinder radius	359
R_o	Outer cylinder radius	359
Sc	Schmidt number	130
t	Time	64
t_i	Time of velocity measurement of i'th observed particle	145
T	Cycle time of applied electrical excitation	34
T_{on}	Corona on-time	80
u_*	Wall friction velocity	133
U	Air-flow velocity	21
U_E	Characteristic corona wind velocity	43
$\bar{v}$	Mean velocity of particles	146
v'	RMS spread in particle velocity	146
v_{eff}	Effective diffusive velocity across boundary layer	130
$v_{f_{exc}}$	Fourier component of particle migration velocity at charging frequency	208
v_i	Velocity of i'th observed particle	145
v_k	Kolmogoroff velocity-scale	132
$\bar{v}_{mig}$	Mean particle migration velocity	150
v'_{mig}	RMS spread in particle migration velocity	150
v_o	Characteristic particle migration velocity	72
V	Applied electric potential	60
V_B	Charging voltage bias	80
V_o	Characteristic applied voltage	43
V_P	Sinusoidal Charging voltage component	80
w	Particle migration velocity	63
w_{ac}	Oscillatory particle migration velocity	63
w_{eff}	Effective particle migration velocity	28
w_{net}	Time-average particle migration velocity	63
w_p	Particle precipitation velocity	119
w_{sat}	Particle saturation migration velocity	20
x	Transverse coordinate in precipitator	115
x_p	Particle position	68
y_*	Wall unit	133
Y	Dimensionless parameter	361
z	Axial coordinate in precipitator	115
β	Dimensionless parameter	342
ϕ	Electric potential	43
ε_o	Dielectric constant of free space	20
ε_ℓ	Dielectric constant of collected particulate layer	33
ε	Energy dissipation per unit fluid mass	132
λ	Resistance coefficient	131
η	1) Viscosity (of air)	20
	2) Precipitator collection efficiency	21
κ	Dimensionless parameter	360
ω	Angular frequency of electrical excitation	36

ν	Kinematic viscosity (of air)	129
ρ	1) Air mass-density	44
	2) Particle charge density	228
$\tilde{\rho}$	Complex amplitude of particle charge density	229
ρ_c	Ion charge density	43
ρ_i	Ion charge density	43
ρ_o	Initial ion charge density	188
ρ_p	Characteristic particle charge density	224
ρ_ℓ	Resistivity of collected particulate layer	24
γ	1) Ion current density fraction	39
	2) Fourier decay coefficient	208
γ_r	Ratio of Fourier decay coefficients	217
τ_c	Air residence time in precipitator	22
τ_C	Air residence time in precipitator (same as τ_c)	230
τ_{ch}	Particle charging time	20
τ_{charge}	Particle charging time	82
τ_d	Turbulent diffusion time	22
$\tau_{d,L}$	Diffusion time, based upon precipitator length (same as τ_D, below)	340
τ_{dev}	Flow development time	241
τ_D	Turbulent diffusion time, based upon precip. length	230
τ_e	Electric relaxation time in collected particulate layer	27
τ_{ev}	Electroviscous time	226
τ_m	Particle migration time	22
$\tau_{m,\pm}$	Ion migration times	60
τ_p	Particle self-precipitation time	224
$\tau_\pm$	Ion self-precipitation times	60
ξ	Transformed spatial coordinate	334
δ	Thickness of zone of no turbulent transport	122
χ	1) Dimensionless constant (0.042)	130
	2) Volume fraction of precip. occupied by particles	226
ζ	Eigenvalue	343
ℓ	1) Wire length	44
	2) Charging length	166
ℓ_{dev}	Flow development length	241
ℓ_k	Kolmogoroff length-scale	132
ℓ_{max}	Maximum particle displacement, due to migration, during one half-cycle of electrical excitation	114
$\ell_{max,\pm}$	Maximum particle displacement due to migration during positive/negative excitation half-cycle	330
ℓ_{net}	Net particle displacement, due to migration, during one half-cycle of electrical excitation	71
$\ell_{net,\pm}$	Net particle displacement due to migration during positive/negative excitation half-cycle	330
Γ_n	1) Diffusive flux-density to wall	130
	2) Total particle flux-density to wall	337
Σ_s	Ion surface charge density on collected layer	33
T/τ	Ratio of times	70

Chapter 1

Introduction

1.1 Motivation for Research on AC Electrostatic Precipitation

There are both practical and scientific reasons for preforming research in the area of electrostatic precipitation. First, from a practical standpoint, it is an efficient, cost-effective means by which to remove particulate from gas flows in a wide range of situations. A good understanding of the phenomena which occur during ESP (Electrostatic Precipitator) operation allows the development of design rules for more reliable, more efficient, and less costly devices. At the same time, these phenomena are of interest in a purely scientific sense. Careful study of the charging and collection processes in an ESP under well-controlled conditions can provide insight into the electrohydrodynamics of particle charging and migration in turbulent flows. Although most present-day ESP's are relatively insensitive to the exact conditions of flow between the collecting plates, it is argued later in this chapter that the collection efficiency of a precipitator can be made to be a strong function of both turbulent mixing in the main flow and the characteristics of the boundary layers at the electrode surfaces.

Motivations for the study of electrostatic precipitation using AC electrical excitation may be stated more specifically. One of the major applications of ESP's today is to collect fly ash produced by the combustion of pulverized coal in power plants. Virtually all commercial ESP's used for this purpose employ a DC (or, at least, unipolar) electric field both for particle charging and collection. If the sub micron particulate is highly resistive, accumulations of charge on the collected layer can produce intense electric fields across it. Electrical discharges which occur in the layer generate positive ions and cause a phenomenon known as "back corona" which greatly reduces the ESP collection efficiency. Conventional solutions to the problem, such as hot-side precipitators and flue-gas conditioning, each entail additional disadvantages of their own.

A precipitator that uses both positive and negative electric fields to collect particles could be designed so as to pass no net current to the collecting electrodes, presumably eliminating problems with charge accumulation and back corona. Therefore, the concept of an AC ESP is of great interest as a possible means of avoiding the conductivity dependence of conventional precipitators.

If an AC ESP could be run with 60 Hz excitation, an additional benefit would be elimination of the need for rectification of power from the AC line. This could conceivably result in a net cost reduction in AC precipitators over their DC counterparts.

From a scientific standpoint, the AC precipitator is capable of providing valuable insight into some of the basic processes of electrostatic precipitation. It offers a sensitive means for comparison of the charging characteristics of positive and negative coronas. Under certain limiting conditions (such that the time-average particle migration velocities are very small), it allows experimental study of the socalled "corona wind" by observation of particle motions. In the case of two-stage precipitation of pre-charged particles, the efficiency of precipitation can be made to be a strong function of both the turbulent mixing in the core flow and the characteristics of the boundary layer at the collection surfaces.

1.2 Overview of Thesis

This thesis describes an experimental and theoretical study of electrostatic precipitation conducted by the author at the Continuum Electromechanics Laboratory (of MIT) during the calendar years, 1982 and 1983. The focus of this study was a comparison of the particle charging, transport, and collection mechanisms for AC and DC excitations. A strong practical motivation behind the work was the desire to obtain an electrostatic precipitator that could operate with relative immunity to the resistivity of the collected particulate.

Electrostatic precipitation is a relatively mature technology, having been introduced near the beginning of the present century. Section 1.3 presents background information on the operation of a typical (ie., DC) device. The basic configuration of single-stage precipitation is examined there. That same section contains a description of problems encountered during the precipitation of highly-resistive particulate, as well as a brief summary of the various measures presently taken to alleviate these problems. The number and diversity of the proposed schemes portrays at once both the great importance of the problem and the inadequacy of any one of these "solutions".

The possibility of exciting a precipitator with an AC voltage is introduced in section 1.4. It is seen there that a bipolar corona current can charge particles, so that they will migrate in the imposed electric field, even though the collected particulate layer need conduct no time-average current. With a unipolar corona, any attempts to increase the particle charging rate are made at the expense of a larger current to be conducted through the layer.

It is not at all obvious, however, that an electrostatic precipitator that is excited by an AC voltage would collect any particles. The maximum displacement per cycle of a 1 μm diameter particle in a 60 Hz charging electric field of strength, 10^6 v/m* is of the order of millimeters. The plate spacing in a typical precipitator is

---

*The imposed electric field is limited by the breakdown strength of air to roughly this value or smaller

roughly 25 cm. Two mechanisms of collection in an AC electrostatic precipitator are proposed. The first utilizes the fact that the flow in a precipitator with practical dimensions and operating parameters is highly turbulent. Mixing due to turbulent eddies can be expected to bring particles to within a short distance of a collection plate, at which point even small-scale oscillatory migrations would cause them to precipitate. The second mechanism relies on an interaction which takes place between the charging and migration mechanisms in a single-stage precipitator. It is argued that, in a single-stage AC precipitator, the particles would undergo a net migration toward the collection plates, despite the continually-reversing fields.

In the general case (DC or AC), electrostatic precipitation requires the interaction of a number of different mechanisms. Particles are charged by the corona current, transported by the mean flow, turbulence, and their own migrations in the imposed electric field, and precipitate onto collection surfaces. Section 1.5 is a review which cites the works of authors that have studied these separate mechanisms. The major topics covered are : (1) particle charging, (2) turbulent diffusion models for electrostatic precipitation, and (3) models for and measurements of the corona wind in precipitators.

The experiments performed for this thesis were designed not only to observe the overall performance of an AC electrostatic precipitator, but to allow closer examination of some of these mechanisms. Chapter 2 gives a brief description of the experimental setup used to provide the data reported in chapters 4 - 6. As might be expected, this setup includes a laboratory-scale electrostatic precipitator, along with some diagnostic instrumentation to permit observation of its operation. Precipitation efficiency measurements are made by means of a mass-monitor, which determines the particulate mass-loading of the air-stream leaving the device. In addition, a laser-Doppler velocimeter (LDV) allows non-invasive measurement of the velocities of individual particles inside the precipitator, so that flow statistics, migration velocities, and particle concentration profiles can easily be obtained.

Much of the complexity involved with interactions between particle motions and their charging results from the spatially-varying electric fields and corona currents in a practical precipitator. Both the

charging rate and limiting particle charge depend upon its location in the non-uniform fields. The migration velocity of a particle (and, in turn, its location) thus depends intimately upon its history of proximity to the corona charging wires. If the electric field and corona current were uniform, then the particle charging rate would be independent of its location. A simplified AC charging model, based upon an assumption of uniform fields, is developed in chapter 3. The major justification for this model is its simplicity; there were no situations examined experimentally for which it was strictly valid. The charging electric fields applied for the experiments of chapters 4 - 6 were non-uniform. In addition, for AC frequencies above several hundred Hz, the finite ion transit times would result in spatially varying corona currents even if the electric fields were uniform. However, this crude charging and migration model is seen in chapter 4 to be able to accurately predict the degradation in the effective particle migration velocity that results from application of a bipolar excitation (as opposed to a unipolar one).

In chapter 4, the simplified charging model of chapter 3 is embedded within a model for the effects of turbulent mixing in the precipitator to predict the collection rate of a single-stage AC device in terms of its behavior with a DC excitation. In the discussions of that chapter, it is concluded that only the time-average particle migration rate is of importance in determining the precipitation efficiency. Although the turbulence is intense enough to be the dominant particle transport mechanism in the bulk flow, it is not capable of bringing particles close enough to the collection plates that their oscillatory motions alone might precipitate them. The existence of a linear flow region, with little turbulence, at each collection surface precludes the possibility of any contribution due to the particle oscillations. The predicted efficiency is presented in terms of an effective precipitation velocity, and compared to experimental data obtained from the laboratory-scale precipitator. It is seen that these rather crude models can be made to predict the AC data in terms of measurements made with positive DC excitations to within experimental error.

Chapters 5 and 6 begin a closer examination of the individual

mechanisms which, together, constitute the electrostatic precipitation process. In chapter 5, the emphasis shifts to two-stage precipitation. The experiments reported there measured the mobility statistics of particle leaving various corona charging sections. The particles' mobilities are measured by observation of their response to an imposed transverse electric field, as described in chapter 2. These mobility measurements show that the competition between positive and negative particle charging in an alternating field depends intimately upon the geometry of the coronas. With electrodes that contain sharp points (such as pins or barbed wires), the positive and negative coronas are both restricted to the same locations. Under such conditions, it is seen that negative corona dominates the charging. For a DC excitation, the particles attain higher mobilities with negative coronas than with positive coronas of equal magnitude voltage or current. With high-frequency AC excitations (ie., > 200 Hz), the particle charge is biased negatively, even though the simplified models of chapter 3 would predict a slight positive bias.

With wire electrodes, where the spatial distributions of positive and negative coronas can be very different*, the negative corona still dominates the DC charging. With high-frequency AC excitations, however, the bias is toward positive charging. Some intuitive models are offered to explain this behavior.

The effects of the fluid flow on particle distributions in the precipitator are investigated in chapter 6. The experiments reported there fall into two major categories : (1) measurements of the turbulent diffusivity of the flow, and (2) corona wind measurements.

For the turbulent diffusivity measurements, the corona pin-charger that was examined in chapter 5 is used as an experimental tool. It imposes a charge per particle (in the vicinity of the pins) that varies sinusoidally with time. Because no electric fields are imposed in the region between the charger and the mobility measurement section, this charge simply acts as a passive scalar contaminant in that region.

---

*With positive corona, the current tends to be distributed uniformly over the length of the wire. With negative voltages, however, the corona is concentrated at discrete "brushes", separated by distances on the order of cm.

Measurements are made of the Fourier component of particle mobility at the corona charging frequency, for various locations downstream of the pins, using the migration plate (as in chapter 5). The decay in this Fourier componen of mobility with increasing downstream distance provides a measure of the degree to which the turbulence is capable of eliminating gradients in the particle charge function. A model is proposed to predict the sinusoidal steady-state distribution of a convected scalar contaminant that is constrained in magnitude at one boundary and subjected to a uniform diffusivity for points downstream of the boundary. The spatial rate of decay of the contaminant is expressed in terms of an equivalent diffusivity for the flow, which can then be determined from experimental measurements of the actual decay. This model, referred to as the "longitudinal turbulent diffusion model", is fitted to the experimental data to yield crude estimates of the effective diffusivity of the flow in the laboratory-scale precipitator.

Although the flow in the tunnel was turbulent even in the absence of corona excitation, the application of a corona current increased the turbulence significantly. The flows induced by effects of the electric field force on the current-carrying ions in the precipitator are referred to here as "corona wind". Measurements of the corona wind variation with position in the tunnel and with different AC and DC electrical excitations are presented with little comment (and no modeling).

Two major issues are addressed in the concluding chapter, chapter 7. The first is the validity of the crude charging, transport, and precipitation models of chapters 3 - 6. The second is the practicality of AC electrostatic precipitation as a viable option for the collection of highly-resistive particulate.

1.3 Background on Conventional Electrostatic Precipitation

This section presents a brief summary of basic concepts that are helpful in understanding the electrostatic precipitation process. Section 1.3.1 describes the operation of a conventional device, and gives approximate values for those parameters which characterize its behavior. Some of the problems that occur during the collection of highly-resistive particles are discussed in section 1.3.2. Finally, section 1.3.3 contains comments on each of several proposed (and implemented) solutions to these problems. The interested reader is referred to White[1,2] and Melcher[3] for further background information pertaining to the fundamentals of precipitator operation, to White[7] for details of the (back corona) problems involved with precipitation of highly-resistive particles, and to Lausen[10] for a review of pulsed electrostatic precipitation (described in section 1.3.3).

1.3.1 Fundamentals of DC Electrostatic Precipitation

A configuration typical of conventional electrostatic precipitators is shown schematically in Fig. (1). It consists of two grounded parallel plates with a set of thin wires that are suspended parallel to the plates and halfway between them. The wires are held at a high electric potential which can, in principle, be either positive or negative. As a practical matter, negative voltages are normally used, and such will be assumed for this example. The asymmetric geometry of the electrodes (ie., the thin wires, in comparison to the flat plates) results in a highly non-uniform electric field in the region between the plates. The electric field intensity is much greater in the vicinity of the wires than it is near the plates. Thus, there exists a range of applied voltages for which the fields at the wires are intense enough to cause electrical breakdown of the air there, yet farther away the fields are not sufficiently strong to allow propagation of catastrophic arcs from wires to plates. For such excitations, a stable corona is created near the wire, in which ion-pairs (ie., positive ions and electrons) are continuously created. With a negative applied voltage, the positive ions follow the electric field lines directly into the wire, while the

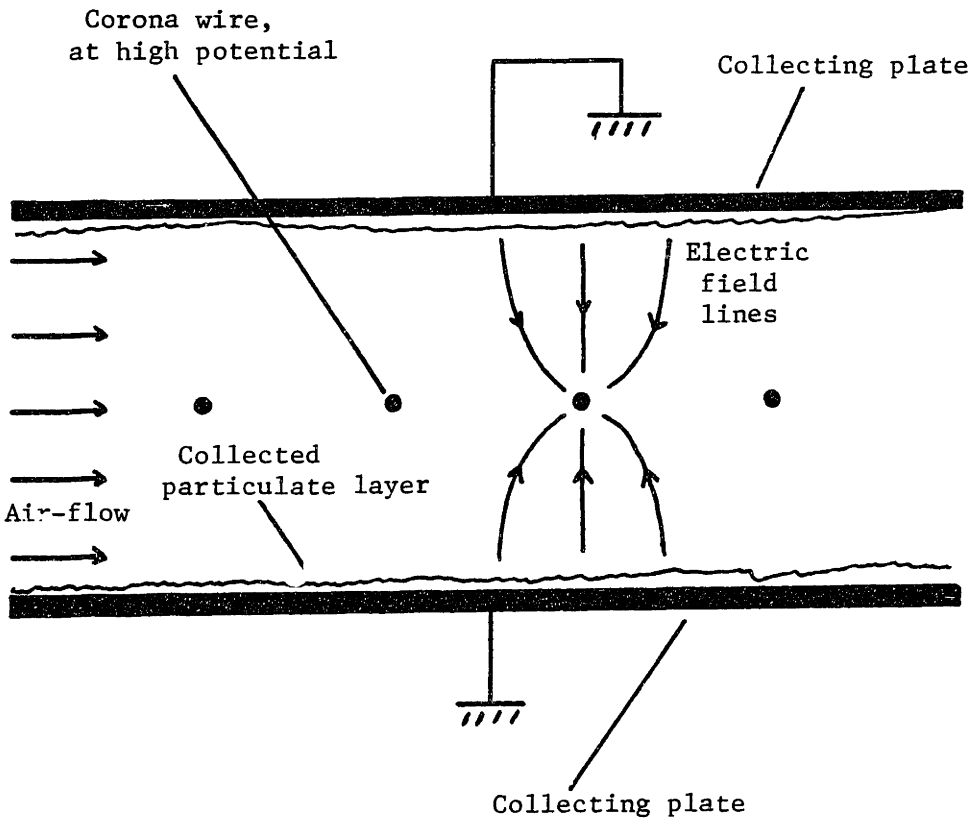

Fig. 1.1. Schematic illustration of a single-stage electrostatic precipitator. Particulate enters at left, connected by air-flow. Particles are charged in corona current and migrate toward collecting plates, where they accumulate in thin layers.

electrons move backwards along these same field lines, toward the plates. Once they leave the region of very intense electric field, the electrons attach to neutral molecules to form more slowly-moving negative ions.

Air, laden with particles to be removed, flows between the plates [from left to right in Fig. (1)]. As they are convected past the wires, the particles intercept some of the ions that are migrating toward the plates. The particles, themselves, become negatively charged and migrate toward the plates, collecting in a thin layer there. In a practical device, the entire arrangement of wires and plates is held in a vertical plane [so that the direction into the page in Fig. (1) is actually down]. Hammers, referred to as "rappers", strike the plates periodically, knocking off pieces of the collected layer into hoppers below, from which the particulate matter can later be removed.

If the voltage applied to the wires were positive, then the electric field lines would point in a direction opposite to that pictured in Fig. (1). In this case, positive ions would occupy most of the region between the plates. The particles would acquire a positive instead of a negative charge. Again, they would migrate toward the plates. As long as the particles are charged to the same sign as the corona ions moving toward the plates, then the particle migration will be in the direction of the plates as well.

The limiting charge that a particle can attain, and the rate at which it approaches this charge, depend upon the local electric field strength and corona current density in the vicinity of that particle. For a given particle radius, R, moving through a gas of viscosity, η, charged by an electric field strength, E_o, with corona current density, J_o, the maximum particle mobility, b_{sat}, is [see eq. (5.4.1)]

$$b_{sat} \equiv \frac{w_{sat}}{E_o} = 2\ \varepsilon_o\ E_o\ R/\eta \qquad (1.3.1)$$

where w_{sat} is the migration velocity of a particle charged to saturation and propelled by an electric field of strength, E_o. The characteristic charging time, τ_{ch}, is [see eq. (5.4.3)]

$$\tau_{ch} = 8\ \frac{\varepsilon_o\ E_o}{J_o} \qquad (1.3.2)$$

This value for τ_{ch} is conservative; a particle is charged to roughly

half its saturation level in about one-half of this time. For R = 1 μm, $E_o = 5 \times 10^5$ v/m, $J_o = 100$ nA/cm^2, $\eta = 2 \times 10^{-5}$ Kg/m · sec,

$$b_{sat} \backsim 5 \times 10^{-7} \frac{m^2}{v \cdot sec} \tag{1.3.3}$$

$$\tau_{ch} \backsim 40 \text{ msec} \tag{1.3.4}$$

Thus, in a typical precipitator, a particle can reach its saturation charge in a small fraction of a second. With the given electric field, the migration velocity of such a particle is

$$w_{sat} \backsim 25 \frac{cm}{sec} \tag{1.3.5}$$

It is important to note that this electric field charging is normally a "one-way" process. Ions that strike a particle remain on that particle until it reaches a collection plate. The only ways that a particle can be discharged are : (1) by conduction to the collection plate after precipitation, or (2) by interception of ions of opposite sign to those that charged the particle originally. Normally, only ions of one sign are present in the collection volume of a conventional precipitator. It is seen in section 1.3.2 that this is not always the case during the collection of highly-resistive particles.

The collection efficiency which results from the migration depends upon the conditions of the flow in the precipitator[4]. For a completely laminar plug-flow of velocity, U, in a precipitator of plate spacing, S = 2H, length, L, with a particle migration velocity, w_{sat}* the efficiency of collection, η [defined in section 4.4.1, eq. (4.4.7)], is

$$\eta = \frac{L/U}{H/w_{sat}} \tag{1.3.6}$$

This efficiency is expressed as a ratio of characteristic times; τ_c, defined as

---

*It is assumed here, for purposes of analysis, that the migration velocity is of uniform magnitude and directed toward the plates over the entire cross-section of the device. This assumption is normally valid only with two-stage precipitation, in which pre-charged particles are injected into a region consisting of two parallel plates between which a large electric potential is imposed.

$$\tau_c \equiv \frac{L}{U} \tag{1.3.7}$$

being the convection time in the imposed flow, and τ_m, defined as

$$\tau_m \equiv \frac{H}{w_{sat}} \tag{1.3.8}$$

being the time required for a particle to migrate from the wire plane to a plate (referred to here as the "migration time").

For a flow whose turbulence is intense enough to result in complete mixing of the particles in a plane transverse to the imposed flow, the efficiency is

$$\eta = 1 - e^{-\frac{L/U}{H/w_{sat}}} \tag{1.3.9}$$

where, in this case, it is understood that U is now the mean flow velocity, upon which turbulent fluctuations are superimposed. The efficiency of collection of a precipitator in these two limits is plotted as a function of the collection parameter, τ_c/τ_m, in Fig. (2). For flows with moderate amounts of turbulence, one can model the effects of turbulent mixing by assignment of an equivalent diffusivity, D_t, to the flow, as was done by Leonard[5]. In that case, a third characteristic time, τ_d, defined as

$$\tau_d \equiv \frac{H^2}{D_t} \tag{1.3.10}$$

also influences the efficiency [within the limiting cases shown in Fig. (2)]. Here, the diffusion time, τ_d, is the characteristic time over which the turbulent diffusion can eliminate particle concentration gradients of spatial extent equal to the wire-plate spacing, H. Appendix 3 contains a generalization of Leonard's model, which allows for both time-average and oscillatory particle migrations.

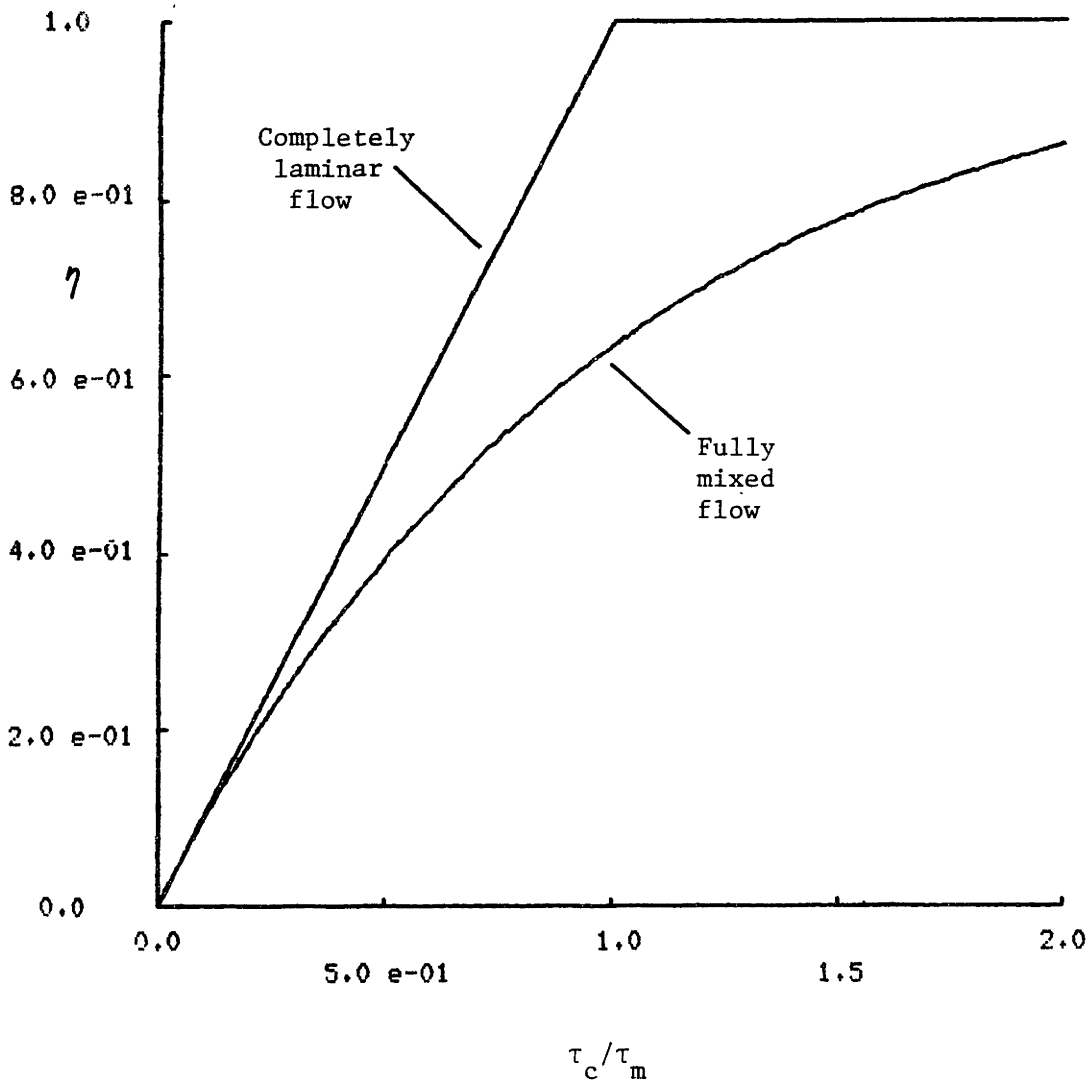

Fig. 1.2. Collection efficiency of a conventional electrostatic precipitator, as a function of the collection parameter, τ_c/τ_m, in the limits of completely laminar and fully mixed flows.

1.3.2 Problems Encountered in Precipitation of Highly-Resistive Particles

According to a recent EPA manual on the use of electrostatic precipitators, "The principle factor responsible for variations in the performance of fly ash precipitators is the resistivity of the ash"[6]. Although other effects, such as reentrainment and turbulent mixing, can affect the collection efficiency in DC precipitators, it is usually the particulate resistivity which determines whether or not effective collection will take place. Because the resistivity of fly-ash particles can range over up to seven orders of magnitude (anywhere from 10^6 - 10^{14} Ω-cm [7]), a precipitator could be expected to show significant variations in behavior from one sample to the next.

In the discussion of the previous section, no mention was made of the electrical characteristics of the precipitated layer. In fact, it was assumed that the layer would behave as a passive extension of the grounded collection plates. For ash of moderate to low resistivity ($\rho_\ell \lesssim 10^{10}$ Ω-cm, ρ_ℓ being the resistivity of the particles in the collected layer), this is usually the case[6]. For a single-stage precipitator, if the layer thickness is significant compared to the wire-plate spacing, then it can actually cause a slightly higher corona current than with the same voltage and a clean plate. This is due to the fact that the voltage is applied over a shorter distance (ie., from the wire to the edge of the layer, rather than to the plate surface).

If the ash is of high resistivity ($\rho_\ell \gtrsim 10^{11}$ Ω-cm), then the voltage drop across the collected layer may become large enough to significantly affect the precipitation process. One of two different effects can occur, depending upon the exact conditions of the ash and electrical excitation. The electric field can, to some extent, be excluded from the collection region by a surface charge on the precipitated layer. In this case, the corona current for a single-stage precipitator would be lower than the corresponding clean plate current. In fact, the corona current could conceivably be shut off if the electric field in the vicinity of the wires fell below the value necessary for breakdown.

A more common occurrence is for the electric field in the interstices between particles in the collected layer to rise beyond the breakdown strength of air, so that a localized corona discharge occurs

within the layer itself. This phenomenon, known as back corona, can have serious effects on the collection process.

Moslehi[49] performed a detailed study of the phenomena which accompany electrical breakdown of particulate layers. He observed small discharges, which he referred to as "microsparks", in a layer of fly ash with the application of macroscopic electric fields of strength, $E_o \backsim 2-3 \times 10^5$ v/m. According to his experimental results, gross breakdown occurred when the average potential gradient was roughly 10^6 v/m. This agrees with empirical observations that back corona begins when the macroscopic electric field strength in the particulate layer becomes of the order of 10^6 v/m[6,29].

Back corona, either in its steady or incipient mode, produces three effects, all of which hinder particulate collection. First, since it is another source of corona current, it can cause the precipitator to draw significantly larger currents than those due to the corona wires alone. Thus, limited power supply capabilities may force operation at lower voltages to bring the current to within a reasonable range.

The second effect is a reduction (for fixed electrode geometry) of the excitation voltage at which sparkover occurs. For negative corona, this reduction can be to less than 70% of the operating voltage with low resistivity dusts[7]. Positive coronas apparently maintain relatively constant sparkover voltages as the particulate resistivity increases.

The third way in which back corona reduces precipitation efficiency is by releasing into the collection region ions of sign opposite to those injected by the primary corona discharge electrode. With negative corona precipitation, for example, the corona wires are held at a high negative potential relative to that of the collection plates. Therefore, the electric field vector generally points away from the plates so as to direct negative ions (as well as particles charged by these ions) towards them. Any negative ions produced by back corona in the collected layer will tend to move towards the adjacent plates, while positive ions go out into the collection region towards the corona wires. These positive ions can partially discharge particles that were previously charged to a negative level by the primary corona. In some cases, the resultant lowered particle migration velocity can cause the efficiency to drop to 50% or less[7].

As stated earlier, for ashes of resistivity less than $\rho_\ell \sim 10^{10}$ Ω-cm, back corona is not normally observed. If the corona excitation voltage is raised indefinitely, the electric fields in the collection region become intense enough to trigger sparkover. For 10^{10} Ω-cm < ρ_ℓ < 10^{11} Ω-cm, sparkover normally occurs shortly after back corona begins. If $\rho_\ell > 10^{11}$ Ω-cm, a stable back corona can be established at low enough voltages that sparkover does not occur.

Since a major conducting component of fly ash particles is sulfur, those coals that contain little sulfur will tend to produce more highly-resistive particulate. Thus, while it is desirable, from the standpoint of SO_2 emissions, to burn coals that have a low sulfur content, this can cause problems in precipitation of the resulting particles.

Theoretically, the onset of back corona can be avoided by operation with a sufficiently low value of corona current. The macroscopic electric field strength in the layer is given by the product of the corona current density and the layer resistivity,

$$E_\ell = \rho_\ell J_o \tag{1.3.11}$$

where E_ℓ is the macroscopic electric field strength in the collected layer. Thus, in order to keep E_ℓ below the value necessary for back corona, one must simply choose an appropriately low corona current density,

$$J_o < \frac{E_B}{\rho_\ell} \tag{1.3.12}$$

where E_B is the value of the average electric field strength in the layer at which back corona begins.

For a fixed electrode geometry, reduction of the corona current requires that the electric field in the charging/collection region be attenuated as well. It was seen in section 1.2 that the particle migration velocity is proportional to both the charging and collection field intensities (or, to E_o^2 in the case of single-stage precipitation with simple wire-plate geometry). Thus, even assuming that the particles are charged to saturation, the collection efficiency suffers with a reduction in corona current. Since the corona discharge current generally rises very rapidly with increasing voltage after the corona is

first formed, the necessary attenuation may be small, however.

The particle charging time, τ_{ch}, also depends upon the value of J_o, as is shown in eq. (2). Thus, it is of interest to determine how it is affected by limiting the macroscopic electric field strength in the layer. Equation (12) can be combined with eq. (2) to yield a value for τ_{ch} in terms of the electric field quantities.

$$\tau_{ch} \backsim 8 \, \varepsilon_o \, \rho_\ell \, \frac{E_o}{E_B} \tag{1.3.13}$$

The product, $\varepsilon_o \rho_\ell$, is recognized as the electric relaxation time of the collected particulate layer, τ_e. The factor, E_o/E_B, is about unity (within a factor of roughly two), so that τ_{ch} is approximately an order of magnitude greater than τ_e, and can be on the order of seconds for highly-resistive collected layers ($\rho_\ell \backsim 10^{12}$–$10^{13}$ $\Omega \cdot$cm). For precipitators with residence times of this order, the effect of reducing the corona current to avoid back corona can be a drastic loss of efficiency. Even precipitators with long residence times can lose some of the major advantage of single stage collection; the ability to quickly charge and recollect particles that are entrained into the flow from the particulate layer.

Another possibly serious consequence of using very low corona currents ($J_o < 10$ nA/cm^2) is non-uniformity in the distribution of current from the discharge wires. In negative corona, which is generally used because of its aforementioned higher sparkover voltage, electrons are not emitted evenly from all parts of the wires. The discharge tends to be localized to distinct points on the wires, sometimes called "corona brushes". According to White[1], the spacing of these localized discharges increases as the corona current is decreased. This could result in non-uniform particle charging for very low currents. Unfortunately, little quantitative evidence is available relating corona brush spacing to imposed voltage or current [see Peak[8]].

In summary, there are four major reasons for the reduction in collection efficiency suffered by a precipitator when the corona current is limited by a highly-resistive particulate layer. They are : (1) The lower particle saturation charge, due to a reduced charging electric field, (2) a decreased particle migration velocity, due to the added

effect of the smaller collection electric field*, (3) a longer characteristic particle charging time, due to the reduced corona current density, and (4) spatial variations in particle charging, due to non-uniform distribution of the corona current.

It is difficult to find quantitative documentation of the effects of particulate resistivity on the overall performance of a precipitator, because many other parameters of the process, such as the particulate size or excitation voltage, can vary between different runs. Figure (3), reproduced from White[7], gives a rough idea of how the effective precipitation rate, w_{eff}, of a commercial device decreases with increasing particulate resistivity, ρ_ℓ. For a precipitator with wire-plate spacing, H, length, L, and flow velocity, U, the effective precipitation rate is defined

$$w_{eff} \equiv U\frac{H}{L}\ln\left(\frac{1}{1-\eta}\right) \qquad (1.3.14)$$

Thus, w_{eff} is the rate at which the particles would have to migrate in order that the precipitator have the efficiency, η, in the limit of complete mixing, as is seen by examination of eq. (9).

At the lowest resistivity level ($\rho_\ell \backsim 3 \times 10^9$ Ω-cm), the effective precipitation rate is roughly 13 cm/sec. This resistivity level is low enough to be considered as one at which no back corona problems exist. For the highest resistivity level ($\rho_\ell \backsim 6.6 \times 10^{11}$ Ω-cm), the effective precipitation rate is about 3.7 cm/sec, or 28% of that obtained with the lower resistivity. Very little data exists on the commercial precipitation of ashes with resistivities higher than 10^{12} Ω-cm [which, in itself, implies that precipitation of such particulate is very difficult]. In a study performed for the Electric Power Research Institute (EPRI), Ensor, et. al.[48] measured the effective precipitation rate of a commercial device burning low-sulfur coal with an ash resistivity of $\rho_\ell \backsim 2.5 \times 10^{12}$ Ω-cm, and obtained $w_{eff} \backsim 2.8$ cm/sec.

---

*The charging and collection electric fields are one and the same in a single-stage precipitator

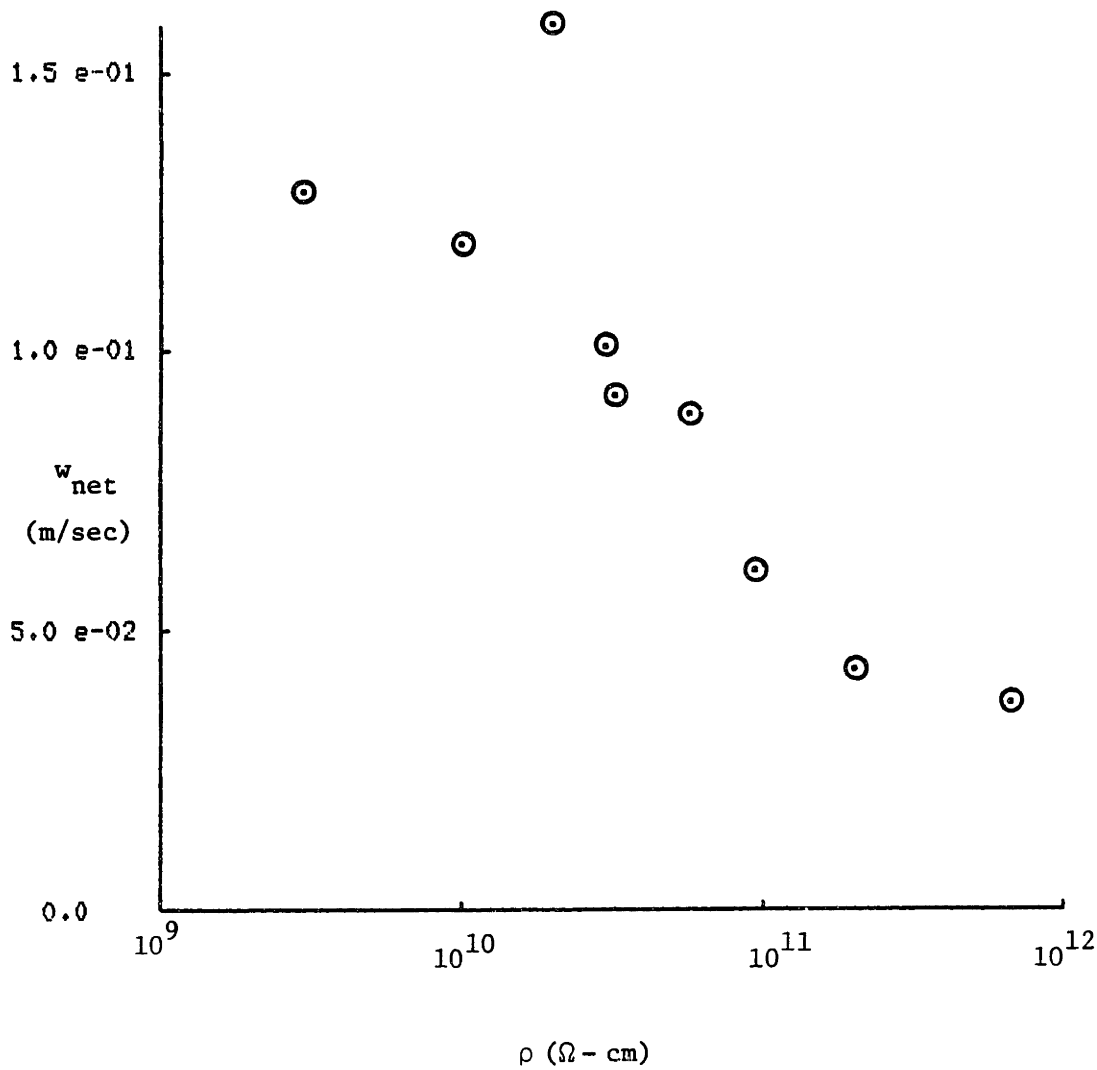

Fig. 1.3. Plot, reproduced from White[7] showing variation of effective particle migration velocity with particulate resistivity.

1.3.3 Methods of Preventing Back-Corona Problems

In a review of the literature concerned with collection of highly resistive particulate, White[7] classified methods of dealing with the above problems into three major categories: (1) keeping the collection surfaces free of dust, (2) modifying the electrical properties of the particulate or gas stream, and (3) altering the electrical excitation. Each option is discussed very briefly here. The first category was dismissed as being impractical on a large scale, due to the difficulty of completely removing a particulate layer from the plates. Even a very thin remnant can cause back corona, if the particulate resistivity is sufficiently high.

Included in the second category were flue gas conditioning methods and operating temperature changes, all of which are designed to lower the effective resistivity of the particulate. Flue gas conditioning involves the addition of chemicals to the air stream. These chemicals are adsorbed by particles and increase surface conduction. The additive most often used is sulfur-trioxide (SO_3). A primary disadvantage of such techniques is that much of the conditioning agent escapes collection and is released into the atmosphere.

Electrostatic precipitators collecting fly ash normally operate with a gas stream temperature of about 250° - 350° F [6]. It is in this same approximate temperature range, unfortunately, that the combined effects of surface and volume conduction for the ash typically yield a maximum effective resistivity[7]. Improved surface conduction at lower temperatures or volume conduction at much higher temperatures can lower the resistivity to a great enough extent that it is no longer the determining factor in collection efficiency.

The necessary cooling for low temperature collection can be provided (at some cost) by enlargement of the boiler inlet air preheater. However, problems can occur with the condensation of moisture and acid in the precipitator at such temperatures[7].

Hot side precipitators are supplied with a gas stream of temperature up to 900° F [6], as they are normally located upstream of the boiler air preheater. This necessitates a larger volume flow-rate than normal, due to the lower density of air at that temperature, as well as a much harsher operating environment. A more serious disadvantage,

however, is the possibility that resistivity problems can re-appear after a long period of operation (on the order of 100 hours or more)[9]. Thus, it seems that even hot side precipitators are not totally immune to problems with highly-resistive ashes.

Most alternative electrical excitation schemes proposed in the recent literature[10-22] involve the application of a pulsed voltage to the discharge electrodes. Typical voltage waveforms consist of a steady minimum bias voltage near the corona onset level, upon which short high voltage intervals are superimposed. The pulse width can be anywhere from a fraction of a microsecond to several milliseconds, with a repetition rate from 25 to over 1000 pulses per second. The peak pulse voltages used range up to almost three times the DC bias level. All systems examined in the above references used negative corona. Proponents of "pulsed energization" claim more uniform distribution of corona current and higher levels of particle charge, resulting in better overall collection efficiency than with DC excitation under the same conditions of ash composition and gas flowrate.

Briefly stated, a pulsed precipitator uses the capacitance of a collected particulate layer to allow application of periodic current pulses of high intensity, while still maintaining a time-average corona current density that is within the limits prescribed by eq. (12)*. If the current pulses occur with a separation in time that is short compared to the relaxation time of the material in the particulate layer, the electric field in the layer can respond only to this time-average current. An analogy can be made to the response of a parallel combination of a resistor of resistance, R, and a capacitor of capacitance, C. A periodic current is applied to the pair, with a cycle time that is much smaller than the RC time-constant of the circuit. If the AC component of the current waveform is not much greater than its time-average value, then the voltage across the resistor and capacitor will be determined essentially by the time-average current alone.

The limiting particle charge, however, is determined by the peak

---

*Because pulsed precipitators normally apply voltage pulses of the same polarity as that of the bias voltage, they must always pass some time-average current. The magnitude of this current can be made very small, however, by simply lowering the pulse repetition rate.

electric field strength experienced by the particle when it is in the presence of corona ions. With a pulsed corona excitation, one can obtain a very low time-average corona current while still maintaining high particle peak charge levels. In addition, restriction of the corona to short intervals, during which the current levels are relatively high, improves the uniformity of distribution of the current (and, thus, of the charging). In this way, pulsed precipitation overcomes two of the four factors listed at the end of section 1.3.2 as reasons for the poor performance of conventional devices with highly-resistive particulate.

The dis-advantages of pulsed precipitation are : (1) it does not significantly increase the time-average imposed electric field, so that the particles still suffer from a somewhat reduced migration velocity despite their high charge levels, (2) the time-average particle charging rate (which depends, essentially upon the time-average corona current density[22]) is not directly affected by pulsing, and (3) the added cost of power conversion components necessary to impose the pulsed voltages.

1.4 AC Electrostatic Precipitation

The concept of exciting an electrostatic precipitator with an AC voltage can be thought of as a natural extension of the pulsed unipolar precipitation discussed in the previous section. With a bipolar corona, however, one can constrain the time-average current through the particulate layer to zero value, while still maintaining large current magnitudes. The two major questions addressed in this section are : (1) Under what conditions would an AC precipitator be able to operate without any effects of back corona, regardless of the particle resistivity?, and (2) would operation under those conditions result in appreciable particulate collection? Section 1.4.3 discusses the use of two-stage AC electrostatic precipitation as a diagnostic aid in studying the turbulence characteristics of the flow in a precipitator.

1.4.1 Back Corona Prevention with AC Electrostatic Precipitation

With zero time-average corona current, the peak macroscopic electric field strength in the collected particulate layer is determined by the transient imposed electric field and current. If the normal electric field intensity immediately outside the layer is denoted by $E_a(t)$, and the surface charge on the layer, by $\Sigma_s(t)$, then the electric field strength inside the layer, $E_\ell(t)$, is

$$E_\ell(t) = E_a(t)\frac{\varepsilon_o}{\varepsilon_\ell} + \frac{\Sigma_s(t)}{\varepsilon_\ell} \qquad (1.4.1)$$

where ε_ℓ is the effective dielectric constant of the particulate layer. The dielectric constant of fly ash at 300° F is roughly[23]

$$\varepsilon_\ell \simeq 3.6\ \varepsilon_o \qquad (1.4.2)$$

With the electric field outside of the layer, $E_a(t)$, limited[6] to roughly 5×10^5 v/m, the contribution due to the first term of eq. (1) is usually negligible in comparison to the maximum allowable macroscopic field strength in the layer, $E_B \simeq 10^6$ v/m. Thus, for purposes of predicting breakdown in the collected layer, eq. (1) may be approximated

$$E_{\ell,max} \backsim \frac{\Sigma_{s,max}}{\varepsilon_\ell} \qquad (1.4.3)$$

where $E_{\ell,max}$ and $\Sigma_{s,max}$ are the maximum values of E_ℓ and Σ_s, respectively. The electric field in the layer is of maximum magnitude at the end of each half-cycle, when the corona current reverses sign. At that point, the surface charge magnitude* is approximately

$$\Sigma_{s,max} \sim \frac{J_o T}{4} \tag{1.4.4}$$

The requirement that $E_{\ell,max}$ be smaller than the breakdown electric field strength, E_B, is thus satisfied if

$$T < 4 \frac{\varepsilon_\ell E_B}{J_o} \tag{1.4.5}$$

The estimate of $\Sigma_{s,max}$ given in eq. (4) is conservative (ie., it is likely to be high), as it assumes no attenuation in the surface charge due to conduction in the layer. Thus, in the limit of very high particulate resistivity ($\rho_\ell \to \infty$), the cycle time should not be much greater than the time on the right in eq. (5). This will insure that the transient accumulations of surface charge are not sufficient to cause breakdown in the collected particulate layer.

1.4.2 Particle Charging and Migration in an AC Corona

It was noted in section 1.3.1 that, as long as the particles were charged to the same sign as the ions that were moving from wires to plates, the particles themselves would also move toward the plates. Particles that are subjected to an AC corona will receive alternately positive and negative charging currents. A particle's charge could change sign during every half-cycle of the excitation. The amount of time that a particle spends during each half-cycle with a charge of the same sign as that of the corona ions around it, relative to the time it spends with an opposite charge is determined by the dynamics of the charging process. Certainly, if the cycle time, T, is much longer than the characteristic charging time, τ_{ch}, then the particles are able to

---

*The current density, J_o, is multiplied by 1/4 of a cycle time, T, to account for the fact that a corona of one sign is present for 1/2 of a cycle, during which time it must first remove the charge remaining from the previous half-cycle, then charge the layer.

reverse their charge very quickly relative to changes in the excitation voltage. In this case, they will spend most of each half-cycle migrating toward the plates In the opposite extreme, the particles could conceivably spend a significant fraction of each half-cycle simply removing the charge that existed at the end of the previous half-cycle, making little net progress toward a collection surface.

In chapter 3, a simplified model is proposed for the charging of particles in spatially-uniform AC electric field and corona current density. In that chapter, the intuitive arguments given above are verified by the use of both analytical and numerical simulations of the model*. It is seen there that, if the excitation cycle time is much longer than the charging time, then the time-average particle migration velocity will be of the order of that which it would attain with a DC excitation of similar field strength. Thus, in order to insure a time-average migration velocity that is of this order, it is not unreasonable to impose the constraint that the time of one half-cycle of the excitation be greater than the characteristic charging time.

$$T > 2\,\tau_{ch} = 16\,\frac{\varepsilon_o\,E_o}{J_o} \qquad (1.4.6)$$

[Equation (1.3.2) was used to substitute for τ_{ch}].

Comparison of eqs. (5) and (6) shows that the cycle time of an AC electrostatic precipitator is tightly constrained. This is due to the simultaneous requirements that : (1) the particles be charged nearly to saturation each half-cycle, while (2) the collected layer not receive enough charge in that time to cause breakdown there. Thus,

$$16\,\frac{\varepsilon_o\,E_o}{J_o} < T < 4\,\frac{\varepsilon_\ell\,E_B}{Jo} \qquad (1.4.7)$$

The constraint of eq. (7) defines an interval of finite width, because $\varepsilon_\ell/\varepsilon_o \simeq 3.6$ and $E_B/E_o \backsim 2$. However, if a 60 Hz excitation is to be used [so that T = 1/60 sec], then the corona current density must be raised to roughly

---

*It should be noted that the models of chapter 3 apply under a restrictive set of conditions, outlined in the problem statement of section 3.2

$$J_o \backsim 0.5\ \mu A/cm^2 \tag{1.4.8}$$

in order to satisfy eq. (7) with the maximum allowable imposed electric field strength.

Thus, it is seen that, if the corona current density is increased by roughly an order of magnitude over the levels commonly used, a 60 Hz AC electrostatic precipitator could be expected to charge and collect particles at a rate that is comparable to that of a conventional device. The analysis of chapter 3 and experimental results of chapter 4 show that the effective migration velocity of particles in such a device is roughly 1/4 of that obtained with a DC excitation of the same RMS voltage magnitude. The AC precipitator would have a great advantage in the precipitation of highly-resistive particles, however, as its operation does not depend upon the ability of the collected particulate layer to conduct any of the corona current.

1.4.3 Two-Stage AC Electrostatic Precipitation

If pre-charged particles are injected into a corona-free region and subjected to a uniform AC electric field with zero time-average value, then they will execute oscillatory migrations. With a particle mobility, b_p, peak electric field strength, E_o, and excitation frequency, ω, the maximum particle displacement, ℓ_{max} (due to migration), is

$$\ell_{max} = 2\,\frac{b_p E_o}{\omega} \tag{1.4.9}$$

Given particles of mobility, $b_p \backsim 5 \times 10^{-7} m^2/v \cdot sec$, a peak electric field strength of $E_o \backsim 5 \times 10^5$ v/m, and a 60 Hz excitation frequency, $\ell_{max} \backsim 1.3$ mm.

This length is much smaller than the typical plate separation in a commercial precipitator. If the flow in such a collector were laminar, then almost negligible collection would be expected*. In most practical precipitators, however, the Reynolds number is of the order of 10,000.

---

*Only those particles that entered within the distance, ℓ_{max}, of a collection plate would be precipitated.

The naturally-occurring flow turbulence in a precipitator could eventually bring each particle to within a short distance of a collection plate, so that their oscillatory migrations alone could precipitate them.

Two conditions must be satisfied if this is to result in significant particle collection : (1) The turbulence must be capable of bringing many of the particles near to the plates in a time that is of the order of or less than the gas residence time in the device, and (2) the region of turbulent mixing must extend to within a short distance of the collecting plates, so that particles are brought to within their maximum migration length, ℓ_{max}.

It is seen that a two-stage AC precipitator can be made to be very sensitive to the flow conditions in its collection region. In particular, the frequency response of such a device could yield valuable information about the turbulent transport of boundary-layer flows.

1.5 Review of Relevant Literature

1.5.1 Particle Charging Studies[21-31]

The works reviewed in this section include theoretical and experimental studies of particle charging both in unipolar and bipolar coronas*.

White[24] reviewed the early theories of Rohmann[25] and Pauthenier[26] for electric field charging and those of Arendt[27] for diffusional charging of particles. He derived a simplified equation for the diffusional charging process that is much more easily applied over a wider range of situations than Arendt's. He cited experimental results from the literature in support of both the field charging and diffusional charging models, concluding that the latter effect is dominant only for particles smaller than 0.2 μm in diameter.

Mizuno[21] included theoretical considerations of particle charging in pulsed coronas and in what he terms as "bi-ionized fields". The latter topic concerns the charging of particles that are simultaneously subjected to both positive and negative ion-fluxes in the presence of an imposed electric field. Research in this area by Mizuno and others[28,29,33] is motivated by a desire to understand the degradation in particle charge that results from effects of ions produced by back corona in a precipitator.

The methods used for experimental observations of particle charging ranged from calculations based upon measured precipitation efficiencies under well-controlled conditions to optical observations of particla trajectories, via photography or laser-Doppler velocimitry.

Anderson[31] measured the charge on individual particles entering and leaving a precipitator, using an apparatus similar to that of the Millikan oil drop experiment. He obtained reasonable agreement with the classical values of saturation charge for particles in the size range of 0.4 - 4.0 μm diameter.

---

*Here, the term bipolar refers to the simultaneous application of both positive and negative corona ion fluxes, not alternating coronas, as is studied in chapter 3

Fjeld[33] subjected particles in the size range, 0.3 - 1.0 μm diameter, to bi-ionized coronas and measured the saturation charge as a function of particle size, charging electric field strength, and a current ratio parameter, γ, defined

$$\gamma \equiv \frac{J_+}{J_-} \tag{1.5.1}$$

where J_+ and J_- are the corona current density magnitudes due to the positive and negative ions, respectively. He measured the charge by optically counting the rate at which the particles exited a precipitator of known dimensions and collecting electric field. He obtained reasonable agreement with a theory based upon bipolar electric field charging, except in the limit of very small electric field strengths. In that case, he found that diffusional charging processes were important in determining the limiting particle charge.

Mazumder[32] measured simultaneously both the size and charge of particles, using an LDV to observe their response to a 40 kHz sinusoidal imposed electric field. By measuring both the magnitude and the phase of the particle motions (relative to those of the electrical excitation), he was able to obtain constraints on the particle size and charge. He made few comparisons between theory and experiment, the major purpose of the publication being, apparently, to present the measurement system as a useful diagnostic tool.

Lawless[34] used an LDV to observe the motions of particles in a single-stage precipitator. He determined particle mobilities from measured velocities through the use of a numerically-calculated solution for the electric field strength in the precipitator. Without accounting for any effects of the induced corona wind upon the particle velocities, he obtained order-of-magnitude correlation with a model that simply assumed that the particles were charged to saturation in an electric field strength equal to that which existed near the collection plates. Masuda[35] performed particle LDV velocity measurements in a single-stage precipitator with results that were similar to those of Lawless.

In summary, those works reviewed above found good agreement between theoretical calculations and experimental measurements of particle charging for situations in which the charging conditions were well-controlled. Even in highly non-uniform fields, crude models could

be used to give order-of-magnitude estimates of the particle charge.

The effects of bi-ionized coronas on particle charging are of interest in AC corona charging, even though the intent there is to prevent the occurrence of back corona. In the limit of high frequency excitations, for which the ion transit times are of the order of or longer than the excitation cycle time, particles could be subjected simultaneously to both positive and negative corona ions, as the ions would not be swept out by the electric field between half-cycles.

The last work to be reviewed in this section was not specifically concerned with particle charging in electrostatic precipitators, but is included because of its relevance to the problems investigated in this thesis. Radun[47] used a mobility analyzer to measure the charges attained by particles convected past a single corona wire suspended transverse to an imposed flow. The practical situation under study in his work was the contamination of high-voltage DC power transmission lines by precipitated atmospheric dusts. He developed a mathematical framework for dealing with the general problem of steady charging and precipitation of particles from a turbulent flow in the presence of non-uniform electric fields and corona current densities.

He accounted for effects of charging, migration, and turbulent diffusion of particles by assigning to each point in space a continuous mobility distribution function and requiring that that function satisfy simultaneously the laws of conservation of particle charge, mass and momentum in the imposed flow, electric and current density fields. The presence of turbulent eddies was modeled by the use of an effective eddy diffusivity, as is discussed in the following section. He was able to predict, with reasonable accuracy, the measured mobility statistics of particles downstream of the single corona wire.

Although his results were derived only for steady processes, they could (in principle) be adapted to the situation of steady-state AC charging and precipitation of particles. The equations are combersome, however, and include many detailed parameters of the imposed electrical and flow conditions.

1.5.2 Turbulent Diffusion in Electrostatic Precipitators[36-41]

This section reviews efforts made by researchers to model the effects of turbulent mixing on precipitator performance. The concept of accounting for flow turbulence via an equivalent diffusivity was introduced by Taylor[40]. Early models for electrostatic precipitation [Deutsch[41]] assumed that the effective flow diffusivity, D_t, was so large as to eliminate any transverse particulate concentration gradients in the precipitator. In recent years, efforts have been directed toward modeling the behavior of precipitators in the presence of moderate diffusivities, so that turbulent mixing is significant, but not the dominant particle transport mechanism.

Leonard[37] provided a review of the theoretical and experimental work that led from the Deutsch model for precipitation to his own, which he termed a "convective diffusion model". Assuming a flow with uniform mean velocity, effective turbulent diffusivity, and particle migration velocity, he solved analytically for the particle concentration as a function of position in the idealized precipitator. To verify these predictions, he injected pre-charged particles into a collection region with a uniform imposed electric field, and measured the concentration profiles in situ using an optical particle counter. The flow turbulence was varied by the use of grids and baffles placed upstream of the precipitation region. With flow parameters similar to those used in this thesis research [H = 5 cm, U ≈ 3 m/sec], he obtained good agreement between theory and experiment. The effective diffusivities fitted to the data ranged from 6×10^{-4} to 3×10^{-3} m^2/sec, depending upon the imposed flow conditions.

Pyle[36] determined the effective diffusivity in a precipitator by injecting particles through a point source at the inlet and measuring the rate at which the beam of particles spread as it was convected downstream by the mean flow. He used an isokinetic sampling probe, combined with an optical particle counter to measure the particle concentration as a function of position in the precipitator. With a flow velocity of 1.9 m/sec, and a plate spacing of 20 cm, he observed diffusivities of the order of $1 - 2 \times 10^{-3}$ m^2/sec. In order to avoid effects of particle migration in the measurement, Pyle ran his initial experiments with no electrical excitation at the corona wires. He then

repeated them with currents present and accounted for differences in the spreading of the beam by an increased diffusivity in the direction normal to the plates. This assumption is questionable, as it is likely that the increased particle spreading was at least partially due simply to the particle migration toward the plates.

Robinson[44] avoided problems with particle charging by measuring the spread of a tracer beam of helium, also injected from a point source at the inlet of a precipitator of dimensions and flow typical of a commercial device [2H = 25.4 cm, U = 1 - 7 m/sec]. He obtained diffusivities ranging from $1 - 8 \times 10^{-3}$ m^2/sec, depending upon the flow conditions and corona excitation level*.

It would seem, from the results of Leonard, Pyle, and Robinson, that the effects of turbulent mixing in a precipitator can be modeled with reasonable accuracy by assignment of an equivalent diffusivity to the flow. Whether or not it is appropriate to assume complete mixing (as did Deutsch) depends upon the specific parameters of the device and flow under consideration.

1.5.3 Corona Wind in Electrostatic Precipitators[42-46]

The corona wind in an electrostatic precipitator is an air flow induced by electric field forces on the corona ions. This force is transmitted to the surrounding neutral air molecules by collisions. The authors cited in this section carried out theoretical and experimental research both into the origins of the corona wind and into its effects on particle distributions in a precipitator.

Yabe[42] measured the current distribution at a plate with a parallel corona wire suspended above it. He also made indirect measurements of the corona wind velocity at the wire and at the plate by observation of the stagnation pressure at each. With a wire-plate spacing of 2 cm, and a current of 200 μA/m, the measured pressure implied a peak induced velocity of 1.4 m/sec. The corona wind was the only flow present in the experiment [ie., there was no imposed

---

*His work is also cited, in the next section, as it pertains to corona wind studies as well.

cross-flow]. Positive corona was used for all measurements.

He used the measured plate current distribution to compute the volume ion charge, ρ_i, and electric potential, Φ, as functions of position in the vicinity of the wire and plate electrodes. An electrostatic (Langmuir) probe was used to verify the potential function. The potential and space charge functions then served as driving functions (ie., a body force) for a numerical determination of the flow field. The computation predicted recirculating convection cells on either side of the wire. He obtained reasonable agreement with the measured pressure profiles at the plate.

Yamamoto[43] extended Yabe's work to include an imposed cross-flow between plates bounding the wire on either side. He observed stagnation pressures at a plate, as well as schlieren visualizations of the flow. He used a plate spacing of 3 cm, corona voltages of up to 15 kV, corona currents of the order of 1 mA/m, and flow velocities of 0 - 9.1 m/sec. His coronas were restricted to positive voltages, as were Yabe's. Because of the high ion migration velocities, he found little effect of the transverse flow on either the corona current distribution at the plate or the electric potential in the region between the plates. The corona wind was, however, strongly influenced by the imposed flow. As the cross-flow velocity was increased, the circulatory convection cells predicted and measured by Yabe were initially shifted downstream, and eventually disappeared. Yamamoto was able to model this phenomenon with a numerical simulation of the electrical and fluid flow equations.

In his analytical work, he defined a parameter that he called the relative Reynolds number, N_{EHD}.

$$N_{EHD} \equiv \frac{R_{EHD}}{R_E} = \frac{U_E}{U} \tag{1.5.2}$$

where R_E is the Reynolds number, based upon the imposed flow velocity, U, and R_{EHD} is the Reynolds number, based upon the characteristic velocity, U_E, and

$$U_E \equiv \left(\frac{\rho_c \, V_o}{\rho} \right)^{\frac{1}{2}} \tag{1.5.3}$$

The velocity, U_E, is seen to represent the velocity attained by a material of charge density, ρ_c, mass density, ρ, when it is accelerated through the electric potential, $V_o/2$. He found that, for values of N_{EHD}

that were greater than 0.6, the effect of the corona wind on the flow was significant.

Leonard[42] observed corona wind and its effects on the turbulence in a single wire precipitator using schlieren photography, smoke visualization, as well as laser and hot-wire anemometry. He defined a dimensionless similarity parameter,

$$\frac{i}{\ell\, b_i\, \rho\, U^2} \tag{1.5.4}$$

where i/ℓ is the corona current per unit length of wire, b_i is the corona ion mobility, ρ is the gas density, and U is the mean streamwise flow velocity. This parameter can be thought of as the ratio of electric field forces to inertial forces on the fluid. It can be argued that Leonard's parameter is closely related to Yamamoto's relative Reynolds number, N_{EHD}. To within an order of magnitude,

$$\frac{i}{\ell} \sim J_o\, H \sim \rho_c\, b_i\, E_o\, H \sim \rho_c b_i\, V_o \tag{1.5.5}$$

where H is the wire-plate spacing and J_o is the corona current density. Thus,

$$N_{EHD}^2 \sim \frac{i}{\ell\, b_i\, \rho\, U^2} \tag{1.5.6}$$

With positive corona, he verified Yamamoto's conclusion that the recirculating convection cells predicted by Yabe were shifted for low cross-flow velocities, and eventually eliminated for higher velocities. He found that the induced cells were significant only for $i/\ell b_i \rho U^2 \sim 5$ or greater [Typical values of this variable for commercial precipitators range from 0.2 - 2.0]. The bulk flow was shown by the schleiren technique to be laminar and steady. He accounted for turbulence generated at the side walls [those perpendicular to the wires] to non-uniformities in the corona current at the ends of the wires, due to "current quenching" effects of the walls.

With negative coronas, the bulk flow was always somewhat turbulent. He claimed that this was due to the non-uniform nature of the negative corona. Multi-wire tests gave similar results. In general he

found little effect of the corona wind for values of $i/\ell b_i \rho U^2 < 0.5$. His line of demarcation between significant and insignificant effects of corona wind was remarkably close to that of Yamamoto. Equations (2) and (6) can be used to provide an estimate of Yamamoto's characteristic velocity, U_E, in terms of the corona current per unit length of wire, i/ℓ, the ion mobility, b_i, and gas density, ρ.

$$U_E \sim \left[\frac{i/\ell}{b_i \rho} \right]^{\frac{1}{2}} \tag{1.5.7}$$

Robinson's[46] study of turbulent diffusion in electrostatic precipitators included a determination of its dependence upon the corona current levels, under a variety of flow conditions. In addition to measuring the spread in the injected helium stream [see section 1.5.2], he measured the translation of its center, to give an indication of the mean transverse flow velocities induced by the corona. For low imposed (cross-flow) velocities, the effective lateral diffusivity was proportional to the corona current. At higher imposed flow velocities, the diffusivity was essentially independent of current. Although Robinson did not use Leonard's dimensionless similarity parameter, it is seen from his data that the point at which the corona current became significant in determining the turbulent diffusivity was for $i/\ell b_i \rho U^2 \sim 0.1$. The measured effective transverse velocities were roughly proportional to the square root of the corona current for a fixed cross-flow velocity, and were of the order of 25 cm/sec. The constant of proportionality decreased with increasing flow velocity.

In summary, it is likely that the theoretical models of both Yabe and Yamamoto included those effects that were significant to the problems that they examined, as they predicted their respective experimental results with fair accuracy. The results of Leonard, Yamamoto, and Robinson leave some doubt as to the importance of the corona wind in determining the effective diffusivity of the flow in a commercial precipitator. There seems to be disagreement between the three over the current level at which it exerts a significant influence over the turbulent mixing processes.

References for Chapter 1

[1] White H.J., Industrial Electrostatic Precipitation, Addison Wesley Publishing Co. Inc., Reading, Mass. (1963).

[2] White H.J., "Review of the State of the Technology", Proceedings International Conference on Electrostatic Precipitation, Monterey, California, p. 16 (October, 1981).

[3] Melcher J.R., Sachar K.S., Warren E.P., "Overview of Electrostatic Devices for Control of Submicrometer Particles", Proceedings IEEE Vol. 65, No. 12 (December, 1977).

[4] Alexander J.C., Davey K.R., Melcher J.R., "Comparative Study of Direct and Alternating Current Electric and Magnetic Precipitation from Laminar and Turbulent Flows", Ind. Eng. Fundam., Vol. 20, No. 3, pp. 207 - 216 (1981).

[5] Leonard G., Mitchner M., Self S.A., "Particle Transport in Electrostatic Precipitators", Atmospheric Environment Vol. 14, pp. 1289 - 1299 (1980).

[6] McDonald J.R., Dean A.H., "A Manual for the use of Electrostatic Precipitators to Collect Fly-Ash Particles", EPA-600/8-80-025, Contract No. 68-02-2114, Task No. 7, Southern Research Institute, 2000 Ninth Avenue South, Birmingham, Alabama, 35205 (May, 1980).

[7] White H.J., "Resistivity Problems in Electrostatic Precipitation", Journal Air Pollution Control Society, 24:314 (1974).

[8] Peak F.W. Jr., Dielectric Phenomena in High-Voltage Engineering, McGraw-Hill, New York (1929).

[9] Bickelhaupt R.E., "Comments on Fly Ash Resistivity", Proceedings International Conference on Electrostatic Precipitation, Monterey, California, p. 375 (October, 1981).

[10] Lausen P., Petersen H.H., Joergensen H.J., "Theory and Application of Pulsed Energization", Proceedings International Conference on Electrostatic Precipitation, Monterey, California, p. 531 (October, 1981).

[11] Petersen H.H., Lausen P., "Precipitator Energization Utilizing an

Energy Conserving Pulse Generator", Second Symposium of the Transfer and Utilization of Particulate Control Technology, Denver, Colorado, (July, 1979).

[12]Piulle W., DuBard J., "Investigation of Key Parameters Affecting Pulsed Precipitator Performance", Proceedings International Conference on Electrostatic Precipitation, Monterey, California, p. 515 (October, 1981).

[13]Feldman et. al., "Pulsed Electrostatic Precipitator" U.S. Patent #4,209,306 (June, 1980).

[14]Milde H.I., Feldman P.L., "Pulse Energization of Electrostatic Precipitators", Paper 2D, Presented at IEEE IAS Annual Meeting, (1978).

[15]Milde H.I., VanHoesen H.E., "Application of Fast Rising Pulses to Electrostatic Precipitators", Paper 6A, Presented at IEEE IAS Annual Meeting (1979).

[16]Rugg D., Durham M., Rinard G., Sparks L.E., "Electrostatic Precipitator Performance With Pulse Excitation", Third Symposium on the Transfer and Utilization of Particulate Control Technology, Orlando, Florida (March, 1981).

[17]Sparks L.E., Ramsey G.H., Valentine R.E., "Comparison of Electrostatic Precipitator Performance with Pulse and DC Energization", Proceedings International Conference on Electrostatic Precipitation, Monterey, California, p. 556 (October, 1981).

[18]Petersen H.H., Lausen P., "Application of Energy Conserving Pulse energization For Precipitators, Practical and Economic Aspects", Third Symposium on the Transfer and Utilization of Particulate Control Technology, Orlando, Florida (March, 1981).

[19]Kumar K.S., Milde H.I., "The Results of First Full-Scale Utility Demonstration of Pulsed Precipitation", Paper 6G Presented at IEEE IAS Annual Meeting (1979).

[20]Thanh L.C., "Characteristics of a Corona System Under Negative Direct and Pulsed Voltage", J. Physics D. : Applied Physics Vol 12 (1979).

[21]Mizuno A., "Review of Particle Charging Research", Proceedings International Conference on Electrostatic Precipitation, Monterey, California, p. 304 (October, 1981).

[22]Masuda S., Doi I., Aoyama M., Shibuya A., "EP-ES Type Precipitator and Bias-Controlled Pulse Charging System", 1975 Conference on Electrostatics, Electrostatic Society of America, University of Michigan, Ann Arbor, Michigan, (June, 1975).

[23]Tassiker O.J., "The Temperature and Frequency Dependence of the

Dielectric Constant of Power-Station Fly Ash", Staub-Reinhalt, Luft Vol. 31 No. 8 (August, 1971).

[24]White H.J., "Particle Charging in Electrostatic Precipitation", AIEE Transactions 70:1186 (1951)

[25]Rohmann H., "Method of Size Measurement for Suspended Particles", Zeitschrift fur Physik, Vol. 17, p. 253, Berlin, Germany (1923).

[26]Pauthenier M.M., Moreau-Hanot M., "Charging of Spherical Particles in an Ionizing Field", Journal de Physique et Le Radium, series 7, Vo., 3, p. 590, Paris, France (1932).

[27]Arendt P., Kallmann H., " The Mechanism of Charging of Mist Particles", Zeitschrift fur Physik, Vol. 35, p. 421, Berlin, Germany (1925).

[28]Oglesby, S. Jr., Nichols G.B., Electrostatic Precipitation, Marcel Dekker Inc., New York (1978).

[29]Masuda S., "Resistivity and Back Corona", Proceedings International Conference on Electrostatic Precipitation, Monterey, California, p. 340 (October, 1981).

[30]Masuda S., Nonogaki Y., "Bi-Ionized Structure of Back Discharge Field in an Electrostatic Precipitator", Record of IEEE/IAS Annual Meeting (1981).

[31]Anderson M.H., McDonald J.R., Mosley R.B., "Particle charge Measurements", Proceedings International Conference on Electrostatic Precipitation, Monterey, California, p. 499 (October, 1981).

[32]Mazumder, M.K., Renninger R.G., Chang T.H., Raible R.W., Hood W.G., Ware R.E., Sims R.A., "Simultaneous Measurements of Aerodynamic Size and Electric Charge of Aerosol Particles in Real Time on a Single Particle Basis", Third Symposium on the Transfer and Utilization of Particulate Control Technology: Volume II (Electrostatic Precipitators), p. 1 July, 1982).

[33]Fjeld R.A., Gauntt G.J., Laughlin G.J., McFarland A.R., "The Application of Measurements of Aerosol Charge Acquisition by Bipolar Ions to the Problem of Back Corona", Third Symposium on the Transfer and Utilization of Particulate Control Technology: Volume II (Electrostatic Precipitators), p. 179 (July, 1982).

[34]Lawless P.A., Damle A.S., Viner A.S., Shaughnessy E.J., Sparks L.E., "Laser Doppler Anemometer Measurements of Particle Velocity in a Laboratory Precipitator", Third Symposium on the Transfer and Utilization of Particulate Control Technology: Volume II (Electrostatic Precipitators), p. 25 (July, 1982).

[35]Masuda S., Akutsu K., Kanno Y., "Motion of Small Charged Particles Inside an Electrostatic Precipitator", IEEE Industrial

Applications Society, 79:5C (1979).

[36]Pyle B.E., Pontius D.H., Snyder T.R., Sparks L.E., "Particle Trajectory Studies in a Scale Model Electrostatic Precipitator", 73'rd Annual Meeting of the Air Pollution Control Association, Montreal, Quebec (June, 1980).

[37]Leonard G.L., "Effect of Turbulence on Electrostatic Precipitator Performance", High Temperature Gasdynamics Laboratory, Report No. 196, NSF Grant No. CPE-7926290 and EPRI Contract No. EPRI-RP-533-1, Mechanical Engineering Department, Stanford University, Palo Alto, California (April, 1982).

[38]Leonard G.L., Mitchner M., Self S.A., "Experimental Study of the Effect of Turbulent Diffusion on Precipitator Efficiency", Journal of Aerosol Science, Vol. 13, No. 4, p. 271 (1982).

[39]Feldman P.L., Kumar K.S., Cooperman G.D., "Turbulent Diffusion in Electrostatic Precipitators", Atmospheric Emissions and Energy Source Pollution (AIChE Symposium Series), Vol. 73, No. 165.

[40]Taylor G.I., "Diffusion by Continuous Movements", Proc. London Math Soc., Vol. A 20, p. 196 (1921).

[41]Deutsch W., Ann. der Physik 68:335 (1922).

[42]Leonard G.L., Mitchner M., Self S.A., "An Experimental Study of the Electrohydrodynamic Flow in Electrostatic Precipitators", J. Fluid Mechanics, Vol. 127, p. 123 (1983).

[43]Yabe A., Mori Y., Hijikata K., "EHD Study of the Corona Wind Between Wire and Plate Electrodes", AIAA Journal, Vol. 16, No. 4 (April, 1978).

[44]Yamamoto T., Velkoff H.R., "Electrohydrodynamics in an Electrostatic Precipitator", J. Fluid Mechanics, Vol. 108, p. 1 (1981).

[45]Mitchner M., Leonard G.L., Self S.A., "Corona-Induced Turbulence", Fourth Symposium on the Transfer and Utilization of Particulate Control Technology, Houston, Texas (October, 1982).

[46]Robinson M., "Effects of the Corona Discharge on Electric Wind Convection and Eddy Diffusion in an Electrostatic Precipitator", PhD Thesis, Cooper Union School of Engineering and Science, New York (1975).

[47]Radun A., "Particle Charging in a Turbulent Air Stream", PhD Thesis, MIT Dept. of Elect. Eng. and Comp. Sci., Cambridge, Mass., (1981).

[48]Ensor D.S., Cowen S., Hooper R., Markowski G., "Evaluation of the George Neal Station #3 Electrostatic Precipitator", EPRI Report #FP-1145, Project #780-1 (August, 1979).

[49]Moslehi B., "Electromechanics and Electrical Breakdown of Particulate Layers", High Temperature Gasdynamics Laboratory, Report No. T-236, EPRI Contract No. EPRI-RP-533-1, Mechanical Engineering Department, Stanford University, Palo Alto, California (December, 1983).

Chapter 2

Description of Test Facility

2.1 Introduction

The hardware and software used for experiments performed on the laboratory-scale precipitator are presented in this chapter. Appendix 1 contains more detailed descriptions of the individual hardware components and computer programs. Only that information which is essential to understanding the results reported in later chapters is included here. Section 2.2 describes the basic setup for charging, mixing, and precipitation experiments. A brief description of the programs used to acquire and process data from the experiments is given in section 2.3.

2.2 Experimental Hardware

Figures 1 and 2 give an overview of the basic experimental setup. Briefly, a monodisperse aerosol of dioctyl-phthalate (DOP) is injected into an air flow entering the precipitator at the left (Fig. 1). A high potential (either DC or AC) is applied to thin steel wires. The wires extend in the flow direction, halfway between grounded metal plates which form the top and bottom walls of the device. Ions that carry the corona currents from wires to plates charge the incoming particles, some of which are precipitated immediately. Those particles remaining in the flow are carried to a second region in which a thin aluminum plate is suspended halfway between the grounded top and bottom tunnel walls. The plate can be held at a high potential (again, either AC or DC), imposing a relatively uniform electric field over the immediate region.

The glass side-walls of the device allow observation of particles in both the charging and precipitation regions with a laser-Doppler-velocimeter (LDV). The entire LDV system, pictured in more detail in Fig. (3), is mounted on a movable structure. It can be positioned to observe either streamwise or transverse particle velocities at most points within the precipitator. Particle velocity and

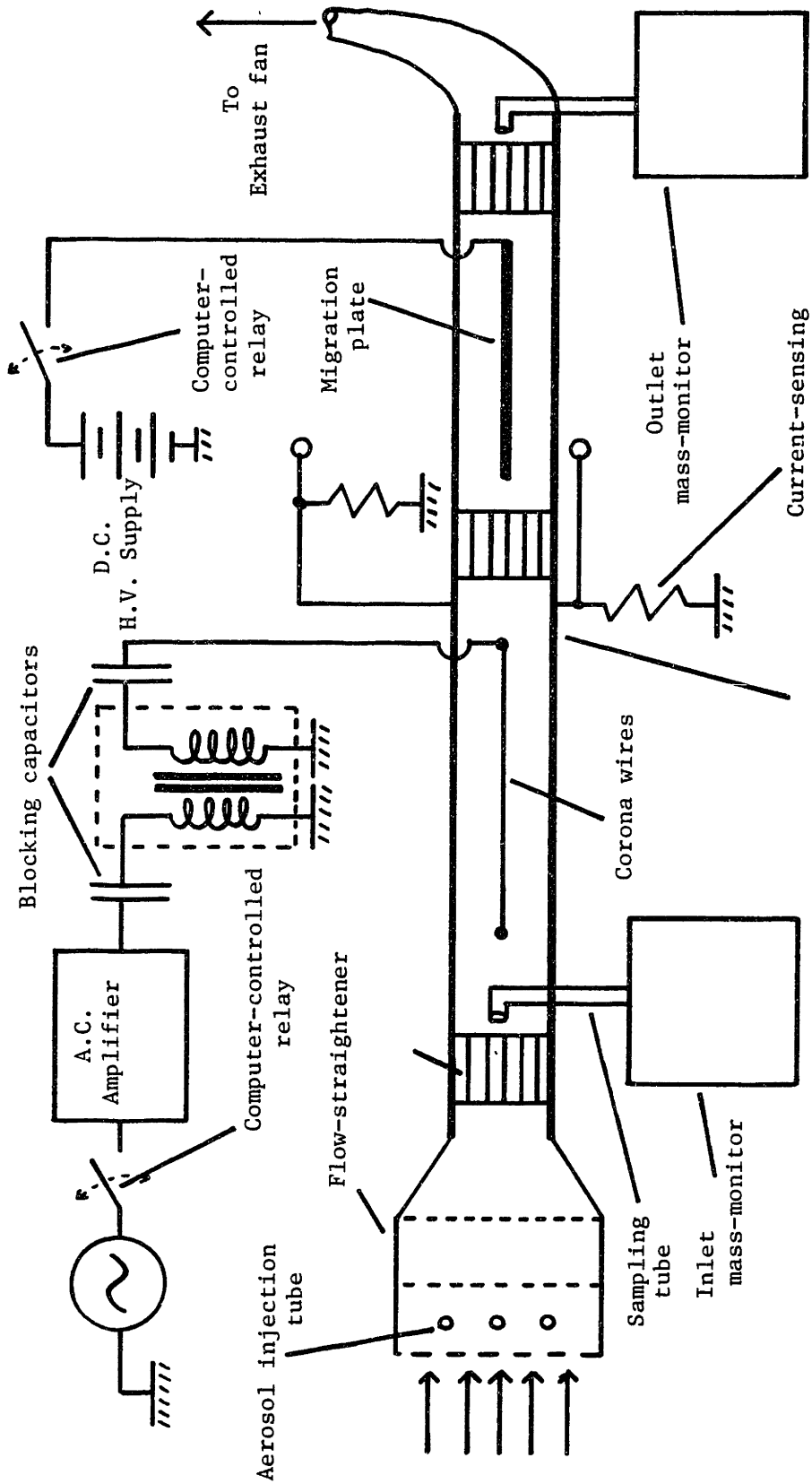

Fig. 2.1 Schematic side-view of laboratory-scale electrostatic precipitator. Air enters at left, driven by fan downstream of the tunnel exit on right (fan not shown).

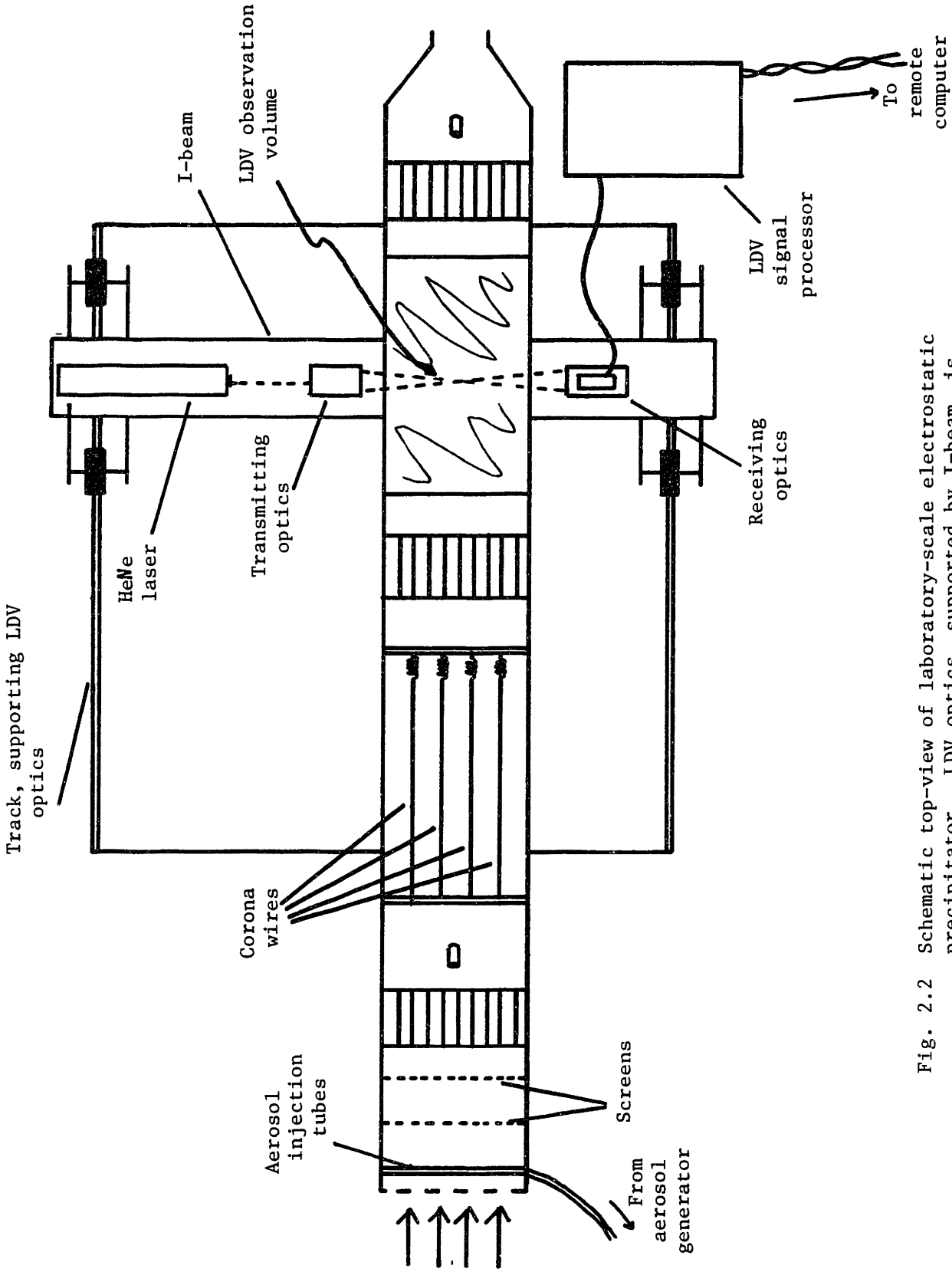

Fig. 2.2 Schematic top-view of laboratory-scale electrostatic precipitator. LDV optics, supported by I-beam, is mounted on a track to allow streamwise movement.

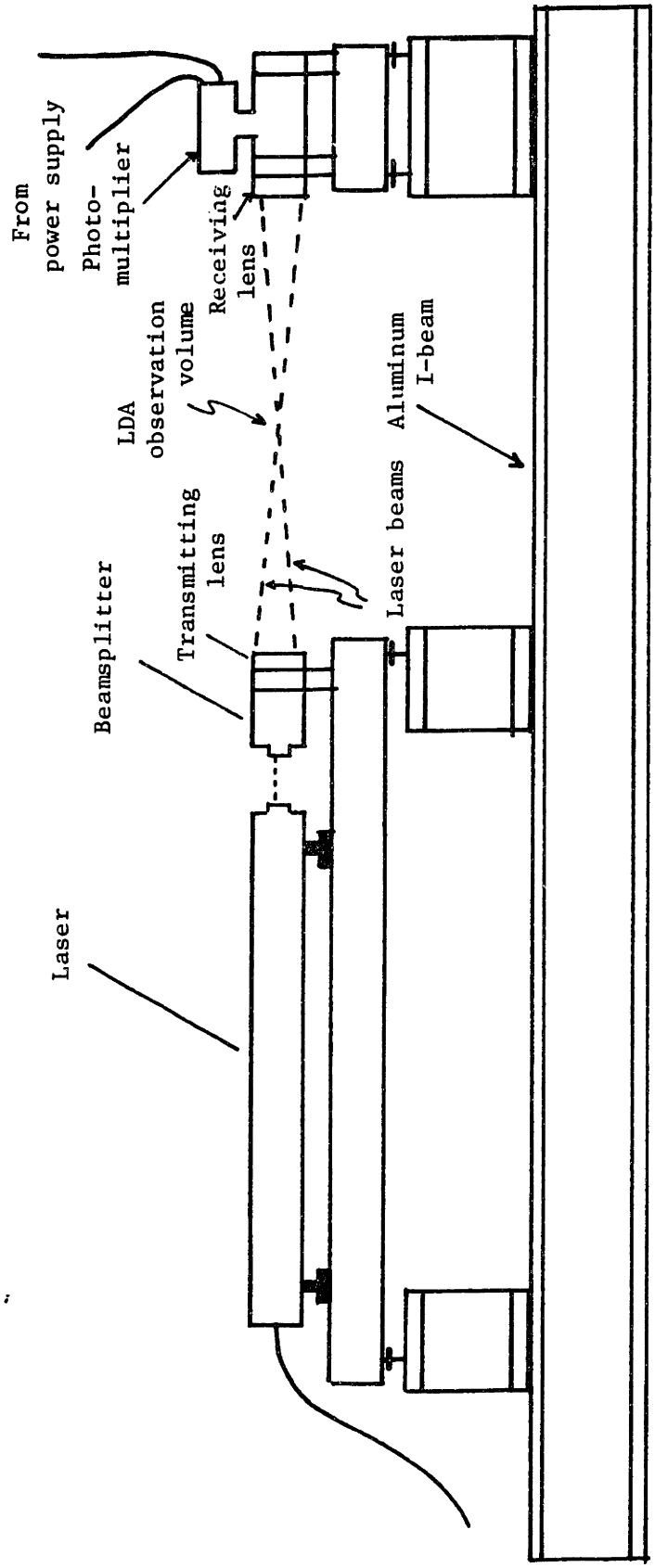

Fig. 2.3. LDV optical system, mounted on an aluminum I-beam. Wind tunnel fits in gap between transmitting and receiving lenses.

concentration measurements are made in the charging region to investigate corona wind (due to electric field forces on the corona ions) and its effects on particle mixing. Vertical velocity measurements made in the collection region (under the influence of the imposed electric field there) give information about the mobility spectrum of particles that exit the charger. In addition, concentration measurements performed in that region indicate the overall efficiency of precipitation in the charging region.

The precipitation efficiency can also be determined by the use of mass-monitors which sample the air-streams entering and leaving the precipitator. These devices measure the particulate mass-loading of an air-stream, averaged over short periods of time (on the order of minutes).

A number of different charging configurations were used for experiments reported in this thesis; only a generalized setup is shown in Figs. (1) and (2). For the precipitation experiments of chapter 4, the migration plate was removed and the corona wires extended over the entire active region of the precipitator (to increase the available collection area). Some of the charging experiments of chapter 5 used a single row of pins, suspended halfway between the top and bottom tunnel walls, in place of the corona wires [see Fig. (5.4)].

The detailed descriptions of Appendix 1 include sections on the wind-tunnel, itself, [section (A1.1)], the aerosol generator and associated diagnostic instruments [(A1.2), (A1.3), respectively], the high-voltage electrical supplies [section (A1.4)], the Laser-Doppler Velocimeter system [section (A1.5)], and the Mass-Monitor sampling system [section (A1.6)].

2.3 System Software

Both the microprocessor-based interface circuit in the LDV system and that in the mass-monitor system function essentially as programmable data buffers, receiving digital data in parallel form and converting it to a format suitable for serial transmission to the remote computer. In addition, each controls the setting of relays that are essential to the operation of their respective experiments.

None of these functions are directly controlled by the user, who apparently communicates only with the remote computer (through the microcomputers). When the user requests either a data-taking, data-transfer, or relay-setting operation, the remote computer "grabs" control of the microprocessor through transmission of an appropriate escape sequence, and causes it to execute programs which fulfill the given request. After such an operation, the microprocessor interface is generally returned to a transparent mode in which the user, again, communicates directly with the remote computer. This strategy was adopted as the best way to provide a "user-friendly" system with the minimum necessary programming of the microprocessor interfaces. Thus, the major responsibility for data-acquisition and processing, automatic control of experimental parameters, and data-recording lies with the computer programs described in Appendix 1, all of which are implemented on the (remote) 68000 computer.

In addition to data acquisition software, a number of programs exist to process data obtained by the LDV system. These programs allow the user to generate various plots from a data file, including the particle velocity vs. time, an approximate Fourier transform of the velocity, the velocity distribution function, and the velocity autocorrelation function. Brief descriptions of the software used to acquire and process data from the Mass-Monitor and LDV systems are presented in Appendix 1 [sections (A1.7) and (A1.8), respectively].

Chapter 3
Uniform-Field AC Particle Charging

3.1 Introduction

Particle charging in a conventional precipitator results from a complex combination of several processes. Figure (1) illustrates the interactions which take place between the flow turbulence, charging, and migration, in determining the total particle motion in a precipitator. Because of the non-uniform electric field and ion current density which exist in the charging region, the total charge on a particle depends not only upon its residence time, but also on the exact history of its proximity to the corona source[1]. The charging/turbulence coupling is pictured as a one-way interaction in Fig. (1). Mixing due to turbulent eddies can strongly affect the particle location in the non-uniform field, but it is unlikely that the electric field forces on the particles will influence the flow significantly. The charging/migration coupling is a two-way interaction. The particle migration velocity is certainly dependent upon its charge, and migration affects the particle's charging rate by changing its location.

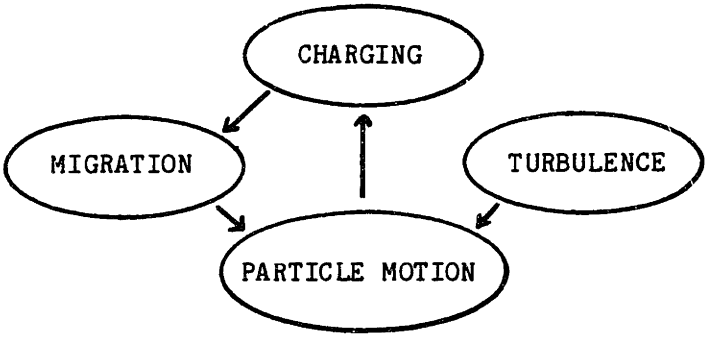

Figure (3.1) Interactions between processes which contribute to particle motions in a precipitator with non-uniform fields.

If the DC electric field and corona current density were uniform in the charging region of a precipitator, then the interactions would be as pictured in Fig. (2). In this case, the particle charging rate is <u>not</u> affected by the resulting migrations, or by turbulent eddies. As long as it is not actually precipitated, the particle will charge at a given rate, regardless of its location. The total particle motion is still

determined by a superposition of turbulence and migration, as illustrated by Fig. (2). The charging problem itself, however, is completely de-coupled from the turbulence and migration, and can be solved without reference to either.

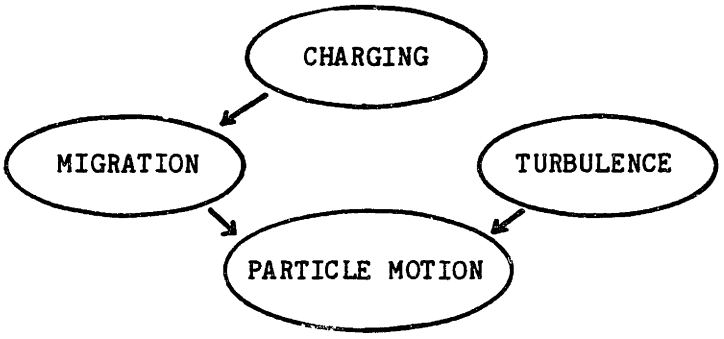

Figure (3.2) Interactions between processes which contribute to particle motions in a precipitator with uniform fields.

The problem of particle charging in a uniform electric field and corona current is treated by Melcher[2]. The formulae developed there are rather easily applied to the case of DC excitation, to determine the particle saturation charge, and the characteristic time, τ_{ch}, required to reach it. With time-varying fields, the solutions to Melcher's equations are more complicated. Even in this simplified case of uniform electric field and corona current, the dynamics of particle charging by AC fields are of interest.

A model is presented in this chapter for the charging and migration of particles subjected to a time-varying, but spatially-uniform electric field and corona current density. It is based on the Whipple-Chalmers charging model[2]. The idealized problem and basic assumptions are presented in section 3.2. Section 3.3 treats the simplest case; that of a piecewise-constant electric field and corona current density. The applied voltage is assumed to be a rectangular-wave, which is eventually restricted to having equal magnitude positive and negative values, biased in time to yield a zero time-average corona current [Fig. (4)]. Analytic expressions are derived for the steady-state peak particle charge, as well as the time-average and oscillatory migration velocities, w_{net} and w_{ac}, respectively (defined in that section). This simplified version of the analysis will

be referred to later in this thesis as the "universal precipitation model", as it predicts that the particles make progress towards the collection plate, regardless of the sign of the corona.

Most of the voltage waveforms used for experiments reported in this thesis were sinusoidal, not rectangular. Thus, the current waveforms included intervals during which the voltage was below the corona onset level [Fig. (8)]. This more realistic case is addressed in section 3.4. Much of the analysis in that section was obtained from Mouayad[3]. Although assignment of an appropriate functional expression to the current waveform would still have allowed an analytic solution to the problem, the complexity of the equations involved made a numerical approach more attractive. Conclusions, based upon the analysis, are drawn in section 3.5.

The results of this chapter are used in the turbulent diffusion model of chapter 4 to predict the overall collection efficiency of the laboratory-scale precipitator. It is seen there that the models developed in these two chapters are able to match the experimental results reported in the latter, even though effects of non-uniform fields are ignored here.

3.2 Problem Statement and Assumptions

The situation is as pictured in Fig. (3). An alternating electric potential difference is imposed between two parallel conducting plates of length, L, width, W, separated by the distance, H. The upper plate is smooth, but the lower one is covered by many needle-like protrusions, whose spacing and length are much less than H. Because of the electric field intensification around the points, there exist ranges of positive and negative applied voltages for which a stabl corona is produced by breakdown of the air near the lower plate, but catastrophic arc-over between the plates does not occur. Ion pairs which originate in the corona are separated by the electric field. Those with a charge-sign opposite to the potential of the lower plate are immediately drawn to that plate, while the others migrate into the region between the plates, eventually reaching the top one. It is assumed that the effect of the ion volume-charge on the electric field between the plates is negligible. This assumption will be satisfied if each of the ion self-precipitation times,

$$\tau_{\pm} \equiv \frac{\varepsilon_o}{\rho_{\pm} b_{\pm}} \tag{3.2.1}$$

is long compared to the corresponding ion migration times from one plate to the other.

$$\tau_{m,\pm} \equiv \frac{H}{b_{\pm} E_o} \tag{3.2.2}$$

In these expressions, ε_o is the dielectric constant of the surrounding air, $\rho_{\pm}$ and $b_{\pm}$ are the positive and negative ion charge densities and mobilities, respectively, and E_o is a typical imposed electric field strength. The small size of the protrusions insures that the electric field throughout most of the volume between the plates is of relatively uniform intensity, simply equal to the ratio of applied potential, V(t), to the plate spacing, H.

$$\bar{E}(t) = \frac{V(t)}{H} \bar{i}_x \tag{3.2.3}$$

The electrical excitation, V(t), is a periodic waveform, with cycle time, T. It is assumed that the ion migration time, $\tau_{m,\pm}$, defined

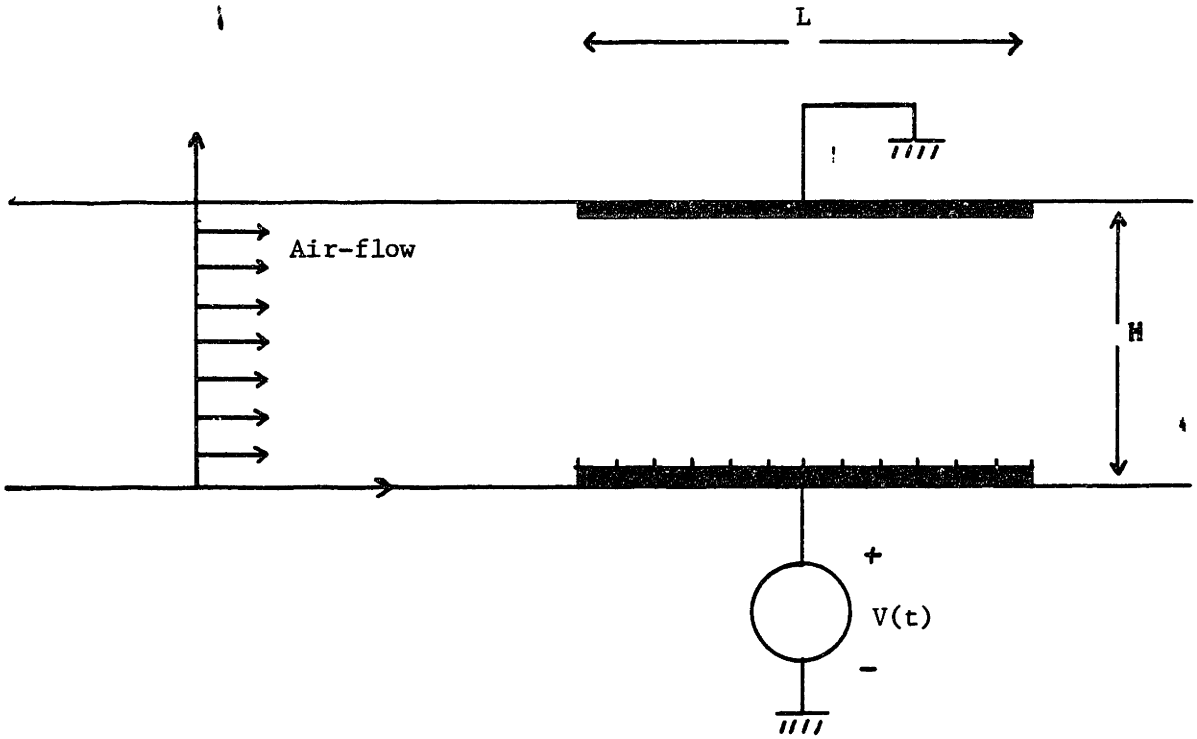

Fig. 3.3 Schematic illustration of single-stage electrostatic precipitator using alternating electrical excitation. Spikes on lower electrode are corona points, to allow discharge at high voltage.

in eq. (2), is short compared to the cycle time, T*.

$$\frac{\tau_{m,\pm}}{T} << 1 \qquad (3.2.4)$$

Thus, the ion distribution is quasi-steady with respect to the excitation, in that it can change much more rapidly than V(t) does.

Air, laden with particles to be charged, flows between the plates, with a uniform mean velocity, U, parallel to the plates. The convection time, τ_c, is assumed to be much longer than the ion migration time, $\tau_{m,\pm}$.

$$\tau_c \equiv \frac{L}{U} >> \tau_{m,\pm} \qquad (3.2.5)$$

Thus, the ion distribution is also undisturbed by the air flow.

Particles are assumed to charge according to the Whipple-Chalmers field charging model[2]. For that model, the following assumptions are made:

1) The particles are perfectly-conducting.

2) The particles accept any ions that impinge upon their surfaces,but will not release any ions once they have accepted them.

3) Effects of space charge on the electric field are negligible.

4) Charging processes occur on time scales that are long compared to the ion migration time, defined in eq. (2)

5) The air flow around the particle is of Reynolds number much less than unity.

The inertia of the migrating (charged) particles is assumed to be negligible, so that the particle migration velocity is determined by a balance between the viscous and electrical forces on it,

---

*That assumption, which may not be valid for high-frequency AC excitations, is examined in the concluding section of this chapter.

$$qE = 6\pi\eta Rw \tag{3.2.6}$$

where q is the particle charge, E is the electric field, η is the fluid viscosity, R is the particle radius, and w is the particle velocity.

It is desired to characterize both the particle charging and migration processes. Those parameters of greatest interest are the time-average migration velocity of the particles, w_{net}, and some measure of the oscillatory component of the migration, w_{ac}.

3.3 Solution with Piecewise Constant Fields

3.3.1 Piecewise Constant Excitation

For this case, the power source supplies a biased, non-symmetric rectangular-wave voltage, as pictured in Fig. (4). Thus,

$$V(t) = \left\{ \begin{array}{ll} V_+ & ; \ 0 \leq \mathrm{mod}(t,T) < T_+ \\ -V_- & ; \ T_+ \leq \mathrm{mod}(t,T) < T_+ + T_- \end{array} \right\} \tag{3.3.1}$$

where

$$\mathrm{mod}(t,T) = \left\{ \begin{array}{ll} t & ; \ 0 \leq t < T \\ \mathrm{mod}(t+T,T) & ; \ t < 0 \\ \mathrm{mod}(t-T,T) & ; \ T \leq t \end{array} \right\} \tag{3.3.2}$$

The quantities, V_+, and V_-, the magnitudes of the applied positive and negative voltages, respectively, are given parameters, as are the times of application of these voltages, T_+, and T_-, and the total cycle time, $T \equiv T_+ + T_-$.

The corona current is assumed to be a single-valued function of the applied voltage, $i(V)$. Since the applied voltage magnitudes, V_+ and V_-, are given parameters of the problem, the corona current magnitudes during the positive and negative voltage intervals, i_+, and i_-, respectively, may be treated as such also. The ion charge densities in the precipitation region are assumed to be uniform. Thus, the current during the positive voltage interval is given by

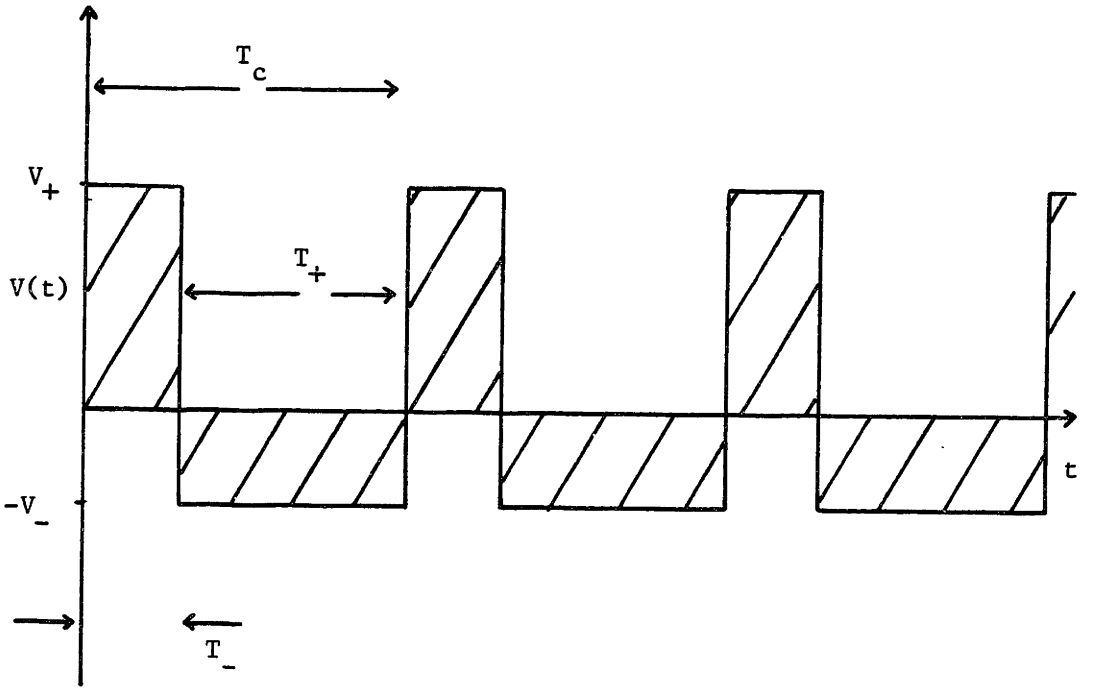

Fig. 3.4 Excitation voltage waveform for single-stage AC electrostatic precipitator.

$$i_+ = \rho_+ b_+ E_+ A$$
$$= \rho_+ b_+ V_+ \frac{A}{H} \tag{3.3.3}$$

where A is the effective precipitator area. During the negative voltage interval, the current is

$$i_- = -\rho_- b_- V_- \frac{A}{H} \tag{3.3.4}$$

3.3.2 Derivation of Equations of Particle Charging and Motion

The following quantities are defined:

$$I_+ \equiv \pi R^2 b_+ \rho_+ V_+ / H \tag{3.3.5}$$

$$I_- \equiv \pi R^2 b_- \rho_- V_- / H \tag{3.3.6}$$

$$q_{c+} \equiv 12\pi\varepsilon_o R^2 V_+ / H \tag{3.3.7}$$

$$q_{c-} \equiv 12\pi\varepsilon_o R^2 V_- / H \tag{3.3.8}$$

The charge densities, ρ_+ and ρ_-, can be expressed in terms of given parameters of the problem, using eqs. (3) and (4), yielding

$$I_+ = \frac{\pi R^2}{A} i_+ \tag{3.3.9}$$

$$I_- = \frac{\pi R^2}{A} i_- \tag{3.3.10}$$

$$\tau_+ = \frac{\varepsilon_o A V_+}{H\, i_+} \tag{3.3.11}$$

$$\tau_- = \frac{\varepsilon_o A V_-}{H\, i_-} \tag{3.3.12}$$

According to the Whipple-Chalmers model[2], the charging rate for a particle in a positive ion flux is

$$\frac{dq}{dt} = \begin{cases} 3I_+ \left(1 - \frac{q}{q_{c+}} \right)^2 & ; -q_{c+} \leq q < q_{c+} \\ -12I_+ \frac{q}{q_{c+}} & ; q < -q_{c+} \\ 0 & ; q_{c+} < q \end{cases} \qquad (3.3.13)$$

where q is the instantaneous particle charge. The quantities, q_{c+} and I_+, defined above, can be thought of as the saturation charge and characteristic charging currents for the particle in a positive ion flux. For the sake of simplicity in the following calculations, it will be assumed that the particle charge never exceeds q_{c+} in magnitude, so that only the top line of eq. (13) is used. This assumption can be relaxed, at the cost of increased complexity in the problem solution. Similarly, for a negative ion flux, the charging rate is

$$\frac{dq}{dt} = 3I_- \left(1 + \frac{q}{q_{c-}} \right)^2 \qquad (3.3.14)$$

If the particle charge at the beginning of a positive voltage interval is q_{o+}, then eq. (13) can be integrated to give q as a function of time.

$$\frac{q(t)}{q_{c+}} = \frac{\left(1 - \frac{q_{o+}}{q_{c+}} \right) \frac{t-t_o}{\tau_+} + 4\frac{q_{o+}}{q_{c+}}}{\left(1 - \frac{q_{o+}}{q_{c+}} \right) \frac{t-t_o}{\tau_+} + 4} \qquad (3.3.15)$$

where t_o is the beginning time of the interval. Equation (15) is valid as long as the positive voltage interval continues. Note that, if q_{o+} is less than q_{c+} in magnitude, then q(t) will be so also. During a negative voltage interval,

$$\frac{q(t)}{q_{c-}} = \frac{4\frac{q_{o-}}{q_{c-}} - \left(1 + \frac{q_{o-}}{q_{c-}}\right)\frac{t-t_o}{\tau_-}}{4 + \left(1 + \frac{q_{o+}}{q_{c-}}\right)\frac{t-t_o}{\tau_-}} \qquad (3.3.16)$$

where q_{o-} is the particle charge at the beginning time of the interval, t_o. Equation (3.2.6) can be solved for w, to give a differential equation that defines the particle motion transverse to the flow direction,

$$\frac{dx_p}{dt} \equiv w = \frac{qE}{6\pi\eta R} \qquad (3.3.17)$$

where x_p is the particle displacement relative to the plate at x=0. With substitution from eqs. (3.2.3) and (15), eq. (17) can be integrated for times during a positive voltage interval,

$$\frac{x_p}{H} = \frac{x_{po}}{H} + \left(\frac{q_{c+}V_+\tau_+}{6\pi\eta RH^2}\right) \cdot \left(\frac{t-t_o}{\tau_+} - 4\ln\left(1 + \left(1 - \frac{q_{o+}}{q_{c+}}\right)\frac{t-t_o}{4\tau_+}\right)\right) \qquad (3.3.18)$$

where x_{po} is the particle position at time, t_o. During a negative voltage interval,

$$\frac{x_p}{H} = \frac{x_{po}}{H} + \left(\frac{q_{c-} V_- \tau_-}{6\pi\eta R H^2} \right) \cdot$$

$$\left(\frac{t-t_o}{\tau_-} - 4 \ln \left(1 + \left(1 + \frac{q_{o-}}{q_{c-}} \right) \frac{t-t_o}{4\tau_-} \right) \right) \qquad (3.3.19)$$

It is of use to define values equal to the dimensionless coefficients used in eqs. (18) and (19).

$$A_+ \equiv \frac{q_{c+} V_+ \tau_+}{6\pi\eta R H^2} \qquad (3.3.20)$$

$$A_- \equiv \frac{q_{c-} V_- \tau_-}{6\pi\eta R H^2} \qquad (3.3.21)$$

3.3.3 Steady State Particle Charging and Motion

Equations (15) and (16) can be used to determine the particle charge at the end of the (n+1)'st electrical cycle in terms of its charge after n cycles. Let q_n be the particle charge at the end of the n'th positive voltage interval. Equation (16) is evaluated, setting $q_{o-}=q_n$, and $t-t_o=T_-$, to give the particle charge at the end of the n'th negative voltage interval. This value is then used as the initial charge, q_{o+}, of the (n+1)'st positive voltage interval, and eq. (15) yields the charge at the end of this interval, q_{n+1}.

$$\frac{q_{n+1}}{q_{c+}} = \frac{G_1 \frac{q_n}{q_{c+}} + G_2}{G_3 \frac{q_n}{q_{c+}} + G_4} \qquad (3.3.22)$$

where

$$G_1 \equiv 16 - 4\left(\frac{T_+}{\tau_+} + \frac{T_-}{\tau_-}\right) + \frac{T_+T_-}{\tau_+\tau_-}\left(1 + \frac{q_{c+}}{q_{c-}}\right) \tag{3.3.23}$$

$$G_2 \equiv 4\left(\frac{T_+}{\tau_+} - \frac{T_-q_{c-}}{\tau_-q_{c+}}\right) + \frac{T_+T_-}{\tau_+\tau_-}\left(1 + \frac{q_{c+}}{q_{c-}}\right)\frac{q_{c-}}{q_{c+}} \tag{3.3.24}$$

$$G_3 \equiv 4\left(\frac{T_-}{\tau_-} - \frac{T_+q_{c-}}{\tau_+q_{c+}}\right)\frac{q_{c+}}{q_{c-}} + \frac{T_+T_-}{\tau_+\tau_-}\left(1 + \frac{q_{c+}}{q_{c-}}\right) \tag{3.3.25}$$

$$G_4 \equiv 16 + 4\left(\frac{T_+}{\tau_+} + \frac{T_-}{\tau_-}\right) + \frac{T_+T_-}{\tau_+\tau_-}\left(1 + \frac{q_{c+}}{q_{c-}}\right)\frac{q_{c-}}{q_{c+}} \tag{3.3.26}$$

Note that $G_1 - G_4$ are defined in terms of given quantities.

For steady state operation, $q_{n+1}=q_n\equiv q_\infty$. Equation (22) can be solved for q_∞,

$$G_3\left(\frac{q_\infty}{q_{c+}}\right)^2 + (G_4 - G_1)\frac{q_\infty}{q_{c+}} - G_2 = 0 \tag{3.3.27}$$

Given this value for the charge at the end of a positive voltage interval, equations (16), (18), and (19) can be used to find the net particle displacement per electrical cycle under steady state conditions.

Only a special case is examined here. Suppose $V_-=V_+\equiv V$ so that $q_{c-}=q_{c+}\equiv q_c$, and that $(T_-/\tau_-) = (T_+/\tau_+) \equiv (\mathcal{T}/\tau)$. In this case, the expressions for $G_1 - G_4$ simplify considerably.

$$G_1 = 16 - 8\frac{\mathcal{T}}{\tau} + 2\left(\frac{\mathcal{T}}{\tau}\right)^2 \tag{3.3.28}$$

$$G_2 = 2\left(\frac{\mathcal{T}}{\tau}\right)^2 \tag{3.3.29}$$

$$G_3 = 2\left(\frac{\mathcal{T}}{\tau}\right)^2 \tag{3.3.30}$$

$$G_4 = 16 + 8\frac{\mathcal{T}}{\tau} + 2\left(\frac{\mathcal{T}}{\tau}\right)^2 \tag{3.3.31}$$

Equation (27) can be solved easily, yielding

$$\frac{q_\infty}{q_{c+}} = \frac{4\tau}{\mathcal{T}}\left(-1 \pm \sqrt{1 + \left(\frac{\mathcal{T}}{4\tau}\right)^2}\right) \tag{3.3.32}$$

The solution obtained using the minus sign in eq. (32) is discarded, as it corresponds to a particle charge whose magnitude is greater than the saturation charge, q_{c+}. If the value obtained using the plus sign is substituted into eq. (16), it is seen that the particle charge at the end of a negative voltage interval in the steady state has the same magnitude as that after the positive interval (under the special condition examined here).

In the steady state, the particle charge at the end of a positive voltage interval is the initial charge for the following negative interval, and vice versa. Thus, eqs. (18) and (19) can be evaluated, using the appropriate initial charges (ie., $\pm q_\infty$), to determine the net particle displacement during one entire electrical cycle, ℓ_{net}.

$$\frac{\ell_{net}}{H} = (A_+ + A_-)\frac{T}{\tau} - 4(A_+ + A_-)\ln\left[1 + (1 + \frac{q_\infty}{q_c})\frac{\tau}{4\tau}\right] \qquad (3.3.33)$$

where A_+ and A_- were defined in eqs. (20) and (21). The time-average particle velocity, w_{net} is defined

$$w_{net} \equiv \frac{1}{T}\int_t^{t+T} \frac{dx_p}{dt'}dt'$$

$$= \frac{\ell_{net}}{T} \qquad (3.3.34)$$

where $T = T_+ + T_-$ is the total time of one cycle of the electrical excitation. Because the system is assumed to be in a periodic steady state, the starting time of the integral in eq. (34) does not affect the value obtained for w_{net}. For the special case examined here, eq. (33) can be further simplified, so that

$$w_{net} = \frac{2\varepsilon_o R}{\eta}\left(\frac{V}{H}\right)^2 \cdot \left[1 - \frac{4(\tau_+ + \tau_-)}{T}\ln\left[1 + \left(1 + \frac{q_\infty}{q_c}\right)\frac{T}{4(\tau_+ + \tau_-)}\right]\right] \qquad (3.3.35)$$

The factor,

$$v_o \equiv \frac{2\varepsilon_o R}{\eta} \left(\frac{V}{H} \right)^2 \tag{3.3.36}$$

has the units of velocity, and is the speed of a particle of radius, R, charged to saturation and migrating in the electric field, (V/H), through a liquid of viscosity, η. Thus, eq. (35) predicts the time-average particle migration velocity as a fraction of that which it would attain given a DC electric field equal in magnitude to the AC fields applied here. The expression for q_∞, eq. (32), can be rewritten in terms of the total cycle time, T.

$$\frac{q_\infty}{q_c} = \frac{4(\tau_+ + \tau_-)}{T} \left[\sqrt{1 + \left(\frac{T}{4(\tau_+ + \tau_-)} \right)^2} - 1 \right] \tag{3.3.37}$$

At the beginning of each half-cycle of the excitation, the particle travels in the $-\vec{x}$ direction until its charge is reversed in sign by the corona current. Thus, the maximum particle excursion during a half-cycle is greater than the net displacement from beginning to end. It is of interest to compute this maximum excursion, as it is important in determining the rate of precipitation of particles in the vicinity of a collection plate. Equation (18) can be differentiated with respect to time, to give the particle velocity as a function of time during a positive voltage interval.

$$\frac{dx}{dt} = \frac{q_c V}{6\pi\eta R h} \frac{\left(1 + \frac{q_\infty}{q_c} \right) \frac{t-t_o}{4\tau_+} - \frac{q_\infty}{q_c}}{1 + \left(1 + \frac{q_\infty}{q_c} \right) \frac{t-t_o}{4\tau_+}}, \tag{3.3.38}$$

The particle reaches its minimum vertical position when its velocity is equal to zero. The time at which this occurs, t_{min}, can be determined by setting the right hand side of eq. (38) to zero.

$$t_{min} - t_o = 4\tau_+ \frac{\frac{q_\infty}{q_c}}{1 + \frac{q_\infty}{q_c}} \tag{3.3.39}$$

Since the particle travels in the $+\vec{x}$ direction from this time until the next voltage reversal, and its net forward progress for the half-cycle is always positive (in the steady-state), its maximum excursion for the half-cycle, $\ell_{max,+}$, is equal to the difference between its position at the end of the half-cycle and that at $t=t_{min}$. This difference is determined by evaluation of eq. (18), for the two times, $t=t_o+T_+$, $t=t_o+t_{min}$, and subtraction of one value from the other.

$$\frac{\ell_{max,+}}{H} = \left(\frac{4q_c V\tau_+}{6\pi\eta RH^2} \right) \cdot \left\{ \frac{T}{4\tau} - \frac{\frac{q_\infty}{q_c}}{1 + \frac{q_\infty}{q_c}} - \ln \left(\frac{1 + \left(1 + \frac{q_\infty}{q_c} \right) \frac{T}{4\tau}}{1 + \frac{q_\infty}{q_c}} \right) \right\} \tag{3.3.40}$$

Similar reasoning can be used to show that the maximum particle excursion during a negative voltage interval in the steady state, $\ell_{max,-}$, is given by

$$\frac{\ell_{max,-}}{H} = \left(\frac{2q_c V\tau_-}{6\pi\eta RH^2} \right) \cdot \left\{ \frac{T}{4\tau} - \frac{\frac{q_\infty}{q_c}}{1 + \frac{q_\infty}{q_c}} - \ln \left(\frac{1 + \left(1 + \frac{q_\infty}{q_c} \right) \frac{T}{4\tau}}{1 + \frac{q_\infty}{q_c}} \right) \right\} \tag{3.3.41}$$

An effective AC velocity can be defined as the maximum particle excursion during a half-cycle, divided by the time duration of the half-cycle. It is seen that, with the restrictions made, this quantity, w_{ac} is the same for both positive and negative voltage intervals.

$$w_{ac} = v_o \left[1 - \frac{4(\tau_+ + \tau_-)}{T} \frac{\frac{q_\infty}{q_c}}{1 + \frac{q_\infty}{q_c}} - \right.$$

$$\left. \frac{4(\tau_+ + \tau_-)}{T} \ln \left[\frac{1 + \left(1 + \frac{q_\infty}{q_c} \right) \frac{T}{4(\tau_+ + \tau_-)}}{1 + \frac{q_\infty}{q_c}} \right] \right] \qquad (3.3.42)$$

where v_o is the velocity defined in eq.(36).

As the formulae of eqs. (35), (37), and (42) are to be used in later chapters of this thesis, they are repeated below, using a more convenient notation. The charging time constant, τ_{ch}, is defined

$$\tau_{ch} \equiv 4 [\tau_+ + \tau_-] \qquad (3.3.43)$$

so that

$$\frac{4 [\tau_+ + \tau_-]}{T} = f \tau_{ch} \qquad (3.3.44)$$

where $f \equiv 1/T$ is the excitation frequency. A normalized peak particle charge, $\underline{q}_\infty$, is defined as the ratio of q_∞ to the saturation charge, q_c. From eq. (37),

$$\underline{q}_\infty \equiv \frac{q_\infty}{q_c} = (f \tau_{ch}) \left[\sqrt{1 + (f \tau_{ch})^{-2}} - 1 \right] \qquad (3.3.45)$$

The normalized net and oscillatory velocities, $\underline{w}_{net}$, and $\underline{w}_{ac}$, respectively, are thus

$$\underline{w}_{net} \equiv \frac{w_{net}}{v_o} = \left[1 - (f \tau_{ch}) \ln \left[1 + (1 + \underline{q}_\infty) \cdot (f \tau_{ch})^{-1} \right] \right] \qquad (3.3.46)$$

$$\underline{w}_{ac} \equiv \frac{w_{ac}}{v_o} = \left[1 - (f \tau_{ch}) \frac{\underline{q}_\infty}{1 + \underline{q}_\infty} - \right.$$

$$\left. (f \tau_{ch}) \ln \left[\frac{1 + (1 + \underline{q}_\infty) (f \tau_{ch})^{-1}}{1 + \underline{q}_\infty} \right] \right] \qquad (3.3.47)$$

The normalized charge density, $\underline{q}_\infty$, is plotted as a function of the normalized excitation frequency, $f\tau_{ch}$, in Fig. (5). The normalized time-average migration velocity, $\underline{w}_{net}$, and oscillatory migration velocity, $\underline{w}_{ac}$, are plotted as a function of the normalized frequency in Fig. (6). The upper curve corresponds to $\underline{w}_{ac}$, and the lower one to $\underline{w}_{net}$.

Given a value for the steady-state peak particle charge, q_∞, one can use eqs. (15) and (16) to compute statistical properties such as the mean value and RMS spread in particle charge. These quantities are of interest, as they can be measured experimentally in the laboratory-scale precipitator.

Because of the assumption of positive and negative imposed electric fields that are of equal magnitude, the mean particle charge is closely related to the mean particle migration velocity, w_{net}. In fact, the normalized mean particle charge, $\underline{\bar{q}}$, is given by

$$\underline{\bar{q}} \equiv \frac{1}{T}\int_t^{t+T} \frac{q(t')}{q_c}\, dt' \tag{3.3.48}$$

$$= \frac{1 - \frac{T_-}{T_+}}{1 + \frac{T_-}{T_+}}\ \underline{w}_{net} \tag{3.3.49}$$

The definition of eq. (48) utilizes the fact that, in the steady-state, the particle charge, q(t), is a periodic function of time. Thus, the starting time of the integral, t, does not affect the value of $\underline{q}_{net}$. If the negative corona current, i_-, is greater than the corresponding value for positive corona, i_+ (so that $T_- < T_+$, to give zero net current), then the particle charge will be biased positively. A physical interpretation of this phenomenon is that the particles are charged in the positive corona for a longer time, and thus attain a net positive charge, even though the positive charging process may occur more slowly.

The normalized RMS spread in particle charge, $\underline{q}'$, is defined

$$\underline{q}'^2 \equiv \frac{1}{T}\int_t^{t+T} \left(\frac{q(t')}{q_c} - \underline{\bar{q}} \right)^2 dt' \tag{3.3.50}$$

Equations (15), (16), (32), and (50) can be used to compute $\underline{q}'$.

$$\underline{q}'^{2} = 1 - 2(f\tau_{ch}) \ln \left[1 + \left[1 + \underline{q}_{\infty} \right] (f\tau_{ch})^{-1} \right] + \frac{\left[1 + \underline{q}_{\infty} \right]^{2}}{1 + \left[1 + \underline{q}_{\infty} \right] (f\tau_{ch})^{-1}} \qquad (3.3.51)$$

This normalized RMS spread is plotted as a function of $(f\tau_{ch})$ in Fig. (7).

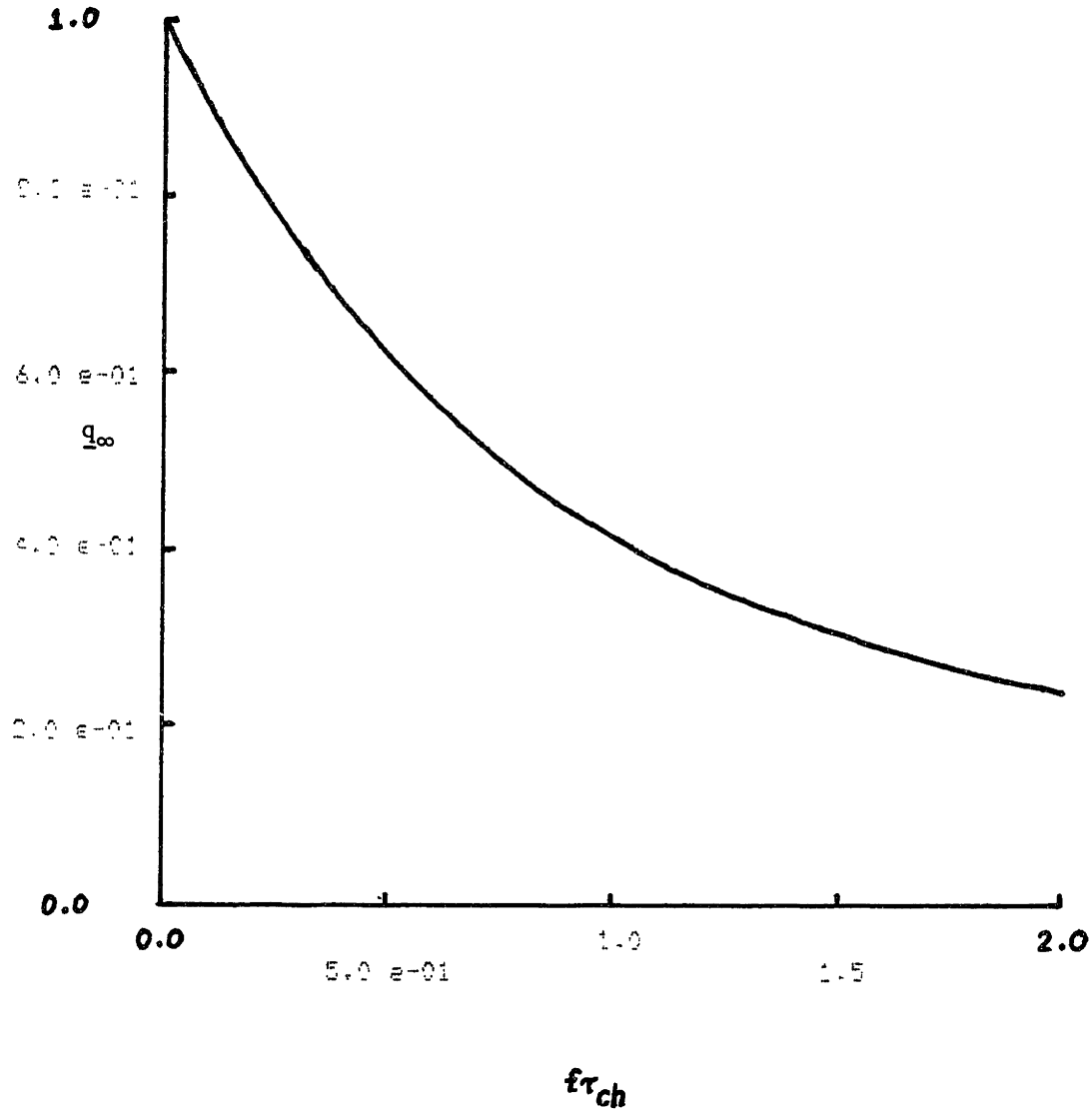

Figure 3.5. Plot of normalized steady-state peak particle charge, q_∞, as a function of normalized charging frequency, $(f\tau_{ch})$. Simplified Universal precipitation model was used (rectangle-wave applied voltage).

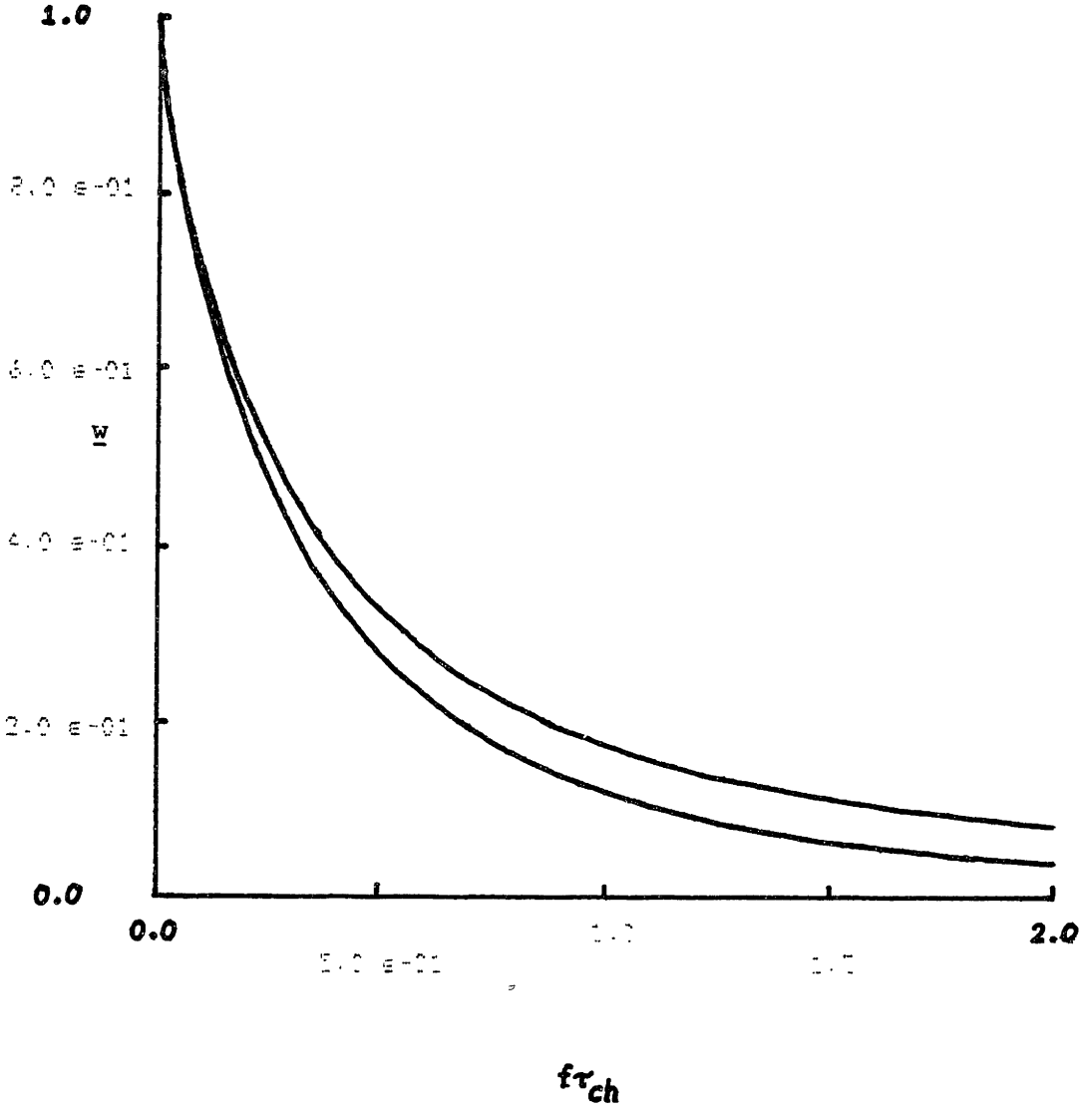

Figure 3.6. Plots of normalized steady-state time-average particle migration velocity, $\underline{w}_{net}$ (lower curve), and oscillatory migration velocity, $\underline{w}_{ac}$ (upper curve), as a function of normalized charging frequency, ($f\tau_{ch}$). Simplified Universal precipitation model was used (Rectangle-wave applied voltage).

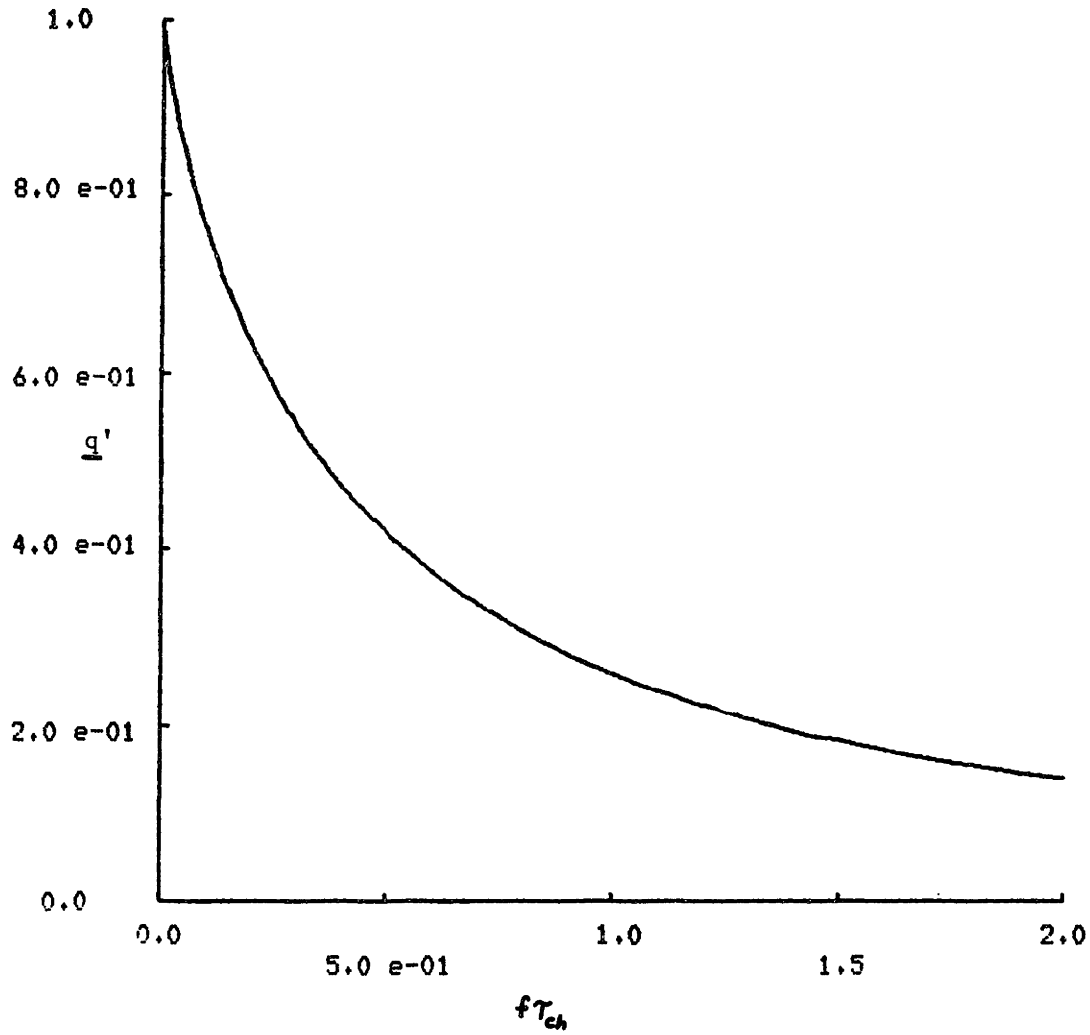

Figure 3.7. Plot of normalized RMS spread in particle charge vs. normalized charging frequency (The charge is normalized to the saturation charge). Simplified Universal Precipitation model was used for this prediction.

3.4 Solution With Biased Sinusoidal Electric Field

In this section, the Whipple-Chalmers model is used to predict the statistics of particle charging in an electric field that varies with time as a biased sinusoid. The excitation and particle charging equations are presented in sections (3.4.1) and (3.4.2), respectively. For the case of very low frequency excitation, the equations can still be solved analytically, as is done in section (3.4.3). In the general case, a numerical solution of the charging equations is required. The behavior of the particle charging in this regime is addressed in section (3.4.4).

3.4.1 Electric Field and Corona Current Excitation

A more realistic electrical excitation is that pictured in Fig. (8).

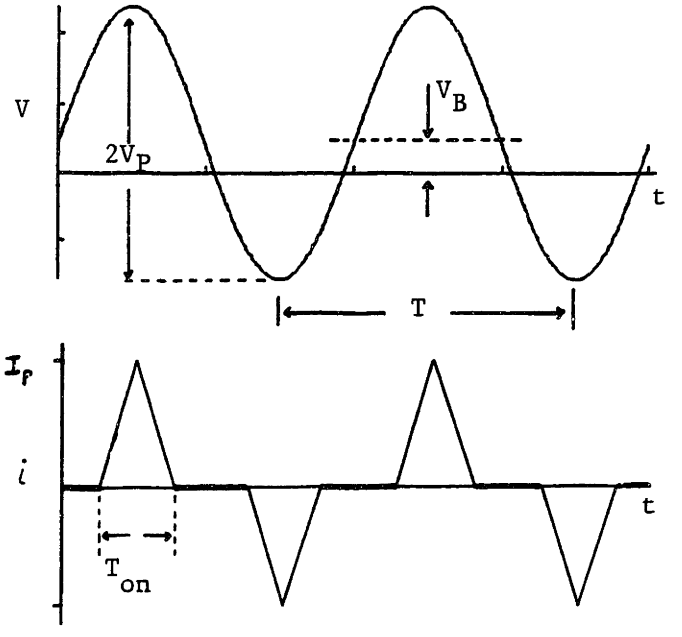

Figure 3.8. Voltage and current excitation for particle charging.

The applied voltage is a biased sinusoid*.

$$V(t) = V_B + V_P \sin(2\pi \frac{t}{T}) \tag{3.4.1}$$

The resulting corona current, i(t), is taken to be a set of detached, symmetric triangle pulses of peak current, I_P, and width, T_{on}, centered about the voltage extremes. Thus, it is assumed that the voltage bias compensates for differences between the turn-on voltages and equivalent conductances of positive and negative coronas.

3.4.2 Equations of Particle Charging

The instantaneous particle charging rate is still determined by an equation that is similar to eq. (13). The charging current and saturation charge, however, must now vary with time, in accordance with the voltage and current of Fig. (8).

$$\frac{dq}{dt} = \begin{cases} 3\, I(t) \left[1 - \dfrac{q(t)}{q_c(t)} \right]^2 ; & \left| \dfrac{q(t)}{q_c(t)} \right| \leq 1 \\ -12\, I(t) \dfrac{q(t)}{q_c(t)} ; & \dfrac{q(t)}{q_c(t)} < -1 \\ 0 ; & \dfrac{q(t)}{q_c(t)} > 1 \end{cases} \tag{3.4.2}$$

where

$$q_c(t) = 12\, \pi\, \varepsilon_o\, R^2\, V(t)/H \tag{3.4.3}$$

$$I(t) = \frac{\pi R^2}{A}\, i(t) \tag{3.4.4}$$

Equations (3) and (4) are analogous to eqs. (3.3.7) - (3.3.10) for the case of piecewise-constant fields. It should be noted here that, while eqs. (2) - (4) can be used for more general voltage and current excitations than those of Fig. (8), they are valid only if the sign of the voltage and current are the same.

---

*In order to supply a biased voltage to the corona source in a practical device, one could place a capacitor in series with the output of a high-voltage transformer, as is shown in the experimental setup of Fig. (2.1). In fact, this arrangement would automatically prevent any time-average currents, as the capacitor presents an infinite impedance to DC voltages.

A characteristic charging time, analogous to the time, τ_{ch}, used in the previous section, is defined here.

$$\tau_{charge} \equiv 8 \frac{\varepsilon_o A V_p}{H I_{eff}} \tag{3.4.5}$$

where the effective current, I_{eff}, is defined as the average current magnitude over a cycle of the excitation. With the corona current waveform of Fig. (8),

$$I_{eff} = I_p \frac{T_{on}}{T} \tag{3.4.6}$$

A characteristic particle charge, q_o, is defined here, for later use.

$$q_o \equiv 12 \pi \varepsilon_o R^2 V_p / H \tag{3.4.7}$$

3.4.3 Low-Frequency Limit

If the electrical excitation, V(t), varies slowly enough that

$$f \tau_{charge} << 1 \tag{3.4.8}$$

then the dynamics of the charging process are unimportant Whenever the corona current is zero, the particles will retain a constant charge. Otherwise, they will either attain the saturation charge corresponding to the instantaneous electric field present or, if their charge is already of the same sign and greater in magnitude than the saturation charge, they will remain at the same charge level. This behavior is illustrated in Fig. (9), for the voltage and current excitations presented in Fig. (8). It is seen that the particles spend a considerable fraction of their time charged to the saturation levels which correspond to the peak positive and negative imposed electric fields. The normalized time-average charge of particles passing by a fixed location in the charger, $\bar{q}$, will be as defined in eq. (3.3.48), except that the saturation charge, q_c, is replaced by q_o [Because the saturation charge is a function of time, its value with $V = V_p$ is used instead]. This modified version of eq. (3.3.48) can be used, along with eq. (2), to yield.

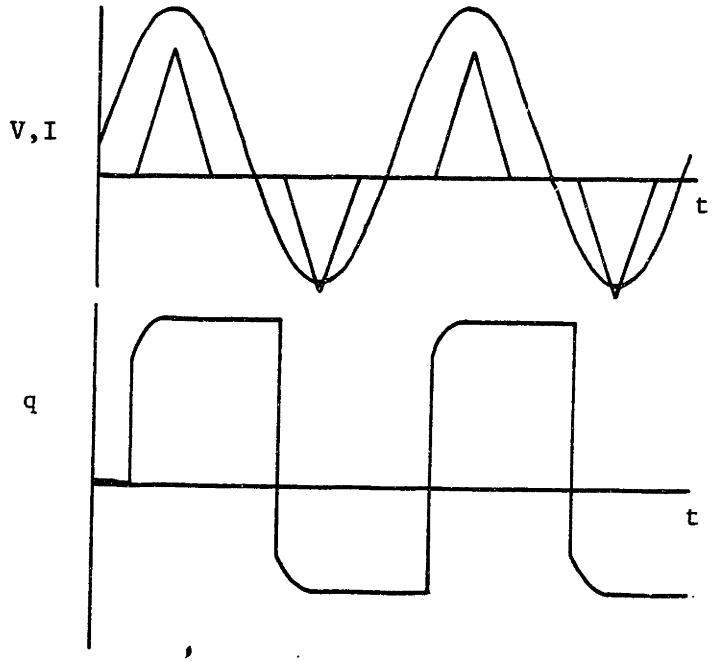

Figure 3.9. Schematic plots of corona voltage and current waveforms (a), along with resulting charge vs. time (b), for low-frequency excitiation. The functionality of q(t) can be divided into 4 regions:

1) For $\emptyset < \text{mod}(t,T) < \frac{T}{4} - \frac{T_{on}}{2}$
   or $\frac{3T}{4} < \text{mod}(t,T) < T$: $q(t) = q_c(\frac{3T}{4})$

2) For $\frac{T}{4} - \frac{T_{on}}{2} < \text{mod}(t,T) < \frac{T}{4}$: $q(t) = q_c(t)$

3) For $\frac{T}{4} < \text{mod}(t,T) < \frac{3T}{4} - \frac{T_{on}}{2}$: $q(t) = q_c(\frac{T}{4})$

4) For $\frac{3T}{4} - \frac{T_{on}}{2} < \text{mod}(t,T) < \frac{3T}{4}$: $q(t) = q_c(t)$

$$\underline{\bar{q}} = \frac{V_B}{V_P} \tag{3.4.9}$$

Thus, the average value of the actual particle charge in this case depends only upon the bias voltage, V_B. The normalized RMS spread in particle charge is computed using eq. (3.3.50) [with q_c, again, replaced by q_o] and eq. (2)

$$\underline{q'}^2 = 1 - \frac{1}{2}\frac{T_{on}}{T} + \frac{1}{4\pi}\sin\left(2\pi\frac{T_{on}}{T}\right) \tag{3.4.10}$$

Equation (3.3.17) is used to compute the instantaneous particle migration velocity, which can then be averaged to give the net migration velocity, w_{net}, defined in eq. (3.3.34) It is most convenient here to normalize w_{net} to the migration velocity of a particle charged to saturation by a DC voltage equal in magnitude to V_P. This velocity is simply that which was defined in eq. (3.3.36), with the voltage, V, being replaced by V_P.

$$\underline{w}_{net} \equiv \left(\frac{w_{net}}{2\,\varepsilon_o\,R\,V_P^2/\eta\,H^2}\right) =$$

$$\left(\frac{V_B}{V_P}\right)^2 + \frac{1}{2}\frac{T_{on}}{T} + \frac{1}{4\pi}\sin\left(2\pi\frac{T_{on}}{T}\right) + \frac{1}{\pi}\sin\left(\pi\frac{T_{on}}{T}\right) \tag{3.4.11}$$

The normalized RMS spread in particle charge and time-average particle migration velocity are plotted as functions of (T_{on}/T) in Figs. (10) and (11), respectively. For purposes of comparison to the results of the following section, the quantity plotted in Fig. (10) is $\sqrt{2}\,\underline{q'}$, and the normalized quantity plotted in Fig. (11) is $2\,\underline{w}_{net}$. For Fig. (11), it was assumed that $V_B = 0$, as the effect of a bias voltage is easily ascertained from eq. (11).

3.4.4 Numerical Solution for Arbitrary Frequencies

If the inequality of eq. (8) is not satisfied, then eqs. (2) - (4) must be solved numerically. The solution obtained can then be used to determine both the charging statistics and the resulting time-average particle migration velocity. The following normalization is used.

$$q(t) = q_o\,\underline{q}(\underline{t}) \tag{3.4.12}$$

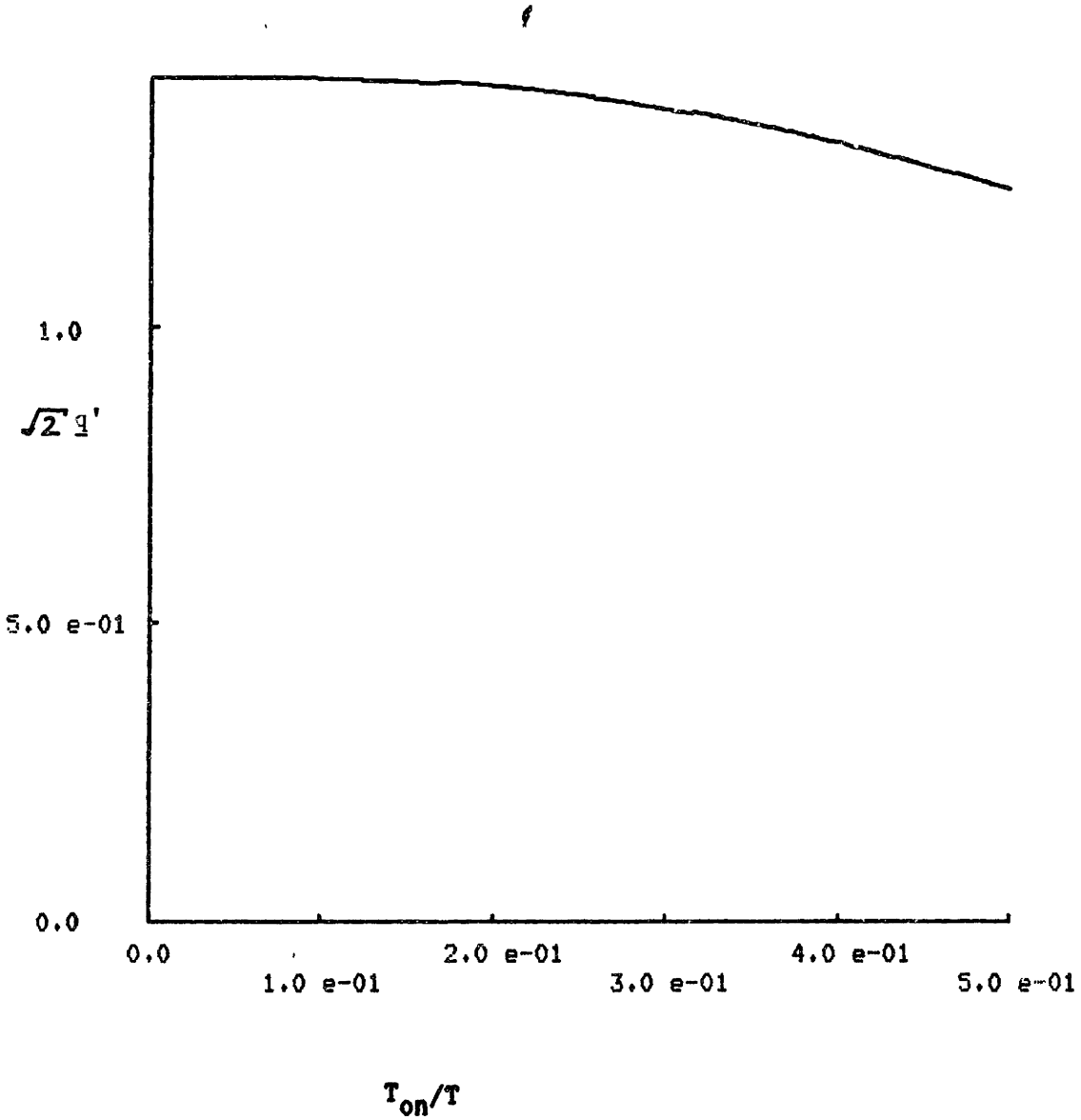

Figure 3.18. Plot showing RMS spread in particle charge vs. corona on-time fraction, T_{on}/T. Very low-frequency charging is assumed.

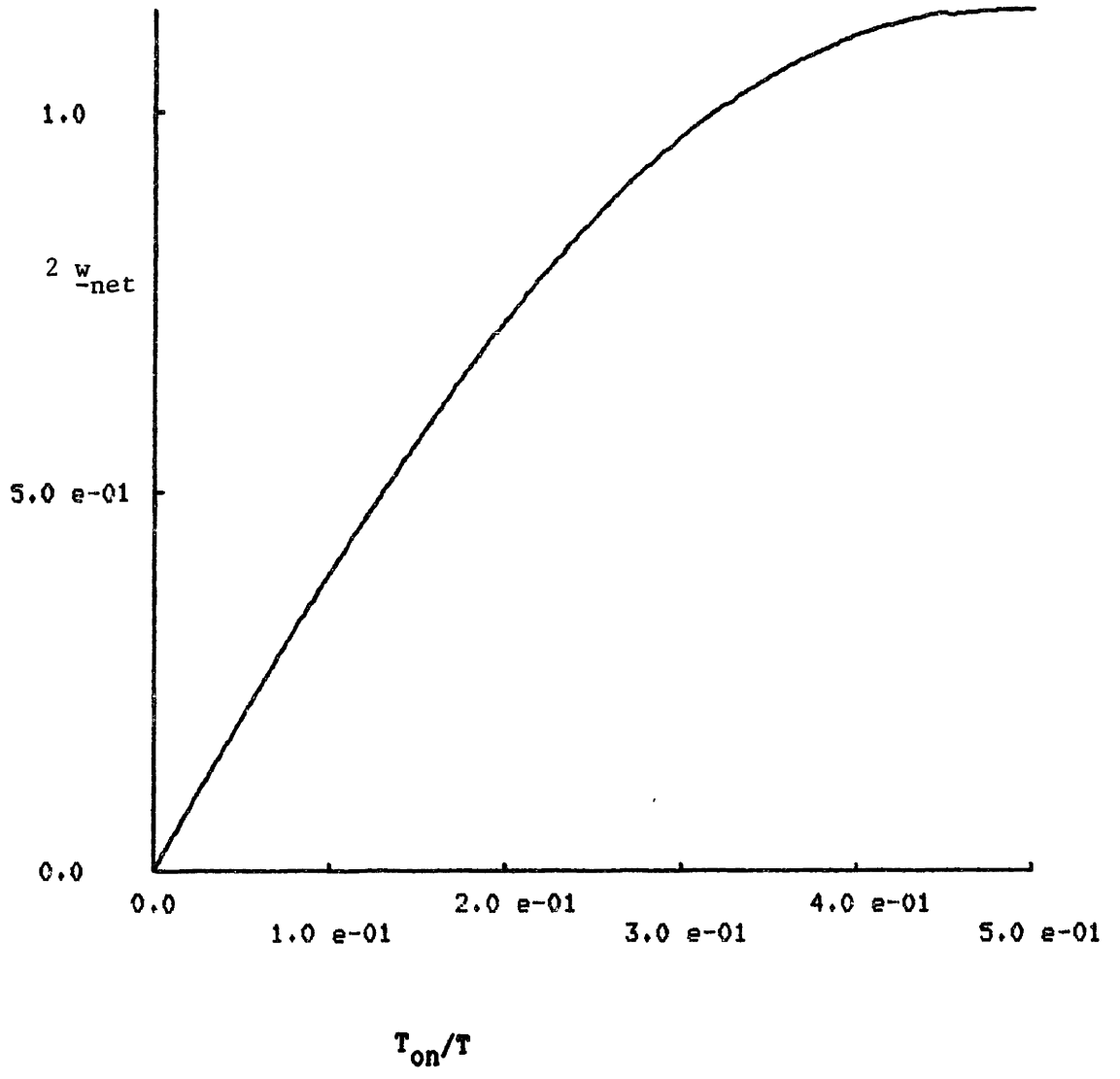

Figure 3.11. Plot showing time-average particle migration velocity vs. corona on-time fraction, T_{on}/T. Very low-frequency charging is assumed. V_B = 0.

$$q_c(t) = q_o \, \underline{q}_c(t) \tag{3.4.13}$$

$$I(t) = I_{eff} \frac{\pi R^2}{A} \, \underline{i}(t) \tag{3.4.14}$$

$$t = \tau_{charge} \, \underline{t} \tag{3.4.15}$$

When applied to eq. (2), this normalization yields

$$\frac{d\underline{q}}{d\underline{t}} = \begin{cases} 2 \, \underline{i}(t) \left[1 - \dfrac{\underline{q}(t)}{\underline{q}_c(t)} \right]^2 ; & \left| \dfrac{\underline{q}(t)}{\underline{q}_c(t)} \right| \leq 1 \\ -8 \, \underline{i}(t) \dfrac{\underline{q}(t)}{\underline{q}_c(t)} ; & \dfrac{\underline{q}(t)}{\underline{q}_c(t)} < -1 \\ 0 ; & \dfrac{\underline{q}(t)}{\underline{q}_c(t)} > 1 \end{cases} \tag{3.4.16}$$

The three independent simulation parameters are:

1) The corona on-time fraction, T_{on}/T.

2) The normalized excitation frequency, $f \, \tau_{charge}$.

3) The bias voltage fraction, V_B/V_P.

Simulations were run with $T_{on}/T = 0.5$ and with $T_{on}/T = 0.34$, with normalized frequencies ranging from 0.002 to 4.0. A second-order Runge-Kutta scheme (also known as a "predictor-corrector" scheme) was used to integrate the charging equation. Figure (12) shows the variation of RMS spread in particle charge with excitation frequency for $T_{on}/T = 0.5$ and $V_B = 0$. The time-average particle velocity is plotted as a function of excitation frequency for this case in Fig. (13). The vertical coordinate in Fig. (12) is $\sqrt{2}\underline{q}'$, instead of $\underline{q}$. In Fig. (13), the plotted quantity is $2\underline{w}_{net}$, instead of w_{net}. These substitutions are made so that the RMS spread in charge and mean particle velocity are effectively normalized to the respective values that they would have were the excitation a DC electric field of the same RMS value as that actually applied. Figure (14) contains charge vs. time plots and charge distribution functions for three selected frequencies*. Figures (15) -

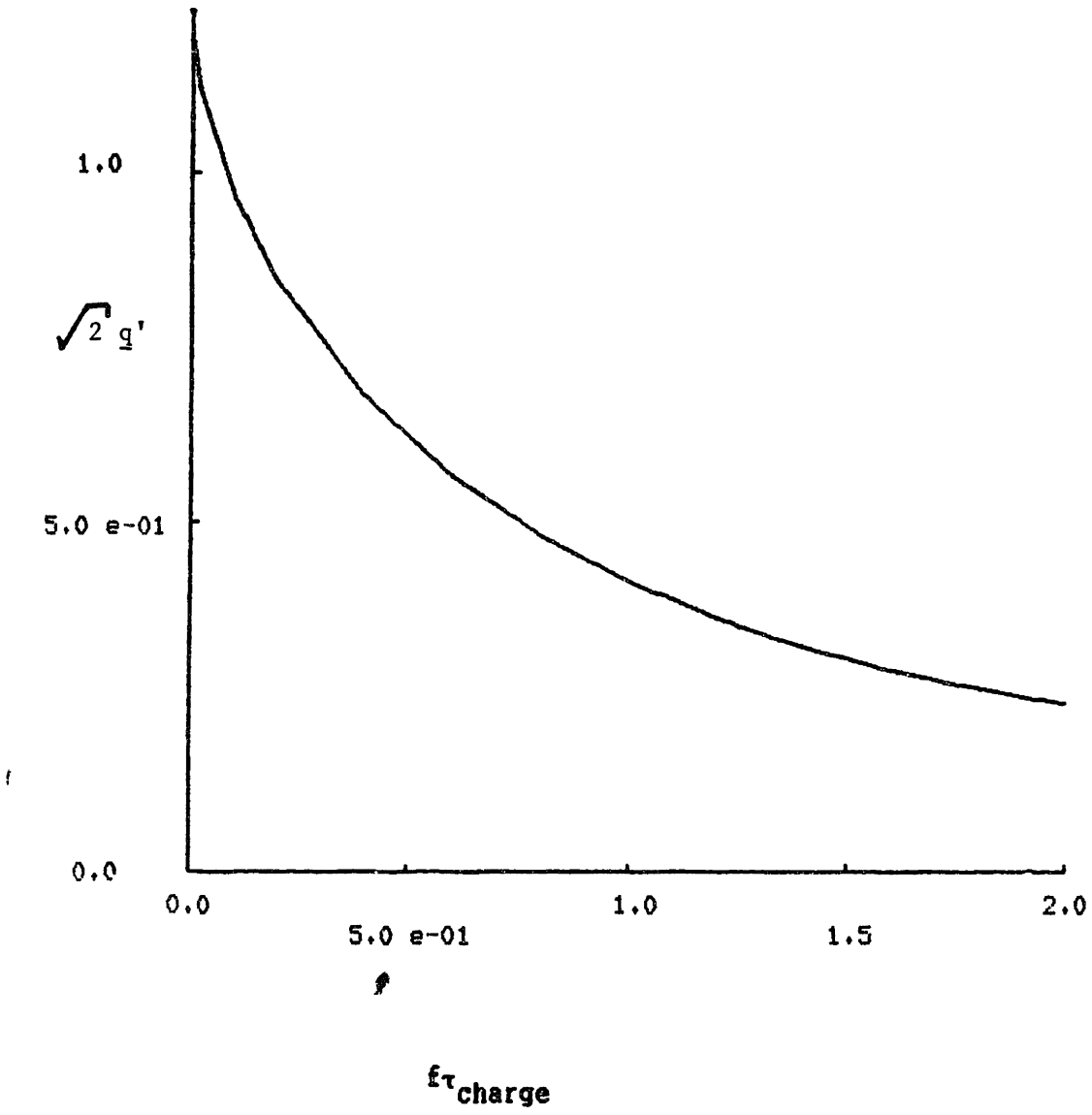

Figure 3.12. Plot showing RMS spread in particle charge vs. AC excitation frequency. Particle charge is normalized to that obtained with DC excitation at the same RMS voltage level. Numerical model simulation was run with T_{on} = 0.5 T, V_B = 0.

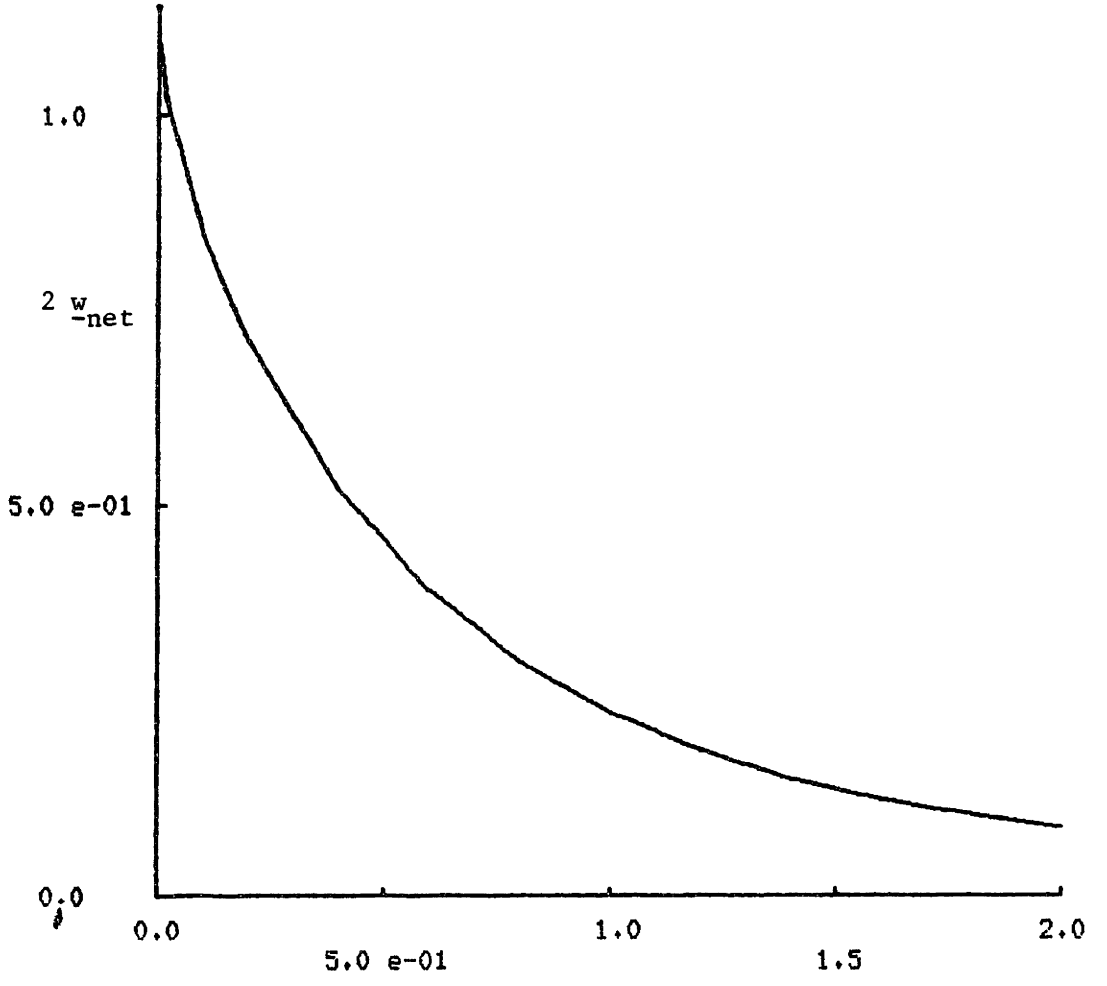

Figure 3.13. Plot showing time-averaged particle migration velocity vs. AC excitation frequency. Particle velocity is normalized to that obtained with DC excitation at the same RMS voltage level. Numerical model simulation was run with T_{on} = 0.5 T, V_B = 0.

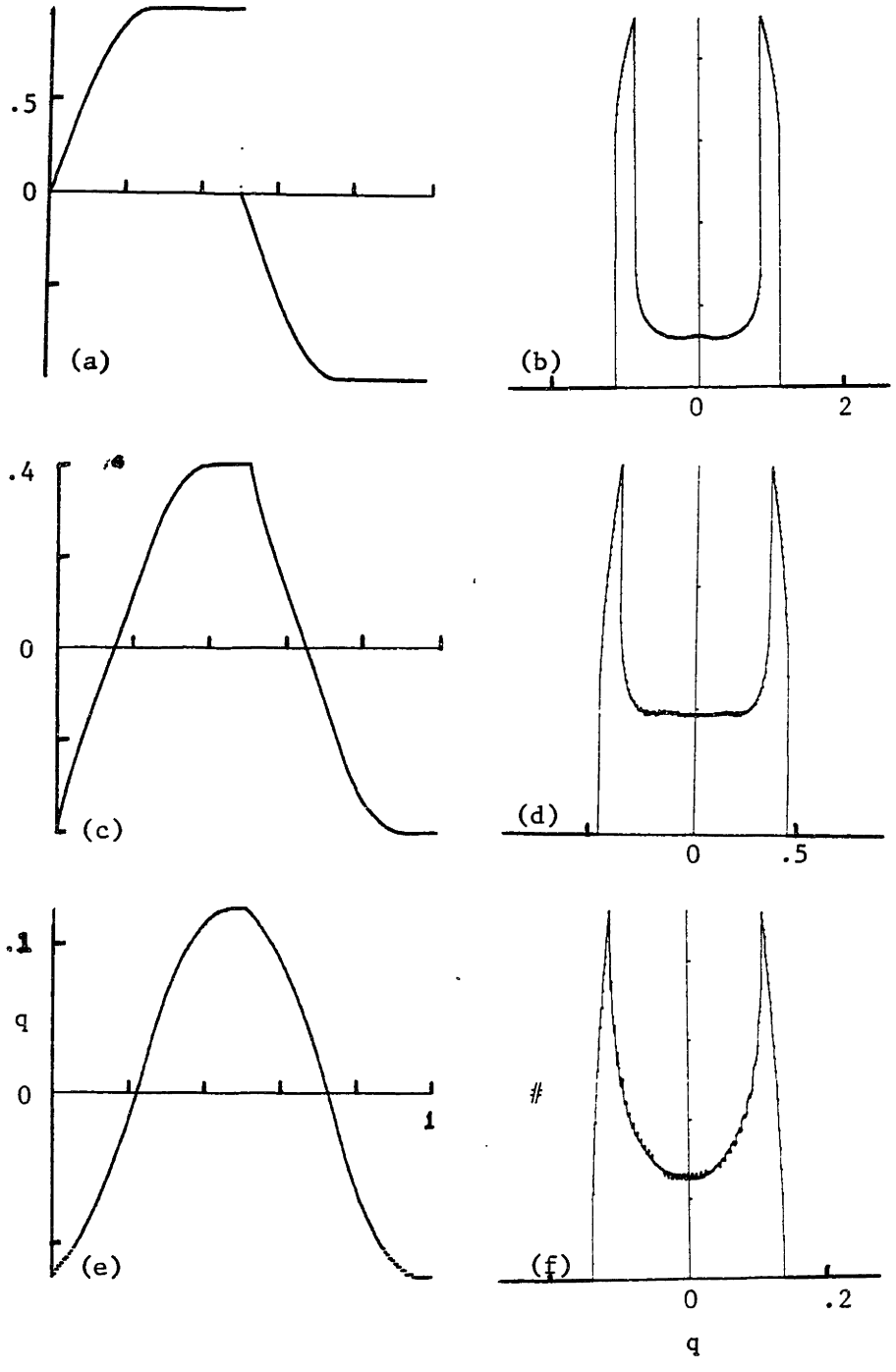

Fig. 3.14. Plots showing particle charge vs. time [(a), (c), (e)] and particle charge distribution functions [(b), (d), (f)] predicted by uniform-field charging model of Section 3.4. T_{on}/T = 0.5, V_B = 0. For (a) and (b), $f\tau_{ch}$ = .002. For (c) and (d), $f\tau_{ch}$ = 1.0. For (e) and (f), $f\tau_{ch}$ = 4.0.

(17) present the corresponding curves for $T_{on}/T = 0.34$, $V_B = 0$. This value is roughly equivalent to the actual corona on-time fraction in the laboratory-scale precipitator.

Figure (18) shows the variation of the mean and RMS spread in particle charge with excitation frequency for the case, $T_{on}/T = 0.34$, $V_B/V_P = 0.07$. The bias voltage is, thus, roughly 10% of the RMS sinusoidal component. The mean charge, which is normalized to the same value as is q', is seen to decrease with rising frequency. The corresponding plot of net particle migration velocity vs. excitation frequency is shown in Fig. (19)

---

*These charge predictions correspond to the migration velocity distributions presented in chapter 5 [see Fig. (5.7), for example]

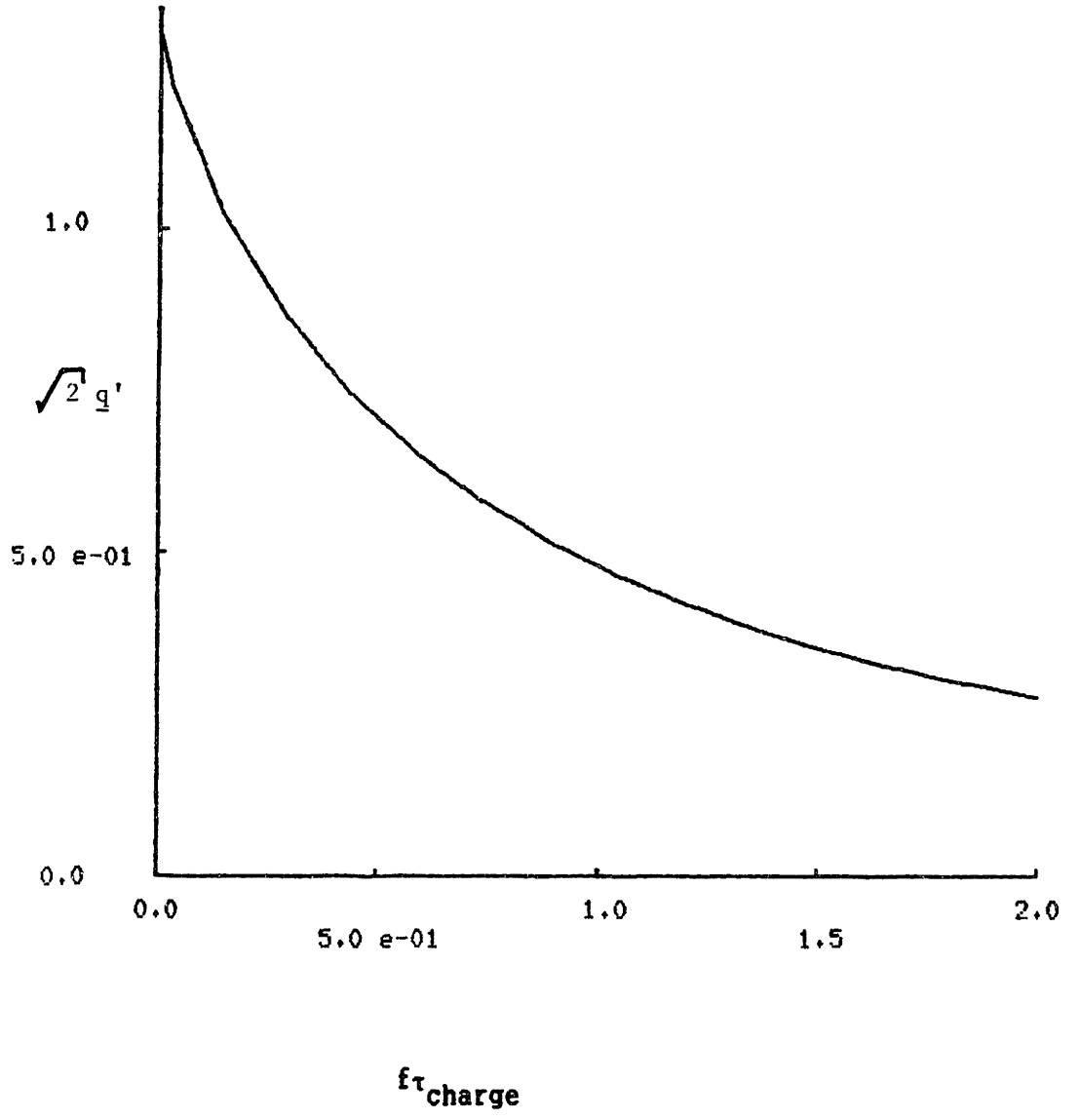

Figure 3.15. Plot showing RMS spread in particle charge vs. AC excitation frequency. Particle charge is normalized to that obtained with DC excitation at the same RMS voltage level. Numerical model simulation was run with T_{on} = 0.34 T, V_B = 0.

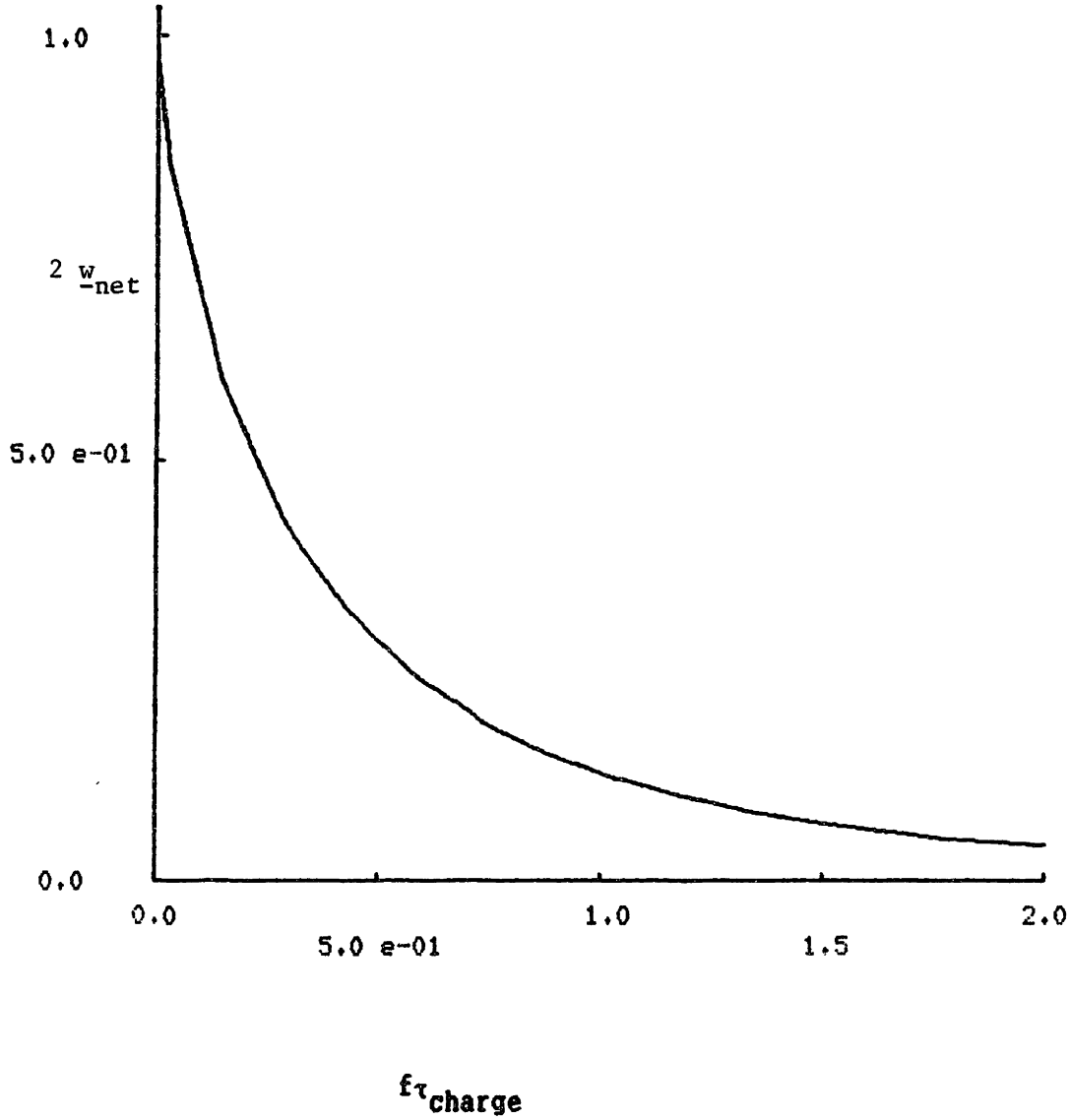

Figure 3.16. Plot showing time-averaged particle migration velocity vs. AC excitation frequency. Particle velocity is normalized to that obtained with DC excitation at the same RMS voltage level. Numerical model simulation was run with T_{on} = 0.34 T, V_B = 0.

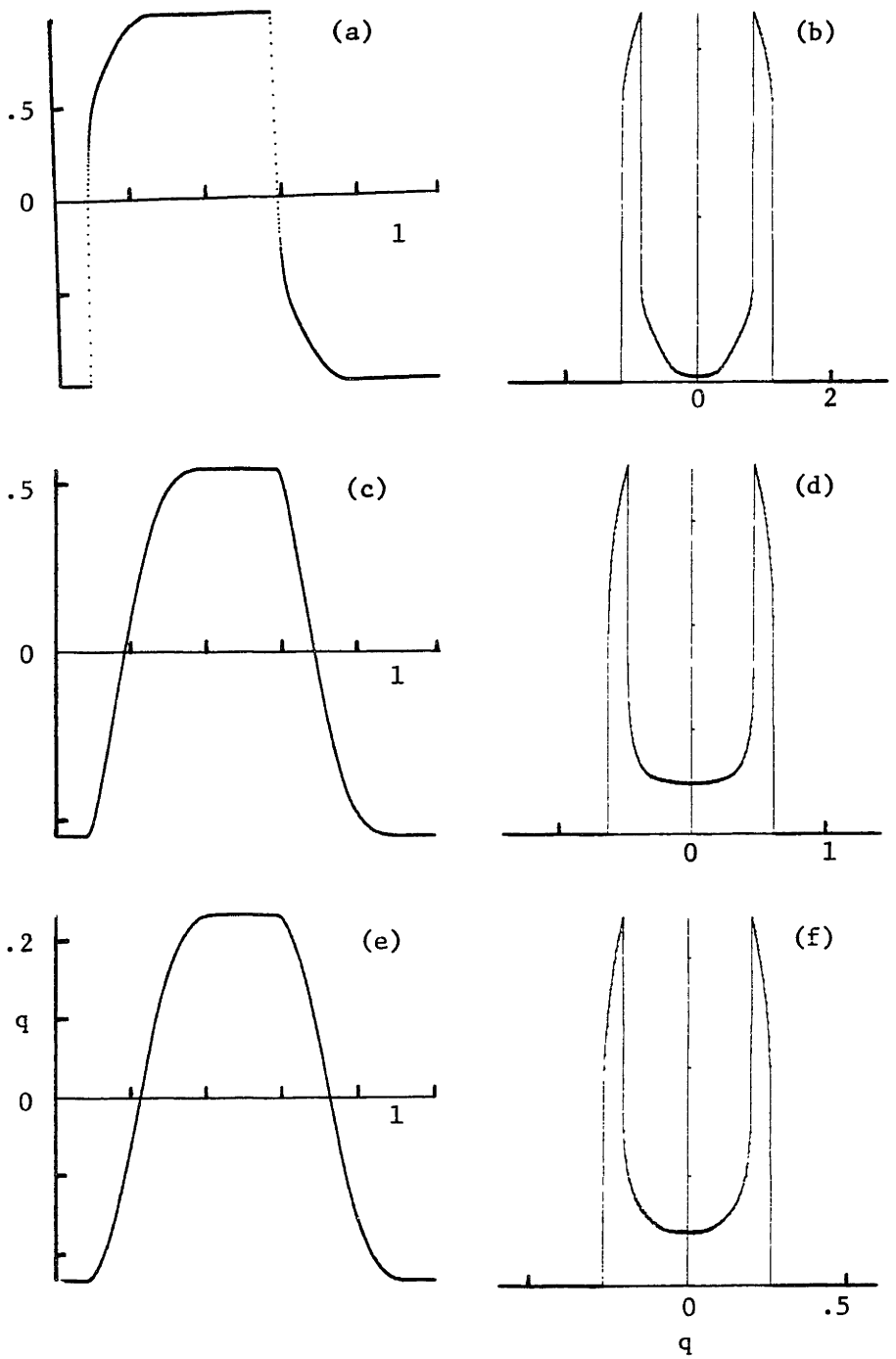

Fig. 3.17. Plots showing particle charge vs. time [(a), (c), (e)] and particle charge distribution functions [(b), (d), (f)] predicted by uniform-field charging model of Section 3.4. $T_{on}/T = 0.34$, $V_B = 0$. For (a) and (b), $f\tau_{ch} = .0029$. For (c) and (d), $f\tau_{ch} = .5882$. For (e) and (f), $f\tau_{ch} = 2.0$.

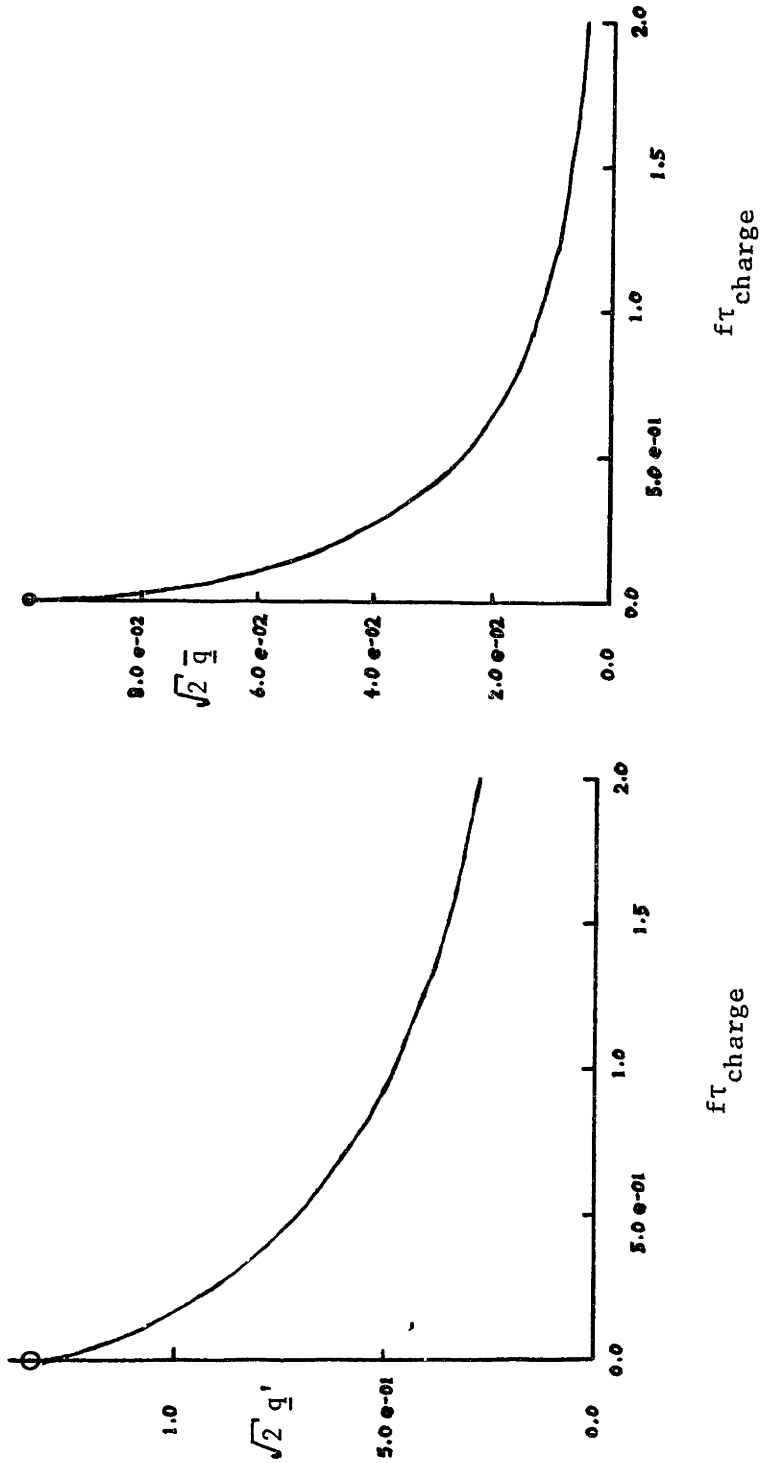

Fig. 3.18. Plots showing mean (b) and RMS spread (a) of particle charge vs. normalized charging frequency, $f\tau_{charge}$. Particle charges are normalized to that obtained with DC charging at the same RMS level. Uniform-field charging model of Section 3.4 was used, with $T_{on}/T = 0.34$, $V_B/V_P = 0.07$.

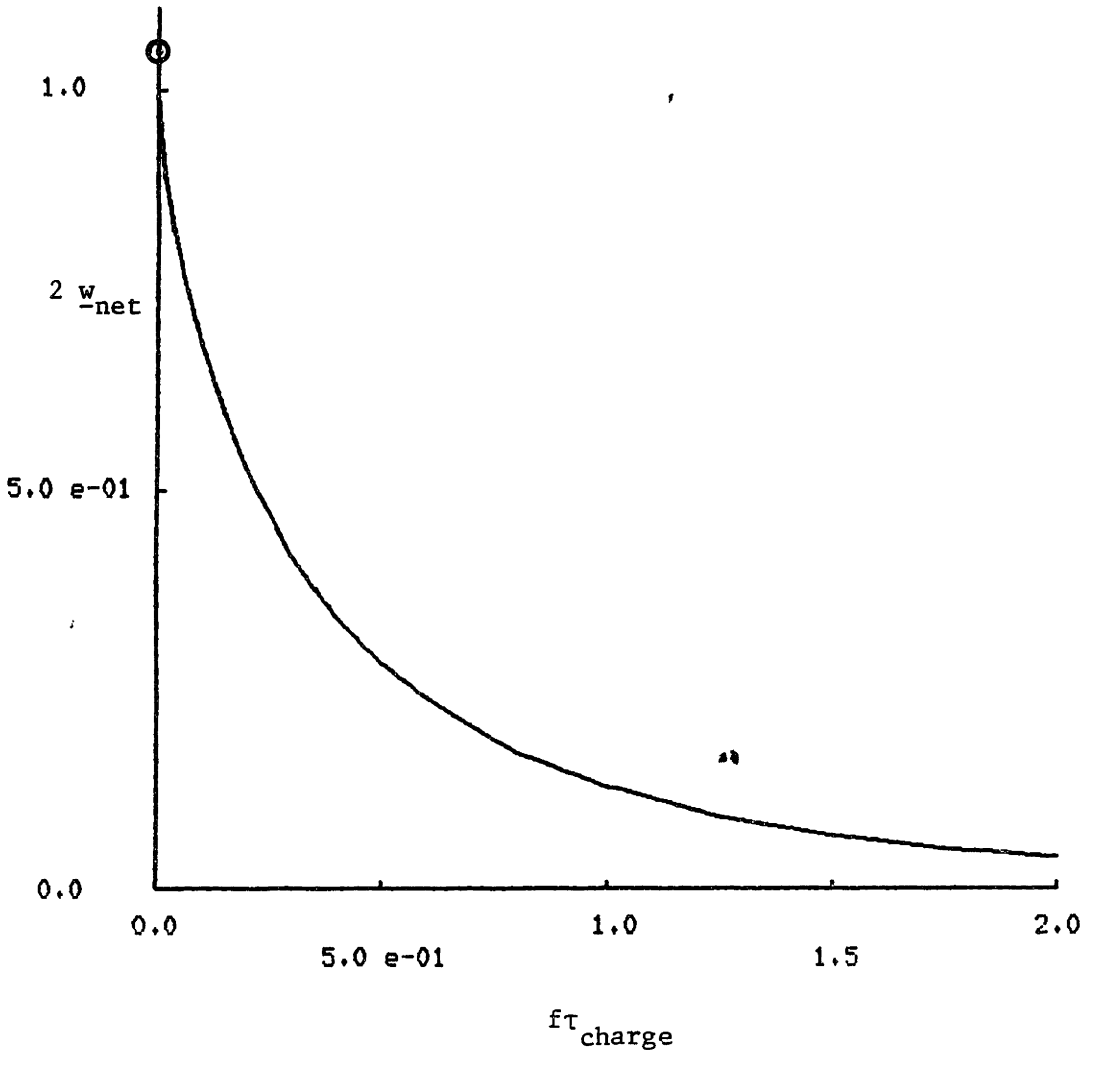

Fig. 3.19. Plot showing time-averaged particle migration velocity vs. AC excitation frequency. Particle velocity is normalized to that obtained with DC excitation at the same RMS voltage level. Numerical model simulation was run with $T_{on}/T = 0.34$, $V_B/V_P = 0.07$.

3.5 Conclusions

In the idealized case of uniform electric fields and corona ion-fluxes, the equations which predict the electric field charging of particles can be solved without any reference to the particle motions. The simplifications which result from this approximation are so great as to justify its examination even in situations for which it it is not entirely valid. It accounts for the rate-dependence of the electric field charging mechanism, which can be a limiting factor in the charging of particles by AC coronas. For some purposes, this crude approximation to the actual problem provides sufficient insight into the charging process. The two issues addressed in this section are : (1) the limits of applicability of the uniform field charging model, and (2) the general behavior of its solution, as determined in this chapter.

3.5.1 Applicability of Uniform Field Charging Model

The two most important assumptions of the model* are also its most questionable. In a wire-plate corona, the electric field is highly non-uniform. In the limit of negligible effects of space charge, the field strength can vary in magnitude by a factor that is of the order of the ratio between the wire radius and the wire-plate spacing#. The corona current can vary similarly with distance from the wires. In the case of a negative corona, non-uniformities can also exist due to localization of the corona current along the wire.

Despite these field and current variations, however, the results of Lawless[4] and Masuda[5] suggest that the DC charging of particles in a precipitator can be adequately modeled by that which occurs in a uniform electric field [see section 1.5.1].

With AC charging, another source of non-uniformity in the charging

---

*The assumptions are those of uniform electric field and uniform corona current density

#See appendix 4 for an analysis which includes the effects of ion space charge on the electric field with a simplified corona electrode structure.

currents is the finite ion migration velocity. Even with a uniform imposed electric field, the ion-density would be non-uniform if the ion transit time, from wires to plates, were significant compared to the excitation cycle time. The transit time, based upon an ion mobility, $b_i \backsim 10^{-4}$ $m^2/v \cdot sec$, electric field strength, $E_o \backsim 10^5$ v/m, wire-plate spacing, H $\backsim$ 1.5 cm, is 1.5 msec*. Thus, for frequencies above roughly 300 Hz, the finite ion migration velocity could play an important role in determining the behavior of the laboratory-scale precipitator as a particle charger.

3.5.2 Behavior of Solution

When particles are subjected to AC charging electric fields and currents of the forms proposed in this chapter, they are seen to attain, alternately, positive and negative charges. The statistics of the particle charge may or may not be biased, depending upon the parameters of the excitation. In all of the cases examined here, however, the time-average particle migration velocity was away from the corona electrode.

The piecewise-constant voltage excitation pictured in Fig. (4) is a gross simplification of the voltage waveform actually applied to conventional precipitators. Still, the RMS spread in particle charge and the time-average particle migration velocity predicted by that model [Figs. (7) and (6)] are remarkably similar to those predicted by the more realistic numerical simulations reported in section 3.4 [Figs. (18) and (19), for example]. Because of the simplicity and the analytic form of its solution, the former will be used to model the results of the precipitation experiments of chapter 4.

---

*The electric field strength of 10^5 v/m is that which would exist in the vicinity of the ground plates in the absence of significant ion space-charge effects. That which is calculated in section 5.4 is based upon an assumption of a steady-state ion charge distribution, and is roughly three times larger. The former estimate is used here because, with high frequency AC excitations, it is unlikely that a steady-state charge distribution is established [see section 6.6].

References for Chapter 3

[1] Radun A., "Particle Charging in a Turbulent Air Stream", ScD Thesis, MIT Dept. of Elect. Eng. and Comp. Sci., Cambridge, Mass., (1981).

[2] Melcher J.R., Continuum Electromechanics, MIT Press, Cambridge, Mass., section 5.5 (1981).

[3] Mouayad L., "AC Electrostatic Precipitation", BS Thesis, MIT Dept. of Elect. Eng. and Comp. Sci., Cambridge, Mass., (1983).

[4] Lawless P.A., Damle A.S., Viner A.S., Shaughnessy E.J., Sparks L.E., "Laser Doppler Anemometer Measurements of Particle Velocity in a Laboratory Precipitator", Third Symposium on the Transfer and Utilization of Particulate Control Technology: Volume II (Electrostatic Precipitators), p. 25 (July, 1982).

[5] Masuda S., Akutsu K., Kanno Y., "Motion of Small Charged Particles Inside an Electrostatic Precipitator", IEEE Industrial Applications Society, 79:5C (1979).

Chapter 4
AC Precipitation Efficiency Measurements

4.1 Introduction

As a practical matter, the final justification for the use of AC electrostatic precipitation must rest with its ability to effectively remove particulate from an air stream. Similarly, the ultimate value of any models for the charging and transport processes which occur in an AC ESP is determined by their ability to accurately predict the performance of an actual device in terms of overall precipitation efficiency.

The mass-monitor experiments, in which the overall collection efficiency of the laboratory-scale precipitator was measured under a wide range of conditions, are described in this chapter. Experimental procedures are outlined in section 4.2, followed by the raw data in 4.3. Section 4.4 presents the turbulent diffusion model, which accounts for turbulent particle transport by an equivalent diffusivity, D_t. This simplified model characterizes the particle motions due to charging and migration in the imposed electric fields by a time-average migration velocity, w_{net}, and an oscillatory velocity, w_{ac}. A discussion of the appropriate values for parameters representing the effects of the turbulent flow on particle mixing is contained in section 4.5.

Values for these parameters are taken from experimental measurements and theoretical models described in chapters 3 and 6 of this thesis, and used in the turbulent diffusion model to predict the efficiency. It is seen in section 4.6 that the efficiency predictions of the model come reasonably close to the actual data. Some conclusions, based upon the comparison between the theoretical and experimental results, are made in section 4.7.

The particle migration characteristics provided by the simple universal precipitation model of chapter 3 result in accurate predictions of the overall precipitation efficiency here. However, that model will be seen to have several shortcomings when its particle charging predictions are compared to actual charge measurements made in the precipitator (see chapter 5).

4.2 Experimental Setup and Procedures

The setup used in the precipitation efficiency measurements was similar to the general setup described in chapter 2. Details of the exact experimental configuration and procedural changes that occurred during the course of the research are to be found in Appendix 2. Only those points essential to understanding the results are included here.

For the collection efficiency experiments, the migration plate pictured in Fig. (2.1) was removed, and the corona wires extended throughout the entire active region of the precipitator. The plate served no purpose in these measurements, and doubling the length of the wires increased the precipitation efficiency to more easily measured values (especially with the high-speed runs).

Only one of the two mass-monitors was used in these experiments (the one at the outlet of the tunnel). By measuring precipitation efficiency through comparison of the outlet mass loading with and without electrical excitation, one could avoid problems associated with calibration differences between mass-monitors. In addition, the measurements made were more conservative, in that any collection due to inertial impaction in the normal tunnel flow was ignored.

Each data point consisted of three measurements of the outlet mass-loading. The first and third were performed with no applied electrical excitation. For the second run of each series, a specified voltage (either ±DC or AC) was applied to the corona wires. The electrical response of the system (ie., the corona current) was recorded, along with the three mass-loadings. For DC excitations, the current was characterized simply by its mean value. For AC coronas, the positive and negative peak currents were observed, along with the "RMS" measurement from a multimeter (<u>not</u> a "true RMS" measurement, though). The collection efficiency, η, was then calculated from the formula,

$$\eta = 1 - \frac{\dot{f}\Big|_{\substack{\text{with}\\ \text{field}}}}{\dot{f}\Big|_{\substack{\text{no}\\ \text{field}}}} \qquad (4.2.1)$$

where

$$\dot{f}\Big|_{\substack{\text{with}\\ \text{field}}} \tag{4.2.2}$$

was the time-average rate of change of the resonant frequency of the deposition crystal in the mass-monitor with the electrical excitation applied, and

$$\dot{f}\Big|_{\substack{\text{no}\\ \text{field}}} \tag{4.2.3}$$

was the average of the corresponding values for the preceding and following zero-voltage runs. Since the rate of change of crystal resonant frequency was taken as proportional to the rate of mass deposition upon the crystal (and, thus, proportional to the aerosol mass-loading of the precipitator exit stream), the fraction in eq. (1) was equal to the ratio of particulate exiting the precipitator with the applied excitation to that without it.

In all, 13 experimental runs were made. Seven of the runs were performed with a horizontal mean flow velocity of 4.3 m/sec, and will be referred to hereafter as the low-speed runs. The remaining six (high-speed runs) were performed with an 8.9 m/sec mean flow velocity. Of the seven low-speed runs, two used DC corona excitations of various magnitudes (one run positive, one negative). Two used an AC excitation of fixed RMS voltage (one 8 kV RMS, the other, 6 kV) and varied the frequency, while three ran with fixed frequency (either 30, 60, or 100 Hz) and variable voltage magnitude. The high-speed runs used the same set of conditions, except that only a single fixed-voltage AC frequency scan was performed (using 8 kV RMS excitation).

4.3 Experimental Data

This section contains reduced data from mass-monitor collection efficiency measurements made on the laboratory-scale precipitator. Figures (1) - (7) show the results from 7 of the 13 experimental runs performed. Appendix 2 presents results from the remaining 6 runs, as well as more plots of the data reported here. Although the collection efficiency is reported for each run, the variable plotted in Figs. (1) -(7) is the effective migration velocity, w_{eff}, defined by the equation

$$\eta = 1 - e^{-\frac{L/U}{H/w_{eff}}} \tag{4.3.1}$$

where η is the collection efficiency, L is the length of the precipitation region, H is the wire-to-plate spacing, and U is the mean horizontal flow velocity. Equation 1 can be solved for w_{eff}, yielding

$$w_{eff} \equiv - U\frac{h}{L}\ln(1-\eta) \tag{4.3.2}$$

The physical significance of the effective migration velocity arises from the behavior of a precipitator under conditions of complete mixing in the collection region (the Deutsch model). With such conditions, so that no appreciable particulate concentration gradients exist in the direction transverse to the mean flow, and with particles migrating at the velocity, w_{eff}, the precipitation efficiency will be as predicted by equation (1). Thus, if turbulent mixing dominates all other particle transport mechanisms in the bulk flow of the tunnel, experiments performed under identical electrical conditions (ie., electric fields and particle charges), but with different flow conditions (ie., mean flow, plate spacing), should yield similar values for w_{eff}, even though the collection efficiencies for the experiments may be different.

Each dot on the plots of Figs. (1) - (7) corresponds to a single efficiency measurement. The solid lines on Figs. (3) - (7) result from application of the turbulent diffusion model presented in section 4.4, and will be explained in section 4.6 [see also Appendix 3]. For the frequency scans [Figs. (3), (4)], the effective migration velocity is plotted as a function of frequency. For the other five experiments, the

effective migration velocity is plotted as a function of the RMS excitation voltage. The RMS voltage measurement was performed by an electrostatic voltmeter which reacts to the "true" RMS value of the voltage.

Before performing any of the analyses of later portions in this chapter, one can make some important observations about the data. The complex wire-plate geometry makes even such elementary tasks as computing the electric field with consideration of ion space-charge effects difficult. However, since both AC and DC collection data were obtained at roughly the same voltage and corona current levels, comparisons can be made amongst them. From Figs. (2) and (3), one can determine that the effective migration velocity for an 8 kV RMS, 60 Hz excitation (3.45 cm/sec) is roughly one-fourth of that attained with a negative DC excitation of 8 kV ($\sim$ 12.5 cm/sec). If one were to simply assume that this comparison will be valid for a full-scale precipitator, then under ideal conditions (from the standpoint of particle resistivity), a 60 Hz AC precipitator would have to have about four times the collection area of a corresponding DC precipitator to deliver the same precipitation efficiency using similar electrical excitation.

The most straightforward model of precipitation, in which one ignores effects of ion space-charge on the electric field and assumes that all particles reach their saturation charge very quickly, would predict little difference between the performance with positive and negative DC excitations. This is quite obviously not the case in these experiments, with a positive corona voltage of 8 kV resulting in $w_{eff} \sim$ 5.6 cm/sec [Fig. (1)]. One might be tempted to account for the improved performance of the negative DC corona by the fact that the corona current at -8 kV is $\sim$ -2.3 ma, almost double the 1.3 ma obtained with +8kV DC. However, even with a voltage of -7.25 kV DC, corresponding to -1.3 ma, the effective migration velocity ($\sim$ 7.5 cm/sec) is greater than the +8 kV DC value. Examination of Fig. (2) shows that the effective migration velocity at low AC frequencies tends towards the +DC value as $f \to 0$, rather than the -DC value.

It is seen, in chapter 5, that differences in the spatial distribution of positive and negative coronas can have a significant effect on charging processes. While the positive corona is normally

uniformly distributed over the wire surface, negative corona tends to occur at distinct points along the wire, separated by distances on the order of a centimeter. Since the total negative corona current for a given voltage magnitude is larger than the corresponding positive corona, the current density near these distinct (negative corona) points must be very much greater than it is for the positive. The model proposed in section 4.4 will not take into account these differences, but will simply normalize predicted effective migration velocities to those obtained with +DC excitation.

Perhaps the most important observation to be made from the data is the fact that data from experiments performed with identical electrical conditions (but different horizontal flow velocities) are very nearly identical. For example, the differences between effective velocities measured for the frequency scans of Figs. (3) and (4) are within experimental error. It is tempting to conclude from this that an assumption of complete mixing in the collection region (ie., the Deutsch model) is justified, as that was the basis for presenting the data in its present form.

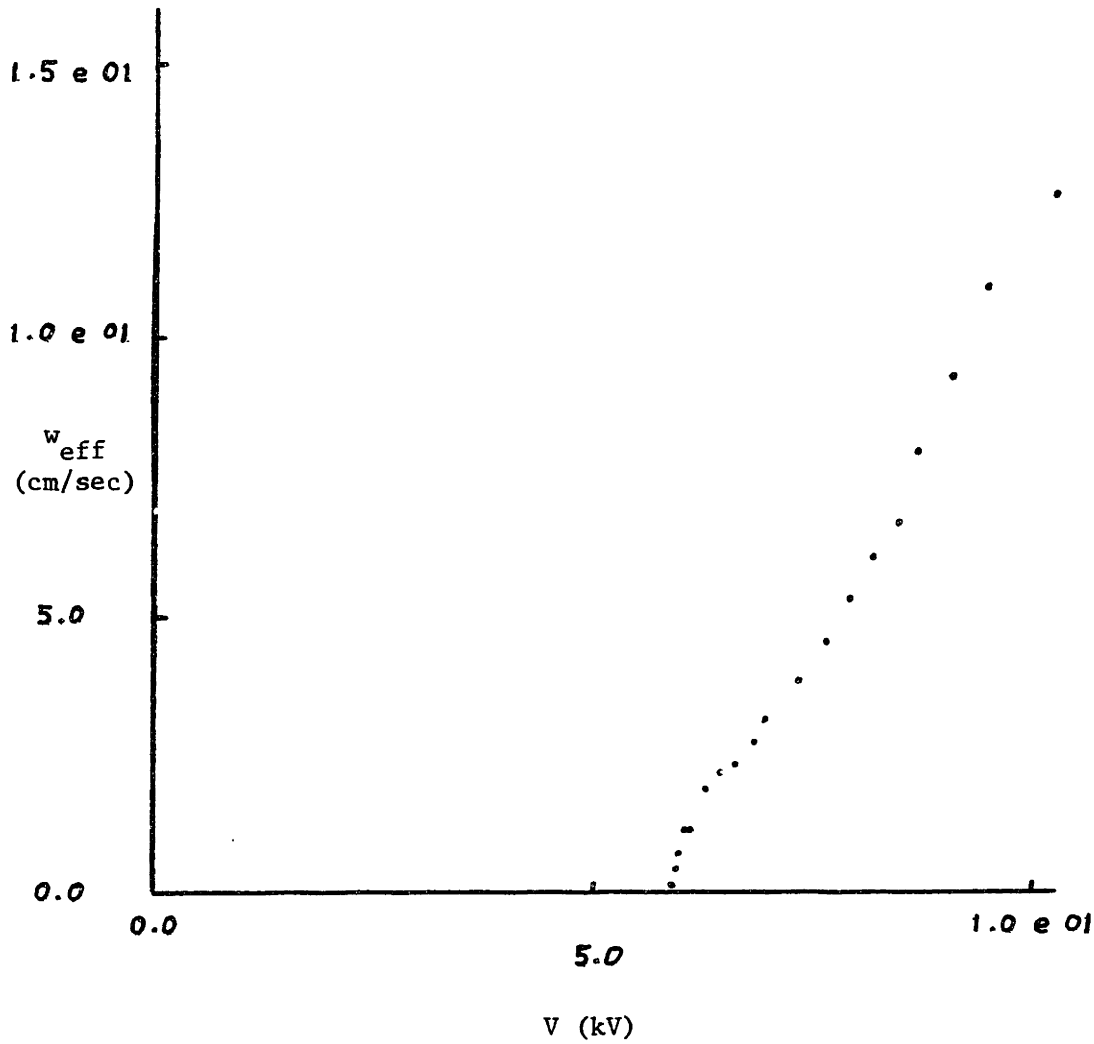

Figure 4.1. Plot of effective particle migration velocity vs. (positive) DC corona excitation voltage magnitude. Horizontal flow velocity was 4.3 m/sec (6/10/83).

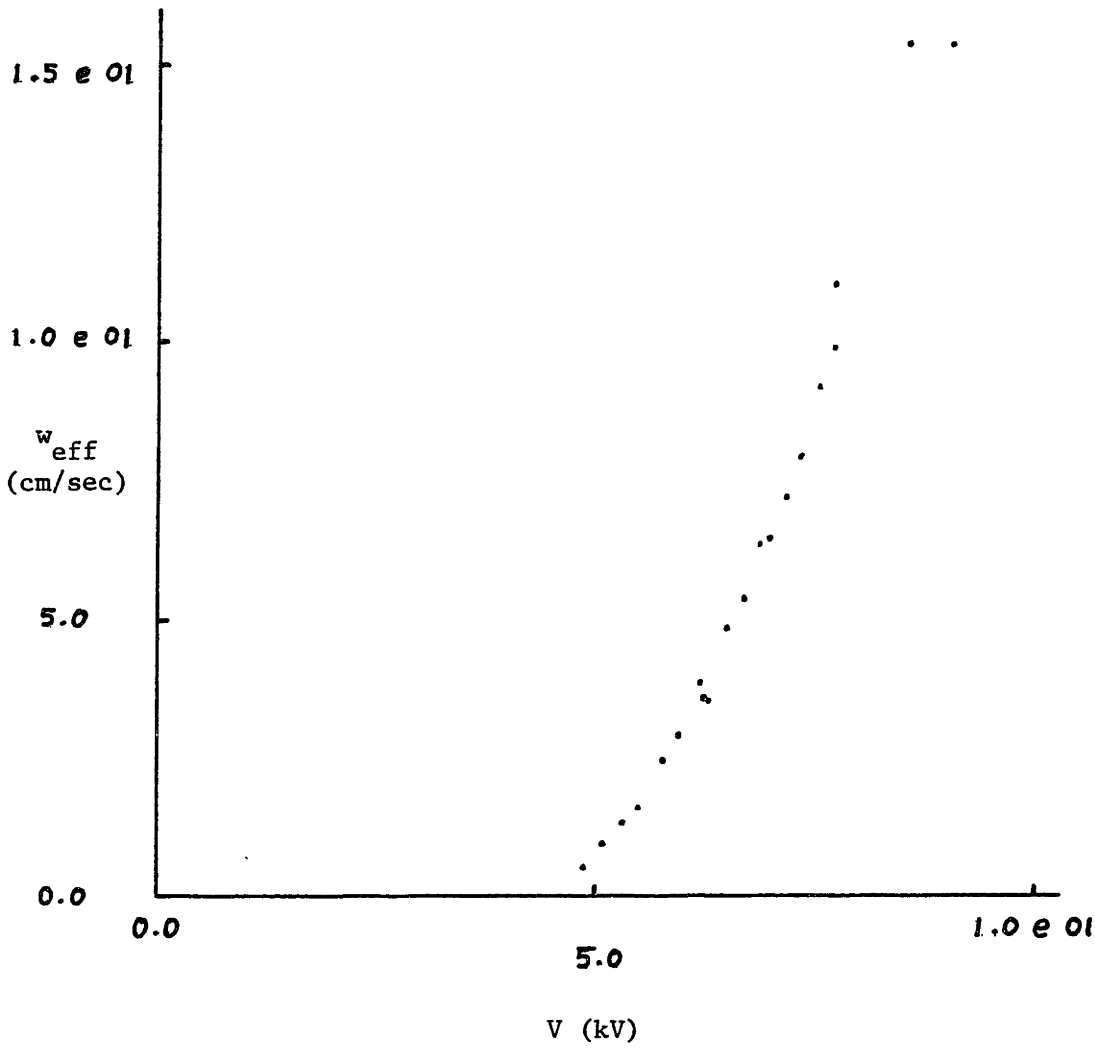

Figure 4.2. Plot of effective particle migration velocity vs. (negative) DC corona excitation voltage magnitude. Horizontal flow velocity was 4.3 m/sec (6/8/83).

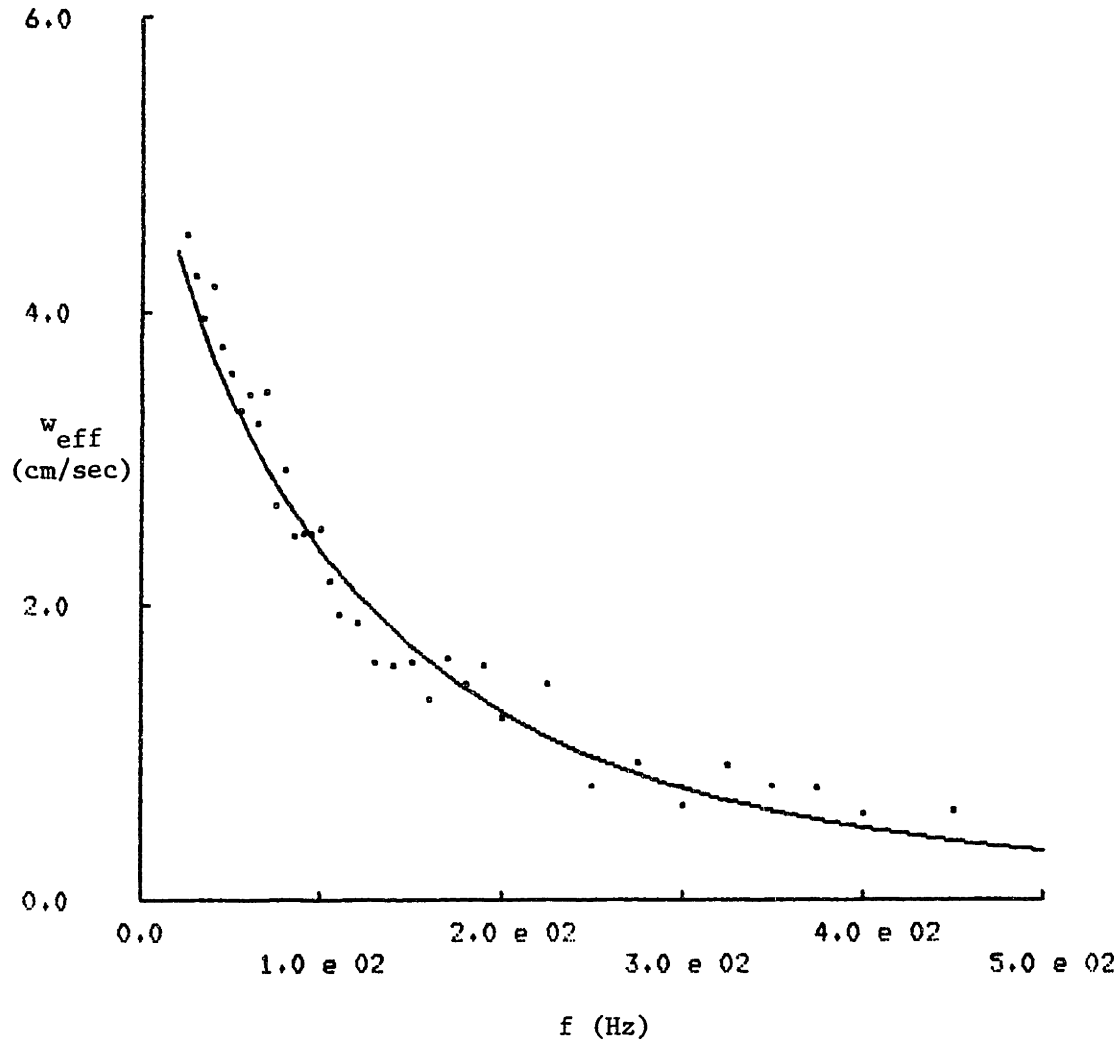

Figure 4.3 Plot of effective particle migration velocity vs. Corona excitation frequency. Data from low-speed run [Fig. (2)]. Theoretical curve is from universal precipitation model. The boundary layer is assumed to be very thick. The characteristic charging time is 3.0 msec.

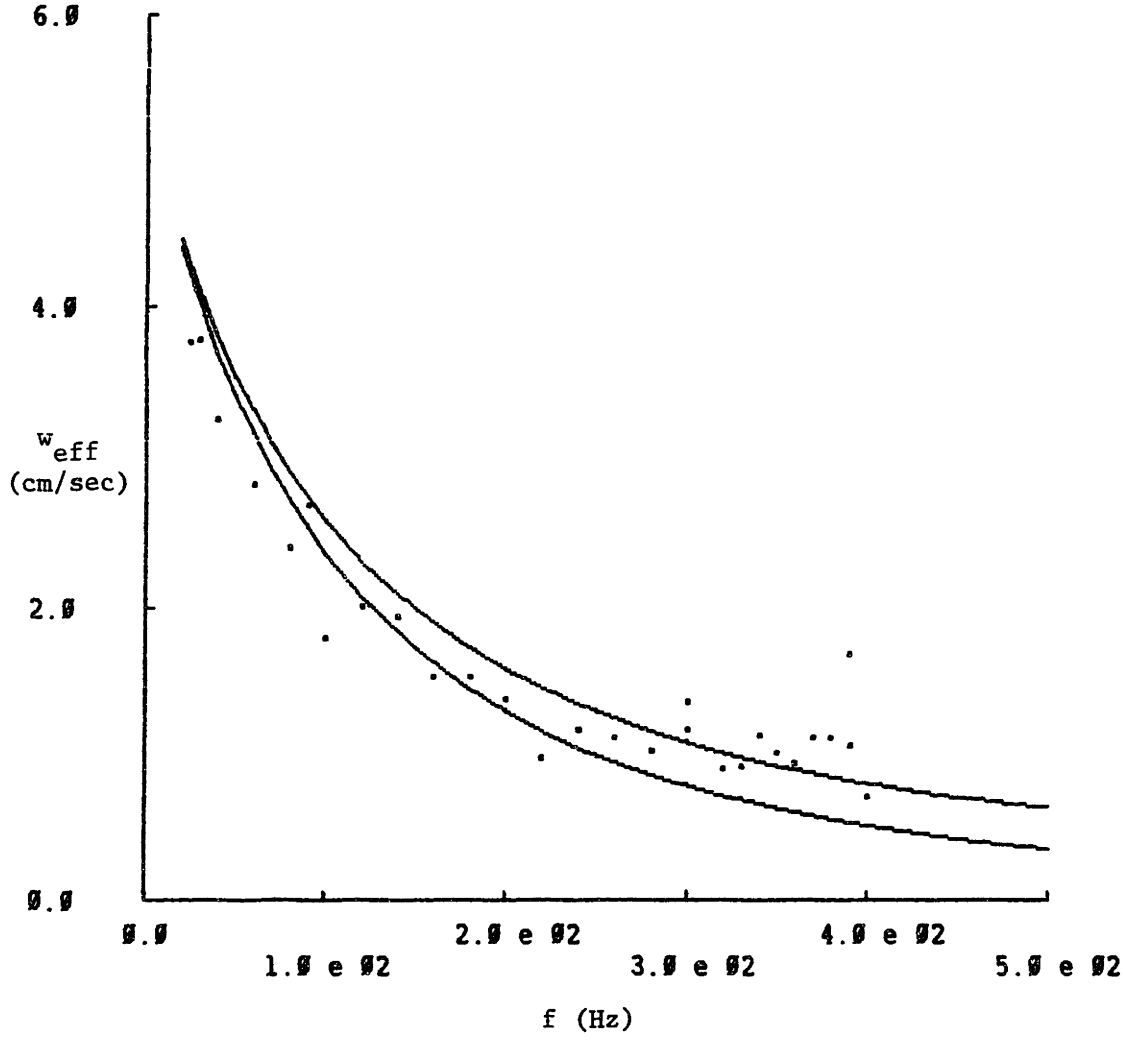

Figure 4.4 Plot of effective particle migration velocity vs. Corona excitation frequency. Data from high-speed run [Fig. (21)]. Theoretical curves are from universal precipitation model. Upper one is for zero boundary-layer thickness; lower one is with very thick boundary layer. The characteristic charging time is 3.Ø msec.

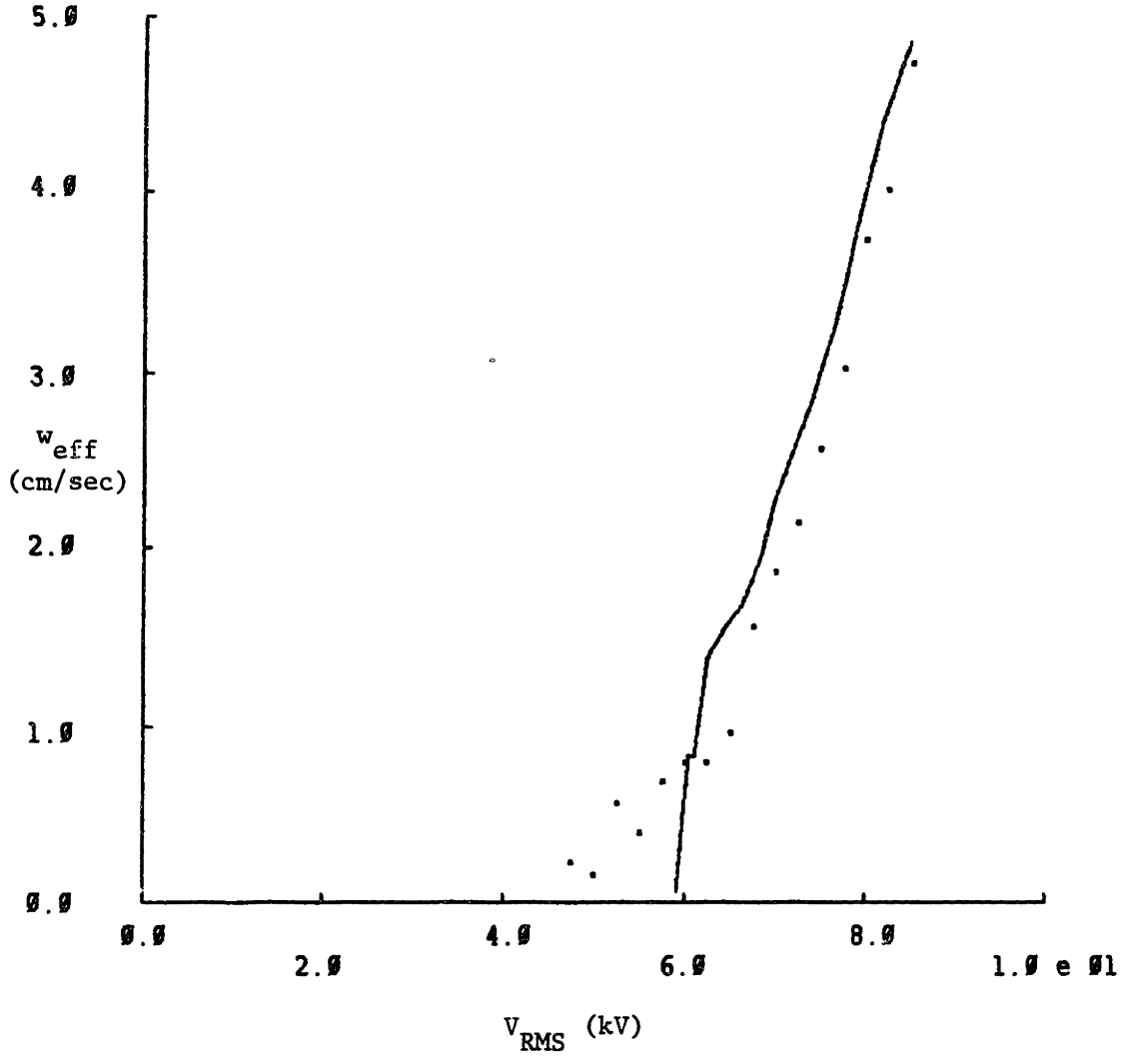

Figure 4.5 Plot of effective particle migration velocity vs. RMS Corona excitation voltage. Data from low-speed run [Fig. (9)], with excitation frequency fixed at 3Ø Hz. Theoretical curve is from universal precipitation model, using positive DC precipitation data [Fig. (8)]. The boundary layer is assumed to be very thick. The characteristic charging time is 3.Ø msec.

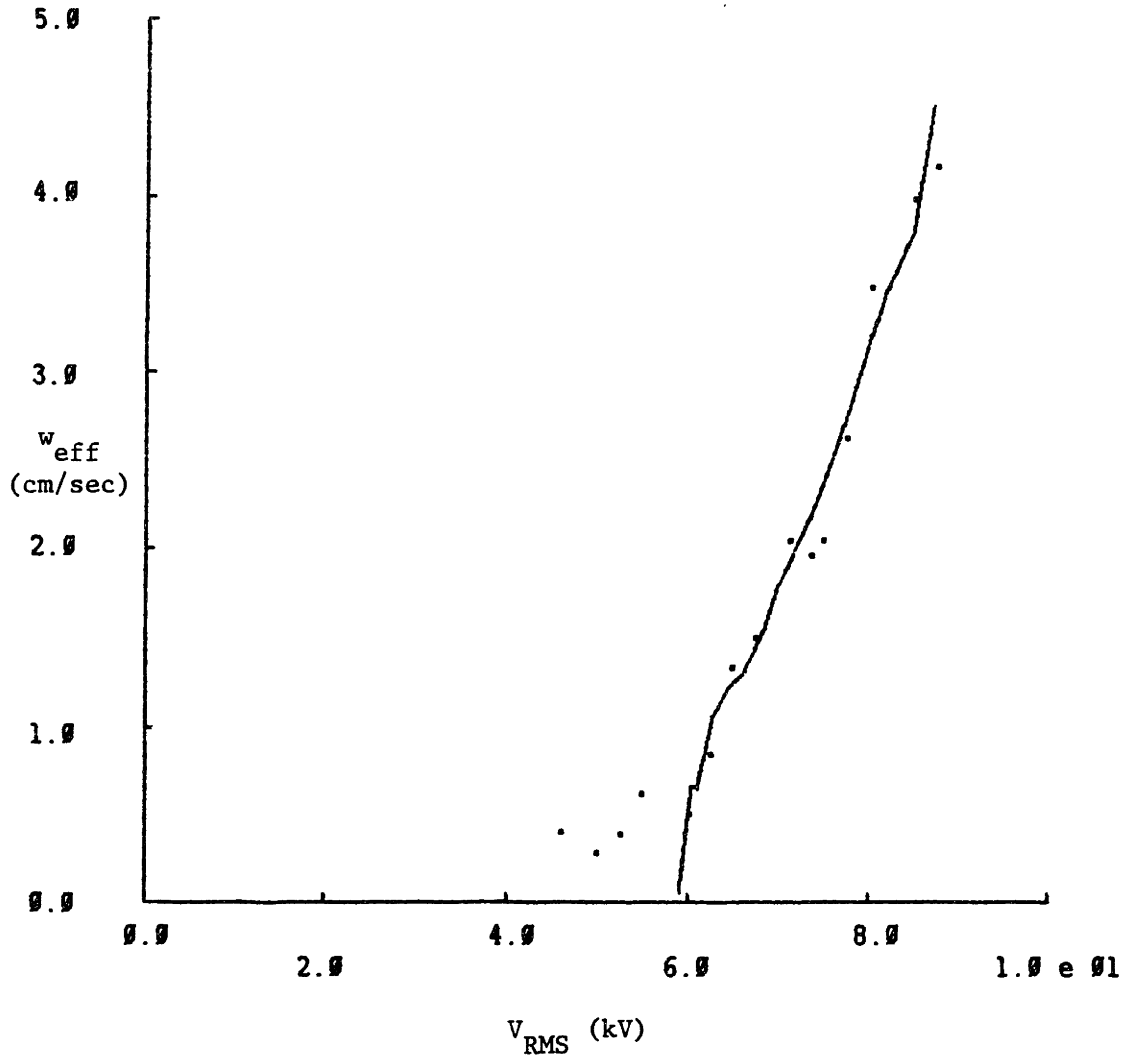

Figure 4.6 Plot of effective particle migration velocity vs. RMS Corona excitation voltage. Data from low-speed run [Fig. (10)], with excitation frequency fixed at 60 Hz. Theoretical curve is from universal precipitation model, using positive DC precipitation data [Fig. (8)]. The boundary layer is assumed to be very thick. The characteristic charging time is 3.0 msec.

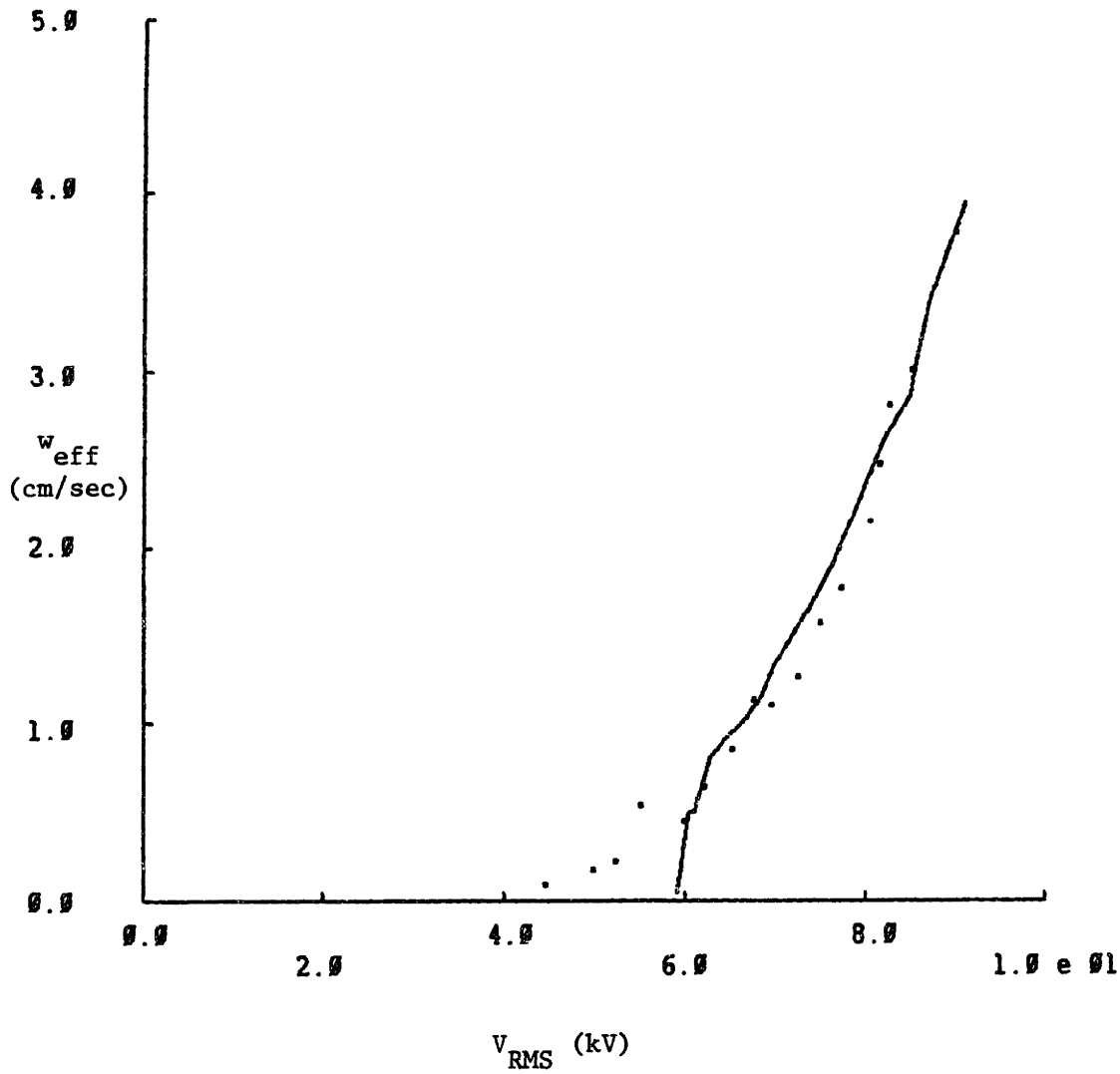

Figure 4.7 Plot of effective particle migration velocity vs. RMS Corona excitation voltage. Data from low-speed run [Fig. (11)], with excitation frequency fixed at 100 Hz. Theoretical curve is from universal precipitation model, using positive DC precipitation data [Fig. (8)]. The boundary layer is assumed to be very thick. The characteristic charging time is 3.0 msec.

4.4 Simplified Turbulent Diffusion Model

From the discussion of chapter 1, it is apparent that the air-stream turbulence conditions in an AC precipitator can be a major factor in determining its collection efficiency. In order to predict the behavior of such devices, one must adequately model the effects of turbulent mixing on particle distributions. It is common[1-7] to account for these effects by use of an equivalent turbulent diffusivity, whose value can then be empirically determined.

This section presents a model, based on that concept, for the precipitation of particles subjected to a bipolar charging current and electric field. Effects of turbulence on the particle distribution in the core flow are represented by the uniform turbulent diffusivity, D_t. The charging and migration processes are characterized by a net (time-average) particle migration velocity, w_{net}, an oscillatory velocity, w_{ac}, and the cycle time of the excitation. A boundary condition is proposed to account for the reduced influence of turbulent transport on very small length scales near the collecting wall, by assuming the existence of a wall-layer of thickness, δ, in which no turbulent mixing takes place.

The model is simplified considerably by two assumptions: (1) that turbulent diffusion is the dominant mechanism of particle transport in the bulk flow, but (2) that it does not bring particles close enough to the collection plate that they can be precipitated by their oscillatory migrations alone. Both of these assumptions are examined at length in section 4.5.

The idealized situation is described in section 4.4.1. In section 4.4.2, the conservation law for particles is applied to yield the familiar Deutsch equation[14,15], which predicts an exponential decay in the particle concentration with increasing downstream distance. The spatial rate of this decay is expressed there in terms of an effective precipitation velocity at the collection surface. A boundary condition is proposed in section 4.4.3 to supply the necessary effective particle precipitation velocity. For the simplified situation dealt with here, that quantity is equal to the time-average particle migration velocity, w_{net}. The solution to this simplified problem is presented in section

4.4.4.

A more detailed treatment of the problem is to be found in Appendix 3. The model presented there accounts for a finite turbulent diffusivity in the bulk flow and for possible effects of the oscillatory particle migration on the effective precipitation velocity. It is seen there that, in the limits of large bulk diffusivity and thick zone of no turbulent transport, that model predicts the same overall behavior as the simplified one developed here.

4.4.1 Problem Description

The situation is as pictured schematically in Fig. 8. Air, laden with particles, flows between two parallel plates of length, L, width, B, and separation, H. The mean flow velocity, U, is assumed to be uniform in the core flow, decreasing rapidly to zero across thin boundary layers at each plate. The particle concentration, $n(x,z,t)$, is taken as uniform at the inlet.

$$n(x,0,t) = n_o \tag{4.4.1}$$

As a result of the corona ion flux and imposed electric field, the particles experience both a time-average migration toward the lower plate and an oscillatory motion. If the air-flow were completely laminar, then a typical particle path would be as illustrated in Fig. 9. Because of flow turbulence, however, these motions are superimposed upon turbulent velocity fluctuations.

The particle migration will be characterized entirely by two lengths and the cycle time of the motion. The lengths, ℓ_{net} and ℓ_{max}, represent the net particle movement and maximum particle excursion, respectively, during a single half-cycle of the corona excitation. The relationships between these lengths and the characteristic particle migration velocities, w_{net} and w_{ac}, are

$$w_{net} \equiv \frac{\ell_{net}}{T/2}$$

$$w_{ac} \equiv \frac{\ell_{max}}{T/2} \tag{4.4.2}$$

where T/2 is the time of one half-cycle of the corona excitation. It is

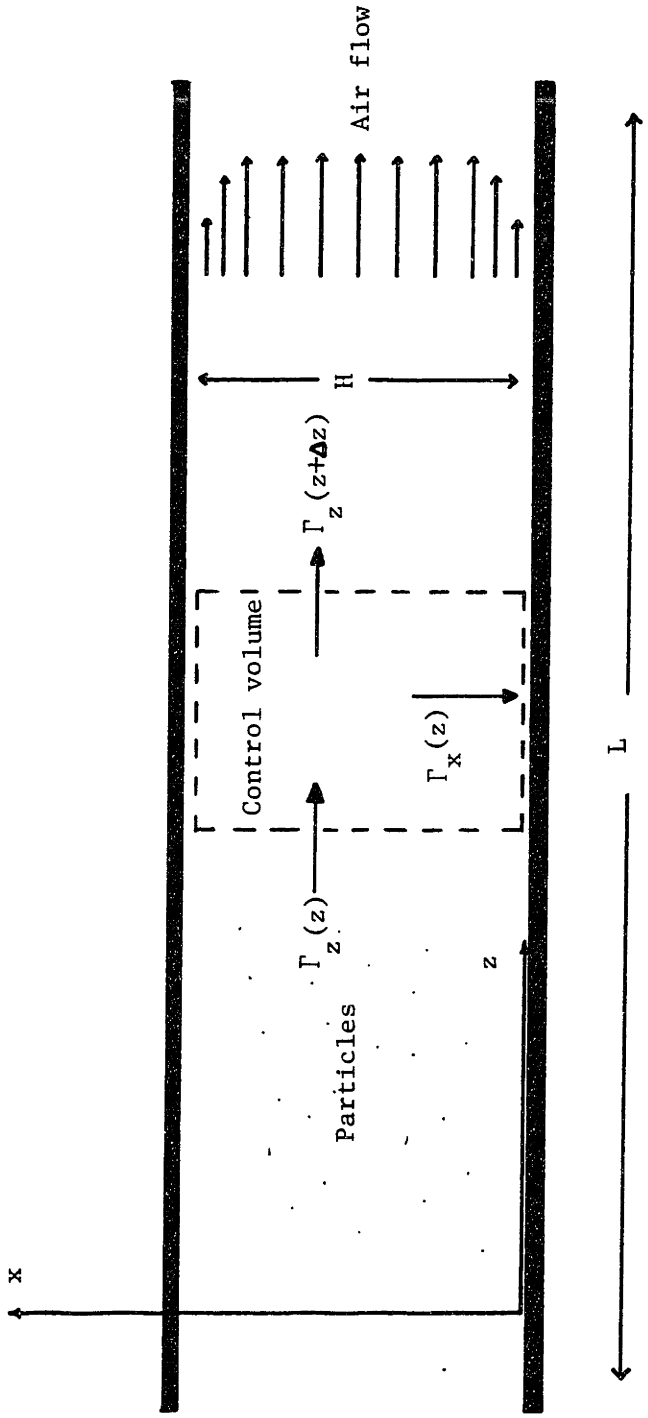

Fig. 4.8. Schematic illustration of situation for turbulent diffusion model. Particles enter at left, convected by air flow. Density decreases with increasing axial coordinate (z), due to precipitation onto lower plate.

assumed, for the sake of simplicity, that the particle migration is identical for positive and negative half-cycles of the corona. Such an assumption is not very restrictive, here, as it will be seen that only the net particle displacement per unit time is of importance. The detailed model of Appendix 3 allows for asymmetry between the two half-cycles of the particle motion. Although it is not the case in Fig. 9, it is possible for ℓ_{net} to be much smaller than ℓ_{max}, because particles can undergo nearly equal backward and forward displacements each half-cycle, as is the case for very high frequency charging (see chapter 3). It is assumed that both ℓ_{net} and ℓ_{max} are much smaller than any other physical dimensions of the system described thus far.

The sole effect of the turbulence will be to introduce an equivalent diffusivity, D_t, to the region between the plates. For the sake of simplicity, D_t will be taken as uniform throughout the core flow. The behavior of the flow in the thin boundary layer, and the corresponding boundary condition imposed upon n(x,z,t) at each plate, are the subject of section 4.4.3.

It is convenient, here, to define several characteristic times. The convection time, τ_c, is the residence time of air in the region.

$$\tau_c \equiv \frac{L}{U} \tag{4.4.3}$$

The diffusion time, τ_d, is based on turbulent particle diffusion over the plate separation distance.

$$\tau_d \equiv \frac{H^2}{D_t} \tag{4.4.4}$$

A migration time, τ_m, can be defined.

$$\tau_m \equiv \frac{H}{w_{net}} \tag{4.4.5}$$

Thus, τ_m is the time that it would take for a particle to cross the gap from upper to lower plate by migration alone. Because the progress made during any one cycle is small, only the net migration per cycle is important in determining this time.

It will be assumed that the characteristic diffusion time, based on the plate separation, H, is much smaller than either the convection time or the migration time. This simplifies the problem considerably. A

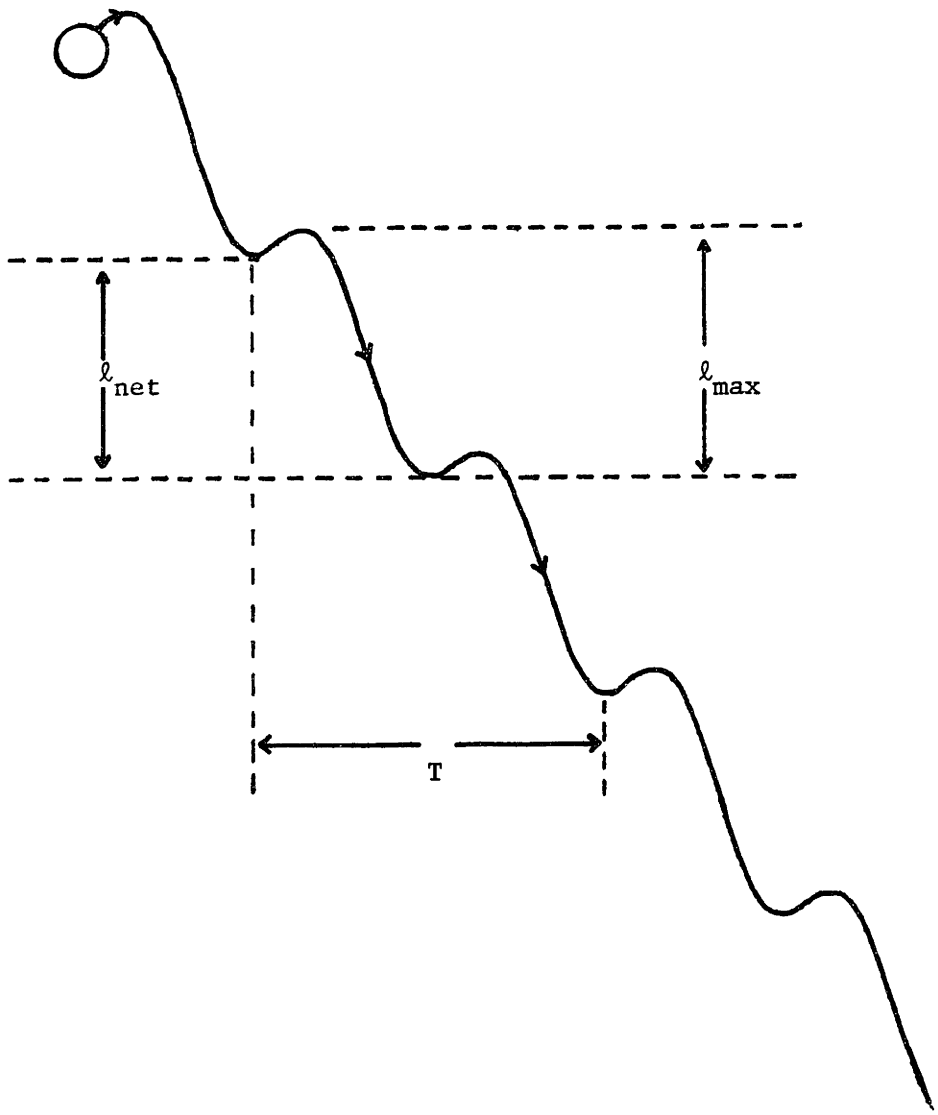

Fig. 4.9 Path of a particle undergoing universal precipitation. The length, ℓ_{net}, is the net particle progress in a half-cycle. The length, ℓ_{max}, is the maximum particle excursion during the same interval.

physical interpretation of this assumption would be that turbulent diffusion is able to eliminate any transverse particulate concentration gradients more quickly than the time-average particle migration can cause them. Indeed, if the flow entered the precipitator with a non-uniform concentration profile, the transverse gradients would be significantly reduced in the time during which it passed through the collection region. Thus, the only possible effect of the particle migrations is to precipitate them from the edge of the core flow to the collection plate. It should be noted that, since the precipitator can be much longer than the plate separation (ie., $L >> H$), turbulent diffusion might not be able to eliminate all concentration gradients in the longitudinal direction. Thus, the particle concentration in the core flow region can vary significantly with the longitudinal coordinate, z, but not with the transverse coordinate, x.

It is desired to determine the overall precipitation efficiency of the device. The efficiency, η, is defined in eq. (4.2.1) as the ratio of particulate removed from the flow to that which enters the region, or unity minus the ratio of particulate leaving the precipitator to that entering it. As a practical matter, time-averaged quantities are used in the computation. The time-averaged particle concentration, $\langle n(z)\rangle$, is defined

$$\langle n(z)\rangle \equiv \frac{1}{T} \int_{t}^{t+T} n(z,t')\, dt' \qquad (4.4.6)$$

Two assumptions are implicit in the definition of eq. (6). First, the lack of significant transverse particle concentration gradients was used to express the time-dependent concentration as a function of longitudinal displacement, z, and time, t, alone. It is also assumed that the system is in a steady state, so that $\langle n(z)\rangle$ does not depend upon the starting time, t, of the integral in eq. (6). Thus, the efficiency, η, is

$$\eta = 1 - \frac{\langle n(L)\rangle}{n_o} \qquad (4.4.7)$$

4.4.2 Volume Equation

The law of conservation of (particle) mass can be applied to the control volume defined by the dotted line in Fig. (8). The air flow carries particles into and out of the volume through surfaces at the longitudinal locations, z, and z+Δz, respectively. Any difference between the convective particle fluxes through these two surfaces must be accounted for by an additional flux of particles to one of the tunnel walls. It is argued in the following section that there should be no particle flux to the upper surface. (it corresponds to the wire plane in the actual experiment). Thus, whatever particles enter at z and do not leave at z+Δz must have precipitated onto that section of the collection surface which is between those two locations. This fact can be expressed quantitatively in terms of an effective precipitation velocity, w_p.

$$H \cdot \left[\langle \Gamma_z(z) \rangle - \langle \Gamma_z(z+\Delta z) \rangle \right] = \langle \Gamma_x(z) \rangle \cdot \Delta z \qquad (4.4.8)$$

where

$$\langle \Gamma_z(z) \rangle = U \cdot \langle n(z) \rangle \qquad (4.4.9)$$

$$\langle \Gamma_x(z) \rangle = w_p \cdot \langle n(z) \rangle \qquad (4.4.10)$$

In eq. (8), the quantity in parentheses on the left is the difference between the convective particle flux densities at z and z+Δz. The flux density to the collection plate is represented by Γ_x. The velocity, w_p, may be interpreted physically as the time-average rate of migration of particles from the outer edge of the core flow region to the collection plate. In the limit , $\Delta z \to 0$, the approximation of eq. (8) becomes exact.

$$U \cdot H \cdot \frac{d\langle n(z) \rangle}{dz} = - w_p \cdot \langle n(z) \rangle \qquad (4.4.11)$$

4.4.3 Boundary Conditions

There exist four significant boundaries to the system, one each at z=0, L, and one each at x=0, H. The constraints at the first two can be dealt with rather easily; the latter two are more involved. Equation (1) states the constraint on $\langle n(z) \rangle$ at z=0. Because of the assumption of negligible turbulent diffusion in the longitudinal direction, it is not necessary (or, even appropriate) to constrain the particulate concentration at the precipitator outlet. Thus, the only boundary condition that applies to the surfaces at z=0 and z=L is that the inlet concentration be equal to n_o.

It will be assumed that once a particle touches the collection plate, it will adhere to it mechanically, rather than returning to the flow. This assumption is illustrated in Fig. 10, for the case of a particle undergoing universal precipitation in laminar flow; but it applies when turbulent diffusion is present as well. From the standpoint of diffusive processes, this is equivalent to constraining the particle concentration to zero just below the plate, as particles can diffuse toward it, but not away. Thus, the concentration immediately above the plate must also be zero (otherwise, the discontinuity in concentration would result in an infinite diffusive flux).

If the bulk diffusivity, D_t, were finite, such a boundary condition,

$$n \Big|_{x=0,H} = 0 \qquad \text{(WRONG)} \qquad (4.4.12)$$

could conceivably be used alone to constrain the particle concentration, n(x,z) [with a finite diffusivity, concentration gradients in the transverse direction could exist]. With the situation under examination here, however, application of eq. (12) would be disastrous. In the limit of an infinite diffusivity (corresponding to the very small transverse diffusion time, τ_d), the constraint of zero concentration at x=0 and x=H would result in an infinite diffusive flux to the plates, and thus, zero concentration throughout the precipitator. Even in the case of a finite bulk diffusivity, the boundary condition of eq. (12) would be incorrect, as it does not take into account the decrease in turbulent particle transport near the plates, due to the boundary layers there. The

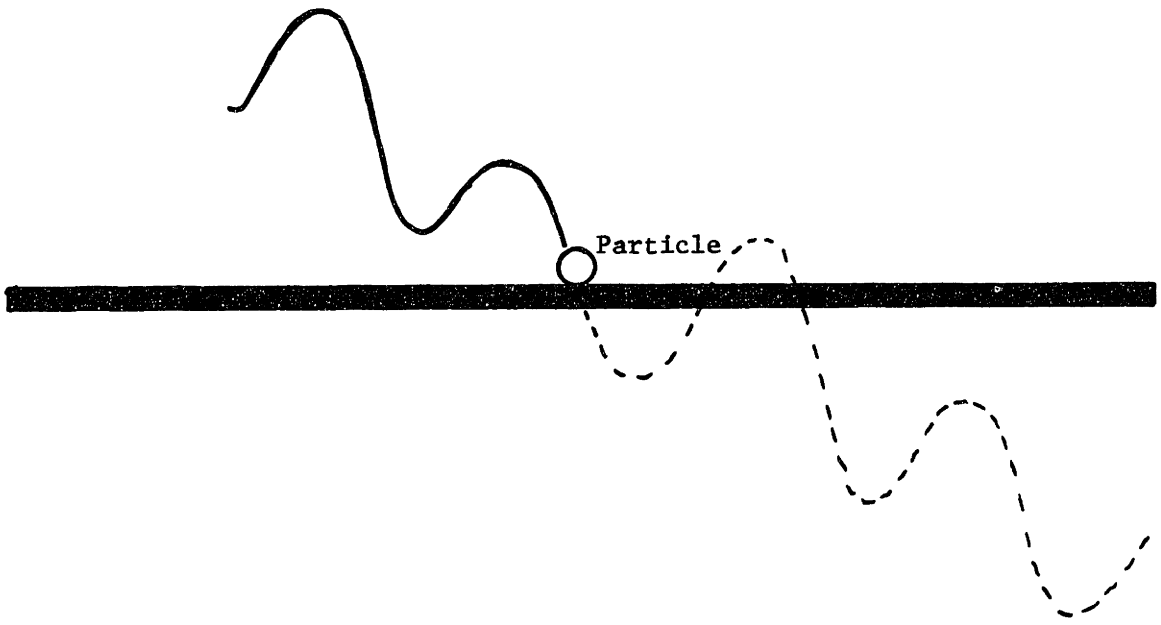

Figure 4.10 Particle undergoing universal precipitation in laminar flow, near the collection plate. If the plate was not present, the particle would move up after the second half-cycle shown. Because it impacts on the plate, however, it sticks.

impedance to turbulent diffusion presented by these boundary layers can significantly affect the particle flux to a plate.

In the bulk flow, the turbulent diffusivity, D_t, can easily be three orders of magnitude larger than the molecular diffusivity, D, for micron-size particles. Due to the no-slip condition on the fluid flow at the walls, effects of turbulent transport there are greatly reduced. Thus, the total diffusivity changes rapidly across the boundary layer, from its value in the bulk flow, D_t, to the much smaller D. Evidence is presented in the following section that diffusive processes are such poor particle transport mechanisms in the linear region of the boundary layer flow that they are completely dominated by particle migrations there. Rather than attempting to model the detailed dependence of the total diffusivity on distance from the wall, the arguments of this section will assume that the diffusivity is uniform in the bulk flow, and equal to zero over a small region of thickness, δ, near each wall. Because the thickness, δ, is much smaller than any other physical dimensions of the precipitator, the presence of this zone of no turbulent transport can be accounted for by an appropriate boundary condition at each wall.

Figure (11a) shows a portion of the collection region in the vicinity of the zone, immediately before a positive half-cycle of the particle motion. Outside of the zone, the turbulent transport time, based on the oscillating migration length, ℓ_{max}, is assumed to be very short. Significant gradients in the particle concentration cannot exist on such length scales, even for times on the order of the cycle time, T. Particles initially move away from the collection plate [The physical reason for this is the fact that, at the beginning of a positive corona half-cycle, the particles are still charged negatively from the previous (negative corona) half-cycle]. Some particles that are initially in the zone travel out of it, and a small region near the collection plate is entirely cleared of particles. Outside, however, the concentration remains relatively constant. Turbulent diffusion is able to overcome the migration away from the plate [The issue of whether the turbulent eddies can affect concentration differences on very small length scales is discussed in section 4.5].

Once the particles begin to migrate toward the collection plate,

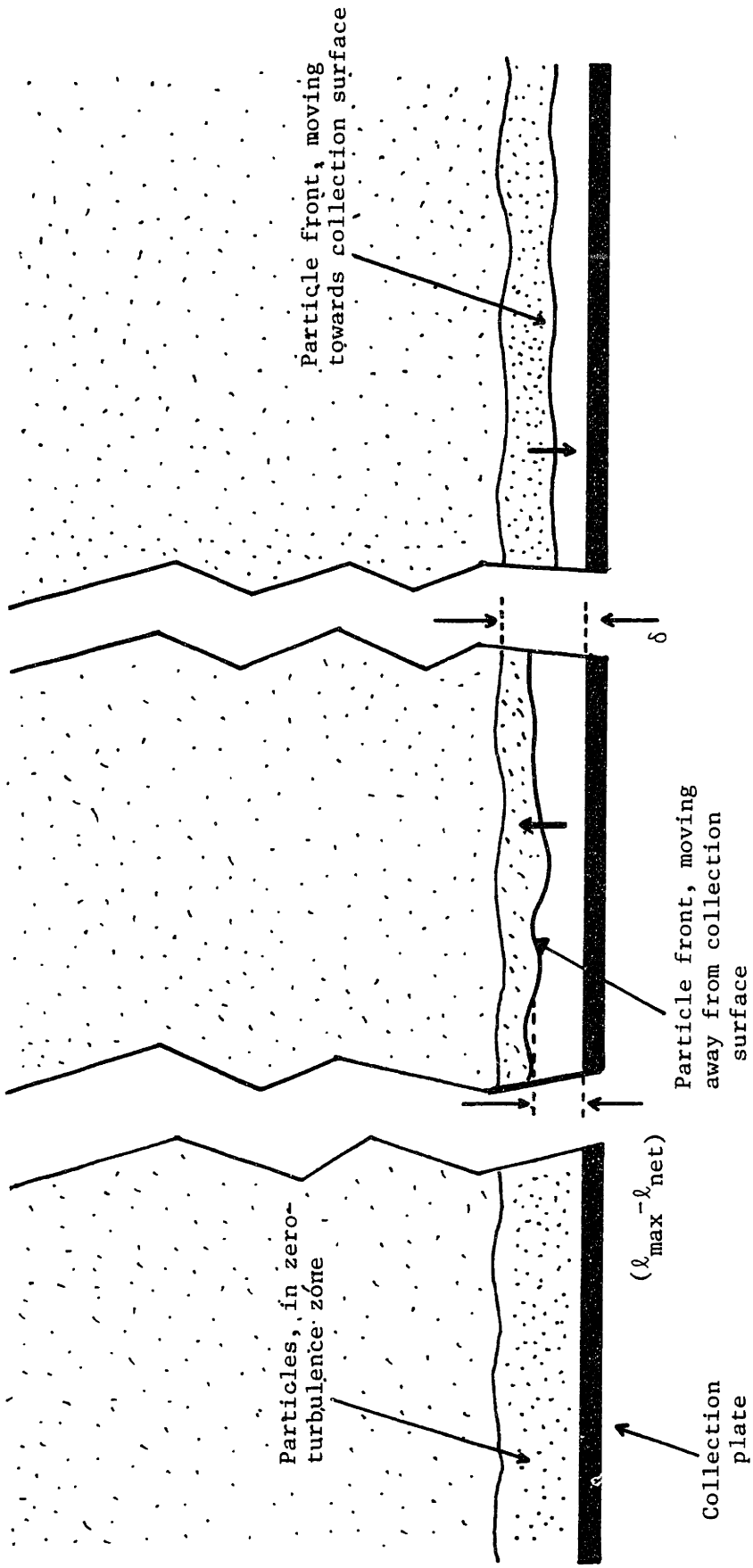

Fig. 4.11 Illustration of successive instants during a half-cycle of the particle migration. In (a), a half-cycle is about to begin. Particles fill the region of zero turbulence. In (b), the particles migrate away from the collection surface, until they reach a maximum distance of (ℓ_{max}-ℓ_{net}). In (c), the particles move towards the collection surface. After they reach the surface, collection continues until the end of the half-cycle.

the outer edge of the zone acts as a source, supplying particles at the concentration, $\langle n(z) \rangle$. No collection occurs until the front of particles reaches the plate (where it was at the beginning of the half-cycle). From that time, on to the end of the half-cycle, the flux density to the plate, Γ_x, is given by

$$\Gamma_x(z,t) = \langle n(z) \rangle \cdot w(t) \tag{4.4.13}$$

where w(t) is the (total) particle migration velocity as a function of time. The number of particles per unit area that actually reach the plate is

$$\int_{t_1}^{t_2} \Gamma_x(z,t)\, d\tau = \langle n(z) \rangle \int_{t_1}^{t_2} w(t)\, dt \tag{4.4.14}$$

The time when the particles first reach the plate and the time of ending of the positive half-cycle are denoted by t_1 and t_2, respectively. Since the net progress made by the particles from the beginning of the half-cycle to the time that the front returns to the plate is zero, the integral of equation (14) can be taken from the beginning to the end of the half-cycle.

$$\int_{t_1}^{t_2} \Gamma_x(z,t)\, d\tau = \langle n(z) \rangle \int_{\substack{\text{one} \\ \text{half-cycle}}} w(t)\, dt$$

$$= \langle n(z) \rangle \cdot \ell_{net} \tag{4.4.15}$$

It was assumed, in the above argument, that the initial backwards motion of the particles was not of sufficient magnitude to entirely clear out the zero-turbulence zone. This assumption is valid if

$$\ell_{max} - \ell_{net} < \delta \tag{4.4.16}$$

If the zone is cleared of particles at some time during the half-cycle, then the number of particles which reach the collection plate per unit area will be larger than that predicted by eq. (15) [In that case, turbulent diffusion in the bulk flow prevents the particle front from moving further away from the wall than δ]. Arguments presented in the detailed treatment of Appendix 3 can be used to show that if eq. (16) is

not satisfied, then the number of particles per unit area that reach the plate in a half-cycle is

$$\int_{t_1}^{t_2} \Gamma_x(z,t)\, d\tau = \langle n(z)\rangle \cdot [\ell_{max} - \delta] \qquad (4.4.17)$$

Assuming, now, that the assumption [eq. (16)] is satisfied, the definition of w_{net} [eq. (2)] can be used to express eq. (15) in terms of a precipitation flux density, averaged over the positive half-cycle of particle motion.

$$\langle \Gamma_x(z)\rangle \equiv \frac{1}{T/2} \int_{t_1}^{t_2} \Gamma_x(z,t)\, d\tau$$
$$= \langle n(z)\rangle \cdot w_{net} \qquad (4.4.18)$$

A similar argument applies to the negative half-cycle of the particle motion. For time-scales that are much longer than the cycle time of the microscopic particle motion, only this mean flux is important. Thus, the appropriate precipitation velocity for use in eq. (11) is simply the time-averaged particle migration velocity, w_{net}.

From eq. (18), it is seen that the time-averaged particle flux to the collection plate is equal to the product of the time-averaged migration velocity and the time-averaged particle concentration there. There is, apparently, no correlation between the oscillatory parts of the migration velocity and particle concentration. This can be attributed to the fact that the oscillatory particle migrations are unable to carry particles all the way across the zero-turbulence zone, and thus are ineffective in precipitating them. In the case where eq. (16) is not satisfied, such a correlation does exist, and the particle flux is greater than that predicted by eq. (18) [see Appendix 3].

The situation at the upper plate is reversed, as particles actually travel toward it during the "backward" portion of each half-cycle, and away afterward. A boundary condition that is similar to that of eq. (18) could be derived by following an analogous argument. Consideration of the physical problem at hand, however, dictates a different boundary condition. It will be assumed that the particle flux at the upper plate is zero, for reasons based on the actual geometry of the situation being modeled. The wires, which are suspended halfway between collection plates in an actual precipitator, are represented by

the upper plate in this model. They present a much smaller target for deposition than do the collection plates. This is partially compensated by the concentration of electric field intensity in their vicinity, but the resulting large corona current density also causes very rapid particle charging. Thus, those particles that come very near to the wires are quickly charged to the sign of the corona that exists at the time, and move away from it under the influence of the intense local electric field. No particles can be deposited on the upper plate, but no particles are emitted from it either. Therefore, the appropriate boundary condition is

$$\langle \Gamma_x(z) \rangle \Big|_{x=H} = 0 \qquad (4.4.19)$$

4.4.4 Problem solution

The first-order, constant-coefficient, ordinary linear differential equation constraining the particle concentration, eq. (11) can easily be solved, subject to the boundary condition, eq. (1), using w_{net} as the precipitation velocity. The solution is

$$\langle n(z) \rangle = n_o \, e^{-\frac{z}{U}\frac{w_{net}}{H}} \qquad (4.4.20)$$

The expression of eq. (7) for the collection efficiency can be applied to eq. (20)

$$\eta = 1 - e^{-\frac{L/U}{H/w_{net}}} \qquad (4.4.21)$$

Comparison of eqs. (21) and (4.3.1) justifies the format of presentation of the data in section 4.3. Under the conditions assumed in the development of the simplified turbulent diffusion model, the experiments described in this chapter provide an indirect measurement of the time-average particle migration velocity. As was pointed out in that section, experiments performed under identical electrical conditions, but using different air flow velocities, gave similar values for the effective migration velocity. That fact gives further support to the assumptions made in this section.

4.5 Discussion of Turbulent Diffusion Model

The turbulent diffusion model of section 4.4 attempts to account for mixing due to turbulent eddies by a uniform diffusivity in the core flow, with regions of zero diffusivity adjoining either bounding plate. Its validity hinges upon the degree of accuracy to which diffusion can physically model the turbulent transport processes that actually occur inside a precipitator. Issues to be addressed by this section include: (1) Whether the large-scale turbulent eddies can eliminate transverse particle concentration gradients on time scales that are relevant to the problem at hand, and (2) Whether it is appropriate to neglect diffusive transport of particles right at the collection surface.

4.5.1 Turbulent Transport in the Bulk Flow

There are three major sources of turbulence in the laboratory-scale precipitator. Turbulent eddies can be produced by the inlet flow, due to jets, sharp edges, or protrusions into the channel (such as that of the upstream support bar for the corona wires). Although the tunnel is not long enough to attain fully developed flow, boundary layers at both the plates and the wires can contribute to the turbulence. The corona wind, induced by electric field forces on the current-carrying ions, can create large-scale convection cells which carry particles from the center of the flow region to its outer portions. The behavior of turbulence due to the first two sources is treated extensively in the literature[9,10]. Measurements of turbulence due to corona discharges have also been reported[11,12]. Observations from chapter six are combined with those references in this section's discussion of turbulent mixing.

In order for the flow turbulence to be able to eliminate transverse particle concentration gradients in the precipitator, two conditions must be satisfied. First, the characteristic transverse diffusion time, τ_d, defined in eq. (4.4.4), must be smaller than either the convection or migration times for the particles. In addition, if the diffusion time is to be a significant quantity, the physical process that is being modeled by the equivalent diffusivity must occur on time-scales that are no longer than τ_d, itself.

The size-scale of the largest eddies in the flow is limited by the plate separation, 2H. A rough estimate of the time necessary to transport particles from the center of the flow to outer regions is obtained by taking the ratio of this length to the eddy velocity. Measured values for the corona wind velocity in the laboratory-scale precipitator (from chapter 6) were of the order of 1 m/sec. Velocity profiles reported there also show that the eddies generally circulate in a plane transverse to the mean flow, resulting in a helical flow path. The transport time of the largest eddies, based on this corona wind velocity and the plate spacing, is much smaller than the residence time ($\tau_{eddy} \backsim$ 30 msec, $\tau_c \backsim$ 350 msec with a 4.3 m/sec flow velocity). Thus, the large-scale eddies have sufficient time to transport particles from anywhere in the core flow to the vicinity of the wall.

The works of Leonard[3], Robinson[11], and Pyle[16] all lend support to the hypothesis that turbulent mixing processes that occur in an electrostatic precipitator can be modeled using an effective diffusivity*.

The above evidence supports the hypothesis that the effects of turbulent mixing in a precipitator are well modeled by an equivalent turbulent diffusivity in the bulk flow region. It remains to be shown that the appropriate value for D_t is essentially infinite (ie., that the flow is completely mixed, with no concentration gradients in the transverse direction). It was assumed in the derivation of section 4.4 that the characteristic diffusion time, τ_d, was much shorter than either the convection time, τ_c, or the migration time, τ_m. A comparison of these times can be made, using parameters and results of experiments reported in this thesis and in the literature. The value for D_t used here will be

$$D_t \backsim 3 \times 10^{-3} \text{ m}^2/\text{sec} \qquad (4.5.1)$$

It is equal to the highest value reported by Leonard[3], roughly three times smaller than Robinson's[11] greatest value, and only slightly larger than those of Pyle[16]. It also agrees with the empirical observation[13]

---

*All three of these authors were reviewed in section 1.5.2

that the effective diffusivity of a fully-developed pipe flow is roughly 150ν, where ν is the kinematic viscosity of the fluid (in this case, air). Crude measurements of the effective diffusion coefficient in the laboratory-scale precipitator reported in chapter 6 give $D_t \approx 8 \times 10^{-3}$ m^2/sec for 4.3 m/sec flow. Corona-wind mixing was not accounted for in that experiment. The diffusion time, based on the wire-plate spacing and this value for D_t is [eq. (4.4.4)]

$$\tau_d \approx 75 \text{ msec} \tag{4.5.2}$$

The convection time, for 4 m/sec flow, is [eq. (4.4.3)]

$$\tau_c \approx 375 \text{ msec} \tag{4.5.3}$$

A migration time can be estimated, based on the 5.6 cm/sec effective velocity with +8 kV DC excitation.

$$\tau_m \approx 270 \text{ msec} \tag{4.5.4}$$

As the diffusion time estimate is conservative [ie., likely to be high], it is not unreasonable to assume that $\tau_d/\tau_m \ll 1$, and $\tau_d/\tau_c \ll 1$.

In conclusion, it is plausible that the effects of turbulent eddies can be modeled by an equivalent diffusivity in the bulk flow. The equivalent diffusivity that corresponds to the problem at hand is large enough that an assumption of complete mixing in the transverse direction is reasonable.

4.5.2 Turbulent Diffusion Near a Wall

It is seen that turbulent diffusion is able to transport particles from the bulk flow to within a short distance of the collection plate with relative ease. However, the model of section 4.4 neglects actual diffusion of particles from the outer edge of the bulk flow to the plate. Even though the effects of turbulent eddies on particle transport are greatly reduced near the plate, molecular diffusion of particles still occurs there. It is of interest to determine the importance of particle diffusion to the collection plate, relative to precipitation by migration. It is argued, below, that it is reasonable to model the

linear region of the boundary layer flow at the plates as a region of no diffusive transport. In addition, estimates are made of the thickness of this effective zero-turbulence zone. Its thickness is of importance, as it determines whether or not the oscillatory migrations of the particles can aid in the precipitation process.

Friedlander[7] gives a theoretical relationship by which one can compute the diffusive flux of particles to the inner wall of a pipe in which a fully-developed turbulent flow exists.

$$\Gamma_n \simeq \chi D \mathrm{Re}\, f^{1/2} \mathrm{Sc}^{1/3} \frac{n_\infty}{d} \tag{4.5.5}$$

where χ is simply a (unitless) numerical constant, equal to 0.042, D is the molecular diffusion coefficient (which depends upon the particle size), n_∞ is the particle concentration at the outer edge of the boundary layer, d is the pipe diameter, Re is the flow Reynolds number, based on the diameter, and Sc is the Schmidt number.

$$\mathrm{Re} \equiv \frac{Ud}{\nu} \tag{4.5.6}$$

$$\mathrm{Sc} \equiv \frac{\nu}{D} \tag{4.5.7}$$

The Fanning friction factor is an empirically determined parameter of the flow, defined by the relation[8]

$$\frac{dP}{dz} = \frac{f}{d} \cdot \frac{1}{2} \rho U^2 \tag{4.5.8}$$

where P is the mean mechanical pressure of the flow, and z is the axial coordinate.

Since the flux density predicted by eq. (5) is proportional to the particle concentration at the outer edge of the boundary layer, one can define an effective diffusive particle velocity, for purposes of comparison to other particle transport mechanisms.

$$v_{eff} \equiv \frac{\Gamma}{n_\infty} = \chi \mathrm{Re}\, f^{1/2} \mathrm{Sc}^{1/3} \frac{D}{d} \tag{4.5.9}$$

For particles of diameter 0.1 μm, Friedlander gives

$$D \simeq 6.75 \times 10^{-10} \ \mathrm{m^2/sec} \tag{4.5.10}$$

$$\mathrm{Sc} \simeq 2.22 \times 10^{4} \tag{4.5.11}$$

Schlicting[10] deals with fully-developed turbulent flows in channels of non-circular cross-section by the use of a hydraulic diameter, d_h, defined as four times the ratio of the channel area to its perimeter (thus, the hydraulic diameter of a circular pipe is equal to its actual diameter). The value of d_h for the laboratory-scale precipitator [with a height of 3 cm and a width of 14 cm] is roughly 5 cm. Thus, with

$$d_h \simeq 5 \times 10^{-2} \text{ m} \tag{4.5.12}$$

$$U \simeq 4 \text{ m/sec} \tag{4.5.13}$$

$$\nu \simeq 2 \times 10^{-5} \text{ m}^2/\text{sec} \tag{4.5.14}$$

the Reynolds number for the flow is

$$\text{Re} \backsim 10000 \tag{4.5.15}$$

Schlicting also introduces the resistance coefficient, λ, defined so that

$$\frac{dp}{dz} = \frac{\lambda}{d_h} \frac{1}{2} \rho U^2 \tag{4.5.16}$$

Comparison of eqs. (8) and (16) shows that, for a pipe of circular cross-section, the resistance coefficient, λ, is exactly equal to the Fanning friction factor, f. According to Schlicting, for Reynolds numbers less than 10^5,

$$\lambda \simeq 0.3164 \, \text{Re}^{-0.25} \tag{4.5.17}$$

Thus, under the conditions defined by eqs. (12) - (14),

$$f = \lambda \backsim .03 \tag{4.5.18}$$

This gives an effective diffusion velocity [see eqs. (9) - (11), (15), (18)] of

$$v_{eff} \backsim 3 \times 10^{-5} \text{ m/sec} \tag{4.5.19}$$

This velocity is small even in comparison to a particle migration velocity of 1 mm/sec. The effective migration velocities reported for the precipitation experiments described in this chapter were of the

order of 1 - 5 cm/sec. Therefore, it is reasonable to neglect diffusive particle transport across the boundary layer in favor of migration (as Friedlander, himself, does).

Thus, because of reduced turbulence in the linear region of the boundary layer at the collection plate, turbulent eddies can only bring particles close to the plate. Particle migration, either the steady component or the oscillating part, is solely responsible for the actual precipitation. It is seen that the relative values of the three length scales, ℓ_{max}, ℓ_{net}, and δ, are important to a determination of the appropriate boundary condition at the lower plate. Another length, the Kolmogoroff microscale of the turbulence, ℓ_k, will be introduced as well. This latter distance is generally interpreted as the size of the smallest eddies in the flow, and thus places a limit on how finely the turbulence can be expected to distribute a contaminant (such as the particles).

The Kolmogoroff length and velocity scales (ℓ_k and v_k, respectively) are determined by two constraints: (1) that the Reynolds number based on ℓ_k and v_k be unity (so that inertial and viscous forces on that scale are roughly equivalent), and (2) that the eddies be capable of dissipating a given amount of energy per unit volume, $\rho\varepsilon$. Thus,

$$\frac{\ell_k v_k}{\nu} \sim 1 \tag{4.5.20}$$

and

$$\eta \frac{v_k^2}{\ell_k^2} \sim \rho\varepsilon \tag{4.5.21}$$

In eq. (19), η is the viscosity and ρ is the density of the surrounding air. The constraint of eq. (19) is obtained by requiring that the dissipation per unit volume of a laminar flow between parallel planes of separation, ℓ_k, and velocity differential, v_k, be $\rho\varepsilon$. Equations (18) and (19) can be solved for ℓ_k in terms of $\nu \equiv \eta/\rho$ and ε.

$$\ell_k = \left(\frac{\nu^3}{\varepsilon} \right)^{1/4} \tag{4.5.22}$$

Normally, the power dissipated per unit volume of a turbulent channel flow can be computed as simply that due to the mean pressure gradient.

$$\rho\varepsilon = U\frac{dp}{dz} \qquad \text{(WRONG)} \qquad (4.5.23)$$

The pressure gradient for a turbulent pipe flow with smooth walls is empirically approximated by the formulae of eqs. (15) - (17), so that

$$U\frac{dp}{dz} \backsim 20 \text{ watts/m}^3 \qquad (4.5.24)$$

In this case, however, another source of power input to the system exists. Although most of the electric energy used by the corona current goes directly into heating of the air, some of it is dissipated by additional induced turbulence. As is reported in chapter 6, the turbulence intensity of a 4 m/sec flow is roughly doubled by the introduction of an 8 kV RMS 50 Hz AC corona. Thus, the turbulent dissipation should be roughly quadrupled, giving

$$\rho\varepsilon \backsim 80 \text{ watts/m}^3 \qquad (4.5.25)$$

Since the density of air is roughly 1 (MKS units), eq. (4) gives

$$\ell_k \backsim 100 \ \mu\text{m} \qquad (4.5.26)$$

One more length-scale of the turbulent flow (one that is related to δ) will be examined here, the thickness of the linear flow region of the boundary layer. The wall friction velocity, u_*, is defined by Schlicting[10] as

$$u_* = \left(\frac{\tau_w}{\rho}\right)^{1/2} \qquad (4.5.27)$$

where τ_w is the viscous stress at the wall. The linear flow region of a boundary layer is that part of the layer in which the mean flow velocity is proportional to the distance from the wall. Its thickness is roughly 5 wall units, where a wall unit, y_*, is defined

$$y_* = \frac{\nu}{u_*} \qquad (4.5.28)$$

It is in this linear flow region that turbulent particle transport is greatly inhibited. The wall stress, τ_w, is estimated by an application

of conservation of momentum to the channel flow. In the interest of simplicity, the pressure force is assumed to be balanced by the viscous stress at the upper and lower plates only (as they are much longer than the side walls).

$$\tau_w = H \frac{dp}{dz} \tag{4.5.29}$$

Equations (22), (23), (27) - (29) can be combined to give an estimate for y_*.

$$y_* \approx 2.51 \frac{\nu}{U} \left(\frac{d_h}{H} \right)^{1/2} Re^{1/8} \tag{4.5.30}$$

With U=4 m/sec, Re $\sim$ 10000, H = 1.5 cm, and d_h = 5 cm,

$$y_* \sim 73 \ \mu m \tag{4.5.31}$$

From this value for y_*, one would estimate that the linear flow region was roughly 0.4 mm in thickness. According to Friedlander[7], the interval over which the particle concentration changes rapidly is contained within the linear flow region, but may be much thinner than five wall units. However, it is unlikely that turbulent diffusion is effective in bringing particles much closer than a single wall unit away from the collection plate.

The universal precipitation model of chapter 3 can be used to predict values of ℓ_{net} and ℓ_{max}, given only the characteristic corona charging time, τ_{ch}, and the velocity, v_o, of particles with a saturation charge. The following values will be used for these parameters:

$$\tau_{ch} = 3 \text{ msec}$$
$$v_o = 5.6 \text{ cm/sec} \tag{4.5.32}$$

The characteristic time and saturation velocity were obtained by fitting the universal precipitation model to the data of section 4.3, for an RMS applied voltage of 8 kV [see section 4.6]. According to the universal precipitation model, as the excitation frequency ranges from 20 → 500 Hz, ℓ_{net} and ℓ_{max} go from $\sim$ 1.10 mm → 3.5 μm, and $\sim$ 1.12 mm → 6.2 μm, respectively. Figure (12) shows a plot of the quantity, $\ell_{max} - \ell_{net}$, as a function of excitation frequency, with v_o and τ_{ch} as given in eq.

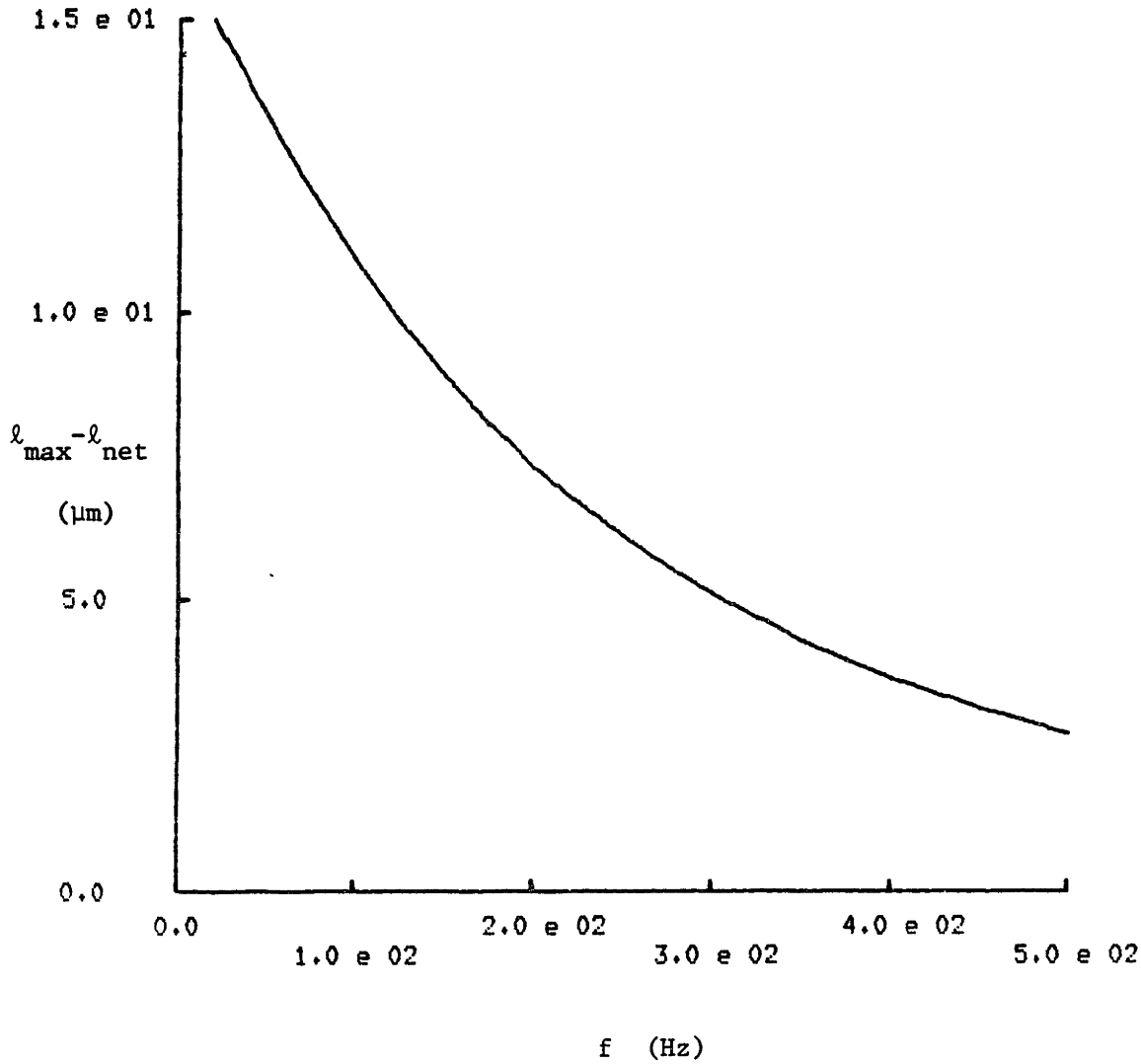

Fig. 4.12. Plot of the quantity, $(\ell_{max}-\ell_{net})$, vs. excitation frequency for the uniform-field charging model of Chapter 3. Parameters used for this plot were v_o = 5.6 cm/sec, τ_{ch} = 3.0 m/sec.

(32). The oscillatory part of the particle migration velocity decreases from approximately 15 μm at 20 Hz to less than 3 μm at 500 Hz.

It would seem, from the values of the Kolmogoroff scale [ℓ_k, eq. (26)], wall length [y_*, eq. (31)], and ℓ_{net}, ℓ_{max} above, that only the time-average particle migration is important in determining the rate of precipitation at the collecting plate. For low frequencies, where the maximum particle migration length is sufficient to cross the linear flow region, $\ell_{net} \approx \ell_{max}$, and so the precipitation velocity, w_p [eq. (1)], is simply w_{eff}. At higher frequencies, where ℓ_{max} is significantly greater than ℓ_{net}, both are smaller than either the Kolmogoroff scale or the wall length.

In conclusion, it is reasonable to assume that, even though the turbulent diffusion is able to rapidly bring particles to within a short distance of the collection plate, it cannot contribute significantly to the actual precipitation of particles to the plate. The distance of the zero-turbulence zone is sufficiently large that the oscillatory particle migrations do not aid the precipitation process.

4.6 Correlation of Theory and Experimental Data

In this section, the turbulent diffusion model of section 4.4 is used to predict the effective migration velocity of particles subjected to AC corona excitations in terms of their behavior with positive DC voltages. The only model parameter that must be obtained from other chapters in this thesis is the time-averaged particle migration velocity, w_{net}. Because of the intense turbulent mixing in the precipitator, the exact value of D_t is unimportant. The thickness of the zero-turbulence zone is great enough that the oscillatory particle migrations do not affect the precipitation rate. It is seen that, if the effective precipitation velocity for AC excitation of a given frequency and RMS voltage is predicted as a fraction of the velocity measured for positive DC excitation at the same voltage, reasonable agreement with the experimental data is obtained. No attempt is made here to predict the DC behavior, or to explain the differences between positive and negative corona precipitation [Some of these issues are to be addressed in chapter 5].

The AC experimental results obtained with a given RMS voltage are compared to those with an equal DC voltage. If the particles were always charged to saturation in whatever electric field was present at any specific time, then their time-averaged migration velocity would be proportional to the RMS value of the electric field strength, $|\bar{E}|$. Thus, at low frequencies, the AC data can be expected to approach those values measured with a DC excitation.

The universal precipitation model of chapter 3 is used to compute the time-average particle migration velocity as a function of the DC velocity at a given voltage level and of the cycle time of the excitation, relative to a characteristic charging time for the corona. The solid lines on Figs. (3) - (7) show the results of application of the model to the data in such a fashion. In Fig. (3), it was constrained to predict the +8 kV DC effective migration velocity of 5.6 cm/sec for zero frequency, and a charging time of 3 msec was used to provide the best fit to the data there. As is seen in chapter 5, this is not an unreasonable value for τ_{ch}. The same charging time is used for all other theoretical predictions in this chapter. The corresponding plot for the high-speed frequency scan is shown in Fig. (4). Two theoretical curves

are shown on that figure. The lower one is the same as that of the previous figure, showing the predicted time-average migration velocity as a function of excitation frequency. The upper one is obtained by assuming an extremely thin zero-turbulence zone, so that the oscillatory particle migrations dominate the precipitation [see Appendix 3]. It predicts a higher effective velocity, since ℓ_{max} is always greater than or equal to ℓ_{net}. The upper curve was included on this plot to show the difference in behavior of the generalized turbulent diffusion model for the two extremes of the universal precipitation model. It is interesting that the measured effective velocity is higher at large frequencies for the high-speed flow than for the low-speed one, as this could be explained by a thinner zone of no turbulent transport. The other data do not corroborate this hypothesis, however, and so it is pursued no further here.

Figures (5) - (7) compare the effective precipitation velocity predicted by the universal precipitation model to that measured from low-speed runs with fixed frequency excitations at 30, 60, and 100 Hz. As with Figs. (3) and (4), the predicted velocity was computed by simply scaling down the velocity measured with positive DC corona at the given voltage level [data from Fig. (1)]. The scaling factors used were: 0.7207 for 30 Hz, 0.5651 for 60 Hz, and 0.4243 for 100 Hz. The fit between experimental and "theoretical" curves is good for voltages larger than 6.0 kV RMS. The deviation for lower voltages can be partially explained by the fact that the corona starting voltage was about 6 kV, and while DC voltages less than 6 kV resulted in little or no corona current, AC excitations of RMS value equal to 6 kV had peak voltages that were well above the onset level. In other words, the assumption that particles always attain the saturation charge corresponding to the local electric field is not valid for the DC excitation, as there were voltages for which no charging current is present.

4.7 Conclusions

Given the apparent fit between theory and experiment in Figs. (3) - (7), it is tempting to close the thesis at this point with the conclusion that the universal precipitation and turbulent diffusion models accurately represent the charging and collection processes in an electrostatic precipitator. The fact that such simple models can predict the experimental results so closely is, in retrospect, amazing. It is seen, from the experiments and analyses of chapter 5, that the close fit obtained here may be only fortuitous.

Both the universal precipitation model of chapter 3 and the turbulent diffusion model presented here assume rectangular geometry in the precipitator, resulting in uniform electric fields and charging currents throughout the region. Even with AC excitation, the particle migration velocity is assumed to be uniform in space (but varying with time).

The simplification introduced by this assumption is tremendous. The migration of a particle does not depend in any way upon its history of proximity to the charging source, as it would if non-uniform electric fields were to be taken into account. With the actual wire-plate geometry used in these experiments, ion space-charge effects make computation of even the electric field for a DC excitation difficult. Prediction of the performance of the laboratory-scale precipitator from theoretical considerations alone would not be a straightforward task.

Many of the complications associated with the geometry of the precipitator were avoided in this chapter by predicting the results of AC experiments in terms of the measured DC performance. In this way, the problem was reduced to predicting the relative performance of the precipitator as only one experimental parameter, the excitation frequency, was varied. The characteristic magnitude and geometry of the electric fields were similar in corresponding DC and AC runs. It was this use of DC data to predict the AC results that gave the good agreement between theory and experiment found in Figs. (3) - (7).

Because of the large thickness of the zero-turbulence zone at the collection plate, only the time-average particle velocity, $\underline{w}_{net}$, was important in determining the precipitation rate. The actual value of the

thickness is unimportant, as long as it is large enough to prevent the zone from being cleared of particles during any half-cycle of the excitation. Thus, for the experiments reported here, the performance of the laboratory-scale electrostatic precipitator does not give a very sensitive measure of the behavior of the boundary layer flow at the plate. This would not be true for a two-stage precipitator, if the second stage were excited with an unbiased sinusoidal voltage. In that case, the time-average particle migration velocity, $\underline{w}_{net}$, would be zero, and the only precipitation would be that due to the oscillatory particle motions. It is seen [eq. (4.4.17)] that the thickness of the zero-turbulence zone has a strong influence on the collection rate if it is on the order of the maximum migration length, ℓ_{max}.

The very significant differences between the precipitator performance with positive and negative DC coronas were not accounted for in this chapter. The problem could be avoided simply by using only the positive DC data to predict the AC results. It is shown in chapter 5 that the differences between the spatial distributions of positive and negative coronas can strongly influence particle charging processes, especially with AC excitation. In that chapter, such differences must be included in the charging model, even to explain the AC results in terms of the DC data. The simple universal precipitation model, which was used to provide values for w_{net} in the analyses of this chapter, does not take these differences into account. Thus, even though its computations of the effective particle migration velocity are accurate, it does not predict measurements of the particle charging statistics well.

In conclusion, measurement of the overall collection efficiency of the laboratory-scale precipitator apparently does not give a very sensitive indication of all of the complicated phenomena which occur inside it. A very simple model, which does not explicitly account for many of these phenomena is able to predict the results of the AC precipitation experiments. As a practical matter, this may be fortunate, as the precipitation efficiency is of great importance to industrial users of electrostatic precipitation. However, there remains the danger that the results of the experiments performed on the laboratory-scale precipitator will not "scale-up" to a full-size device (which has dimensions that are roughly an order of magnitude greater). Therefore,

it is of interest to examine, separately, the mechanisms which together make up the electrostatic precipitation process.

References for Chapter 4

[1]Williams J.C., Jackson R., "The Motion of Solid Particles in an Electrostatic Precipitator", Proceedings Symposium on the Interaction Between Fluids and Particles, Institute of Chemical Engineers, London, pp 282-8 (1962).

[2]Robinson M., "Turbulent Gas Flow and Electrostatic Precipitation", Journal of the Air Pollution Control Association, Vol. 18, No. 4, pp. 235-9 (April 1968).

[3]Leonard G.L., "Effect of Turbulence on Electrostatic Precipitator Performance", High Temperature Gasdynamics Laboratory, Report No. 196, NSF Grant No. CPE-7926290 and EPRI Contract No. EPRI-RP 533-1, Mechanical Engineering Department, Stanford University, Palo Alto, California (April, 1982).

[4]Feldman P.L., Kumar K.S., Cooperman G.D., "Turbulent Diffusion in Electrostatic Precipitators", AIChE Symposium Series, Atmospheric Emissions and Energy Source Pollution, No. 165, Vol. 73, pp. 120-130.

[5]Marietta M.G., Swan G.W., "Particle Diffusion in Electrostatic Precipitators", Chemical Engineering Science, Vol. 31, pp. 795-801, Pergamon Press (1976).

[6]Leonard G., Mitchner M. Self S.A., "Particle Transport in Electrostatic Precipitators", Atmospheric Environment Vol. 14, pp. 1289-1299, (1980).

[7]Friedlander S.K., Smoke, Dust and Haze, John Wiley & Sons, New York, Chapter 3 (1977).

[8]Potter M.C., Foss J.F., Fluid Mechanics, The Ronald Press Company, New York (1975).

[9]Hinze J.O., Turbulence, McGraw-Hill, New York (1975).

[10]Schlicting H., Boundary Layer Theory, McGraw-Hill, New York (1960).

[11]Robinson M., "Effects of the Corona Discharge on Electric-Wind Convection and Eddy Diffusion in an Electrostatic Precipitator", PhD Thesis, Cooper Union School of Engineering and Science, New York (1975).

[12]Leonard G.L., Mitchner M., Self S.A., "An experimental Study of the Electrohydrodynamic Flow in Electrostatic Precipitators", Journal Fluid Mechanics, Vol. 127, pp. 123-140 (1983).

[13]Kays W.M., Convective Heat and Mass Transfer, McGraw-Hill, New York (1966).

[14]White H.J., Industrial Electrostatic Precipitation, Addison Wesley Publishing Co. Inc., Reading, Mass., (1963).

[15]Deutsch W., "Bewegung und Ladung der Elektrizitätsträger im Zylinderkondensator", Ann. Physik, 68, pp. 335-44 (1922)

[16]Pyle B.E., Pontius D.H., Snyder T.R., Sparks L.E., "Particle Trajectory Studies in a Scale Model Electrostatic Precipitator", 73'rd Annual Meeting of the Air Pollution Control Association, Montreal, Quebec (June, 1980).

Chapter 5
Aerosol Charging Measurements

5.1 Introduction

The collection processes which occur inside an electrostatic precipitator can be crudely divided into three categories: (1) corona charging, (2) particle transport in the core flow, due both to migration and to fluid mixing effects, and (3) precipitation from the outer edge of the flow region to the collection plates. Processes included in these three groups cannot be completely separated from one another. For example, because of the non-uniform electric fields that exist within a precipitator, particle charging processes are influenced by the macroscopic movements of particles through the flow region. However, it is still of use to perform experiments which attempt to observe these processes separately. Information obtained from such experiments can be used to differentiate between possible combinations of models for these mechanisms that yield similar results for the overall efficiency of collection.

This chapter documents experiments which were run on the laboratory-scale precipitator to determine the mobility distribution of particles leaving various corona charging sections. Models are proposed to predict the mobility distributions which result from AC corona excitations in terms of those obtained using DC voltages. The universal precipitation model of chapter 3, which was used to provide particle migration parameters for the turbulent diffusion model of chapter 4, does <u>not</u> accurately predict the measured mobility distributions from experiments which used corona wires to charge particles.

A general overview of the experiments performed is in section 5.2, followed by the experimental data in 5.3. Section 5.4 presents analyses of the data, along with a discussion of the applicability of the uniform-field charging models of chapter 3. It is seen there that, although that simplified model can be used to predict the general trends of the charging behavior, it falls far short of accurately modeling biases in the particle charging with AC fields. Conclusions are drawn in section 5.5.

5.2 Summary of Experimental Procedures and Data Reduction Techniques

Due to the number and diversity of charging experiments performed, and the many data reduction techniques used to analyze them, an overview is provided in this section. It is useful, both in understanding the relationships between different experiments, and in tracing the development of the charging theories of section 5.4. Section 5.2.1 reviews the different techniques used to reduce the velocity/time data obtained by the LDV. The experimental procedures are outlined in section 5.2.2, along with a summary of those experiments that were actually performed.

The basic experimental setup was essentially that which was described in chapter 2. Particles were charged in an upstream section of the laboratory-scale precipitator, and then subjected to a uniform transverse (vertical) electric field in the second stage. The LDV measured the vertical component of velocity for those particles that passed through its observation volume. A typical data point consisted of roughly 3000 individual particle velocity measurements.

5.2.1 Data Reduction Techniques

The raw velocity data is expressed as N ordered pairs, (v_i, t_i), where N is the number of individual particle velocities measured, v_i is the measured velocity of the i'th particle observed, and t_i is the time at which that particle was seen. The results of any specific experiment can be expressed in any of four different ways: (1) by the mean and RMS spread (ie., the standard deviation) of the measured velocities, (2) with a discrete plot of particle velocity versus time, (3) with the Fourier transform of a continuous approximation to the velocity/time information, or (4) with a velocity distribution function.

As an artificial example of the relationships between these four reductions of the experimental data, consider a vertical particle velocity which varies according to the formula,

$$v_x(t) = 0.1 + 0.5 * \sin(20\pi t) \qquad (5.1.1)$$

where $v_x(t)$ is the velocity in m/sec. Suppose that 2941 velocity measurements are made, and all are evenly spaced in time (beginning at t=0), with a 0.3 msec interval between succeeding measurements. The computed mean velocity would be .1054 m/sec, and the RMS spread would be .3548 m/sec. The discrete sampling of a non-integral number of cycles of the motion, along with round-off errors in the velocity representation of the LDV, result in values for $\bar{v}$ and v' that are slightly different from the "ideal" results, 0.1 m/sec and $0.5/\sqrt{2}$, respectively. The velocity vs. time plot, its Fourier transform, and its distribution function would be as pictured in Figs. (1) - (3), respectively. Note that the finite data interval (approximately 3 seconds in length) results in a transform that is not simply an impulse at a frequency of 10 Hz The function plotted in Fig. (3) is actually the magnitude of F(f), defined

$$F(f) = \frac{2}{t_N - t_1} \sum_{i=1}^{N-1} v_i \, e^{j\pi(t_i+t_{i+1})f} \, (t_{i+1}-t_i) \qquad (5.1.2)$$

$$\approx \frac{2}{T} \int_0^T v_x(t) \, e^{j2\pi ft} \, dt$$

The normalization of eq. (2) is chosen so that the amplitude of a local peak of the transform will be approximately equal to the Fourier component of the velocity at the frequency of that peak [see Fig. (3)].

The mean velocity and RMS spread are defined

$$\bar{v} \equiv \frac{1}{N} \sum_{i=1}^{N} v_i \qquad (5.1.3)$$

$$v' \equiv \sqrt{\frac{1}{N} \sum_{i=1}^{N} (v_i - \bar{v})^2} \qquad (5.1.4)$$

The mean and RMS spread information are used in plotting the velocity distribution function. The plotting space extends from 3.0825 standard deviations below the mean velocity to 3.0825 above. At each of 411 evenly-spaced velocity points contained in the space, the number of particle velocity measurements which fall within 0.1575 standard deviations of the given point is plotted. The overlap between sample velocities (they are spaced by 0.015 standard deviations) results in a relatively smooth plot.

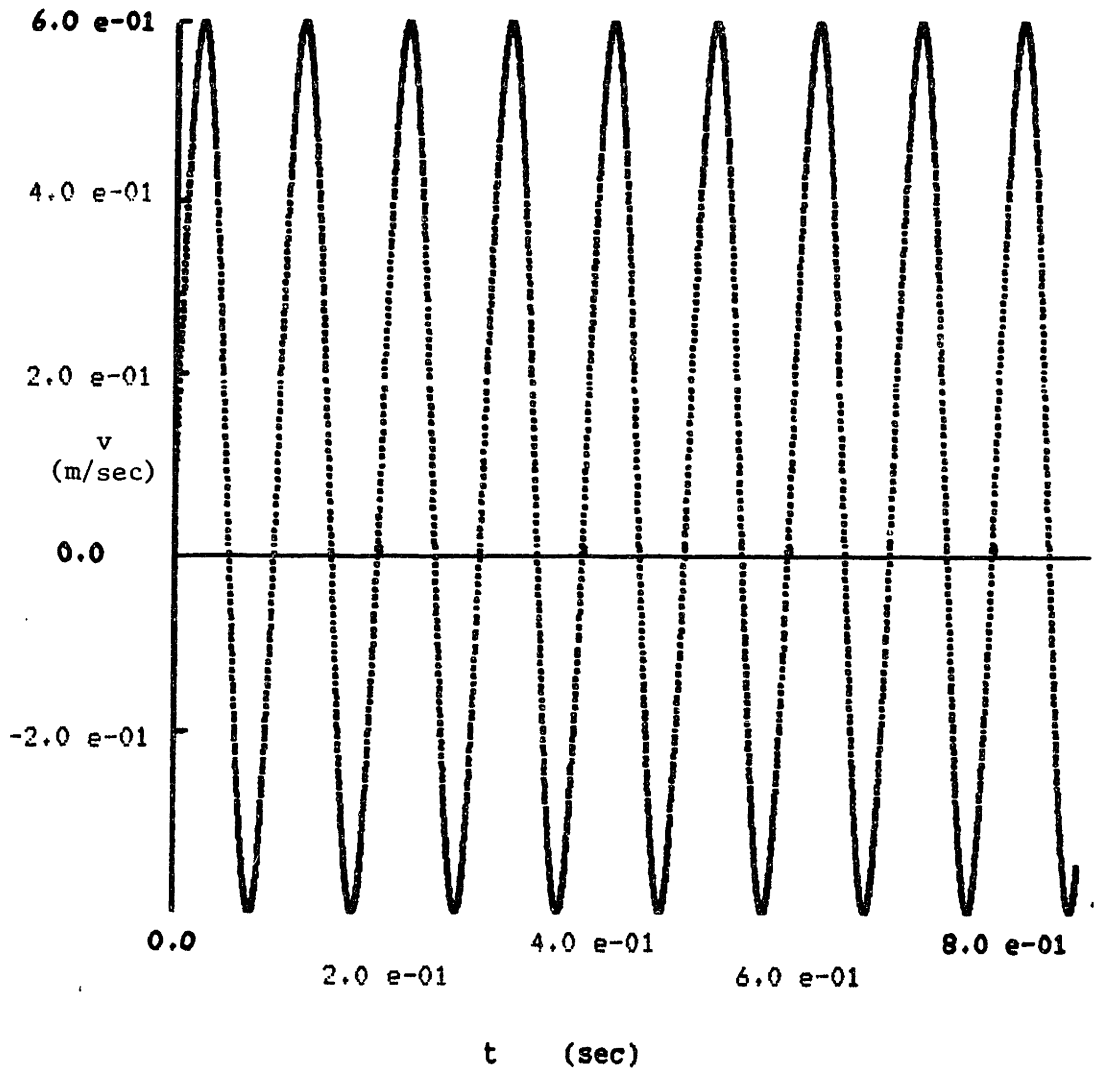

Figure 5.1. Plot of vertical velocity vs. time. Data was generated artificially, to demonstrate data-reduction processes. Individual data points are visable at some locations.

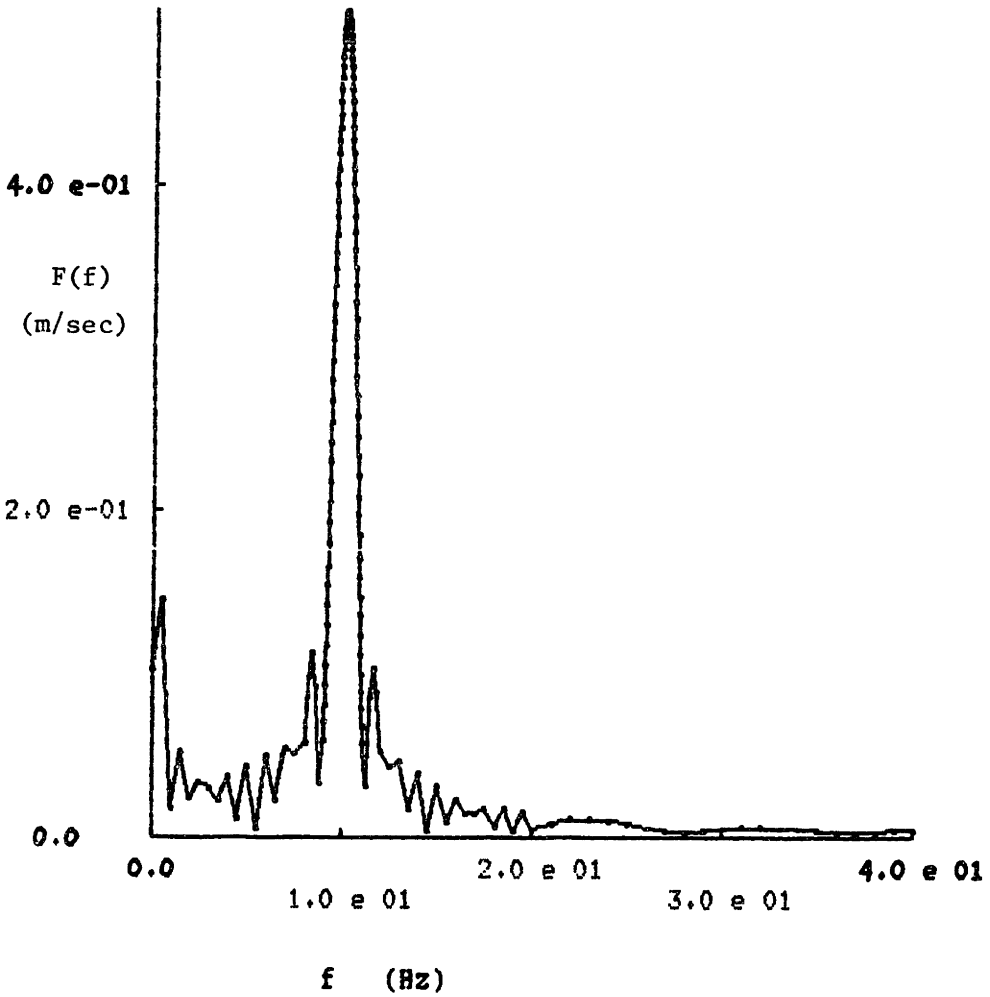

Figure 5.2 Fourier transform of particle velocity. Data was generated artificially, to demonstrate data-reduction processes. Peak value was about 0.506 m/sec, at a frequency of roughly 9.98 Hz.

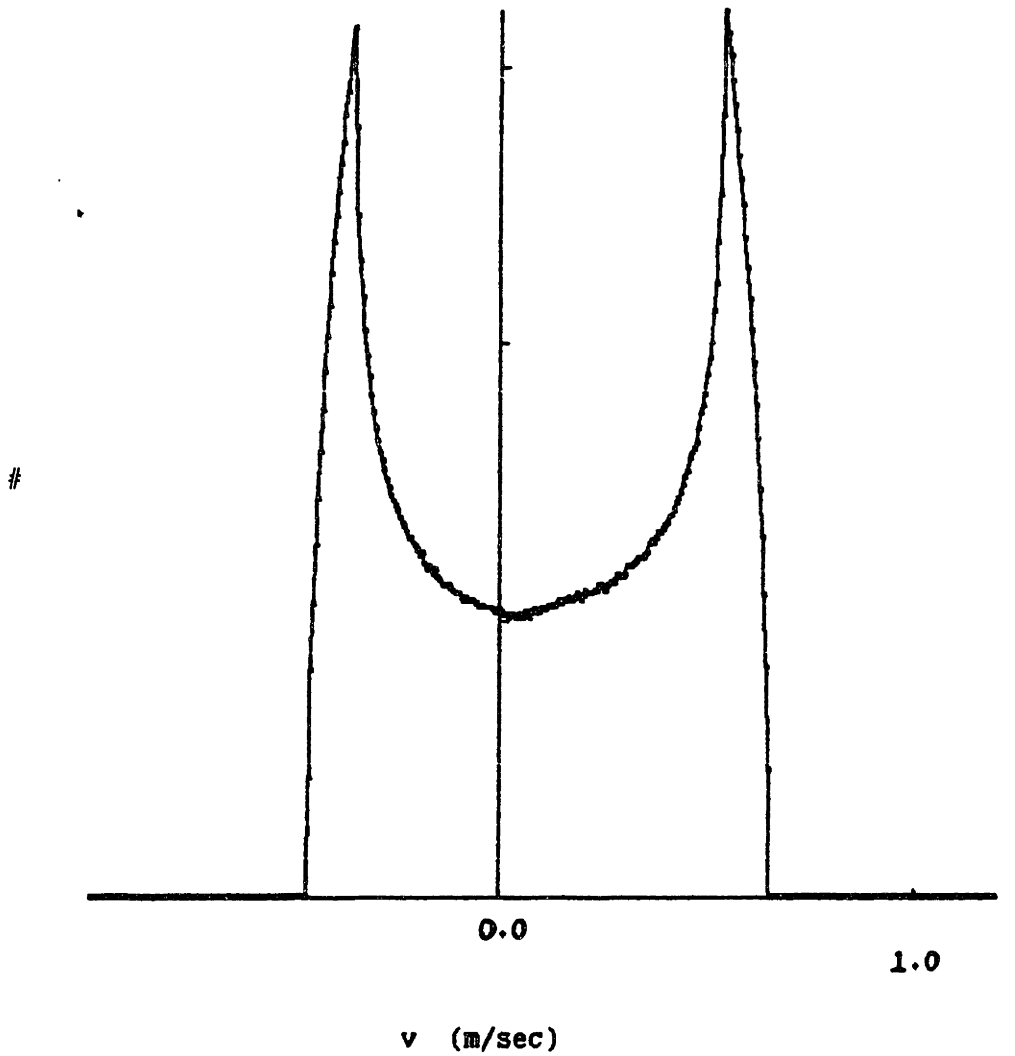

Figure 5.3 Plot of vertical velocity distribution function. Data was generated artificially, to demonstrate data-reduction processes.

A flow-straightener was placed about 15 cm upstream of the migration plate, to minimize effects of the flow turbulence on velocity measurements. If the flow about the migration plate were laminar, the only reason for a measured vertical velocity would be particle migration. Due to flow turbulence and regular eddies induced by the flow-straightener and migration plate, neither the mean velocity nor its RMS spread were zero, even with no applied voltages. Thus, zero-field statistics (taken with the migration plate grounded) are reported with each migration velocity run. Every velocity distribution plot presented in section 3 contains the zero field distribution as well. It was assumed that the velocity fluctuations due to the turbulence and those resulting from particle mobility variations were uncorrelated, so that the RMS spread in migration velocity for a particular data point, v'_{mig}, is given by

$$v'_{mig} = \sqrt{v'^2 - v'^2 \Big|_{\substack{no \\ field}}} \tag{5.1.5}$$

where v' is the RMS spread in the actual measured velocity, and $v' \Big|_{\substack{no \\ field}}$ is that same quantity measured in a previous run with the same conditions at the charger, but no migration field. The mean migration velocity, $\bar{v}_{mig}$, is given by

$$\bar{v}_{mig} = \bar{v} - \bar{v} \Big|_{\substack{no \\ field}} \tag{5.1.6}$$

where $\bar{v} \Big|_{\substack{no \\ field}}$ is, of course, the mean velocity, measured under the same "no-field" conditions described above.

5.2.2 Description of Experiments

The order of presentation of experimental data in section 3 parallels the development of section 4. Beginning with simple situations, in which the positive and negative coronas are constrained to have similar geometries (using pins), it then moves to more complex configurations which allow different spatial distributions for the two coronas (using wires). Since this is almost exactly opposite to the order in which the experiments were actually performed, the continuity of the presentation suffers somewhat. Early experiments that were performed to verify the linear dependence of the mean particle migration velocity on the voltage applied to the migration plate are reported near the middle of section 3. However, the reader should find that this simplifies the job of correlating the data and theories presented.

For experiments referred to as "pin-charging" runs, the corona electrode was a 1/8 inch diameter brass support rod with nine evenly-spaced pins, extending roughly 7/8 inch directly out from its axis. The corona was restricted to the sharp ends of the pins for both positive and negative applied voltages. The bar was, itself, held halfway between the aluminum ground plates by plexiglas squares, 1/8 inch thick. One of these squares had a threaded hole, so that a screw could make electrical contact with the support bar. A wire was attached to the screw, and ran along the glass tunnel wall to a hole, 2-1/2 ft from the end of the tunnel inlet section [Fig. (4)]. The bar was shorter than the tunnel width so that an electrical wire could pass by it along the glass wall opposite to the one used for the corona supply wire. This second wire was used to excite an "ion trap", as described below.

For most of the pin-charging experiments, the pins were pointed upstream (ie., against the mean air flow). For the majority of those run with the pins pointed downstream, a thin aluminum plate, as wide as the tunnel and about 2 inches long, was placed downstream of the pins [Fig. 4]. A small voltage ($\sim$ 1 kV) was applied to this plate, referred to hereafter as the ion trap, to precipitate any ions from the corona which were not already precipitated by the corona electric field, itself. The ion trap was not used with upstream pin-charging, as nearly all of the ions were precipitated as they were convected by the air flow past the bodies of the pins and the support bar. Experiments were run using both

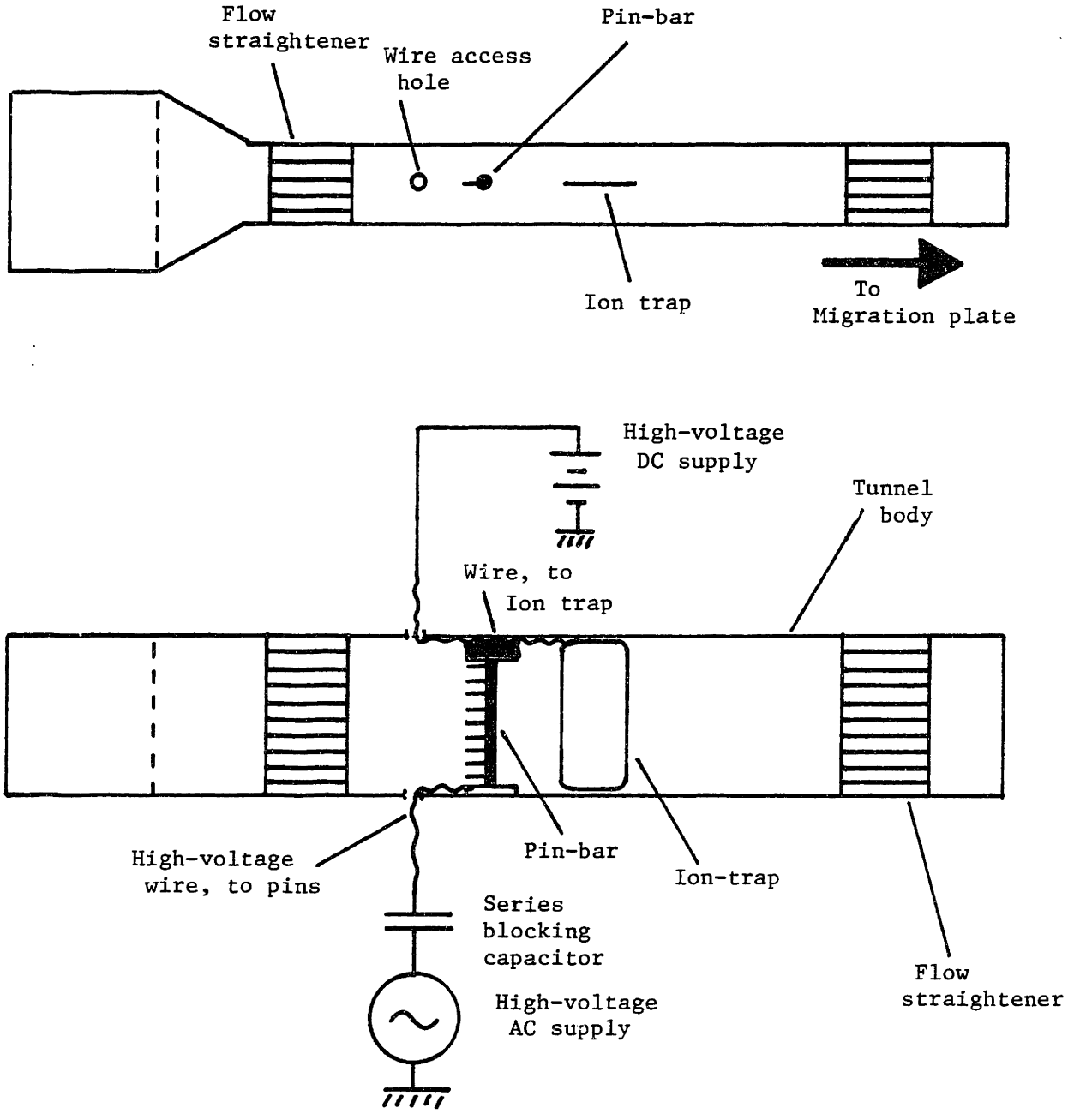

Fig. 5.4. Schematic illustration of setup for pin-charging experiments. Pin-bar is shown in the "far" position [i.e., far from the flow-straightener on the right]. Ion-trap, normally used only when pins are pointed downstream, is shown here for completeness.

± DC corona, as well as with AC coronas of up to 8 kV RMS voltage, ranging in frequency from 20 - 1000 Hz.

The fact that some ions were carried downstream by the air flow with downstream pins was exploited in the ion-mobility measurements. Figure (16) shows the configuration used for these experiments. The convected ions were precipitated by the ion trap, as with the particle charging measurements. This time, however, sections of the ground plates were isolated and grounded through a small resistance, allowing measurement of the precipitated current. These experiments gave rough estimates of the relative mobilities of the positive and negative ions from the corona pins. Positive and negative DC coronas were used to supply ions for these runs.

The setup for the wire-charging experiments was exactly as described in chapter 2, and pictured in Figs. (2.1) and (2.2). Some experiments were run, here, with a fixed DC charging voltage, while the DC voltage at the migration plate was varied. The purpose of these runs was to verify that it was actually the particle mobility that was being measured in the other runs. In addition, measurements were made that paralleled those of the upstream pin-charging runs. Because of the higher capacitance and larger corona currents of the wires (as compared to the pins), the AC frequencies were limited to 500 Hz.

For the wire-charging runs, the spatial distribution of positive and negative coronas could be very different. The positive corona tended to be distributed uniformly over the entire wire surface, as evidenced by a light purple glow around the wire. The negative corona, on the other hand, was concentrated at discrete locations, fairly evenly spaced along the wire ($\sim$ 1 cm apart). Each such point glowed brightly. It is shown in section 4 that these differences can have an important influence on the statistics of particle charging for this configuration, as is verified by the experimental results of section 3.

The last experiments reported in section 3 can be thought of as hybrids, partway between the wire-charging and pin-charging runs. Very thick corona wires (.050 inch diameter) were used here, with barbs of thin wire (.006 inch diameter) tied to them at intervals of roughly 1 cm. As with the pins, the positive and negative coronas were restricted to similar geometries. The purpose of these runs was to observe particle

charging in a situation where the charging electric fields were similar to those in the previous wire-charging runs, but without the disparate geometry of coronas that they suffered.

5.3 Experimental Data

5.3.1 Upstream Pin-Charging

Figure (5) shows distributions of particle migration velocity resulting from DC excitation of upstream-pointed corona pins. As was stated in the previous section, each plot also contains a velocity distribution function obtained with the migration plate grounded. Since the voltage applied to the migration plate was negative (-10 kV), positive particle charges resulted in negative migration velocities, and vice-versa. Equal magnitude positive and negative corona voltages (8.0 kV) were used. In both cases, the excitation resulted in both a translation and spreading of the velocity distribution. It is easily seen that the negative corona (5b) gave larger migration velocity magnitudes. The "high-velocity tail" in the negative charging distribution shows that a small number of particles were very highly charged. The "tail" is much less evident with positive charging. It should be noted that each of the charging velocity distributions contains a small hump immediately below the zero-field distribution, with a shape that is similar to that of the latter. This implies that a small fraction of the particles escaped the charging process altogether. These particles would be expected to have a velocity distribution function that is identical to that obtained with zero field.

Figure (6) shows plots of the mean particle migration velocity as a function of corona voltage magnitude for both positive and negative DC corona charging (still, using upstream-pointed pins). It is seen that, for the entire voltage range examined, a much higher particle mobility is obtained for negative charging than with a positive voltage of the same magnitude. Since the spacing between the migration plate and tunnel top was 1.75 cm, and the plate voltage was -10 kV, the particle mobilities can be estimated from Fig. (6), by using the relation

$$b \equiv \frac{|\bar{v}|}{|\bar{E}|} \qquad (5.3.1)$$

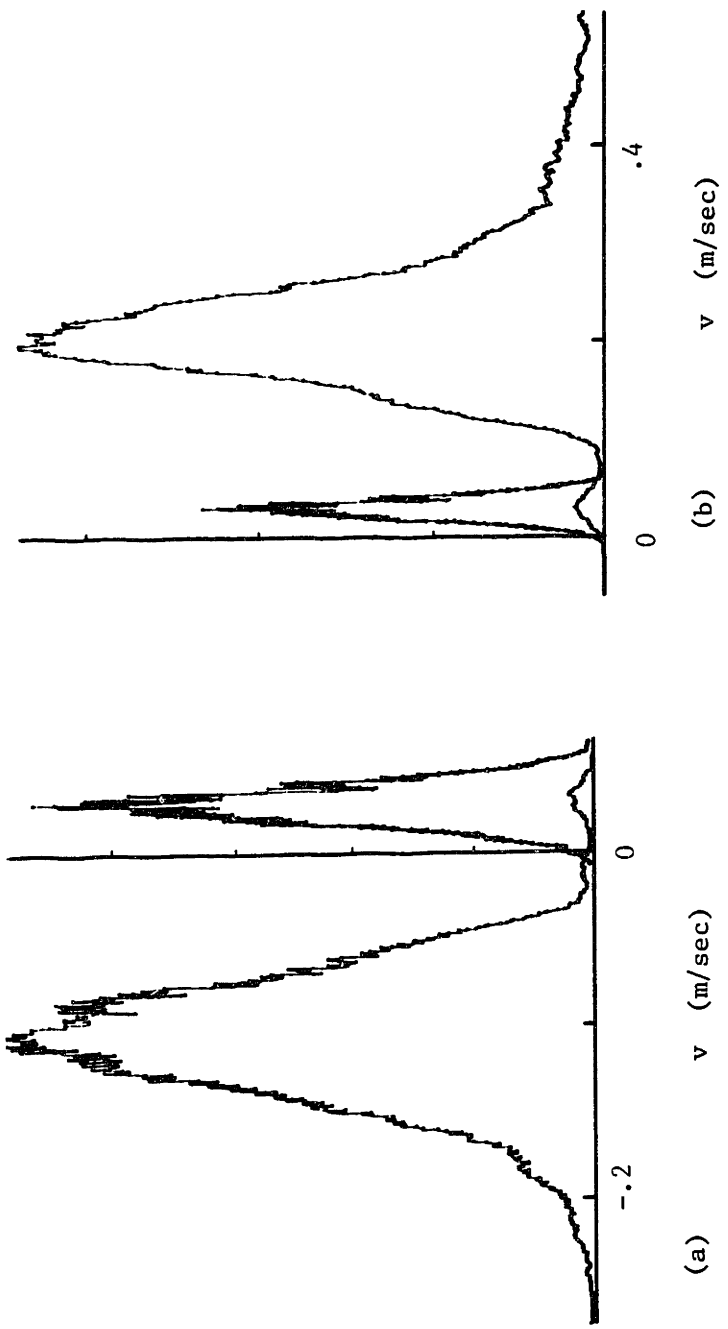

Fig. 5.5. Plots showing vertical velocity distribution function for DC upstream pin-charging experiments. For (a), the corona voltage was +8.0 kV. For (b), the corona voltage was -8.0 kV. The horizontal flow velocity was 2.5 m/sec (data from 10/26/83).

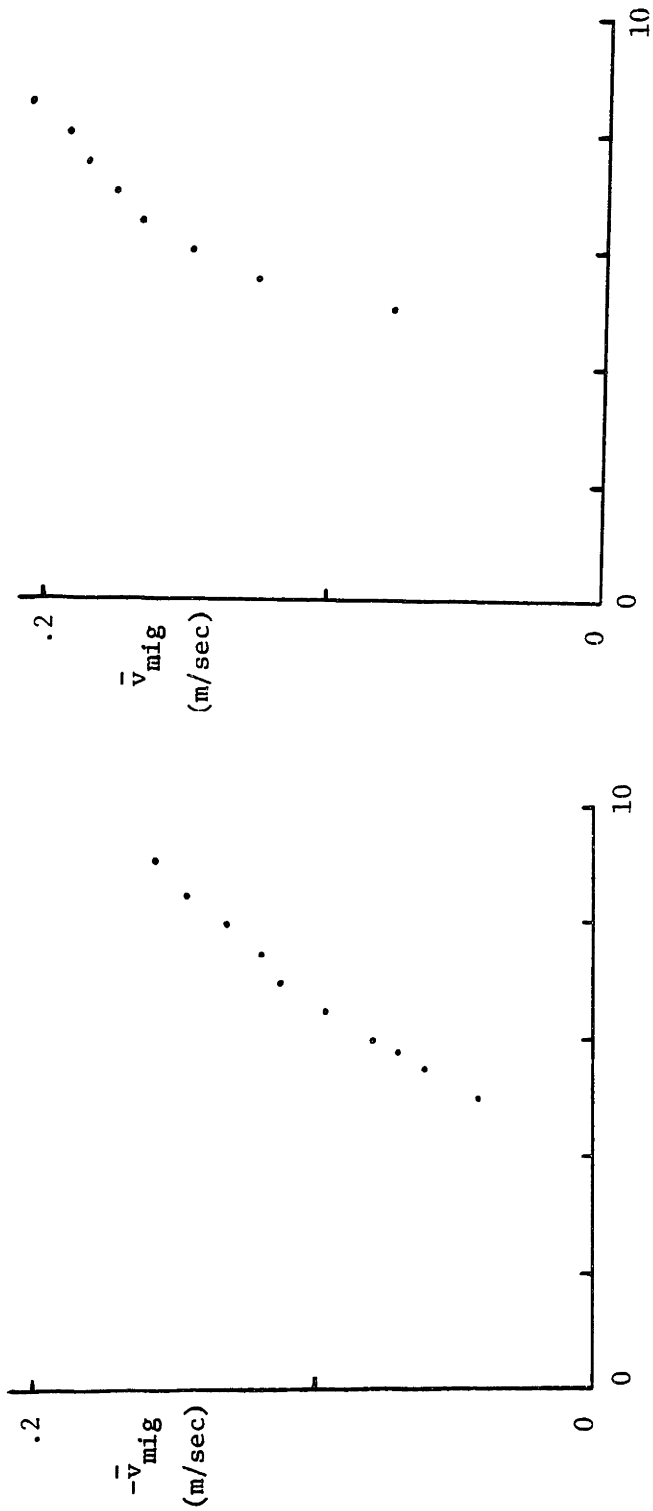

Fig. 5.6. Plots showing particle migration velocity vs. corona voltage for both positive (a) and negative (b) charging. The horizontal flow rate was 2.5 m/sec. The LDV observation volume was 1¼ inch from the upstream edge of the migration plate. Pin-charging was used (data from 11/11/83).

where $|\bar{E}| \sim 5.7 \times 10^5$ v/m. Thus, the highest mobilities observed for the experiments reported in Fig. (6) were about 3.5×10^{-7} $m^2/v \cdot sec$.

Figure (7) shows a progression of particle migration velocity distribution functions obtained from AC charging with pins. The mean and RMS spread of the velocities are plotted as a function of frequency in Fig. (8). For these runs, the RMS corona voltage was held fixed (8.0 kV) as the frequency varied from 20 - 900 Hz. The characteristic "two humps", idealized in Fig. (3), are visible in all of the distributions of Fig. (7). These humps, corresponding separately to positive and negative particle charging, remain distinct and relatively unchanged for frequencies up to 60 Hz. In fact, the level of uncharged particles seems to be lower for 60 Hz than for 20 Hz. It is seen in Fig. (8) that the RMS velocity spread, v'_{mig}, is of roughly the same order as the velocities obtained with $\pm$DC charging. In addition, a significant bias to the charging exists (ie., the mean particle charge is negative).

The velocity distribution functions of Figs. (9) and (10) correspond to similar upstream pin-charging experiments performed without the series blocking capacitor present. Thus, for these experiments, the corona voltage (rather than the current) was unbiased. In the progression of the 11 distributions of these figures, one can clearly see the positive charging "hump" shrink in size until it is no longer visible. It should be noted here that the scaling of the plots was adjusted to fit the data, and changed by roughly a factor of two between the first and last distributions. The distributions of Fig. (7) do not clearly display the same behavior as that of Figs. (9) and (10), but they show results only for frequencies up to 200 Hz. The mean velocity and RMS velocity spread corresponding to the distributions of Figs. (9) and (10) are plotted in Fig. (11).

Figure (12) shows data on the mean and RMS spread in particle migration velocity for experiments run under conditions similar to those of Fig. (8), except that the imposed flow velocity was 4.3 m/sec, where that used for the earlier-reported data was 2.5 m/sec. Two curves are shown in each plot [the connecting lines were drawn in order to distinguish the two]. One curve was obtained with the pins very close to the flow straightener [about 25 cm upstream of the leading edge of the migration plate]. For the other, the pins were far upstream of the

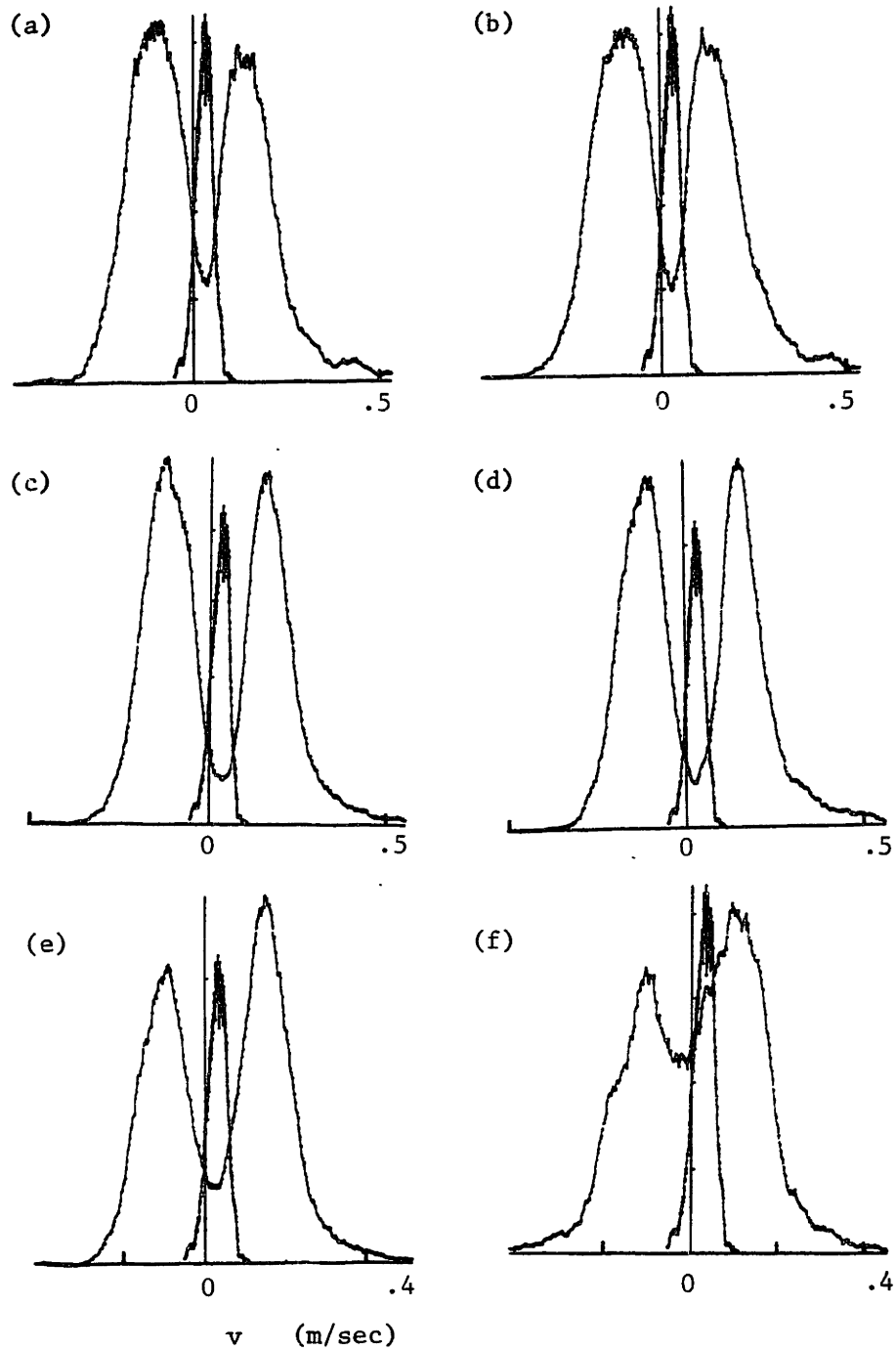

Fig. 5.7. Progression of vertical velocity distribution functions for AC upstream pin-charging experiments. The RMS voltage applied to the corona pins was 8.0 kV, at frequencies of 20, 30, 50, 60, 120, 200 Hz for (a)-(f), respectively. The series blocking capacitor was present for these runs. The horizontal flow velocity was 2.5 m/sec. (Data from 11/12/83)

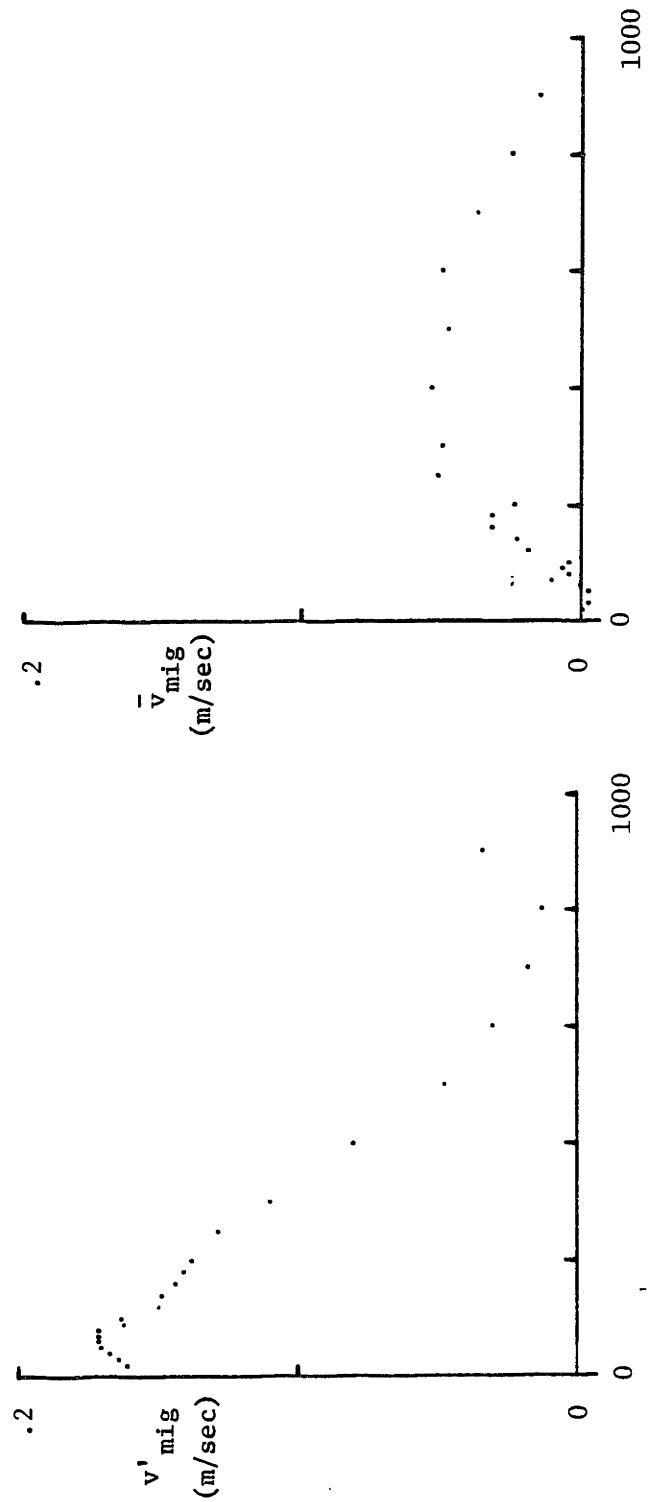

Fig. 5.8. Plots showing variation of mean (b) and RMS spread (a) of particle migration velocity as a function of corona excitation frequency for upstream pin-charging experiments. The RMS corona voltage was 8.0 kV. The series blocking capacitor was present. The horizontal flow velocity was 2.5 m/sec. (Data from 11/12/83)

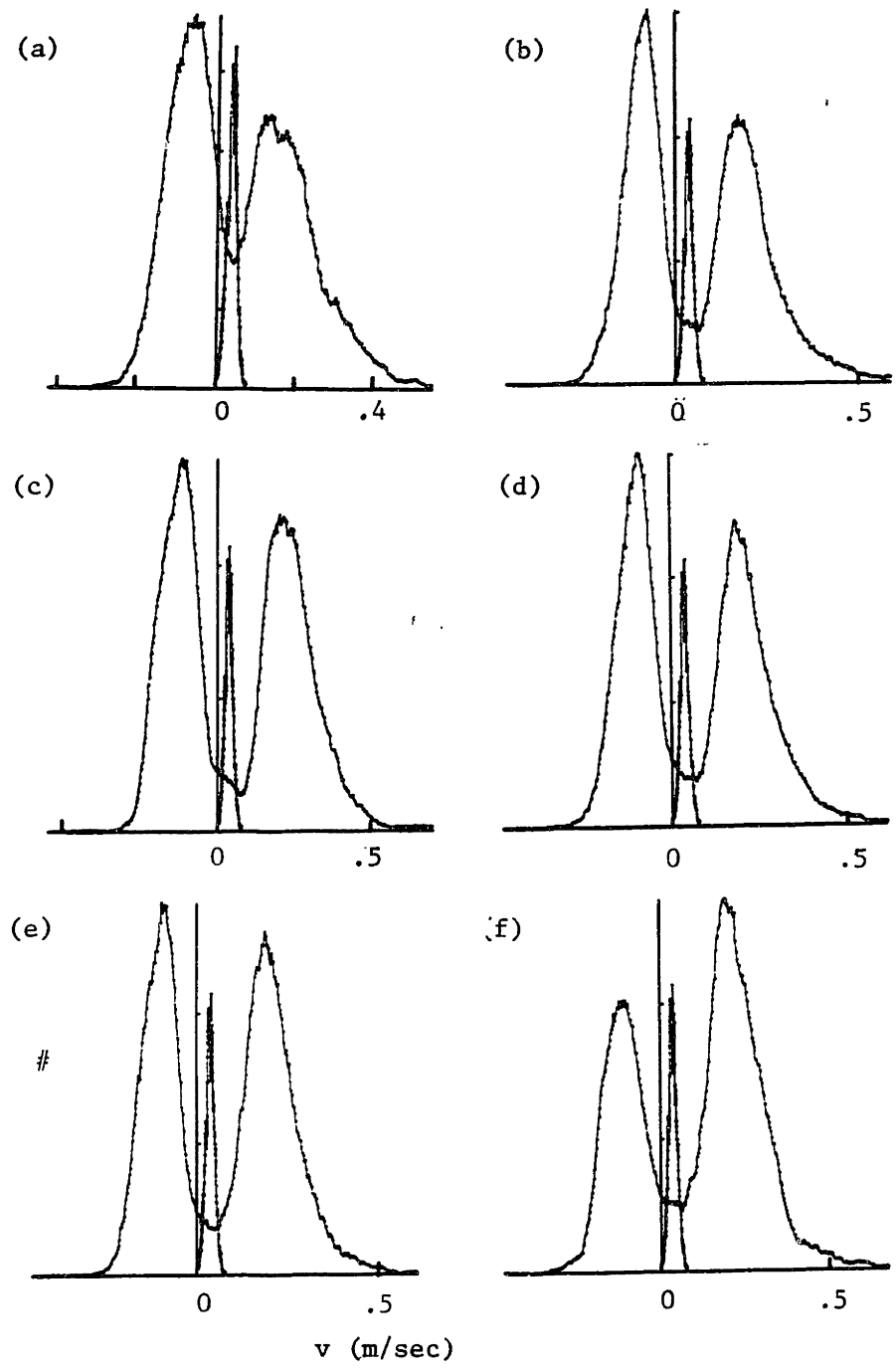

Fig. 5.9. Progression of vertical velocity distribution functions for AC upstream pin-charging experiments. The RMS voltage applied to the corona pins was 8.0 kV, at frequencies of 20, 50, 70, 80, 100, 150 Hz for (a-(f), respectively. The series blocking capacitor was not present for these runs. The horizontal flow velocity was 2.5 m/sec. (Data from 10/29/83)

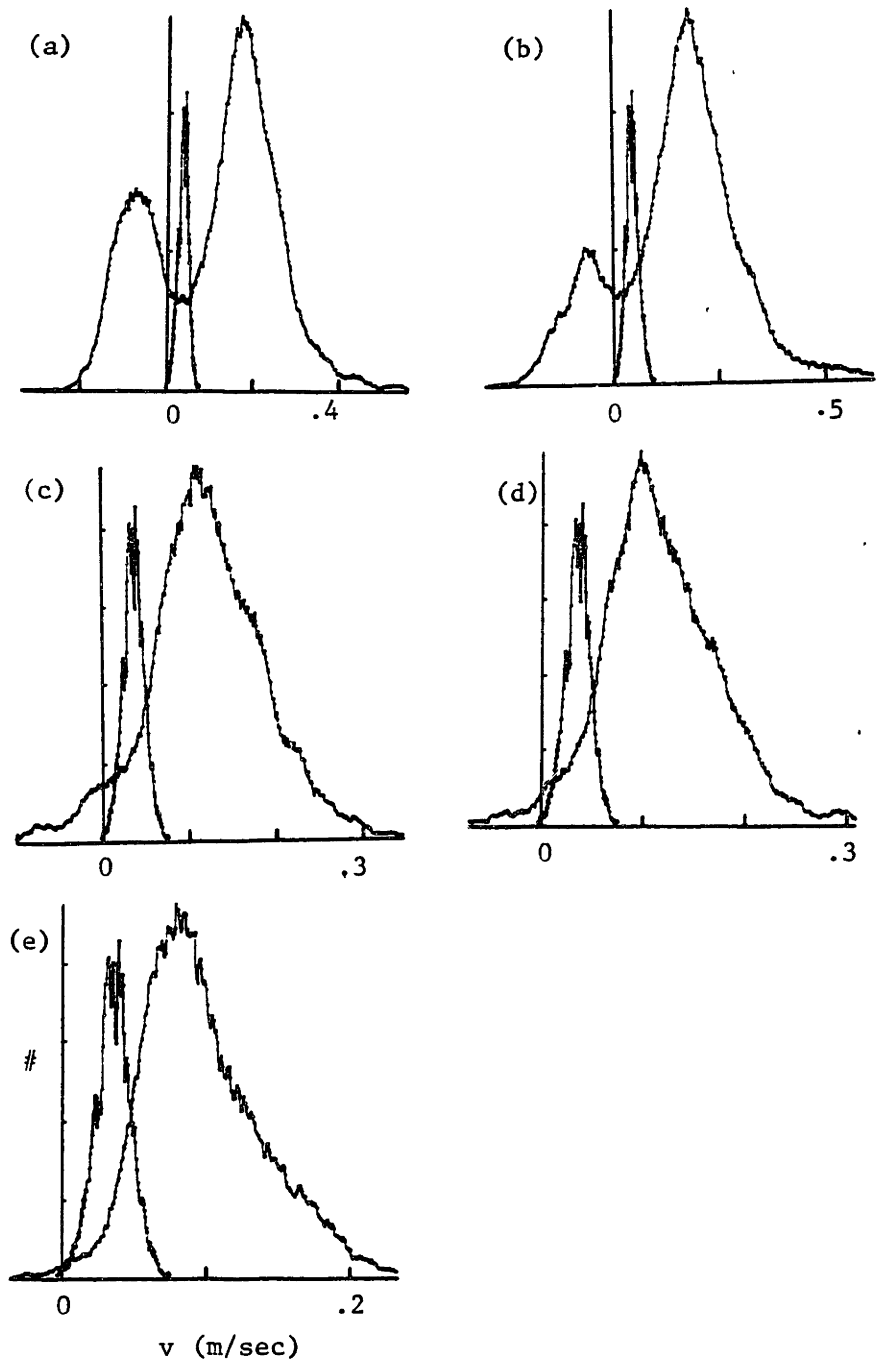

Fig. 5.10. Progression of vertical velocity distribution functions for AC upstream pin-charging experiments. The RMS voltage applied to the corona pins was 8.0 kV, at frequencies of 200, 300, 500, 600, 800 Hz for (a)-(e), respectively. The series blocking capacitor was not present for these runs. The horizontal flow velocity was 2.5 m/sec. (Data from 10/29/83)

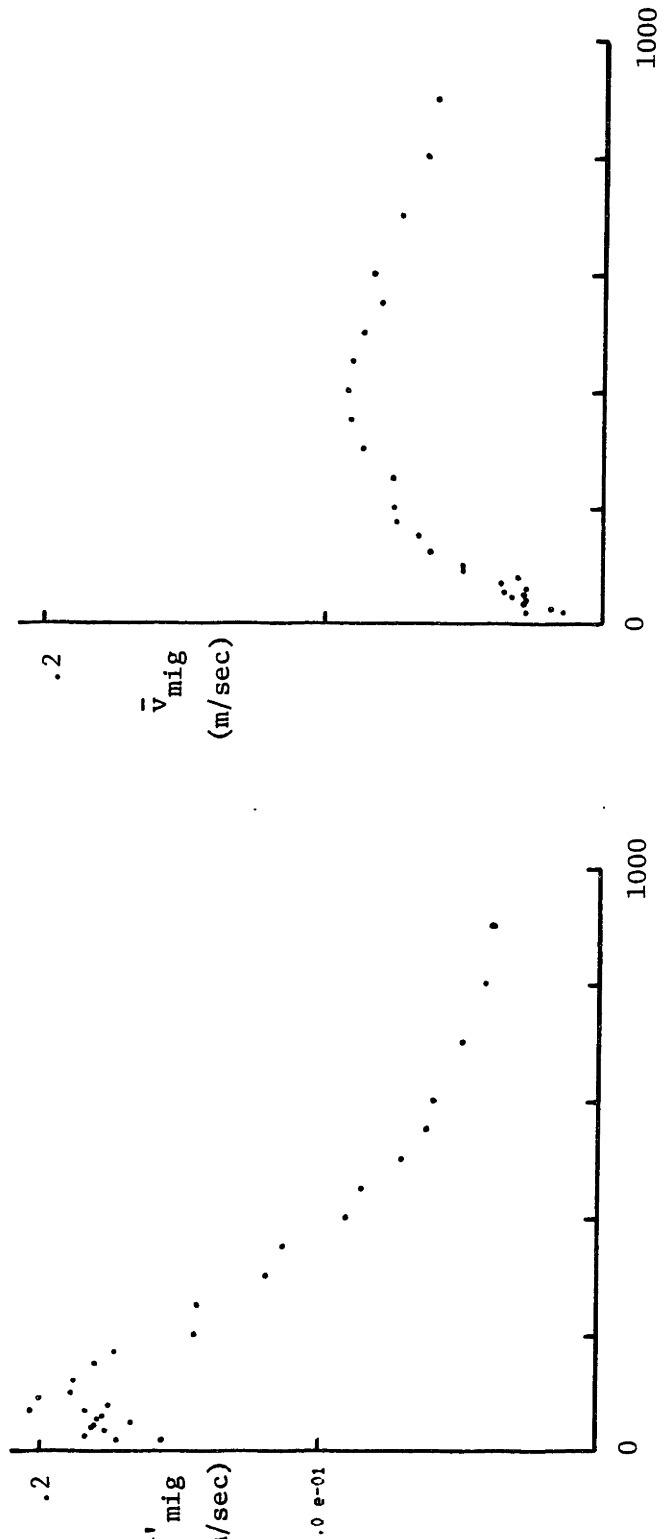

Fig. 5.11. Plots showing variation of mean (b) and RMS spread (a) of particle migration velocity as a function of corona excitation frequency for upstream pin-charging experiments. The RMS corona voltage was 8.0 kV. The series blocking capacitor was not present. The horizontal flow velocity was 2.5 m/sec. (Data from 10/29/83)

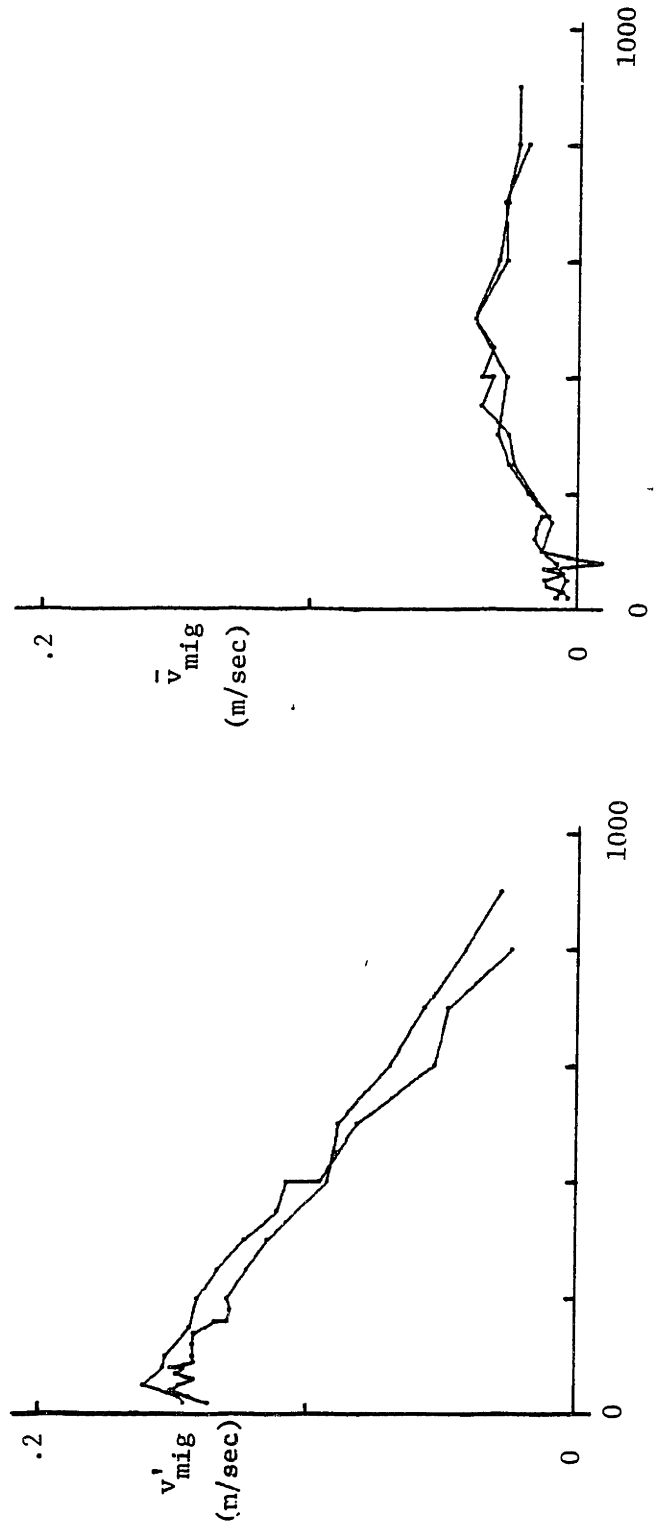

Fig. 5.12. Plots showing mean (b) and RMS spread (a) of particle migration velocity for upstream pin-charging experiments. The horizontal flow velocity 4.3 m/sec. The RMS corona voltage was 8.0 kV. Two curves are shown in each plot. One is for pins close to flow-straightener (~ 25 cm upstream of migration plate), other is for pins far from flow-straightener (~ 100 cm upstream of migration plate).

flow-straightener [so that they were about 1 m away from the migration plate]. They were included to demonstrate that the particle charging statistics do not change significantly as they are convected by the flow through the tunnel.

AC charging data was obtained at three different flow velocities. Figure (13) shows a plot of the RMS spread in particle migration velocity as a function of the flow velocity, for a fixed electrical excitation [20 Hz AC, 8.0 kV RMS]. The horizontal coordinate in that figure is actually inversely proportional to the imposed flow velocity, being equal to (0.5 cm/U), or the convection time for the flow, based upon a 0.5 cm length.

5.3.2 Downstream Pin-Charging

The results of AC charging experiments performed with the pins pointed downstream were radically different from those described above. If one were to repeat the DC charging runs after simply turning the pin-bar around, the observed particle migration velocities would be similar to those reported in Fig. (6). However, with an AC corona excitation, there would be virtually no observed particle migration in the second stage (ie., above the migration plate). The three velocity distributions shown in Fig. (14) were obtained using the ion-trap setup pictured in Fig. (4), with the pins pointed downstream. The narrowest distribution was measured with a 9 kV RMS, 30 Hz AC voltage applied to the pins, but nothing applied to either the migration plate or ion-trap (ie., the "no-field" distribution). The second curve, only slightly wider than the first, resulted from application of -10 kV DC to the migration plate (with the corona excitation still on). The ion-trap was then driven to a potential of -1 kV DC to produce the third and widest curve. The time required to collect the 2941 data points taken in each run was roughly the same for all three runs. It is argued in section 5.4 that the effect of the ion-trap was to precipitate out ions that were convected downstream by the air flow before they could discharge the particles.

The ion-trap was placed roughly 5.9 cm from the ends of the corona pins for the runs of Fig. (14). Figure (15a) shows the variation of the

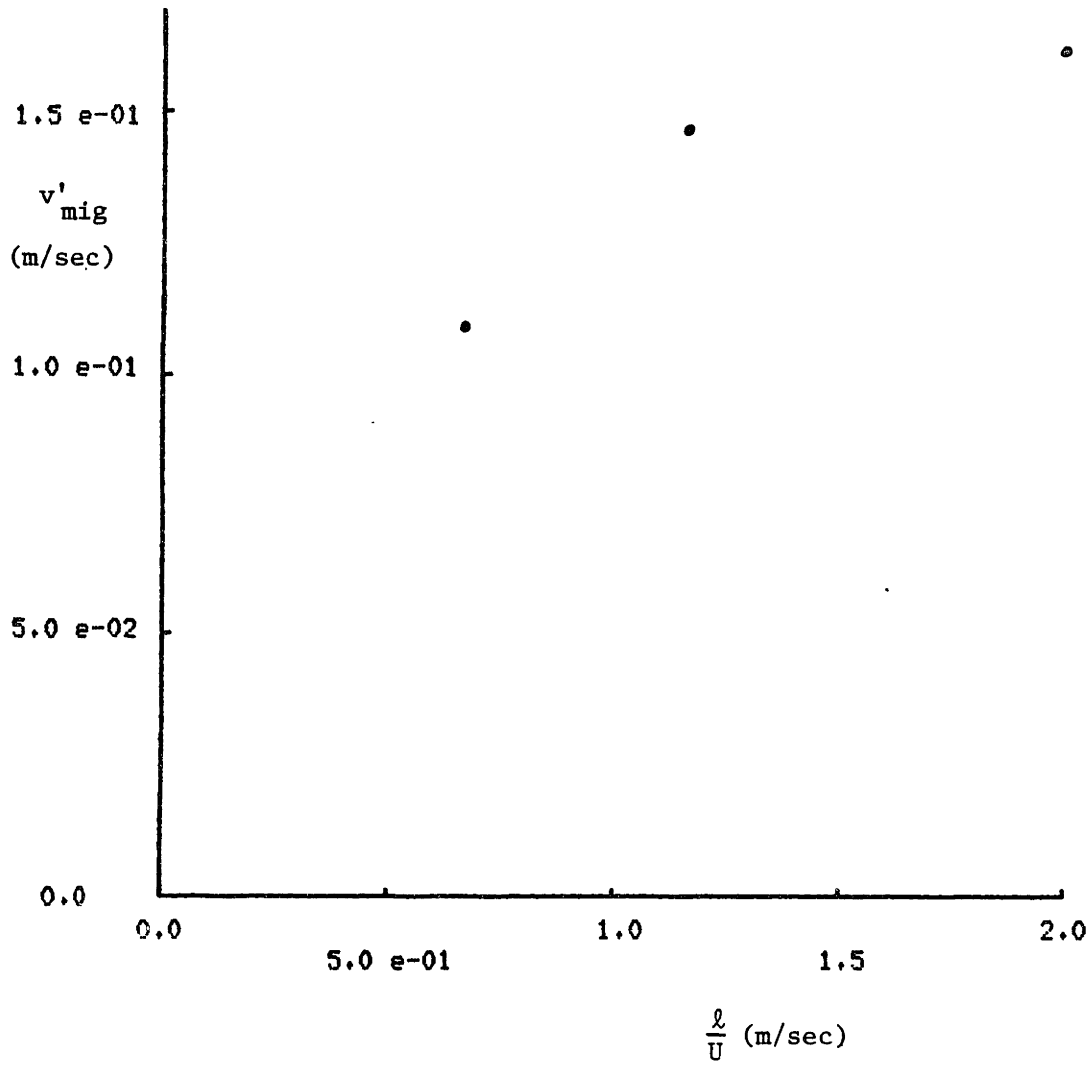

Fig. 5.13. Plot of RMS spread in particle migration, velocity vs. residence time in the vicinity of the pins, for upstream pin-charging experiments. The horizontal coordinate is inversely proportional to the imposed horizontal flow velocity, with the proportionality constant, ℓ=0.5 cm.

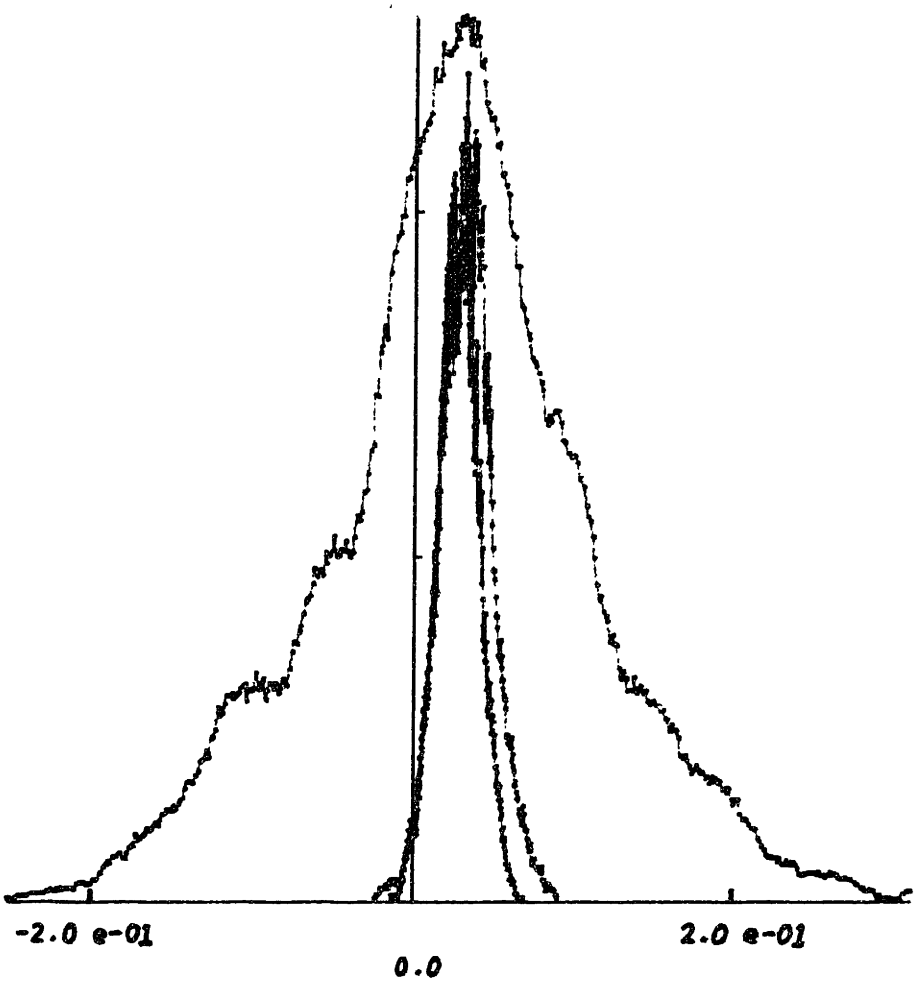

Fig. 5.14. Vertical velocity distribution functions for downstream AC pin-charging. Three distributions are shown here, all with 2.5 m/sec horizontal flowrate, and a 30 Hz AC, 9.0 kV RMS corona excitation at the pins. The narrowest curve is with both the migration plate and ion-trap grounded. For the second (barely discernible from the first), -10 kV DC were applied to the migration plate. The ion-trap was excited with a -1 kV DC voltage (with the migration plate still on) for the third, and widest, curve.

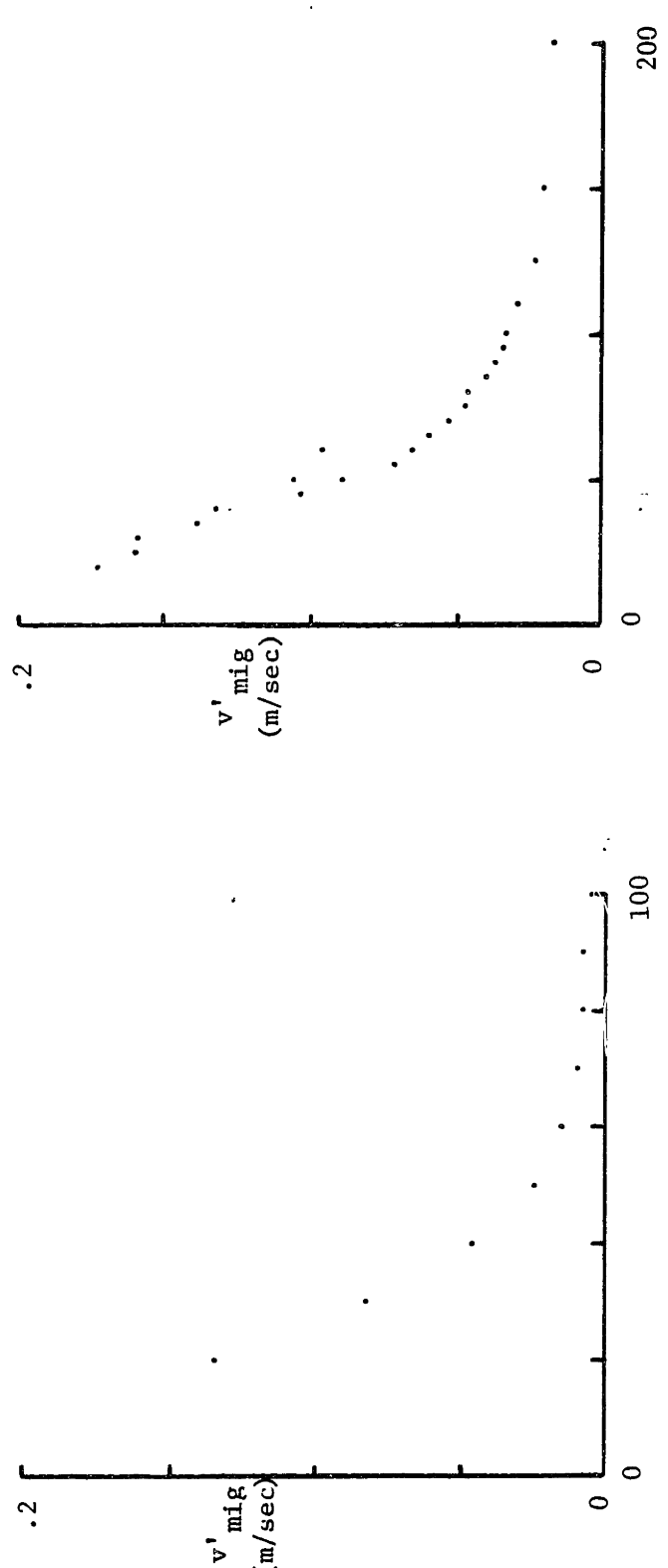

Fig. 5.15. Plots showing RMS spread in particle migration velocity vs. corona excitation frequency for downstream AC pin-charging. An 8.0 kV RMS corona voltage was used for all runs. The distance from the ends of the pins to the ion trap was 5.9 cm for (a), and 2.9 cm for (b). The horizontal flow velocity was 2.5 m/sec.

RMS spread in measured migration velocity with corona excitation frequency for the ion-trap in this position. For Fig. (15b), the ion-trap was moved closer to the pins (2.9 cm away). Comparison of the two plots shows that the characteristic frequency at which the particle charging falls off varies roughly in inverse proportion to the distance of the ion-trap from the pins. In Fig. (15b), at 80 Hz, the RMS velocity spread is roughly 1/4 of its value at low frequencies. A wavelength, characteristic of the distribution of ions convected downstream by the flow, can be determined from this frequency along with the flow velocity of 2.5 m/sec.

$$\lambda_{charge} = \frac{U}{f} \qquad (5.3.2)$$

$$\sim 3 \text{ cm}$$

Thus, the particle charging falls off at about the same frequency at which an entire wavelength of the ion charge fits between the pins and the ion-trap.

5.3.3 Ion Precipitation Experiments

The ion precipitation experiments were performed for two purposes: (1) to estimate, roughly, the magnitude of mobility of the ions used in particle charging, and (2) to determine whether there was a significant difference between the mobility of the positive and negative ions. The setup was similar to that used for the downstream pin-charging experiments, except that the sections of the ground plates immediately above and below the ion trap were electrically isolated and grounded through a small resistance in order to allow measurement of the precipitated ion current. The situation is pictured schematically in Fig. (16). It is expected that, as the voltage at the ion-trap is initially increased from zero, the precipitated current will rise, as ions are driven to the isolated sections. Eventually, however, the fringing electric field in front of the trap will be of sufficient intensity to precipitate most of the ions before they reach the isolated electrodes. The fringing field extends in front of the trap a distance that is roughly equal to the spacing between the trap and ground plates.

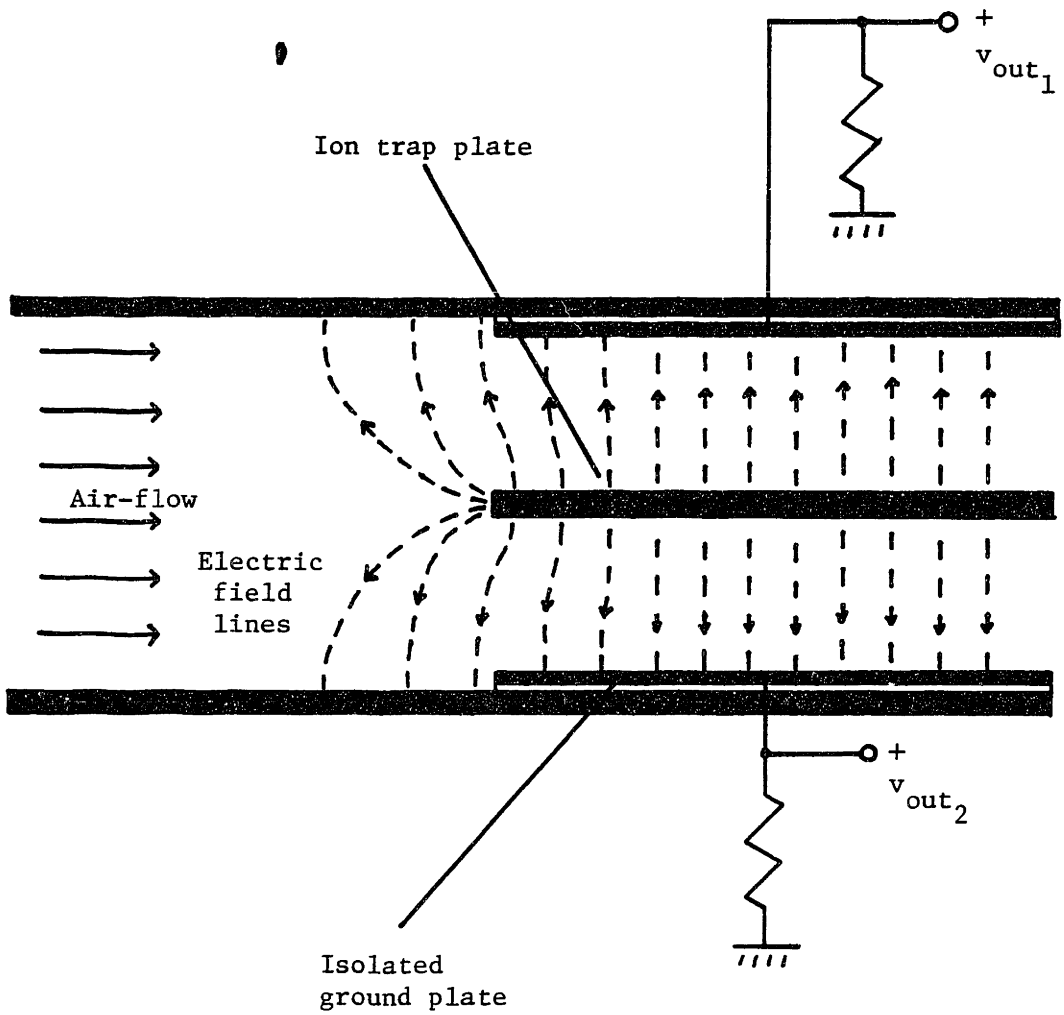

Fig. 5.16. Schematic illustration of experimental setup for ion-precipitation measurements. Ions, convected by air-flow from left to right, precipitate onto isolated electrodes. If fringing electric field is intense enough, most ions precipitate before reaching isolated electrodes.

Thus, the voltage at which the precipitation current falls to 1/4 of its peak value will be taken (rather arbitrarily) as the point at which the ion migration velocity is equal to the perpendicular convection (ie., flow) velocity, so that most of the ions are precipitated before reaching the isolated electrodes.

Figure (17) shows data from 6 experiments in which the precipitated ion current was measured for both positive and negative coronas at 3 different flow velocities. Table 5.1 contains results from application of the above criteria to estimate the ion mobility. Although mobilities computed from the three different flow velocities showed a definite trend towards higher values for larger flow velocities (one would expect the same mobility for each flow velocity), the total variation was less than 25% for either the positive or negative ions alone. The negative ion mobility was consistently the higher one, by at least 12%, but not more than 22%. It was concluded, from these tests, that the ion mobilities were of the order of 5×10^{-5} $m^2/v \cdot sec$, and that the positive and negative ion mobilities were within 20% of one another, with the negative being the higher.

5.3.4 Wire-Charging Experiments

Figure (18) shows the velocity distributions which result from DC excitation of the corona wires. They are similar to the corresponding pin-charging distributions of Fig. (5), except that the distribution for negative corona charging has a wider "tail" of highly-charged particles. The $\pm$DC wire-charging data of Fig. (19) are also similar to the pin-charging results of Fig. (6), except that with the wires, the corona starting voltage is significantly higher for positive coronas ($\sim$6 kV, as opposed to $\sim$-4.5 kV for negative corona). It should be noted that positive and negative coronas of the same voltage magnitude produced roughly equal mean particle mobilities. In Fig. (19), the particle migration velocity is seen to be nearly linear in the wire voltage [for those voltages that are well above the corona onset level]. This is to be expected, as the uniform-field charging model of chapter 3 predicts a particle saturation charge that is proportional to the strength of the imposed electric field.

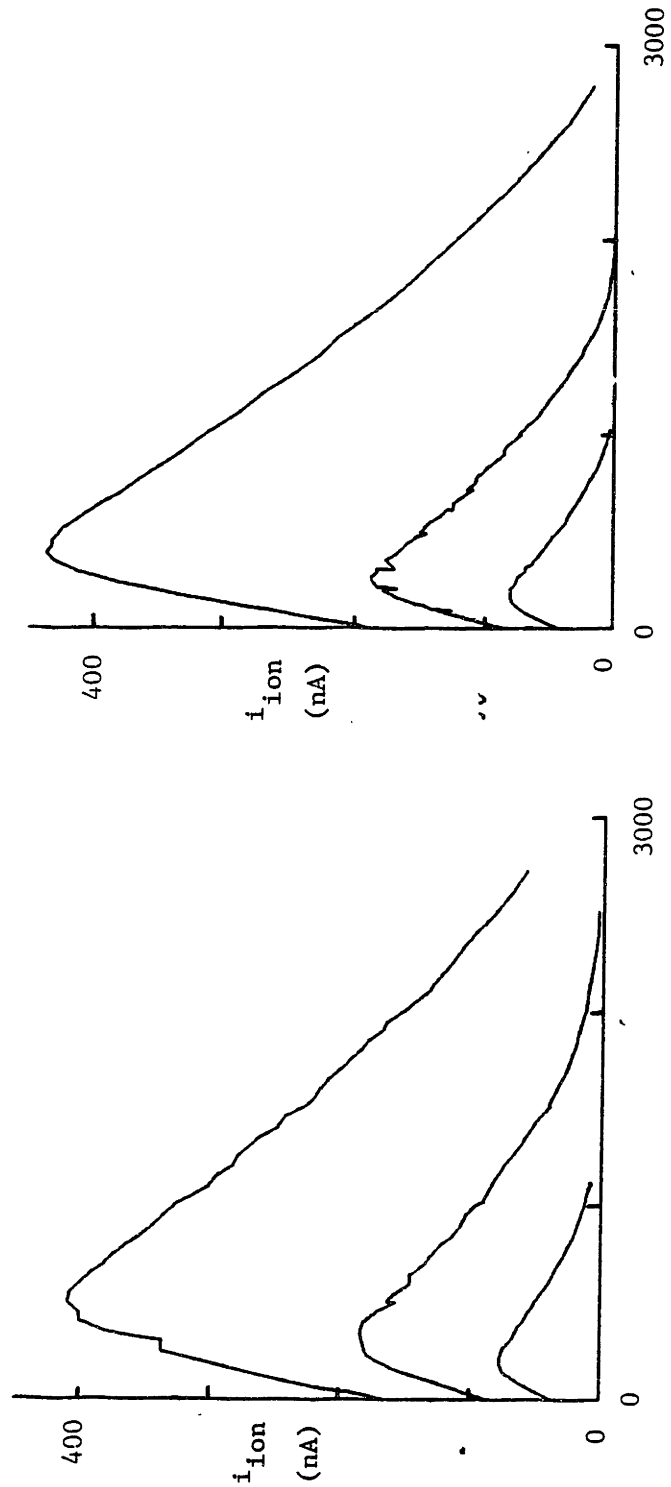

Fig. 5.17. Plots of ion current vs. trap voltage for ion-precipitation experiments. In each plot, curves correspond to horizontal flow velocities of 2.5, 5.12, and 9.08 m/sec for the smallest to largest, respectively. Positive voltages of about 8.5 kV magnitude, giving corona currents of roughly 60 μA were used for plot (a). Negative voltages of similar magnitude, resulting in corona current magnitudes of roughly 100 μA were used for (b). The similarities between the two suggest that the positive and negative ion mobilities are roughly equivalent. (Data from 11/3-6/83)

Flow Velocity (m/sec)	+/-	$V_{critical}$ (volts)	b ($m^2/v \cdot sec$)	b_-/b_+
2.5	+	886	4.23×10^{-5}	
2.5	-	748	5.01×10^{-5}	1.16
5.12	+	1465	5.24×10^{-5}	
5.12	-	1200	6.40×10^{-5}	1.22
9.08	+	2358	5.78×10^{-5}	
9.08	-	2110	6.45×10^{-5}	1.12

Table 5.1. Results from ion-precipitation experiments. The purpose of these experiments was to measure the ion mobilities.

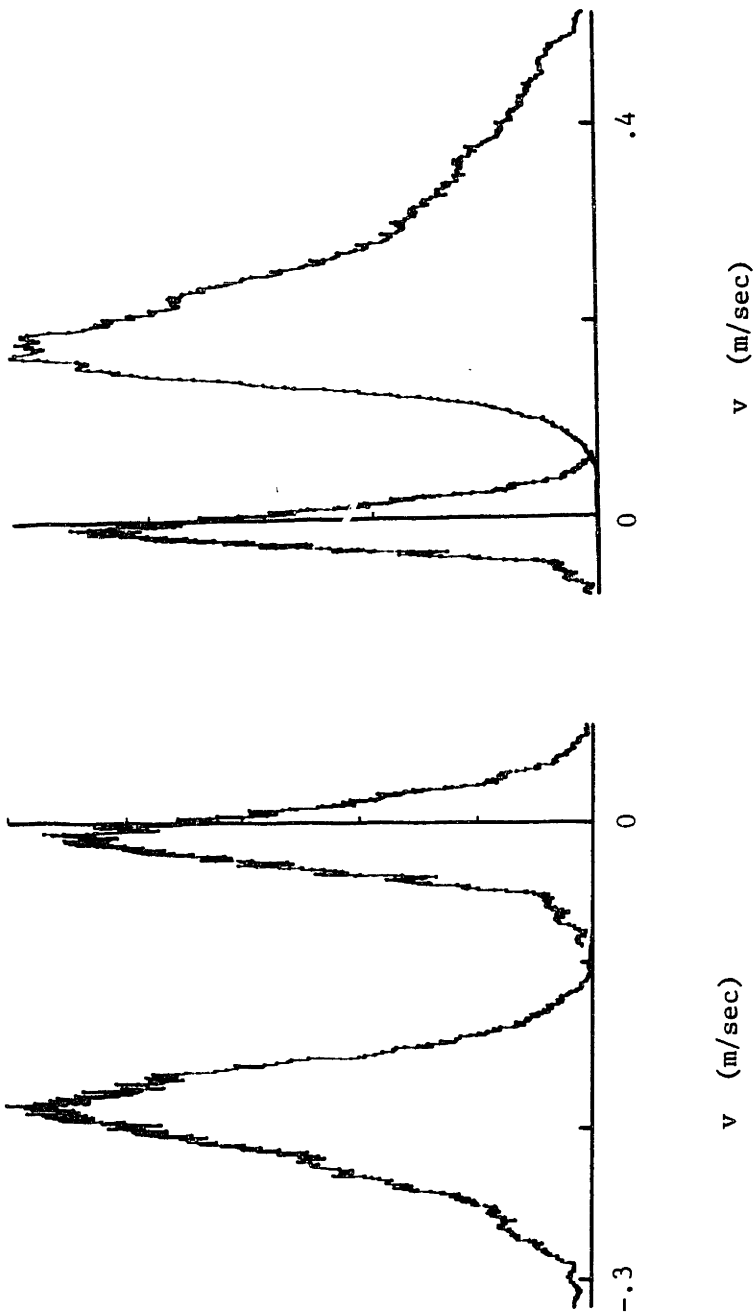

Fig. 5.18. Plots showing vertical velocity distribution function for DC wire-charging experiments. For (a), the corona voltage was +8.0 kV. For (b), the corona voltage was -8.0 kV. The horizontal flow velocity was 2.5 m/sec. (Data from 10/11/83)

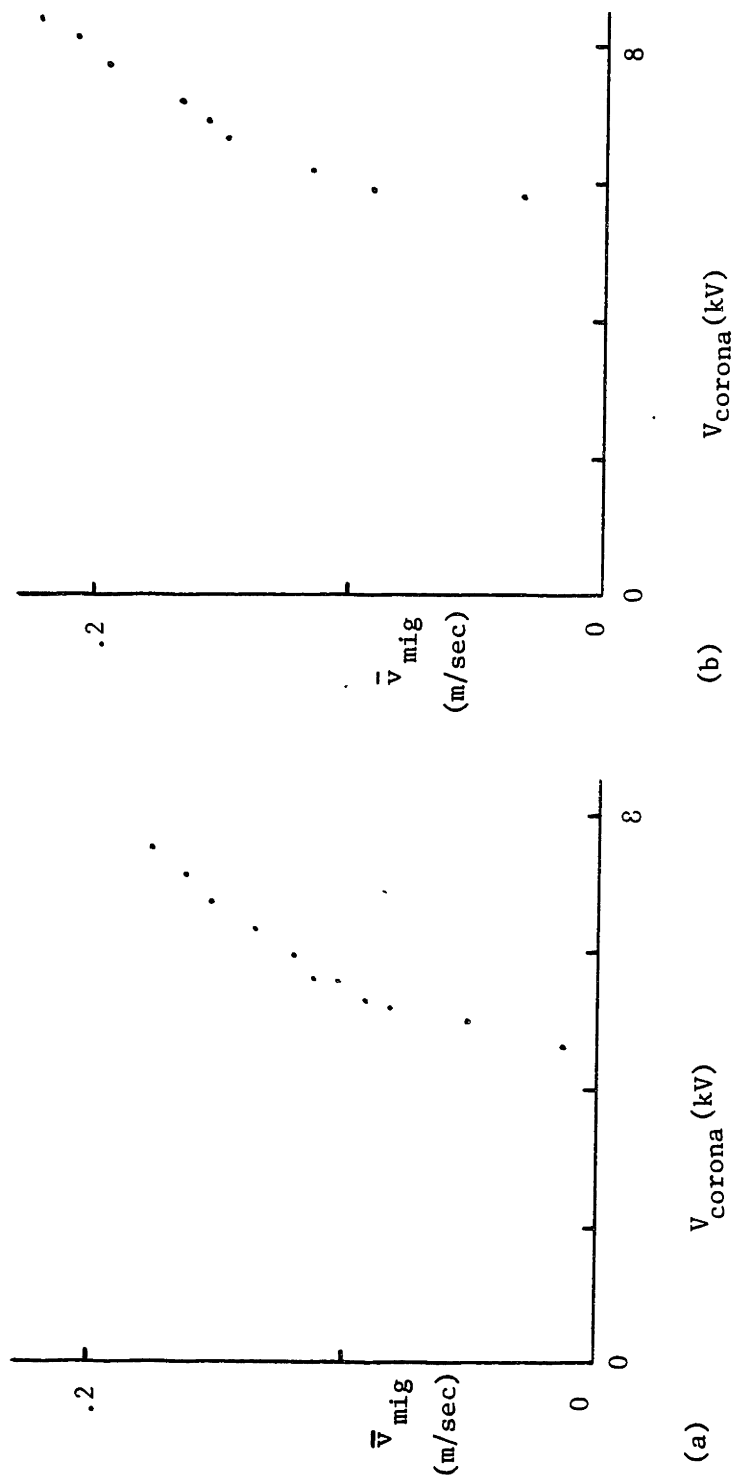

Fig. 5.19. Plots showing mean particle migration velocity vs. corona voltage for both positive (b) and negative (a) charging. The horizontal flow rate was 1.5 m/sec. The LDV observation volume was 4¼ inch from the upstream edge of the migration plate. Wire-charging was used (Data from 8/27/83).

For the plots of Fig. (20), the corona voltage was held constant at +7.95 kV while the migration plate voltage varied from -1 to -10 kV. The purpose of this run was to determine whether the observed mean particle velocity varied linearly with the plate voltage, as would be expected if the particle mobility was indeed the quantity being measured in the experiment. The fact that the RMS velocity spread also varied linearly with the plate voltage implies that it is a good measure of the spread in particle mobility. The value of the RMS spread was roughly 20% of the mean velocity.

Figures (21) and (22) show a progression of velocity distribution functions for AC wire charging. The same fixed RMS voltage used in the pin-charging runs (8.0 kV) was applied here as well. The RMS velocity spread for low frequencies was of a magnitude similar to that obtained with the pins. As the frequency was raised, however, the particles displayed a tendency toward positive charging, in contrast to the negative bias observed in the earlier reported experiments. This bias toward positive charging remained even when the series blocking capacitor was removed from the excitation circuit. Under the latter conditions, there was a significant negative time-average corona current. In Fig. (21), it is seen that the negative charging "hump" disappears rapidly and is almost non-existent for frequencies above 100 Hz. The entire distribution is relatively unchanged for frequencies beyond about 150 Hz. This fact is also apparent from the plots of Fig. (23), which show the mean and RMS spread in particle migration velocity as a function of excitation frequency.

5.3.5 Barbed-Wire Charging Experiments

Table (2) shows the results of the 6 measurements made with the barbed-wire charger described in section (2). Experiments were run at 30, 100, and 300 Hz, both with and without the series blocking capacitor present. The most important result of the experiment was that the mean particle charge was always negative (as is reflected in the positive values of $\bar{v}_{mig}$). It is to be expected that insertion of the series blocking capacitor would decrease the negative charging bias, as it places a positive time-average voltage at the wires.

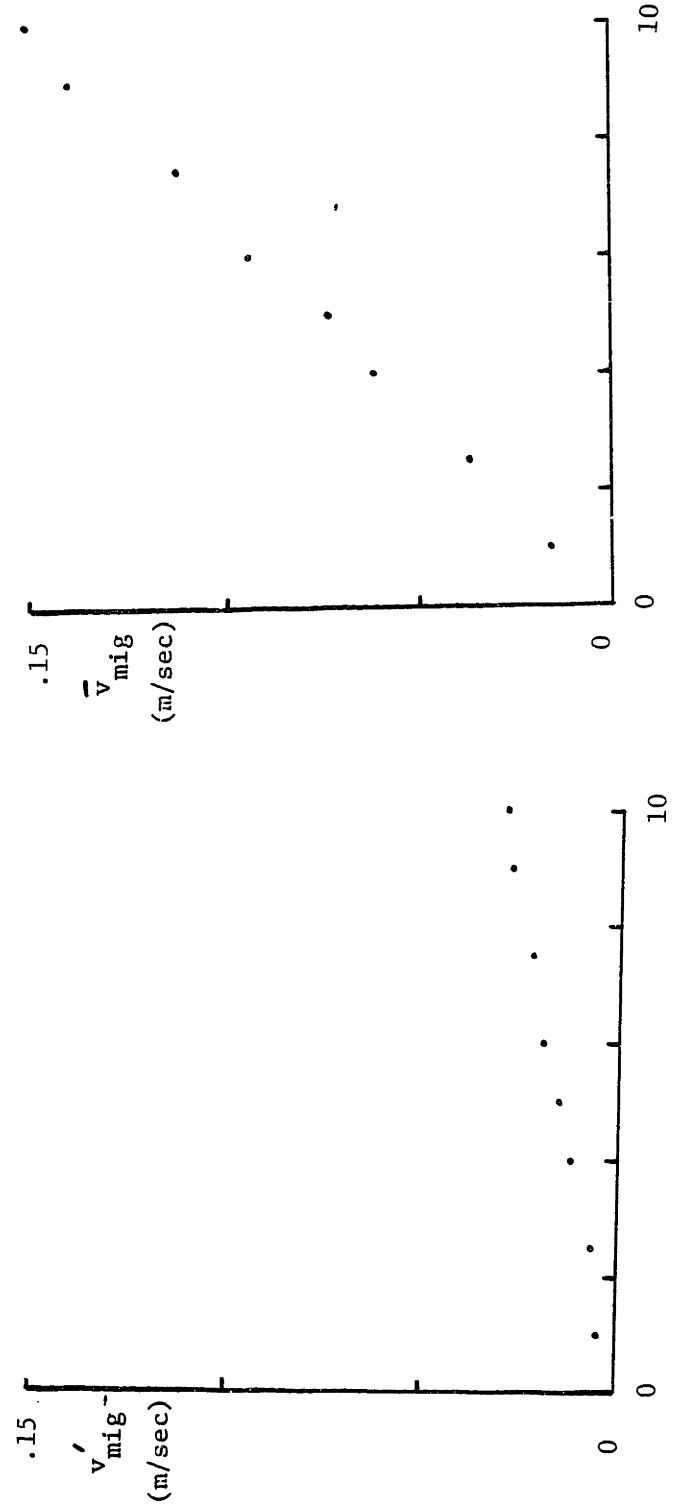

Fig. 5.20. Plots showing mean (b) and RMS spread (a) in particle migration velocity as a function of migration plate voltage. The corona wires were held at a constant potential of +7.95 kV for the test, giving a corona current of 0.75 ma. The horizontal flow rate was 1.5 m/sec. The LDV observation volume was 1¼ inch from the upstream edge of the migration plate. (Data from 9/23/83)

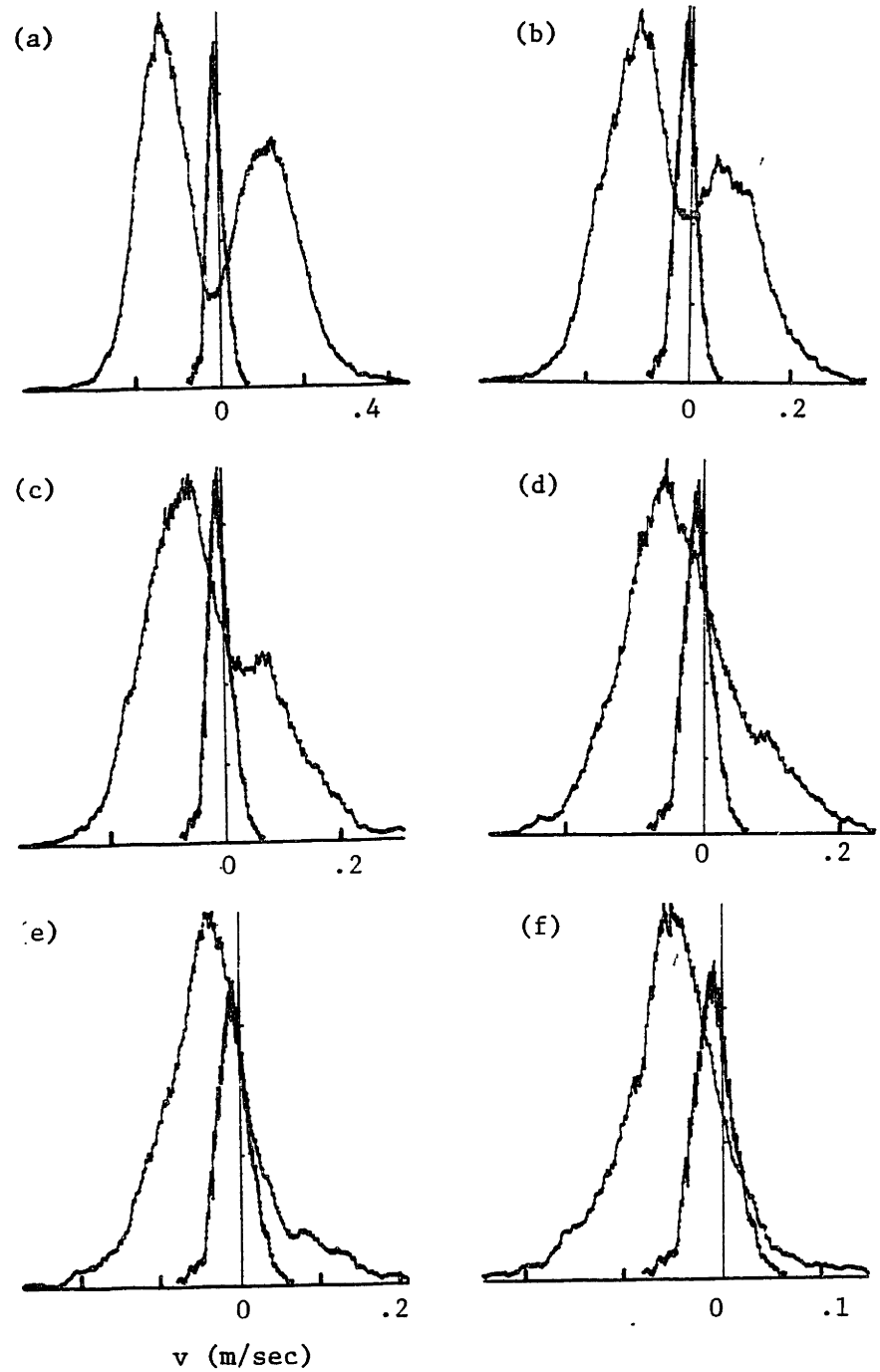

Fig. 5.21. Progression of vertical velocity distribution functions for AC wire-charging experiments. The RMS voltage applied to the corona wires was 8.0 kV, at frequencies of 30, 50, 80, 100, 125, 150 Hz for (a)-(f), respectively. The series blocking capacitor was present for these runs. The horizontal velocity was 2.5 m/sec. (Data from 10/11/83)

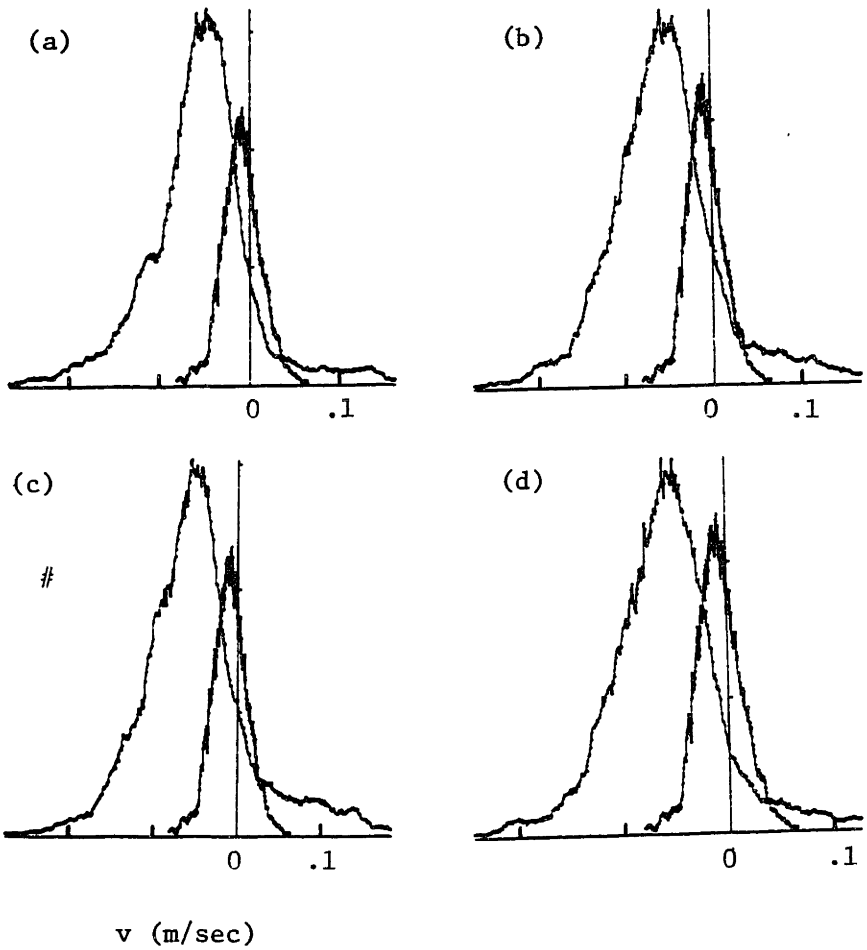

Fig. 5.22. Progression of vertical velocity distribution functions for AC wire-charging experiments. The RMS voltage applied to the corona wires was 8.0 kV, at frequencies of 200, 300, 400, 500 Hz, respectively. The series blocking capacitor was present for these runs. The horizontal flow velocity was 2.5 m/sec.

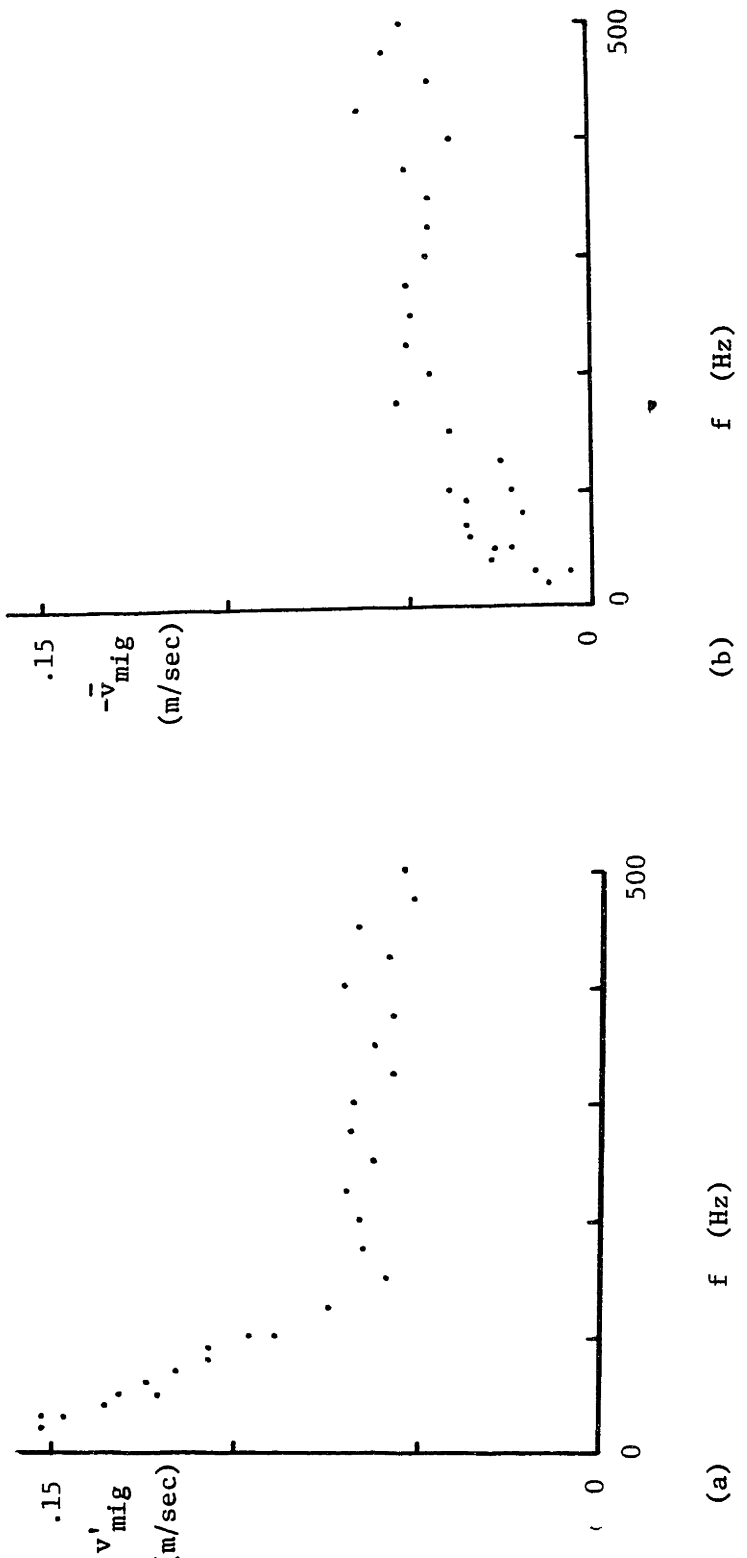

Fig. 5.23. Plots showing variation of mean (b) and RMS spread (a) of particle migration velocity as a function of corona excitation frequency for wire-charging experiments. The RMS corona voltage was 8.0 kV. The series blocking capacitor was present. The horizontal flow velocity was 2.5 m/sec. (Data from 10/11/83)

f (Hz)	Cap. in ?	v'_{mig} (m/sec)	$\bar{v}_{mig}$ (m/sec)
30	No	.218	.027
30	Yes	.196	.005
100	No	.153	.068
100	Yes	.141	.034
300	No	.077	.067
300	Yes	.067	.045

Table 5.2. Data from Barbed-wire charging experiments. Horizontal flow velocity was 2.5 m/sec. The RMS corona voltage used was 8 kV.

AC ELECTROSTATIC PRECIPITATION

by

RICHARD M. EHRLICH

S.B., Massachusetts Institute of Technology
(1977)

S.M., Massachusetts Institute of Technology
(1979)

Submitted in Partial Fulfillment

of the Requirements for the

Degree of

Doctor of Science

at the

Massachusetts Institute of Technology

March, 1984

Signature of Author.....
Department of Electrical Engineering and Computer Science,
March 21, 1984

Certified by.....
James R. Melcher
Thesis Supervisor

Accepted By.....
Arthur C. Smith
Chairman, Department Committee

5.4 Data Analysis and Modeling

In this section, the results of each of the various particle charging experiments are discussed separately. Crude models are proposed to account for the observed behavior. Section 5.4.1 estimates the order of magnitude for the mobilities expected from the pin-charging and wire-charging experiments, as well as the characteristic time-constant associated with the dynamic charging process. The upstream and downstream pin-charging experiments are examined in sections 5.4.2 and 5.4.3, respectively. Models for interpretation of the ion-precipitation experiments are proposed in section 5.4.4. Section 5.4.5 discusses the results from the wire-charging experiments. Conclusions, based upon the entire group of tests, are drawn in section 5.4.6.

5.4.1 Order of Magnitude Predictions of Charging

The particle mobilities expected from the charging measurements of section 5.3 can be determined crudely by the following order-of-magnitude argument. Equation (3.3.35) gives an expression for the migration velocity of a particle charged to saturation in an electric field of strength, (V/H). Denoting the field-strength by $V/H \equiv E_o$, the particle mobility is thus

$$b_{sat} = 2 \varepsilon_o R E_o / \eta \qquad (5.4.1)$$

Determination of the charging electric field strength would require the simultaneous solution of Gauss' law, Faraday's law [in the electroquasistatic limit], and the law of conservation of charge, subject to boundary conditions on the ion charge density at the wire and the electric potential at both electrodes. Such a solution is derived in appendix 4, for the simplified situation of steady-state radially-symmetric unipolar ion injection between concentric cylindrical shells. Given the total ion current, applied voltage, and parameters of the system [such as electrode radii and ion mobilities], the results of that appendix can be used to estimate the electric field strength in the vicinity of the non-ionizing electrode surface.

A parameter is defined there that characterizes the competition

between effects of the imposed voltage and those of space charge in determining the electric field strength.

$$Y^{-\frac{1}{2}} \equiv \frac{V_o/R_o}{\left(\frac{I_o/\ell}{2\pi\varepsilon_o b_i}\right)^{1/2}} \tag{5.4.2}$$

where V_o is the applied voltage, R_o is the radius of the outer cylindrical shell, I_o/ℓ is the ion current per unit length, and b_i is the mobility of the injected ions. For completeness, the radius of the inner cylinder is denoted by R_i.

It is shown in appendix 4 that, in the limit of a very small inner electrode, $R_i << R_o$, if $Y^{-\frac{1}{2}} \gtrsim 1$*, then the electric field strength at the outer electrode will be determined essentially by effects of the ion space charge.

$$E_o \gtrsim \left(\frac{I_o/\ell}{2\pi\varepsilon_o b_i}\right)^{1/2} \tag{5.4.3}$$

With $I_o = 2$ ma, $\ell = 3$ m, $b_i \gtrsim 10^{-4}$ m^2/v·sec, $R_o \simeq H = 1.5$ cm, and $V_o = 8$ kV, $Y \simeq 1.6$, and the electric field strength is $E_o \gtrsim 3.3 \times 10^5$ v/m. From eq. (1), $b_{sat} \gtrsim 1.7 \times 10^{-7}$ m^2/v·sec. This is a conservative estimate of the saturation mobility,[1] as it was obtained using the electric field that exists near the plate, not that in the vicinity of the corona source. The average voltage gradient, based upon the wire-plate spacing, H, and applied voltage, V_o, is about 5.3×10^5 v/m. The electric field strength in the vicinity of the wires should be significantly higher than this value.

The expected time-constant for the particle charging process can be similarly estimated. Equations (3.3.11), (3.3.12), and (3.3.42) define the charging time, τ_{ch}, in terms of an electric field strength ($E_o \equiv V_{\pm}/H$) and corona current density ($J_o \equiv i_{\pm}/A$). If the positive and negative fields and corona currents are assumed to be roughly equivalent, then the charging time can be estimated as

$$\tau_{ch} \gtrsim 8 \frac{\varepsilon_o E_o}{J_o} \tag{5.4.4}$$

---

*The meaning of the sign, "$\gtrsim$", is "of the order of, but greater than".

With the electrical excitation specified above, a corona current (from the wires) of 2 ma, plate area of 2250 cm^2 (15 cm by 75 cm for each of 2 plates), $J_o \backsim .009$ A/m^2, and

$$\tau_{ch} \backsim 2.7 \text{ msec} \qquad \text{(WIRES)} \qquad (5.4.5)$$

The value of τ_{ch} appropriate for the pin-charging experiments could be significantly different, as the corona was restricted to much smaller area than for the wires. The corona currents from the pins were of the order of 100 μA. If it is assumed that these currents were distributed over a length that is of the order of the pin-plate spacing, H = 1.5 cm, then $A \backsim 45$ cm^2, $J_o \backsim 0.02$ A/m^2, and

$$\tau_{ch} \backsim 1.2 \text{ msec} \qquad \text{(PINS)} \qquad (5.4.6)$$

5.4.2 Upstream Pin-Charging Experiments

It is apparent, from Fig. (5), that an asymmetry exists between positive and negative corona charging. Were it not for effects of ion space-charge, the imposed electric field strengths would be of the same magnitude for the two experiments reported there. Since the saturation charge of a particle depends only upon its size and the strength of the imposed electric field, it might be expected that the positive and negative excitations would give similar results.

The charging process is a dynamic one, in that it requires a finite time for the particle to acquire a saturation charge. Since the pins represent point sources of corona ions, it is likely that the particles spend only a short time in the presence of significant current densities. The corona currents for the positive and negative DC charging experiments of Fig. (5) were +41 μA and -85 μA, respectively. If the particles were not charged to saturation, then the resulting difference in charging rates could be significant in determining the particle charge levels. The data of Fig. (13) lends some support to this conjecture. The RMS spread in particle charge was affected by the imposed horizontal flow velocity, rising as the particles spent longer times in the vicinity of the pins*. A charging zone width of 5 mm was

used to scale the horizontal coordinate of that figure. If that width is correct, then it is seen that the particles reach a limiting charge in about 2 msec.

Even if the negative corona voltage is reduced so as to give current magnitude that is equal to that of the positive corona, however, it still charges particles to a higher level. With a DC corona voltage of -6.5 kV, corresponding to a current of -39 μA, the measured mean migration velocity was 0.167 m/sec. The magnitude of the velocity measured for the +8.0 kV DC corona voltage was 0.137 m/sec. Thus, the difference in the charging characteristics of positive and negative coronas cannot be explained by the higher current with the negative corona.

The disparity in the overall magnitude of response, as well as the "high-velocity tail" in Fig. (5b) imply that there exists a difference between the spatial distributions of the two coronas. If the negative corona had a smaller active region, so that particles could approach the ends of the pins more closely, for example, those particles would be subjected to more intense charging electric fields and corona currents

The dominance of the negative corona in charging particles is seen in the AC charging data of Figs. (7) and (8), as well. Even though the series blocking capacitor biased the voltage so as to supply equal amounts of positive and negative ion charge each half-cycle, the mean particle charge was negative for higher frequencies. The uniform-field charging models of chapter 3 predict that the mean particle charge will be of the same sign as the bias voltage (positive, in this case). In addition, the apparent leveling off of the RMS spread in particle charge for low excitation frequencies cannot be explained by the models of chapter 3[#]. For completeness, Fig. (24) shows a comparison of the

---

[*] AC corona charging at a frequency of 20 Hz was used. The half-cycle time of 25 msec is seen to be much smaller than the charging time of roughly 2 msec. Thus, the data of Fig. (13) can probably be examined in the same light as would be DC charging data.

[#] It should be noted that, for excitation frequencies below 40 Hz, the voltage waveform was somewhat distorted, appearing almost as a square-wave for 20 Hz experiments. This occurred due to saturation of the transformer and the high impedance of the blocking capacitors.

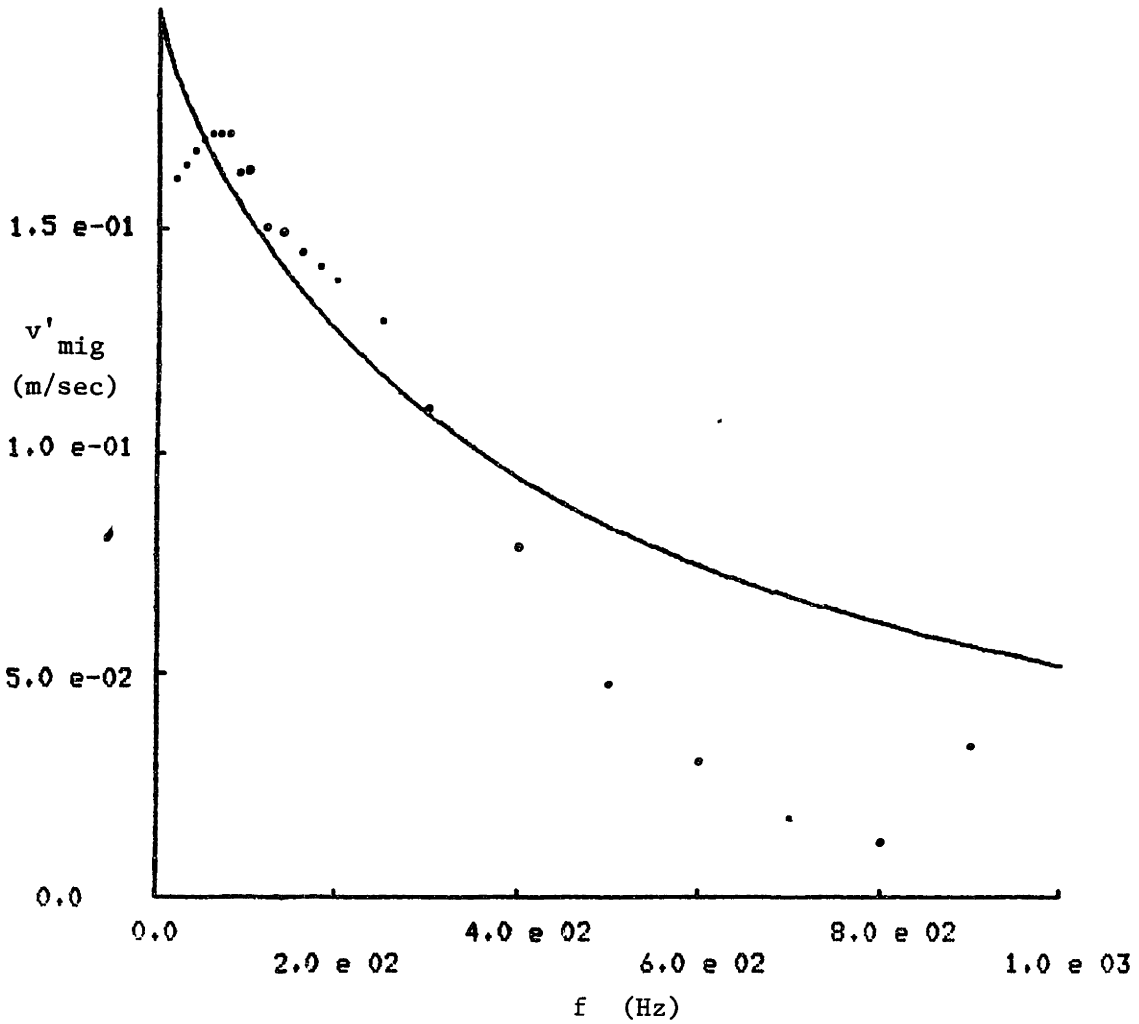

Fig. 5.24. Data from Fig. 8 [dots], with RMS spread in particle migration vs. frequency predicted by uniform-field charging model of Chapter 3 [solid line]. Model parameters used were $v_o = 0.2$ m/sec, $\tau_{ch} = 1$ m/sec.

predicted and measured RMS spread in particle migration velocity vs. excitation frequency, using the simplified universal precipitation model of chapter 3 [v_o = 0.2 m/sec, τ_{ch} = 1.0 msec], and the data of Fig. (8).

In view of the differences between the positive and negative DC corona charging characteristics, it is surprising that the bias charge with low-frequency AC excitations is as small as it is. In Figs. (8), (11), and (12), the low-frequency limit of the bias charge seems to be zero. It is possible that, for the higher voltages and currents encountered with AC charging at 8 kV RMS, the bias between positive and negative charging is less pronounced.

The data of Fig. (12) were included to show that the particle charge statistics did not change significantly as the flow convected them from the pins to the migration plate. Both the mean particle migration velocity and the RMS velocity spread remained relatively unchanged when the pins were moved from 4 cm to 75 cm upstream of the flow-straightener. The turbulent diffusivity measurements of chapter 6 make use of this fact.

5.4.3 Downstream Pin-Charging Experiments

The sign of the charging rate of a particle depends upon the sign of the ions in the vicinity of that particle. If only positive ions are present, the particle will either charge positively, or it will not charge at all, and vice versa for the negative case. If ions of both sign are present, then the charging (or discharging) rate will depend upon the relative ion densities and mobilities, as well as the local electric field strength.

In the special case of zero imposed electric field, with ions of both sign present,[#] the particle will discharge with a time-constant equal to the ion self-precipitation time, $\tau_{\pm}$, defined in eq. (3.2.1).

$$\tau_{\pm} = \frac{\varepsilon_o}{\rho_{\pm}\, b_{\pm}} \tag{5.4.7}$$

where the "+" sign is to be used if the particle is initially negatively

---

[#]It is assumed, here, that diffusional charging is negligible

charged, and vice versa. This can be seen from an separate application of eq. (3.3.13) to the two situations : (1) a charged particle immersed in ions of like sign with no electric field present, (2) a charged particle immersed in ions of opposite sign (again, with no electric field), and superposition of the two resultant charging rates. The particle will discharge exponentially with a characteristic time as given in eq. (7).

During the downstream pin-charging experiments, charged particles are mixed with ions from the pins that have been entrained into the flow. During the upstream pin-charging experiments, most ions that become entrained into the flow from the tips of the pins are precipitated by the intense corona electric field as they are convected past the pin bodies and support bar. In the former case, there is no imposed electric field downstream of the tips of the pins; only that due to the ion-charge, itself.

If the flow downstream of the pins were laminar (so that there would be no turbulent mixing), then positively charged particles would be in the presence of positive ions, and similarly for the negatively charged particles. Then, the particles would simply retain whatever charge they had had when they left the corona charging region. The flow in the experiment is turbulent, however, and mixes both particles and ions. The particles thus discharge with a time-constant determined by the density of oppositely charged ions about them.

The ion densities decay with distance downstream of the pins, due to effects of self-precipitation and recombination. Although both of these processes normally occur with time-scales[1] on the order of $\tau_{\pm}$, the decay is not exponential. A unipolar cloud of ions of initial density, ρ_o, with mobility, b_o, will spread with time so that $\rho(t)$ is given by

$$\rho(t) = \frac{\rho_o}{1 + t/\tau_o} \tag{5.4.8}$$

where

$$\tau_o = \frac{\varepsilon_o}{\rho_o b_o} \tag{5.4.9}$$

For very long times (ie., $t >> \tau_o$), $\rho(t)$ is approximated

$$\rho(t) \sim \frac{\varepsilon_o}{t\, b_o} \tag{5.4.10}$$

so that the particle discharge time given in eq. (7) becomes

$$\tau_{\pm} \sim t \tag{5.4.11}$$

If the initial ion charge density, ρ_o, is very large, so that τ_o is small, then the self precipitation time at a location downstream of the pins will be approximately equal to the transport time from the pins to the point in question.

The particles will be discharged by the entrained ions only if turbulent diffusion is able to mix particles of one charge with ions of the other before the latter are removed by the ion-trap. If the ion density gradients set up by the sinusoidal corona are eliminated by the time that the flow has moved roughly half of the distance from the pins to the trap, then the self precipitation time will be of the order of this time, and the particles will consequently be discharged by the time the ions are removed. Otherwise, the particles will retain a significant charge.

The turbulent diffusion time, based upon the separation between the pins and the ion trap, can be estimated using a value for the turbulent diffusivity, D_t, obtained from the measurements of chapter 6. With a separation of 2.9 cm, and $D_t \sim 10^{-3}$ m^2/sec, the diffusion time, τ_d, is roughly

$$\tau_d \sim 1 \text{ sec} \tag{5.4.12}$$

This is much longer than the convection time, based on this distance and a flow velocity of 2.5 m/sec.

$$\tau_c \sim 12 \text{ msec} \tag{5.4.13}$$

The particles are discharged significantly in that distance, as can be seen by a comparison of the two plots of Fig. (15). When the ion trap was moved from 5.9 cm to 2.9 cm downstream of the pins, the characteristic frequency of the charging process apparently doubled. Thus, it must be that much of the ion/particle mixing occurs in the immediate vicinity of the pins, due to the corona wind there. As was noted in section 5.3.2, the characteristic frequency was roughly equal to that at which one wavelength of the sinusoidal charge wave fit

between the pins and ion trap. For frequencies much lower than that, it would be expected that ion discharging of the particles could not occur to a significant extent, because most of the ions of one sign would be removed by the ion trap before oppositely particles were produced at the pins.

5.4.4 Ion Precipitation Experiments

These experiments were relatively straightforward, and their results require little interpretation. The major conclusions to be drawn from them are : (1) that the ion mobilities in the laboratory-scale precipitator are of the order of 5×10^{-5} $m^2/v \cdot sec$, and (2) that the negative ion mobilities are probably higher than those of the positive ions, but not by more than 20%.

It is interesting to note that, although the negative corona current magnitude was almost twice that of the positive corona, the precipitated currents shown in Fig. (17) were nearly equal for the two. This phenomenon can be explained using the analysis of section 5.4.3. The ion charge density at the ion trap will be essentially independent of its initial value (at the pins) as long as the self precipitation time at the pins is much shorter than the convection time to the trap. In fact, the current density at the trap can be estimated using eq. (10).

$$J_{trap} = \rho_{\pm} b_{\pm} E_{trap} \sim \frac{\varepsilon_o E_{trap}}{\tau_c} \qquad (5.4.14)$$

The convection time from the pins to the trap, τ_c, can be expressed in terms of the distance between the two, ℓ_{trap}, and the flow velocity, U.

$$J_{trap} \sim \frac{\varepsilon_o E_{trap} U}{\ell_{trap}} \qquad (5.4.15)$$

The trap length (in the flow direction) was of the same order as ℓ_{trap}. Thus, when no voltage was imposed at the ion trap, the density of ions at the outlet of the trap was roughly equivalent to that at the inlet. A crude estimate of the peak current to be expected from the experiment is obtained by assuming that, at that peak, the current density over the entire ground electrode of the ion trap is equal to J_{trap}. The current is thus

$$i_{trap} \sim \frac{\varepsilon_o A_{trap} V_{trap} U}{\ell_{trap} H} \tag{5.4.16}$$

The applied voltage is V_{trap}, the trap area is A_{trap}, and the trap is a distance, H, from the isolated ground electrodes. With $A_{trap} \sim 90$ cm^2 (15 cm by 6 cm), $\ell_{trap} \sim 6$ cm, H = 1.5 cm, the current will be

$$\frac{i_{trap}}{U\ V_{trap}} \sim 90\ \frac{nA}{kV\ m/sec} \tag{5.4.17}$$

With the 7.5 m/sec flow, the peak precipitated current was roughly 400 nA, obtained with a voltage of about 500 volts. The current predicted by eq. (17) is 340 nA.

5.4.5 Wire Charging and Barbed-Wire Charging Experiments

There were two major differences between the wire-charging and the upstream pin-charging experiments. They were: (1) the currents used in the former were over an order of magnitude greater, and (2) the positive and negative coronas were not restricted to the same general locations on the wires, while the pins constrained both to exist only at their tips.

The current density was slightly lower for the wire-charging experiments than it was with the pins (by a factor of about 2). The residence time in the former, however, was roughly 50 times greater. Even though particles were apparently charged nearly to saturation by the pin-charger, the long residence time should have allowed more particles to acquire a high charge with DC excitation, simply because there was a higher probability that a given particle would be carried very near to a wire by either a turbulent eddy or by a convection cell induced by the corona wind. Given a corona wind velocity of the order of 0.5 m/sec, a particle that was carried in a convection cell of diameter, H=1.5 cm would pass by the wire at the rate of 10 times per second. If the horizontal flow velocity was 2.5 m/sec, such convections would bring a particle by the wire 3 times before it exits the charger. Presumably, it could increase its charge during each cycle of its motion.

This is not the case for AC excitations, however, as the particles would not be carried by the wire more than once during a single cycle. Thus, the advantage of the longer residence time might not be expected

to offset the lower current density, relative to the pin-charging experiments.

Comparison of the DC charging data of Figs. (6) and (19) shows that the wires gave higher levels of charge than the pins did for all voltages except those near the turn-on voltage for positive corona. At the same time, the RMS spread in particle charge is about 25% smaller than with the pins when low frequency AC excitations are used. The higher frequency behavior is even more difficult to explain, as the bias is toward positive charging. The velocity distribution functions of Figs. (7) and (21) are nearly mirror images of one another. Where the positive charging hump disappears with increasing frequency in Fig. (7) [upstream pin charging], it is the negative one that is attenuated in Fig. (21) [wire charging].

Since the uniform-field charging model of chapter 3 was used to predict the results of the precipitation efficiency measurements of chapter 4, it is of interest to evaluate its accuracy in predicting the wire-charging statistics measured in this chapter. Fig. (25) shows the data of Fig. (23a), along with the predicted RMS spread in particle migration velocity, obtained from the uniform-field charging model of section 3.3. The DC migration velocity, v_o, was set equal to the average of the velocities measured with +8.0 kV and -8.0 kV DC charging, or roughly 19 cm/sec [see Fig. (19)]*. The time constant, τ_{ch}, was set equal to the 3.0 msec value used to fit the precipitation data in chapter 4. The error bars included about selected points in Fig. (25) give an indication of the level of confidence in their accuracy. Each represents a span above and below the point of one standard deviation in the measurement of the RMS spread in particle migration velocity. These errors were determined by splitting each data file (consisting of 2941 individual velocity measurements) into 5 sub-divisions, computing the corresponding statistics for each separately, and taking the standard

---

*This velocity is larger than the 5.6 cm/sec used in fitting the precipitation data. This can be explained, in part, by the fact that the imposed electric field above the migration plate was more intense than those in the vicinity of the plates for the single-stage precipitation experiments. This would not account for a difference of a factor of 3, however.

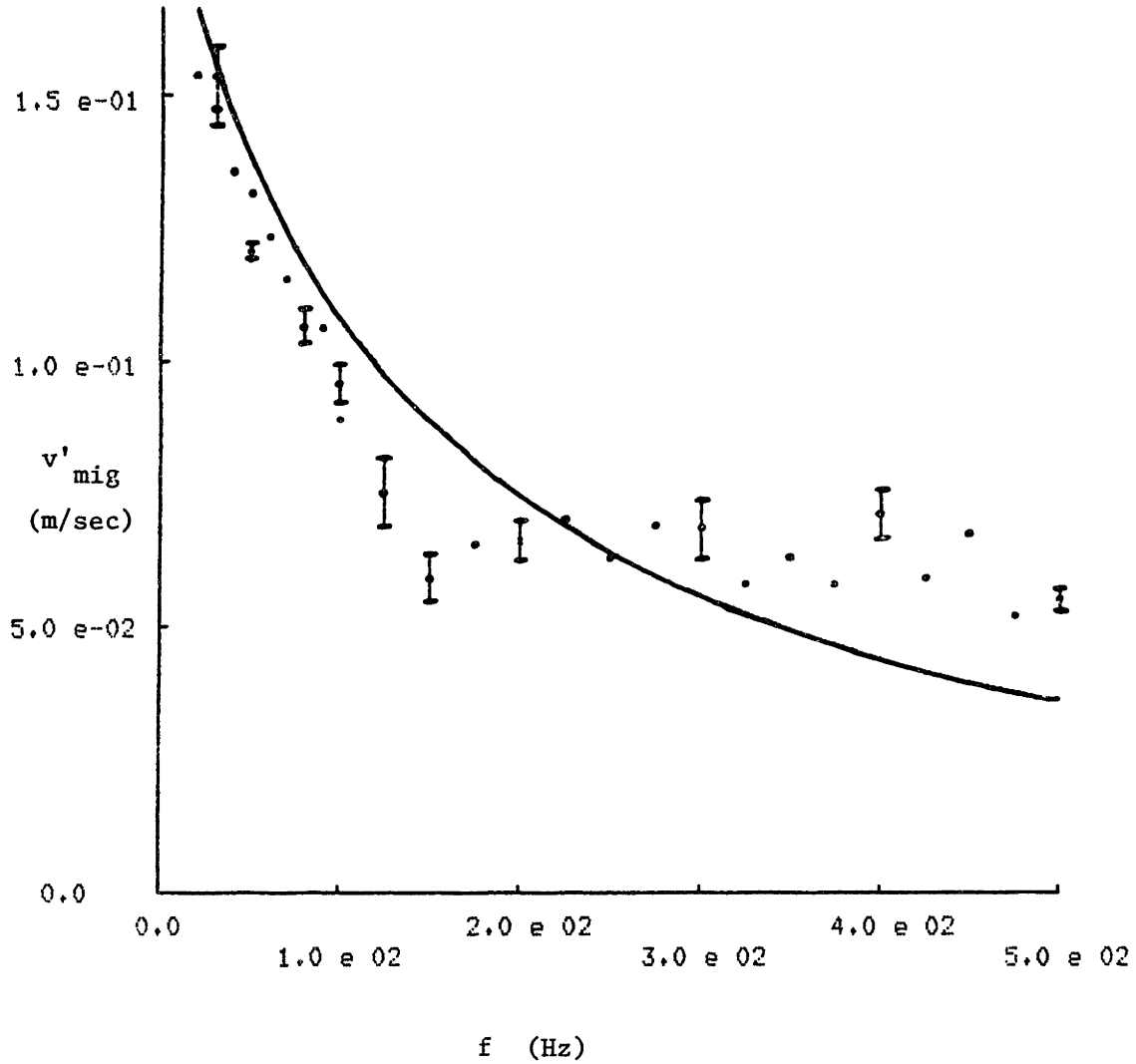

Fig. 5.25. Plot comparing predicted and measured RMS spread in particle migration velocity vs. AC excitation frequency. Data is from wire-charging experiments reported in Fig. (23). Error bars indicate ± 1 standard deviation from selected data points. Prediction is from uniform field charging model of Section 3.3 [v_o = 0.2 m/sec, τ_{ch} = 3.0 m/sec].

deviation of these 5 values. The fit is reasonably close for frequencies below 100 Hz. Had the DC velocity, v_o, been left as a fitting parameter, instead of being constrained by the measured DC data, the low-frequency fit would have been even closer.

The uniform-field charging model cannot predict the frequency dependence of the mean particle charge [shown in Fig. (23b)]. According to the rectangle-wave model of section 3.3, the normalized mean charge is a scaled version of the normalized time-average particle migration velocity, $\underline{w}_{net}$. Thus, that model would predict a mean particle charge that was a monotonically-decreasing function of the excitation frequency.

The results of the barbed wire charging experiments leave little doubt that it is the disparity the in distributions of the positive and negative coronas that causes the positive charging bias with the corona wires. The electric fields imposed by the thick barbed wires are similar to those of the thin wires alone, yet the two produce opposite biases in the mean particle charge with high frequency excitations. When the positive and negative coronas are restricted to similar macroscopic spatial distributions, the bias is toward negative charging, as it was with the pins.

5.4.6 Quasi-Steady Model for Particle Charging with Non-Uniform Corona Currents

This section presents a crude model for AC charging of particles which accounts for differences between the spatial distributions of the positive and negative coronas. It is intended more as an example of how such differences can bias the particle charging than as an accurate portrayal of the actual charging process. Therefore, gross simplifications are made in order to focus upon those features which are of immediate interest.

The situation is as pictured in Fig. (26). Particles enter the AC charger shown in Fig. (26a) at the left and are convected through it by a laminar air flow of velocity, U. The particles are subjected alternately to positive and negative corona ions in the presence of uniform electric fields. The applied voltage is of the form shown in Fig. (3.4), with $V_+ = V_- \equiv V_o$. The cycle time of the electrical

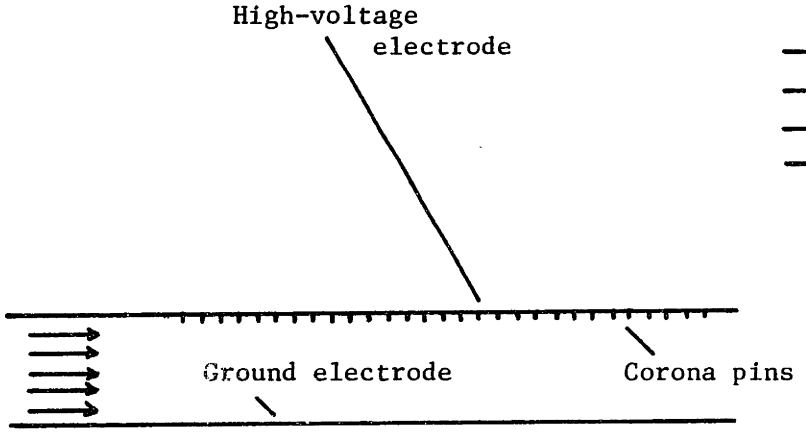

(a)

Side-view

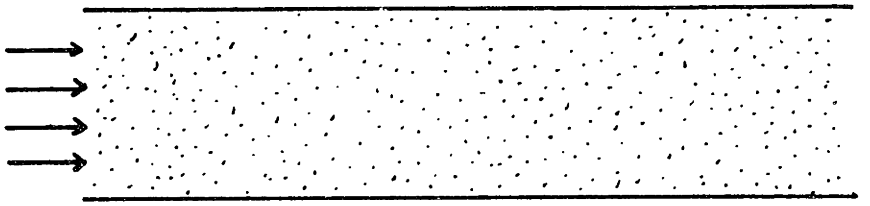

(b)

Top view, showing distribution of corona current during positive corona half-cycle. Corona fills entire charging region.

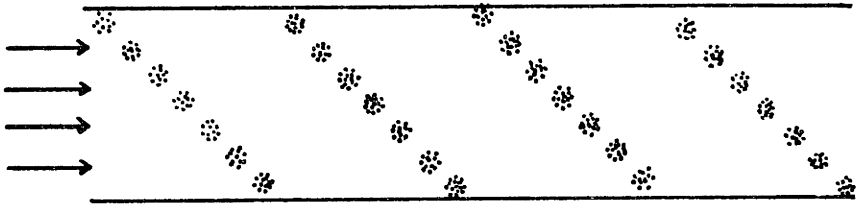

(c)

Top view, showing distribution of corona current during negative corona half-cycle. Corona is restricted to skewed lines of charging.

Fig. 5.26. Schematic problem illustration for quasisteady corona charging model of section 5.4.6. In (a) side-view of charger is shown.

excitation is $T \equiv 1/f$, where f is the excitation frequency. The voltage-current relations of the positive and negative coronas are such that no time-bias is needed to obtain zero time-average corona current (ie., each half-cycle is of duration, T/2). The spatial distributions of the two are very different, however. During the first half of each cycle, the entire charging region is filled with positive ions, as is illustrated by the dotted area in Fig. (26b). Figure (26c) shows the distribution of corona ions during the negative half of an electrical cycle. The charging is restricted to localized areas in the charger, which will be idealized as thin lines that are skewed, relative to the flow direction. The line separation in the flow direction is denoted by ℓ_{brush}, as it characterizes the spacing between the corona brushes in the actual wire-charging experiments. The lines are skewed in order to crudely simulate the effects of turbulent mixing in the charger. If a finite turbulent flow diffusivity were retained in the model, then the negative corona could be modeled by a series of localized sources, arranged in lines parallel to the flow, in much the same fashion as the discrete corona brushes that actually existed in the wire-charging experiments. With a laminar flow, however, this would allow particles which were convected along paths that passed between the the charging areas to escape negative charging altogether.

It is assumed that both the positive and negative coronas are intense enough to instantaneously* charge to saturation any exposed particles. This assumption is unrealistic for high-frequency charging, but is made in the interest of simplicity.

The particles that exit the charger are to be examined statistically. The quantity that is of greatest interest is the mean particle charge.

Because the positive corona fills the entire region, all of the particles exiting the charger will be charged to positive saturation for the total duration of each positive half-cycle. This saturation charge level will be denoted simply by $+q_o$. Immediately after a negative

---

*It is only necessary that the particles be charged in a time that is much smaller than the electrical cycle time, T, and that they be charged to saturation in the short time during which they cross a negative corona line

half-cycle starts, only those particles that are exposed to the corona very near to the outlet [ie., those particles at the lower right of Fig. (26c)] will be charged negatively. A critical time, τ_{brush}, is defined.

$$\tau_{brush} \equiv \frac{\ell_{brush}}{U} \tag{5.4.18}$$

Thus, τ_{brush} is the time that passes from the moment that a negative corona is initiated to the moment that all of the particles leaving the charger are charged negatively. The space-average particle charge, $\langle q(t)\rangle_{outlet}$, is defined as the particle charge averaged across the cross-section of the charger outlet. This quantity changes linearly with time, from $+q_o$ to $-q_o$, in the critical time, τ_{brush}.

Two cases must be considered separately here. If $T/2 > \tau_{brush}$ [or, equivalently, if $(f\tau_{brush}) < 1/2$], then the space-averaged particle charge, $\langle q(t)\rangle_{outlet}$, will be as shown in Fig. (27a). In that case, the time-average value of $\langle q(t)\rangle_{outlet}$ is

$$\frac{\bar{q}}{q_o} = f\tau_{brush} \tag{5.4.19}$$

For excitations that vary quickly enough that $T/2 < \tau_{brush}$ [so that $(f\tau_{brush}) > 1/2$], $\langle q(t)\rangle_{outlet}$ never reaches $-q_o$. Figure (27b) shows the variation of $\langle q(t)\rangle_{outlet}$ with time for such excitations. Then the time-average particle charge is

$$\frac{\bar{q}}{q_o} = 1 - \frac{1}{4(f\tau_{brush})} \tag{5.4.20}$$

The variation of $\bar{q}$ with the normalized excitation frequency, $(f\tau_{brush})$, is shown in Fig. (28). It is seen to have the same general behavior as that of the wire-charging experiments [Fig. (23)]. Given a brush spacing of 1 cm, and a flow velocity of 2 m/sec, $\tau_{brush} = 5$ msec, and the critical frequency, at which $(f\tau_{brush}) = 1/2$, is 100 Hz.

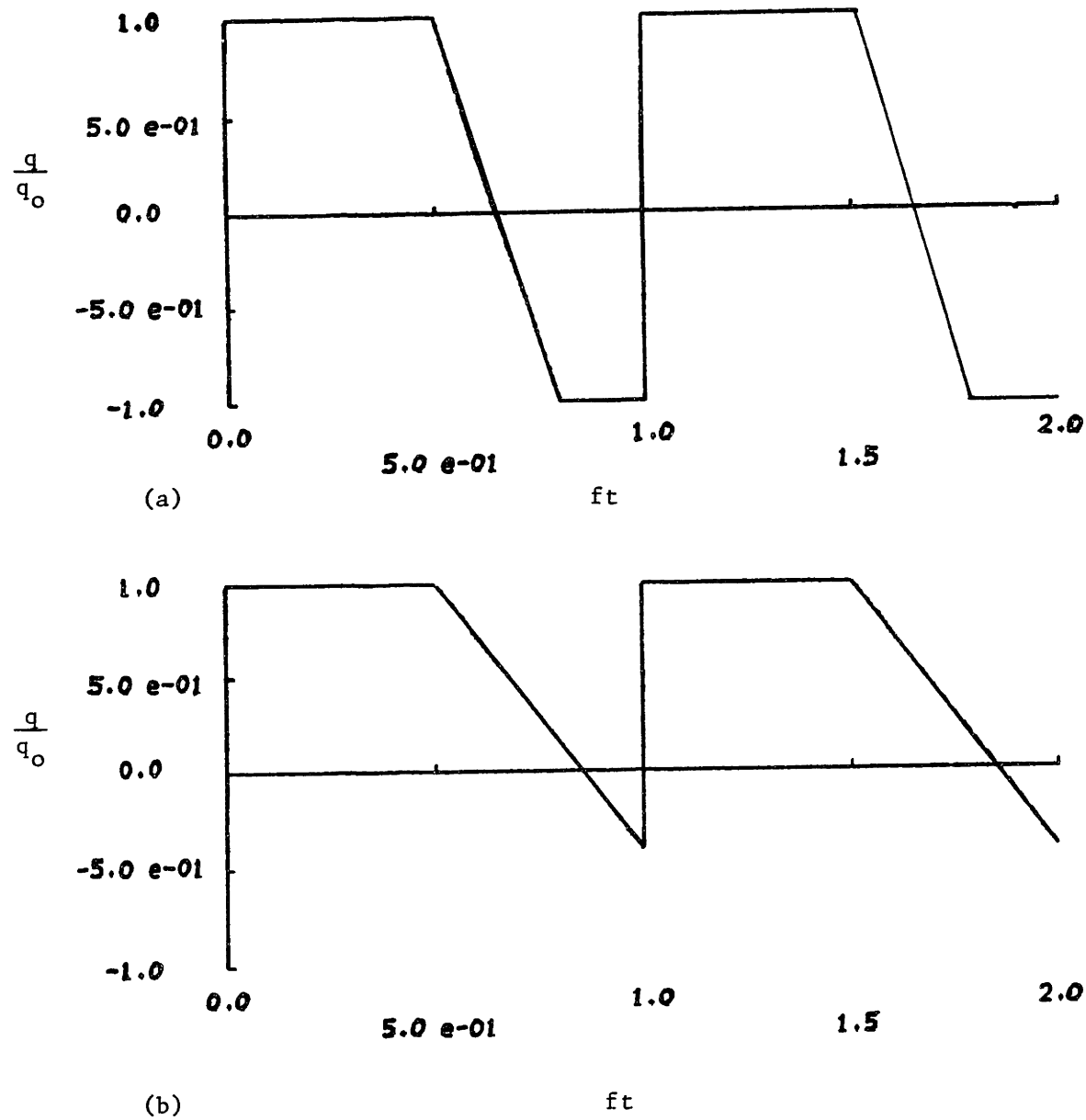

Fig. 5.27. Plots showing variation of <q(t)> outlet with normalized time. For (a), $(f\tau_{brush}) = 0.3$. For (b), $(f\tau_{brush}) = 0.714$. Two cycles of the excitation are shown in each case.

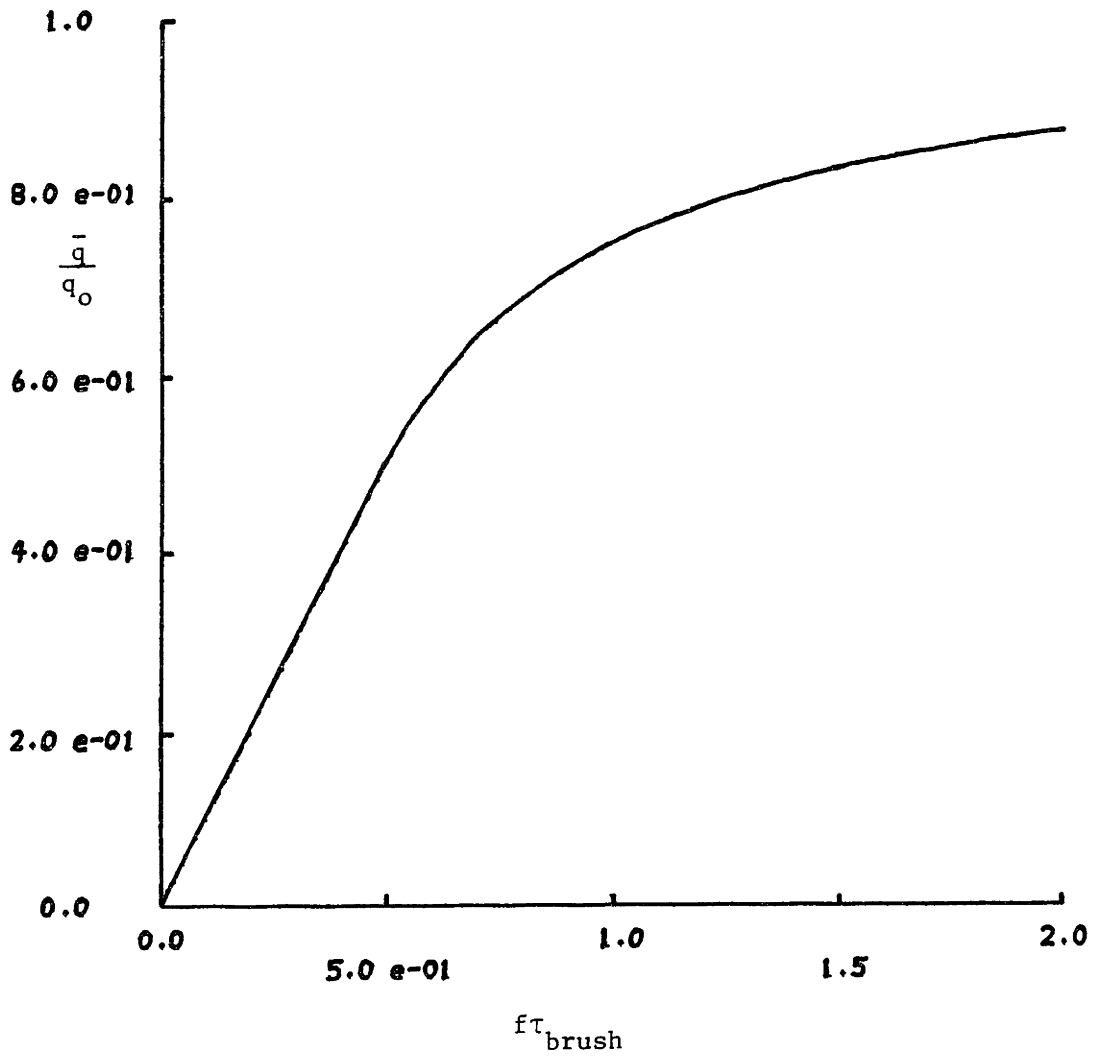

Fig. 5.28. Plot showing predicted normalized mean particle charge vs. normalized charging frequency, from quasisteady charging model of Section 5.4.6.

5.5 Conclusions

The direct measurement of particle mobility statistics by laser-doppler velocimetry can provide a wealth of information about corona charging processes. A large number of individual particle mobility measurements, each obtained by observation of the particle migration velocity in response to an imposed electric field, are combined to give an essentially continuous distribution function that is characteristic of the charging situation under examination. Although AC corona charging is the central focus of the experiments reported in this chapter, the general diagnostic technique should be useful in the evaluation of other charging schemes, such as those using pulsed coronas, for example.

This section summarizes the findings of the experiments and models presented in chapter 5. Section 5.5.1 discusses the general behavior of AC corona charging, in comparison to that observed with positive and negative DC excitations. An evaluation of the uniform field charging model of chapter 3, in light of the data of this chapter, is made in section 5.5.2.

5.5.1 Summary of Experimental Findings

Both positive and negative DC corona charging in the laboratory-scale precipitator gave mobilities that were of the order of 3×10^{-7} $m^2/v \cdot sec$ to 1 μm diameter particles. In the upstream pin-charging experiments, where the finite charging rate may have been a significant factor, the negative corona produced larger mobilities than positive coronas of either the same voltage or current magnitude. In the wire-charging experiments, where the particle residence time in the charger was relatively long, equal-magnitude positive and negative voltages resulted in mean particle mobilities that were roughly equal*. For both experiments, the velocity distribution functions obtained with $\pm$DC coronas imply that the negative corona is better able to achieve

---

*This was true for those voltages that were well above the turn-on level for positive coronas.

high particle mobilities, as evidenced by the "high-velocity tails" in Fig. (5b) and (16b).

Low-frequency AC charging in the laboratory-scale precipitator (ie., f < 50 Hz) can be characterized as a quasi-steady process. This is certainly to be expected with the pin-charging experiments, as the particle residence time in the vicinity of the pin tips is of the order of milliseconds. For those experiments, the spread in particle migration velocity for an AC excitation of a given RMS voltage magnitude was actually higher than the mean values obtained with ±DC voltages of that same magnitude[#]. Even with the wire-charging experiments, it is not surprising that the low-frequency behavior should approach that obtained with DC excitations. The ion transit time, based upon the dimensions and parameters of the experiments ($\sim$ 0.5 msec)[*] was much smaller than the excitation cycle time ($\sim$ 20 - 50 msec). The low-frequency AC velocity distribution functions of Figs. (7) and (19) resemble superpositions of the ±DC curves of Figs. (5) and (16). The characteristic "high-velocity tails", associated with negative charging, are discernable in both.

With higher-frequency AC excitations, the charging process is degraded, in that the magnitude and RMS spread in particle mobilities are smaller. The extent to which the individual positive and negative charging processes are seperately attenuated depends upon details of the charging configuration used. In the upstream pin-charging experiments, the negative corona proved superior for DC charging. It also dominated the charging process with high-frequency AC excitations, producing a sinificant bias toward negative particle charges. In the wire-charging experiments, where the two coronas were roughly equivalent for DC

[#]This could be due to the non-linear nature of the corona V-I characteristic. The peak voltage with the AC excitation was, of course, higher than the RMS voltage, resulting in intervals of considerably larger current densities. During these intervals, the particle charging may have proceeded much more quickly, more closely approaching saturation levels.

[*]As is noted in chapter 6, this time was estimated based upon the electric field strength which exists in the presence of a steady-state ion space-charge distribution. The transit time could be significantly longer ($\sim$ 1.5 msec) in the absence of the ion space charge, but still does not approach the half-cycle time for a 50 Hz AC excitation.

excitations, the high-frequency bias was toward positive charging. The experimental evidence presented in section 5.3 implies that this bias is caused by a disparity between the spatial distributions of positive and negative corona currents.

5.5.2 Evaluation of Uniform-Field Charging Model

In order for the uniform-field charging model to be strictly valid, both the charging electric field and the corona ion flux-density must be spatially uniform. This was not the case with the experiments reported in this chapter for several reasons: (1) The electrode configuration produced an electric field that had significant intensity gradients in a direction transverse to the main air flow*. In the case of DC wire-charging, the effect of the ion space charge was to make the field more uniform, but it was still significantly more intense near the wires than it was in the vicinity of the ground plates. (2) With negative DC wire charging, the ions were not emitted uniformly over the surface of the corona electrode. (3) The ion transit time (from wires to plates) was of the order of the half-cycle time for high-frequency AC excitations.

Thus, it is not surprising that this simplified model was unable to accurately predict the behavior of the corona charging process for high-frequency AC excitations. The only factor that it takes into account in modeling the degradation in particle charging with increasing excitation frequency is the finite particle charging rate. There are several other factors that could become important in determining the charging characteristics at high frequencies; the quasi-steady charging model of section 5.4.6 only suggests one possibility. For example, the finite ion migration velocities could prevent ions from reaching all points in the charging region within one half-cycle time of the excitation. Another possible explaination is that the structures of the coronas, themselves, change with the excitation frequency.

Lawless[2] suggested the use of a uniform-field charging model to

---

*It was noted in chapter 1 that a non-uniform electric field intensity is necessary in order to obtain a stable corona

predict DC corona charging of particles in a precipitator [see section 1.5.1]. It is seen in Fig. (25) that the model is able to predict, roughly, the RMS spread in particle migration velocity for low frequency AC excitations in the wire-charging experiments. It does not, however, accurately predict the mean particle migration velocity, having a frequency dependence that is almost opposite to that of the data [see Fig. (23) for data, Fig. (3.6) and eq. (3.3.45) for model]. At higher frequencies, the model predictions of both mean charge and RMS spread in charge deviate significantly from the corresponding experimental data presented in this chapter. Further experimentation and/or modeling is necessary in order to determine which (if any) of the factors discussed above should be included in the model to account for the observed behavior.

References for Chapter 5

[1] Melcher J.R., Continuum Electromechanics, MIT Press, Cambridge, Mass. (1981).

[2] Lawless P.A., Damle A.S., Viner A.S., Shaughnessy E.J., Sparks L.E., "Laser Doppler Anemometer Measurements of Particle Velocity in a Laboratory Precipitator", Third Symposium on the Transfer and Utilization of Particulate Control Technology: Volume II (Electrostatic Precipitators), p. 25 (July, 1982).

Chapter 6

Measurements of Corona Wind and Turbulent Mixing

6.1 Introduction

Turbulent mixing has an important influence on almost every process occurring inside a precipitator. That it can be the dominant particle transport mechanism in the bulk flow is seen by a comparison of characteristic diffusion and migration times based on the plate separation in the laboratory-scale precipitator. The migration time, $\tau_m \backsim 270$ msec, is estimated from precipitation data in chapter 4 [eq. (4.5.4)]. The diffusion time, $\tau_d \backsim 75$ msec, is obtained using measurements that are documented in this chapter [eq. (4.5.2)]. Another useful comparison can be made between the peak particle migration velocities measured in chapter 5 ($v_m \backsim 0.2$ m/sec)* and typical turbulent velocity fluctuations reported here ($v' \backsim 0.1$ m/sec). Measured corona wind velocities ranged up to an order of magnitude higher than the latter value ($\backsim$ 1 m/sec). In the bulk flow, fluid convection can compete with migration as a means of transporting particles toward (or away from) the plates.

The only mechanism of particle transport across the linear sub-boundary layer at the collection plates is migration. However, the particle charge (and, hence, its migration velocity) is influenced by its history of proximity to the corona wires. Therefore, even precipitation of particles from the outer edge of the core flow is at least indirectly influenced by turbulent mixing.

This chapter documents experiments that were performed to characterize the air-flow in the laboratory-scale precipitator, both with and without corona excitation present. These experiments were

---

*It should be noted that these migration velocities were measured in the second stage of the laboratory-scale precipitator, where the electric field strength was significantly higher than it was near the ground plates in the charging region [$\backsim 6 \times 10^5$ v/m in the former, as opposed to $\backsim 3 \times 10^5$ v/m in the latter].

performed with two objectives in mind. The primary reason for the turbulent mixing measurements was simply to provide parameters for the turbulent diffusion model of chapter 4. However, the corona wind, induced by electric field forces on the corona ions, is of interest in itself. Numerous transverse particle velocity measurements are reported with corona present, to determine the spatial and temporal dependences of the corona wind. Finally, for completeness, measurements of horizontal velocities and some velocity profiles (with no corona present) are reported as well.

The experiments which were performed to estimate the effective diffusivity of the flow in the laboratory-scale precipitator are described in section 6.2. In these experiments, the longitudinal mixing in the flow was actually measured. It is assumed that the transverse and longitudinal diffusivities are roughly equivalent. The experimental data is reported in that section as well. A simple diffusion model is proposed in section 6.3, to allow computation of equivalent turbulent diffusion coefficients from the data of the previous sub-section. The model is applied to the data in section 6.4. The corona wind measurement experiments are described in section 6.5, and the data from them is reported in 6.6. Section 6.7 contains the remaining miscellaneous flow velocity measurements. Conclusions, based upon the models and measurements, are drawn in section 6.8.

6.2 Turbulent Diffusivity Measurements

6.2.1 Description of Experiment

The experimental setup and procedure used in the diffusivity measurements is identical to that used for the AC "upstream pin-charging" experiments of chapter 5 [Fig (5.4)]. In fact, were it not for the different ranges of voltages and frequencies used in the two experiments, they could have been done simultaneously. The major difference between the two lies in the data reduction techniques used. In chapter 5, only time-independent statistical quantities, such as the mean and RMS spread of the migration velocity, or the total transverse velocity distribution function, were interpreted. Neither the velocity vs. time plots, nor their Fourier transforms were used, as turbulent mixing downstream of the pins partially destroyed the coherence of the AC charging waveform. It is precisely this decay in the coherence of the particle charge waveform that is to be measured here.

It is assumed, for the purposes of the diffusivity computation, that the particles leave the charging region with a mobility that varies (from particle to particle) sinusoidally with time, at the frequency of the corona excitation. Thus, if the migration plate could be placed immediately downstream of the pins without disturbing the charging process or the flow, the measured transverse particle velocity would be sinusoidal as well (with superimposed turbulent velocity fluctuations).

As the flow proceeds downstream, turbulent mixing introduces progressively greater amounts of disorder into the sequence of particle charges. It is assumed that the charge and identity of each particle remains unaltered; only their ordering changes. That assumption is partially substantiated by the charging statistics reported in chapter 5 for upstream pin-charging from various locations in the tunnel [see Fig. (5.12), for example]. It is argued in section (6.3) that self-precipitation and recombination of particles in the precipitator take place over time scales that are long compared to the gas residence time. Thus, it is reasonable to assume that the sole effect of the turbulence on the particles is to alter their relative spatial ordering.

The particles eventually pass through the migration region, where

velocity/time information is measured. If the particle charge were truly a sinusoidal function of time, then the Fourier component of velocity at the charging frequency would be exactly equal to $\sqrt{2}$ times the RMS spread in velocity. Thus, the ratio

$$\gamma \equiv \frac{v_{f_{exc}}}{\sqrt{2}v'} \tag{6.2.1}$$

where $v_{f_{exc}}$ is the Fourier component of particle velocity at the excitation frequency, f_{exc}, and v' is the RMS velocity spread for the same data point, is taken as a measure of the decay in coherence due to turbulence [ie., $\gamma = 1$ if no decay has taken place]. In the following section, a relationship is derived between the decay factor, γ, the effective diffusivity, D_t, and other physical parameters of the flow (the flow velocity, U, tunnel length, L, and excitation frequency, ω). Both the RMS spread of the velocity and its Fourier component at the charging frequency can be obtained from the same data file. Thus, a single run of (2941) velocity measurements can be used, along with the above-mentioned parameters, to determine the effective diffusivity of the flow. As a practical matter, the variation of this decay factor with location downstream of the pins was used to estimate the effective diffusivity of the flow. Measurements were made with the pins in either of two positions, referred to hereafter as "near" (for "near to the flow-straightener") and "far" (for "far from the flow-straightener"). For the "far" measurements, the pins were placed as shown in Fig. (4.4), about 75 cm upstream of the flow-straightener. For the "near" measurements, the pins were placed very close to the flow-straightener. The upstream edge of the flow-straightener, itself, was about 25 cm from the LDV observation volume. above the migration plate. The ratio between decay factors, γ, with the pins in the two different locations was taken as a measure of the decay that took place in the 75 cm length of the tunnel that extended between the two pin positions. This gave a more reliable measure* of D_t for two reasons: (1) The particle charging was

---

*The technique described here is more reliable than simply using a single measurement of γ (at one location) to determine the diffusivity, D_t.

most likely not sinusoidal in time, and (2) The mixing region did not have uniform flow properties along its entire length. The flow straightener and migration plate caused significant disturbances in the flow over the last 25 cm of the mixing region. If it is assumed that the mixing process was linear, then comparison of the Fourier component of particle velocity at the two locations should eliminate biases due either to non-sinusoidal particle charging or to the mixing that took place downstream of the "near" pin position.

Figure (1) illustrates idealized typical progressions of particle velocity vs. time for locations immediately after the charger (1a) and for points progressively farther downstream [(1c), (1e)]. The Fourier transforms corresponding to these velocity sets are in (1b), (1d), and (1f), respectively. Note that the same particle velocity statistics are valid at all three locations, only the ordering is changed by the turbulent mixing. The Fourier component at the base frequency, however, shrinks as the coherence of the particle ordering decays. The velocity plots of Fig. (1) were generated by beginning with a sinusoidal velocity function, sampled at equal intervals, and adding a random component to the time of each data point. In this way, the velocity statistics were preserved. The Fourier transforms were generated by the same programs that were used to analyze the data presented in this section.

6.2.2 Experimental Data

Tables 6.1 - 6.3 contain all of the relevant data for experiments performed to measure the effective flow diffusivity. Eight columns of data appear in Tables 6.1 and 6.2. The first is the name of a computer file in which the actual LDV data resides. The date of the measurement can also be determined from the filename, being contained in the last four digits before the decimal point ("1029" refers to 10/29, or October 29'th). The second and third columns give the horizontal flow velocity and charging frequency, U and f, respectively. The fourth column, labeled "pin loc.", refers to the location of the charging pins, as described in section 6.2.1. As the first four experiments reported in table 6.1 were performed without a series blocking capacitor [see chapter 2, Fig. (2.1)], a column is included to indicate whether the

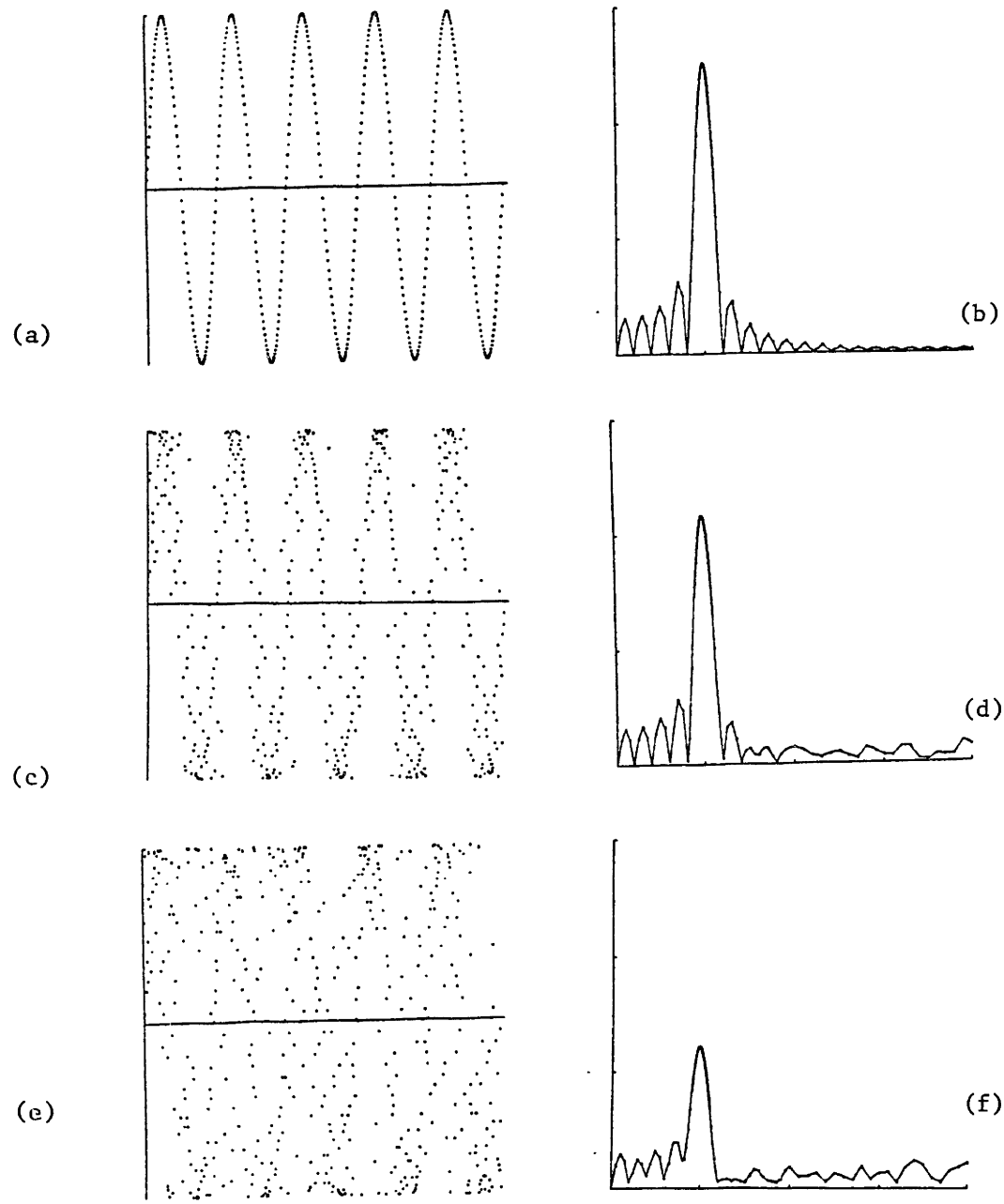

Fig. 6.1. Typical progression of particle migration velocity vs. time immediately downstream of the charger (a), and points further downstream [(c),(e)]. Fourier transforms corresponding to the velocity functions are shown in (b), (d) and (f).

filename	U $\frac{m}{sec}$	f Hz	pin loc.	cap.?	v'_{mig} $\frac{m}{sec}$	$\lvert v_{f_{exc}} \rvert$ $\frac{m}{sec}$	γ
ld1029.001	2.5	29.2	far	no	.157	.0276	.124
ld1029.004	2.5	50	far	no	.167	-	-
ld1110.003	2.5	29.6	near	no	.113	.0536	.335
ld1110.004	2.5	29.4	near	no	.112	.0772	.486
ld1111.006	4.3	29.9	near	yes	.148	.0814	.389
ld1111.007	4.3	29.5	near	yes	.146	.0994	.481
ld1111.008	4.3	48.3	near	yes	.160	.0593	.262
ld1111.009	4.3	76.5	near	yes	.154	.0380	.174
ld1111.010	4.3	92.8	near	yes	.153	.0231	.107
ld1112.006	2.5	29.2	near	yes	.161	.0653	.287
ld1112.007	2.5	29.8	near	yes	.164	.0405	.175
ld1112.009	2.5	39.0	near	yes	.167	.0263	.111
ld1112.010	2.5	48.4	near	yes	.170	.0158	.066
ld1112.011	2.5	57.5	near	yes	.171	.0238	.098
ld1113.005	4.3	29.1	far	yes	.137	.0271	.140
ld1113.006	4.3	29.9	far	yes	.144	-	-
ld1116.001	2.5	29.2	far	yes	.136	.0216	.112
ld1116.003	2.5	30	far	yes	.145	-	-
ld1118.003	7.5	29.4	far	yes	.105	.0841	.566
ld1118.004	7.5	29.9	far	yes	.115	.0432	.266
ld1118.005	7.5	48.2	far	yes	.108	.0288	.189
ld1118.006	7.5	82.8	far	yes	.127	.0150	.084
ld1118.007	7.5	100	far	yes	.107	-	-
ld1121.003	7.5	29.4	near	yes	.119	.1226	.729
ld1121.004	7.5	29.8	near	yes	.119	.1270	.755
ld1121.005	7.5	39.1	near	yes	.123	.1136	.653
ld1121.006	7.5	48.2	near	yes	.128	.0891	.492
ld1121.007	7.5	57.6	near	yes	.119	.0825	.491
ld1127.008	7.5	67.1	near	yes	.125	.0811	.459
ld1121.009	7.5	76.4	near	yes	.123	.0866	.498
ld1121.010	7.5	85.7	near	yes	.127	.0693	.386
ld1121.011	7.5	95.2	near	yes	.119	.0523	.310
ld1129.003	7.5	29.2	far	yes	.112	.0478	.302
ld1129.005	7.5	29.8	far	yes	.125	.0409	.231
ld1129.017	7.5	25.0	far	yes	.137	.0613	.316
ld1129.018	7.5	35	far	yes	.127	-	-

Table 6.1. Summary of Data from Turbulent Diffusivity measurements. All experiments were run with a transverse horizontal position of approximately 0 cm.

filename	U $\frac{m}{sec}$	f Hz	pin loc.	cap.?	v'_{mig} $\frac{m}{sec}$	$\lvert v_{f_{exc}} \rvert$ $\frac{m}{sec}$	γ
ld0303.003	7.5	20.32	far	yes	.123	.0752	.432
ld0303.004	7.5	20.32	far	yes	.121	.0670	.391
ld0303.006	7.5	48.20	far	yes	.134	.0254	.134
ld0303.007	7.5	73.92	far	yes	.131	.0199	.107
ld0303.008	7.5	29.70	far	yes	.126	.0565	.317
ld0303.010	7.5	29.88	far	yes	.125	.0397	.215
ld0303.011	7.5	29.76	far	yes	.128	.0360	.199
ld0303.012	7.5	25.15	far	yes	.127	.0536	.298
ld0303.013	7.5	39.20	far	yes	.127	.0237	.132
ld0303.014	7.5	34.58	far	yes	.129	.0277	.152
ld0303.016	7.5	43.65	far	yes	.135	.0233	.106
ld0303.017	7.5	52.91	far	yes	.133	.0309	.164
ld0303.018	7.5	56.28	far	yes	.139	.0186	.095
ld0303.020	7.5	57.72	far	yes	.129	.0194	.106
ld0303.023	7.5	58.08	far	yes	.136	.0312	.162
ld0303.024	7.5	25.15	far	yes	.113	.0569	.356
ld0303.026	7.5	20.32	far	yes	.131	.0671	.362
ld0303.027	7.5	20.32	far	yes	.130	.0699	.380
ld0303.028	7.5	29.76	far	yes	.138	.0501	.257
ld0303.030	7.5	20.32	far	yes	.159	.1674	.744
ld0303.031	7.5	39.04	far	yes	.141	.1383	.694
ld0303.032	7.5	57.72	far	yes	.149	.1066	.506
ld0303.033	7.5	76.32	far	yes	.152	.0840	.391
ld0303.034	7.5	95.20	far	yes	.148	.0752	.359
ld0303.037	7.5	29.76	far	yes	.144	.1485	.729
ld0303.038	7.5	48.40	far	yes	.142	.1219	.607
ld0303.039	7.5	67.06	far	yes	.141	.0865	.434
ld0303.040	7.5	85.50	far	yes	.150	.0783	.369
ld0303.041	7.5	104.72	far	yes	.151	.0770	.360
ld0303.043	7.5	25.00	far	yes	.140	.1487	.751
ld0303.044	7.5	34.44	far	yes	.150	.1472	.694
ld0303.045	7.5	43.83	far	yes	.141	.1185	.594
ld0303.046	7.5	52.91	far	yes	.153	.1218	.563
ld0303.047	7.5	20.36	far	yes	.154	.1565	.719

Table 6.2 Summary of Data from Turbulent Diffusivity measurements. Experiments were run with transverse horizontal positions that ranged from roughly -1.0 cm to 0.0 cm.

filename	Tansverse Horiz. Pos. mm	v'_{mig} $\frac{m}{sec}$	$\lvert v_{f_{exc}} \rvert$ $\frac{m}{sec}$	γ
1d1130.002	-5.08	.099	.0500	.357
1d1130.004	-1.27	.108	.0617	.404
1d1130.006	2.54	.115	.0642	.395
1d1130.007	3.81	.113	.0623	.390
1d1130.008	2.54	.127	.0556	.310
1d1130.009	-2.54	.115	.0633	.389
1d1130.011	-7.62	.124	.0548	.312
1d1130.012	-12.70	.117	.0538	.325
1d1130.013	-8.89	.113	.0642	.402
1d1130.014	-5.08	.133	.0580	.308
1d1130.015	-16.51	.134	.0439	.232
1d1130.017	-5.08	.122	.0631	.366

Table 6.3 Summary of Data from turbulent diffusivity measurements. All experiments were run with AC excitation at approximately 20 Hz. The horizontal flow velocity was 7.5 m/sec. The corona pins were far from the migration plate. The transverse horizontal position was measured relative to the approximate transverse position of the second corona wire from the photomultiplier side (The wire was not present for these measurements).

voltage or current was biased. If the entry in the column marked ,"cap.?", contains a "yes", the series blocking capacitor was present, the voltage was biased, and the time-average corona current was zero. If it contains a "no", then the voltage was unbiased, and a (negative) time-average corona current existed.

The next two columns contain the RMS spread in measured particle migration velocity, v'_{mig}, and the Fourier component of the velocity at the charging frequency, $\left| v_{f_{exc}} \right|$, respectively. The decay coefficient, γ, defined in eq. (6.2.1), is in the last column.

All of the measurements reported in Table 6.1 were obtained with the LDV observation volume at a single location. For the measurements reported in table 6.2, the LDV observation volume was relocated each time the tunnel was cleaned*. Its position was set so as to minimize the mean and RMS spread of measured particle velocity when no voltage was applied to the migration plate (ideally, the there would be no mean and no spread in the particle velocity under these conditions). For the data of Table 6.3, the electrical and flow conditions were fixed, and the LDV observation volume was moved to various transverse horizontal locations. The model of section 6.3 assumes uniformity of the particle mixing in the transverse directions, and thus would predict no variation in the measured results with the transverse horizontal position of the LDV observation volume. The fact that some variations were observed indicates that local flow conditions (most likely, due either to the flow-straightener or to the migration plate) had some effect on the particle mixing.

Figures (2) and (3) contain examples of Fourier transforms from the LDV data files, ld1029.001 and ld1112.006, respectively. They both correspond to measurements made with a horizontal flow velocity of 2.5 m/sec and an electrical excitation frequency of roughly 20 Hz. The first one (ld1029.001) was run with the pins far away from the flow-straightener, and the second one (ld1112.006) had them close. Although the RMS spread in the particle migration velocity was nearly the same for both (see Table 6.1), the Fourier component of velocity at the charging frequency is obviously much lower for the former. The peak

---

*The glass walls were cleaned approximately once in every 5 - 10 runs.

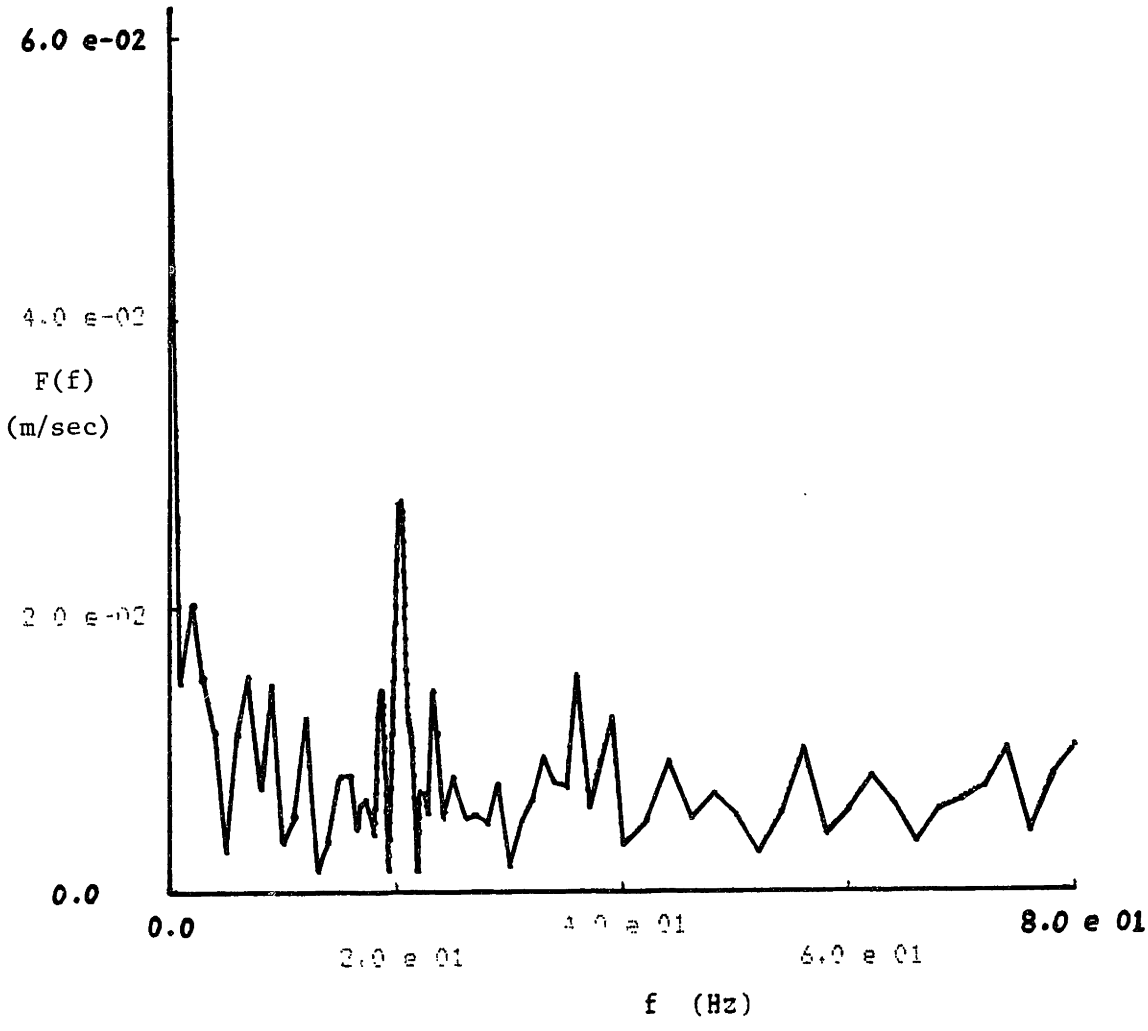

Figure 6.2. Fourier transform of transverse particle velocity.
The data is from the file, 1dl029.001.
The excitation frequency was approximately 20 Hz.
The series blocking capacitor was not present.
The corona pins were far from the migration plate.
The horizontal flow velocity was 2.5 m/sec.
The RMS velocity spread was approximately
15.7 cm/sec.

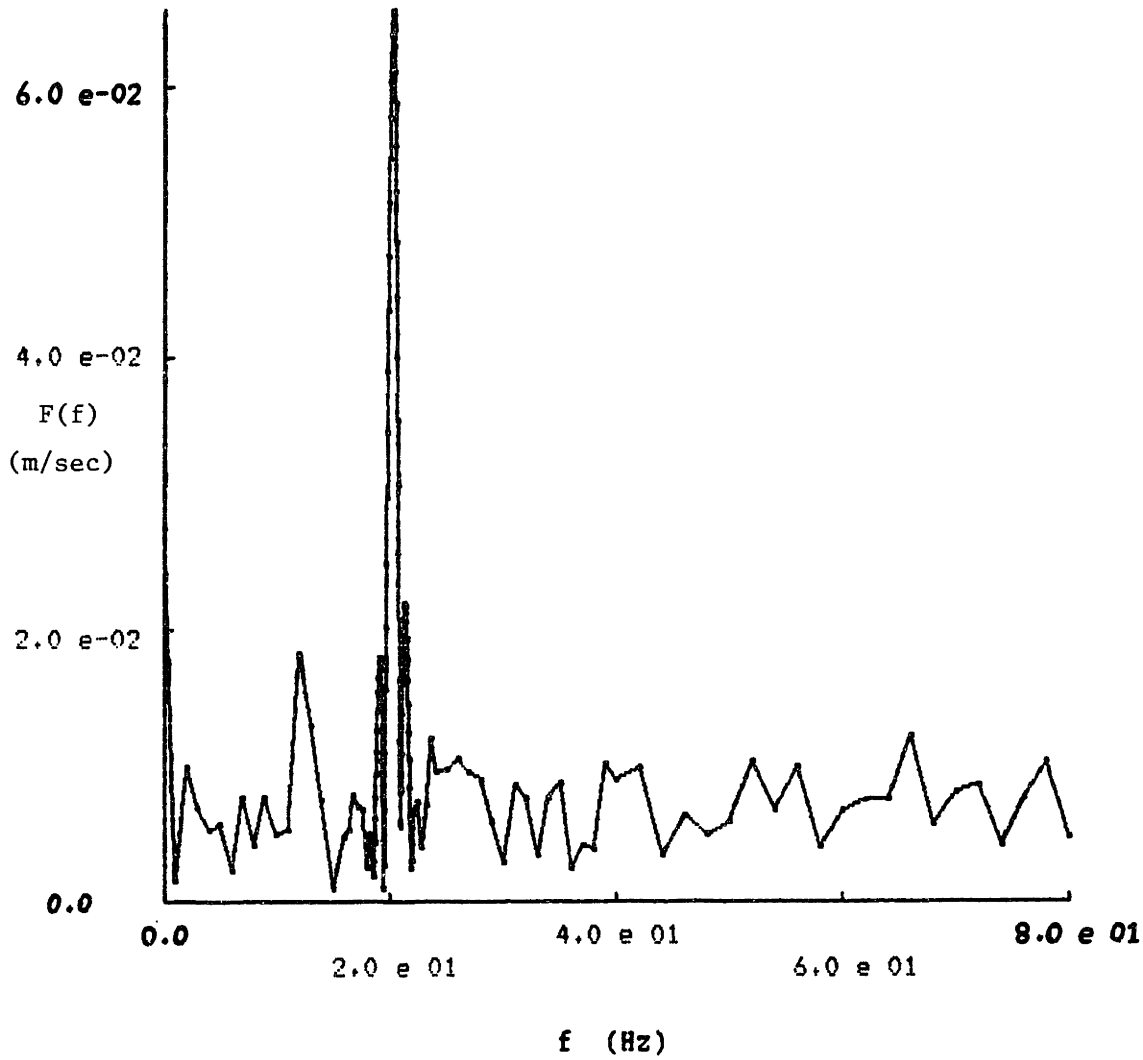

Figure 6.3. Fourier transform of transverse particle velocity.
The data is from the file, ld1112.006.
The excitation frequency was approximately 20 Hz.
The series blocking capacitor was present.
The corona pins were near to the migration plate.
The horizontal flow velocity was 2.5 m/sec.
The RMS velocity spread was approximately
16.1 cm/sec.

is still clearly distinguishable in that figure, however. Figures (4) - (7) contain plots showing the variation of the decay coefficient, γ, with excitation frequency, f, for various flow conditions. Data is presented for each of three flow velocities (2.5, 4.3, and 7.5 m/sec) with the pins near to the flow-straightener. Only the highest-speed flow gave a recognizable Fourier velocity component at any frequency other than 20 Hz with the pins in the "far" position. Therefore, Fig. (7) contains the only plot of γ vs. f with the pins far away from the flow-straightener, measured with a 7.5 m/sec horizontal flow velocity. Figure (8) shows the variation of the ratio between the decay coefficient at the two pin locations with frequency. For each individual frequency, the quantity plotted is the ratio between γ with the pins in the "far" position to that with the pins "near". To reduce problems associated with scatter in the experimental data, the five points shown in Fig. (8) were obtained in the following manner. First, lines were fitted to the experimental data shown in Figs. (6) and (7), using the method of least squares over a frequency range that included all data points on each graph that were between 20 and 45 Hz. The values of the decay coefficients at the frequencies, f = 20, 25, 30, 35, and 40 Hz were obtained from these fitted lines and used to compute the relative decay coefficient, defined as

$$\gamma_r \equiv \frac{\gamma \big|_{\text{pins far}}}{\gamma \big|_{\text{pins near}}} \qquad (6.2.2)$$

The solid curve corresponds to the variation of this quantity with frequency that is predicted by the model of section 6.3, and is explained in section 6.4.

The variation of the measured decay coefficient, γ, with transverse horizontal position of the LDV observation volume, with fixed excitation and flow parameters, is shown in Fig. (9). It is seen that γ is not extremely sensitive to the transverse horizontal position of the LDV observation volume.

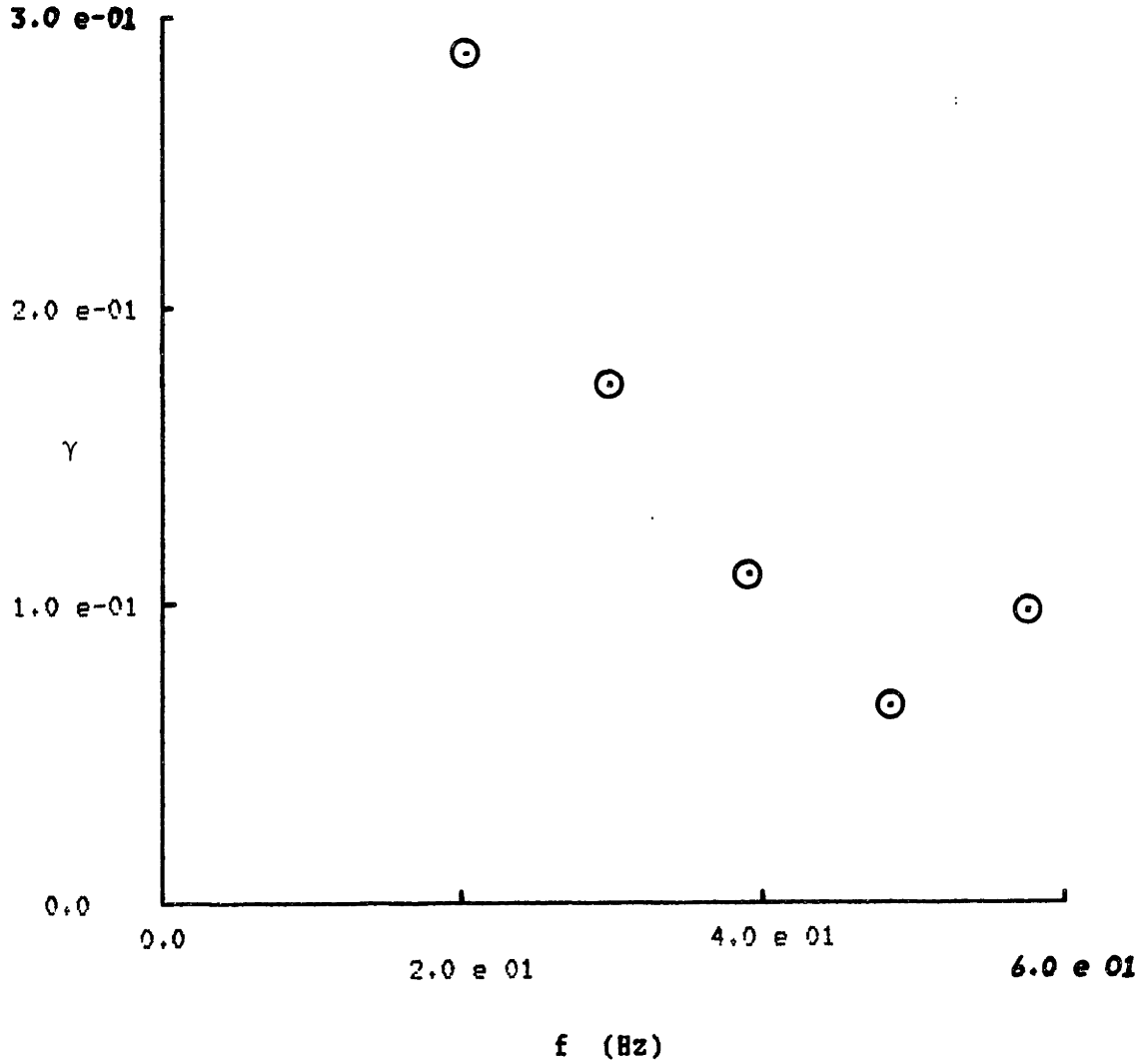

Figure 6.4. Plot of decay factor, γ, versus charging frequency used. The data was taken on 11/12/83. The series blocking capacitor was present. The corona pins were near to the migration plate. The horizontal flow velocity was 2.5 m/sec. The transverse horizontal position was approximately 0 cm.

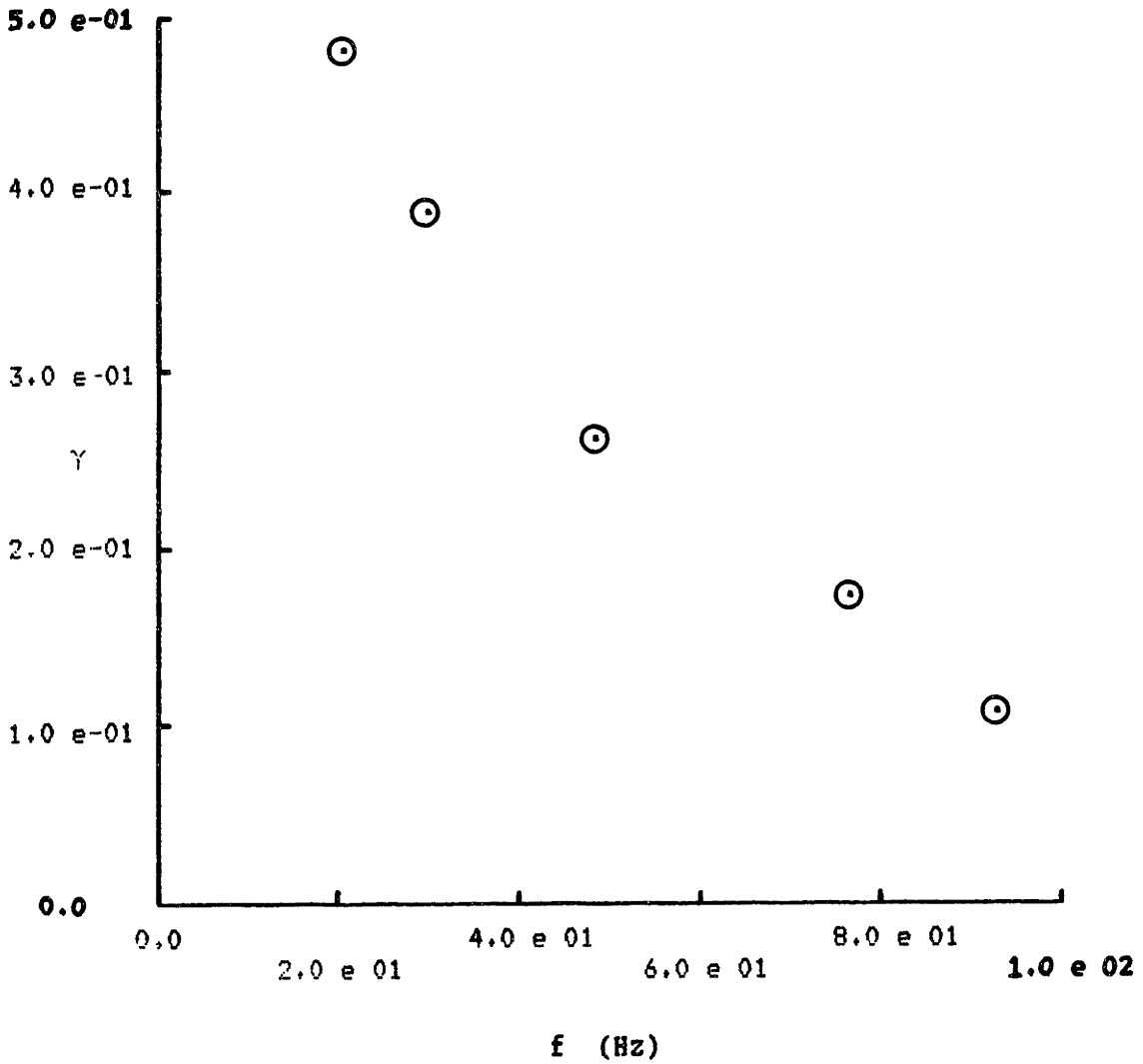

Figure 6.5. Plot of decay factor, γ, versus charging frequency used. The data was taken on 11/11/83. The series blocking capacitor was present. The corona pins were near to the migration plate. The horizontal flow velocity was 4.3 m/sec. The transverse horizontal position was approximately Ø cm.

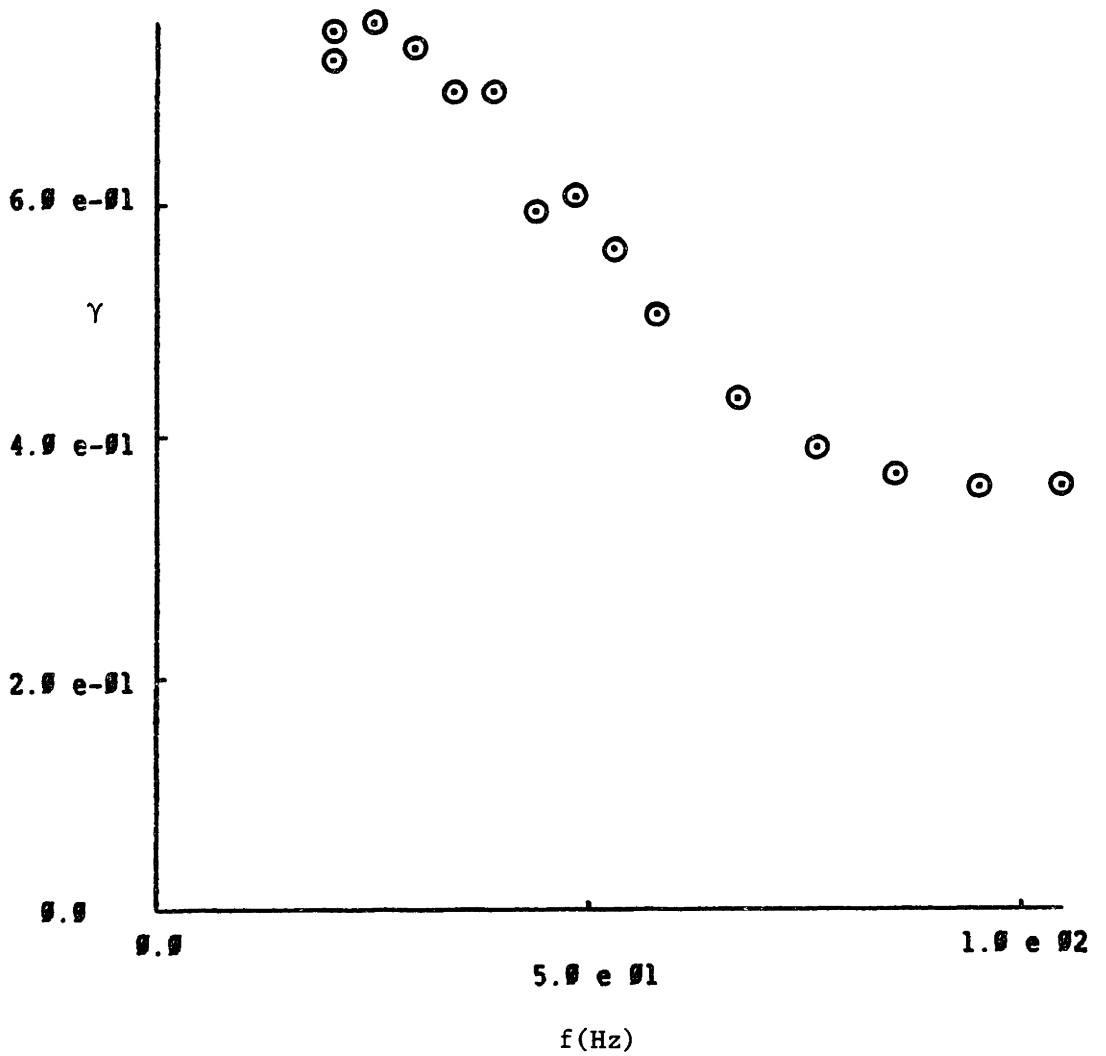

Fig. 6.6. Plot of decay factor, γ, versus charging frequency used. The data was taken on 3/3/84. The series blocking capacitor was present. The corona pins were near to the migration plate. The horizontal flow velocity was 7.5 m/sec. The transverse horizontal position ranged from -1.0 to 0.0 cm.

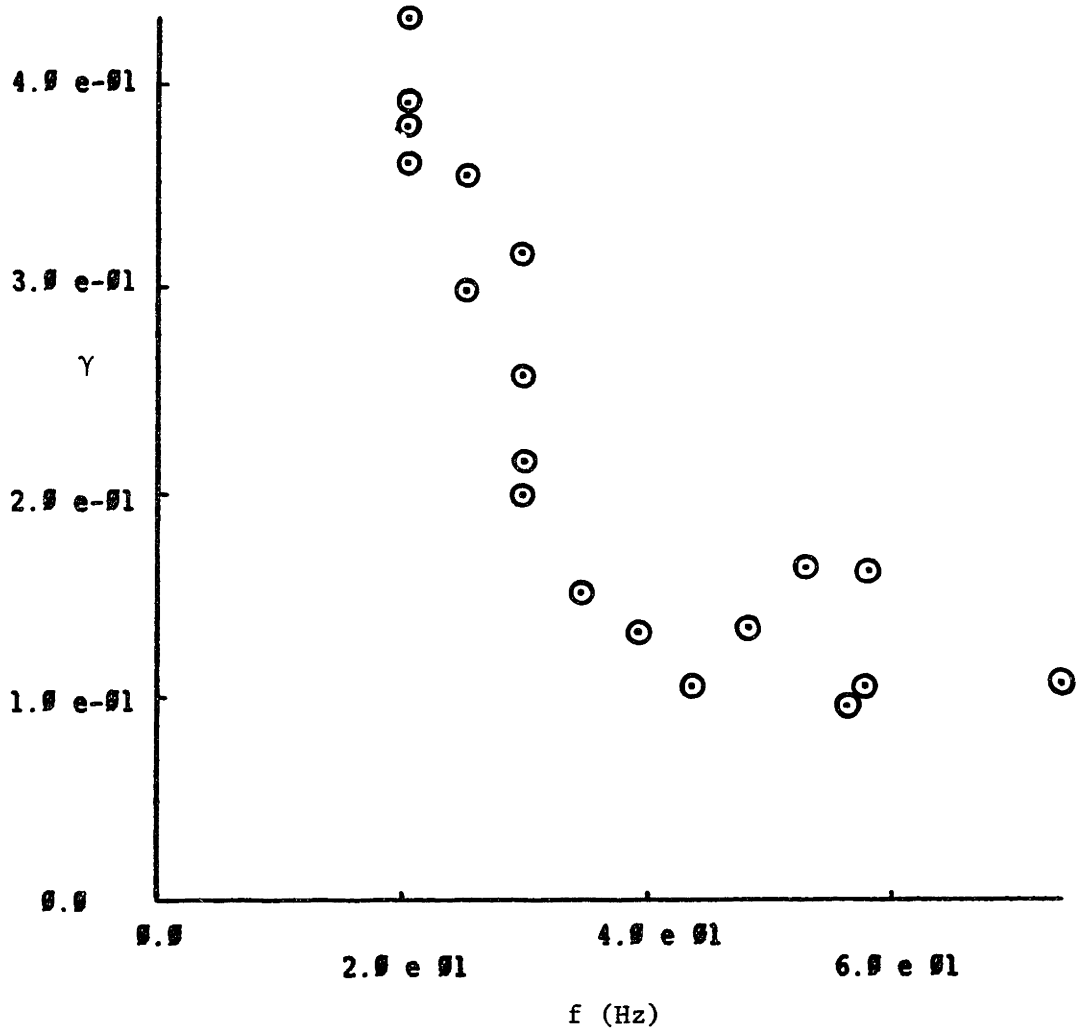

Fig. 6.7. Plot of decay factor, γ, versus charging frequency used. The data was taken on 3/3/84. The series blocking capacitor was present. The corona pins were far from the migration plate. The horizontal flow velocity was 7.5 m/sec. The transverse horizontal position ranged from -1.0 to 0.0 cm.

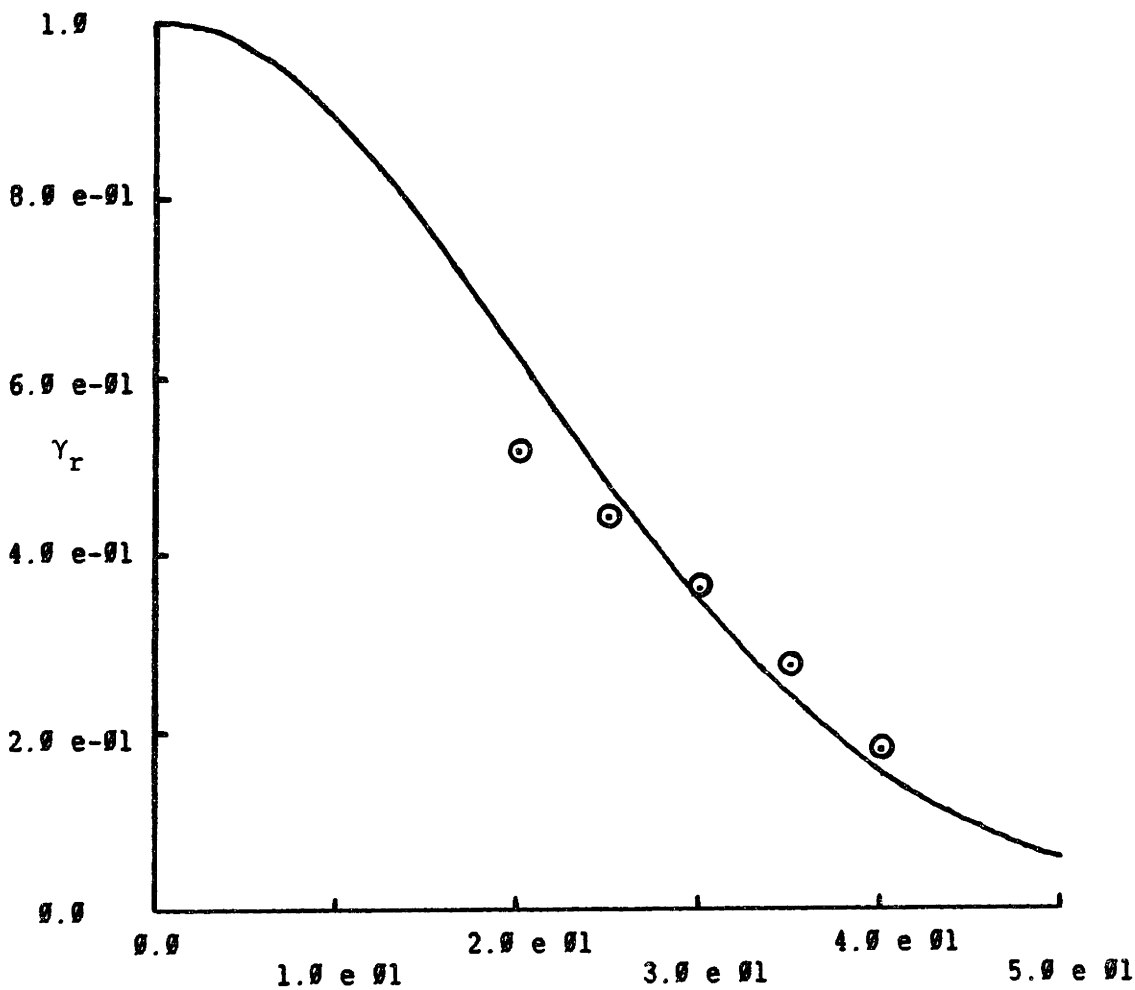

Fig. 6.8. Plot of the ratio of decay factors (γ's) measured with "far" pins to that obtained with "near" pins, as a function of the charging frequency, f. Flow velocity was 7.5 m/sec. Data from 3/3/84. Solid line corresponds to theoretical model of Section 6.3, with $D_t = 1.7 \times 10^{-2}$ m^2/sec.

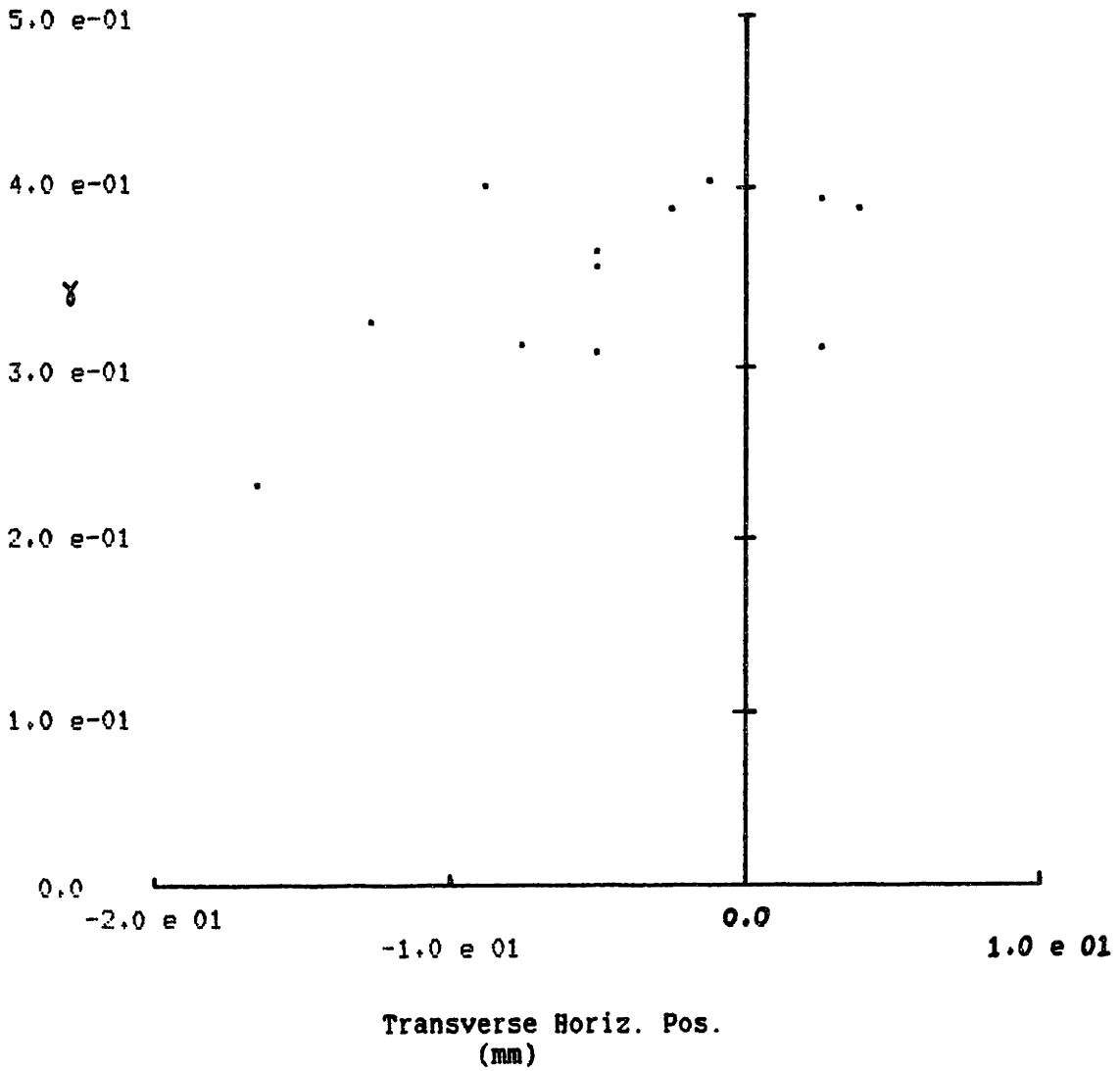

Figure 6.9. Plot of decay factor, γ, as a function of transverse horizontal position, relative to position of second corona wire from photomultiplier side (The corona wire was not present for this measurement). The charging frequency used was approximately 20 Hz. The data was taken on 11/30/83. The series blocking capacitor was present. The corona pins were far from the migration plate. The horizontal flow velocity was 7.5 m/sec.

6.3 Model for Longitudinal Turbulent Mixing

6.3.1 Problem Presentation

The situation is as pictured in Fig. (10). A turbulent airflow of uniform mean velocity, $U\bar{i}_z$, and effective diffusivity, D_t, carries neutrally buoyant particles of number density, n. As particles pass through the plane, z=0, they are charged by a time-varying (corona) source so that the charge, q, on a particle that is at z=0 at the time, t, is given by

$$q_{particle} = \text{Re } Q_o e^{j\omega t} \tag{6.3.1}$$

where Q_o is the amplitude of the charging source and ω is its angular frequency. The density of particles far downstream of the charging plane is assumed to be equal to the inlet density, n. It is desired to predict the time dependence of the particle charge at some fixed location downstream of the charger, say, at z=L. It will be argued later that it is the charge density, $\rho(z,t)$, which is measured by the experiments reported in section 6.2.

6.3.2 Evaluation of Self-Precipitation Effects

The particles are assumed to act as inert markers in the flow. Effects of self-precipitation, due to repulsion between particles of like charge, and recombination, due to attraction between particles of opposite sign, are assumed to be negligible. That assumption is examined in this sub-section.

The only electric fields that exist in the problem (outside of the charging and mobility measurement regions) are those due to the particle charge. Both the self-precipitation and recombination processes will occur over time-scales that are on the order of

$$\tau_p \equiv \frac{\varepsilon}{\rho_p b_p} \tag{6.3.2}$$

where $\rho_p \equiv Q_o n$ is a characteristic particle charge density and b_p is a characteristic mobility of the particles. The mobility, b_p, depends upon the particle charge as well.

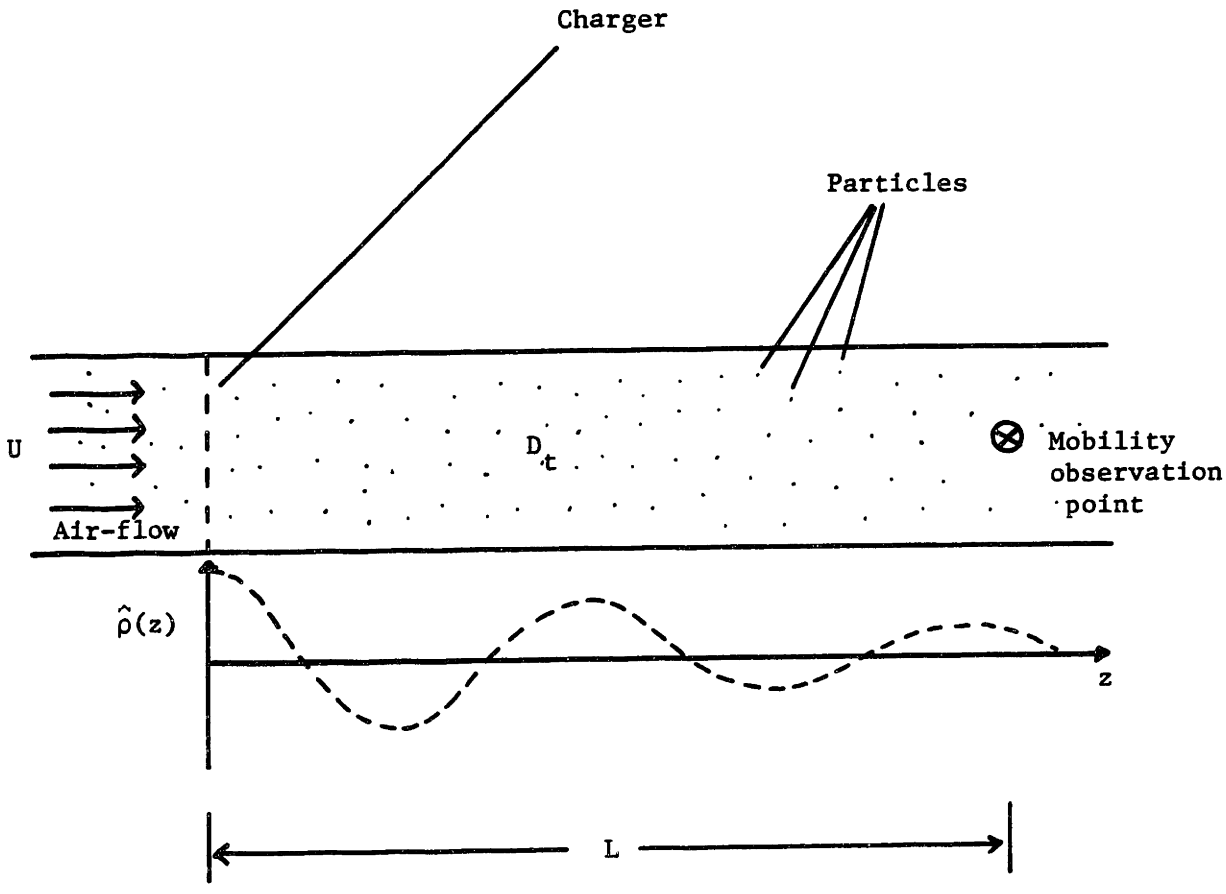

Fig. 6.10. Schematic illustration of situation for longitudinal turbulent mixing model. Particles are convected by air-flow from left to right, being charged at the surface, z=0. Induced charge density decays with increasing axial coordinate, z. Particle mobilities (which indicate the particle charges) are measured at z=L.

$$b_p = \frac{Q_o}{6\pi\eta R} \tag{6.3.3}$$

Equation (3) was obtained from the definition of a particle mobility, by balancing the electric force on a particle of charge, Q_o, with the viscous drag, according to Stokes' formula for low Reynold's number flow. For particles charged to saturation in an electric field, E_o,

$$Q_o = 12\pi\varepsilon R^2 E_o \tag{6.3.4}$$

Thus,

$$\tau_p = \frac{1}{18}\ \frac{1}{\frac{4}{3}\pi R^3 n}\ \frac{\eta}{\varepsilon E_o^2}$$

$$= \frac{1}{18}\ \frac{1}{\chi}\ \tau_{ev} \tag{6.3.5}$$

where

$$\chi \equiv \frac{4}{3}\pi R^3 n \tag{6.3.6}$$

is the volume fraction of the flow occupied by particles, and

$$\tau_{ev} \equiv \frac{\eta}{\varepsilon E_o^2} \tag{6.3.7}$$

is the electroviscous time for the flow. With

$$\eta \backsim 2 \times 10^{-5}\ \frac{Kg}{m \cdot sec}$$

$$E_o \backsim 10^6\ \frac{V}{m} \tag{6.3.8}$$

$$\varepsilon \simeq 8.85 \times 10^{-12}\ \frac{f}{m}$$

one obtains

$$\tau_{ev} \backsim 2 \times 10^{-6}\ sec \tag{6.3.9}$$

The particle number density in the laboratory-scale precipitator can be estimated using knowledge of the maximum LDV data rate, along with the cross-sectional area of its observation volume, A_{LDV}.

$$\dot{N} = n A_{LDV} U \tag{6.3.10}$$

where $\dot{N}$ is the number of particles passing through the observation volume per unit time. With

$$A_{LDV} \sim 2\,mm \times 0.2\,mm = 4 \times 10^{-7}\ m^2 \tag{6.3.11}$$

a typical maximum data rate of 2 kHz,

$$\dot{N} \sim 2 \times 10^{3}\ sec^{-1} \tag{6.3.12}$$

and a mean flow velocity of

$$U \sim 2\ m/sec \tag{6.3.13}$$

the number density is

$$n \sim 2.5 \times 10^{9}\ m^{-3} \tag{6.3.14}$$

If the particle radius, R, is 1 μm,

$$R \sim 10^{-6}\ m \tag{6.3.15}$$

χ is

$$\chi \sim 8 \times 10^{-9} \tag{6.3.16}$$

Thus, from eqs. (6), (9), and (16),

$$\tau_p \sim 10\ sec \tag{6.3.17}$$

As this is much longer than the convection time for a 2 m/sec flowrate,

$$\tau_c \sim 0.5\ sec \tag{6.3.18}$$

effects due to the self-fields of the charged particles can be neglected.

6.3.3 Continuum Model for Particle Charge Density

Since the particle density is uniform at all boundaries and self-field effects on the particle motions are negligible, the particle density will not vary at all throughout the volume. Only the relative positions of differently charged particles are affected by the turbulent mixing. It is convenient to define the net charge density, $\rho(z,t)$.

$$\rho(z,t) \equiv \lim_{\text{small } \Delta V} \sum_{i=1}^{n_{\Delta V}} q_i \Delta V \tag{6.3.19}$$

where ΔV is the volume of a small cube that is centered at the streamwise location, z. The cube must be much smaller than any other physical dimension of the system, yet large enough to contain many particles. The number of particle contained within the volume, M, is approximately

$$M \approx n \Delta V >> 1 \tag{6.3.20}$$

The only other characteristic length of the system is the wavelength of the excitation,

$$\lambda \equiv \frac{2\pi U}{\omega} \tag{6.3.21}$$

The existence of a volume, ΔV, which satisfies both of the above requirements is dependent upon the validity of a continuum model for the process.

$$\lambda >> n^{-1/3} \tag{6.3.22}$$

With an excitation frequency, f = 50 Hz, and a horizontal flowrate of 2 m/sec,

$$\lambda \backsim 4 \text{ cm} \tag{6.3.23}$$

From eq. (14), it is seen that the continuum assumption is easily satisfied for the situation in question.

6.3.4 Quasi-One-Dimensional Approximation

The equation of conservation of charge, in the face of convection and turbulent diffusion, is

$$\frac{\partial \rho}{\partial t} = D_t \nabla^2 \rho - U \bar{i}_z \cdot \nabla \rho \tag{6.3.24}$$

It is assumed that no significant gradients of flow or charge parameters exist in either transverse direction. Equation (24) becomes

$$\frac{\partial \rho(z,t)}{\partial t} + U \frac{\partial \rho(z,t)}{\partial z} = D_t \frac{\partial^2 \rho(z,t)}{\partial z^2} \tag{6.3.25}$$

The assumption of negligible charge density gradients in the transverse directions is satisfied by the boundary conditions posed above. However, even if the inlet boundary condition [eq. (1)] were dependent upon the transverse coordinates, an argument could be made that such gradients would quickly be eliminated by the flow turbulence. If the turbulent diffusion time, based on the actual transverse dimensions of the laboratory-scale precipitator, were short compared to the residence time [eq. (18)], then such an argument would be valid. A value for this diffusion time was presented in chapter 3 [eq. (3.6.2)], using a typical turbulent diffusion coefficient obtained from the measurements of this chapter. It was seen there that the turbulent diffusion time is significantly smaller than the convection time.

6.3.5 Steady-State Solution

In the steady-state, the response of the system will be harmonic at the excitation frequency, ω.

$$\rho(z,t) = \mathrm{Re}\ \tilde{\rho}(z)\, e^{j\omega t} \tag{6.3.26}$$

where $\tilde{\rho}(z)$ satisfies the ordinary differential equation

$$D_t \frac{d^2\tilde{\rho}(z)}{dz^2} - U \frac{d\tilde{\rho}(z)}{dz} - j\omega \tilde{\rho}(z) = 0 \tag{6.3.27}$$

The boundary conditions on $\tilde{\rho}(z)$ are

$$\tilde{\rho}(z)\Big|_{z=0} = Q_o n \equiv \rho_o \tag{6.3.28}$$

and

$$\tilde{\rho}(z)\Big|_{z\to\infty} \neq \infty \tag{6.3.29}$$

The restriction of eq. (29) eliminates solutions which grow exponentially with the downstream coordinate, z.

6.3.6 Normalization

With the understanding that "→" means "is normalized to", the following normalization is applied to the problem at hand.

$$\rho \to \rho_o \tag{6.3.30}$$

$$z \to L$$

Characteristic diffusion and convection times are defined, based upon the length, L.

$$\tau_D \equiv \frac{L^2}{D_t} \tag{6.3.31}$$

$$\tau_C \equiv \frac{L}{U} \tag{6.3.32}$$

Equation (27) becomes

$$\frac{d^2\underline{\tilde{\rho}}}{dz^2} + \frac{\tau_D}{\tau_C}\frac{d\underline{\tilde{\rho}}}{dz} - j\omega\tau_D\underline{\tilde{\rho}} = 0 \tag{6.3.33}$$

The quantities, $\underline{z}$, and $\underline{\tilde{\rho}}$, are the normalized downstream coordinate and complex charge density, respectively. The boundary conditions become

$$\underline{\tilde{\rho}}(z)\Big|_{z=0} = 1 \tag{6.3.34}$$

and that $\underline{\tilde{\rho}}(\infty)$ not be infinite.

6.3.7 Problem Solution

The elliptic ordinary differential equation and boundary conditions stated in eqs. (33) and (34), along with the requirement of a non-infinite solution for large z, form a well-posed problem. The solution is

$$\underline{\tilde{\rho}}(\underline{z}) = e^{-j\underline{\tilde{k}}z} \tag{6.3.35}$$

where

$$\underline{\tilde{k}} = -j\frac{UL}{2D_t}\left(\sqrt{1 + j\frac{4\omega D_t}{U^2}} - 1\right) \tag{6.3.36}$$

The normalized complex wavenumber, $\underline{\tilde{k}}$, determines the spatial rate of decay of the charge density. At $z = L$,

$$\rho(z,t)\Big|_{z=L} = \mathrm{Re}\ \rho_o\, e^{j(\omega t - \underline{\tilde{k}})} \tag{6.3.37}$$

6.3.8 Application of Solution to Determine Equivalent Diffusivity

The amplitude of the time-varying charge-density at $z = L$ decays exponentially with the downstream distance, z. The decay ratio, γ, defined in section 6.2, is

$$\gamma = \left|\frac{\underline{\tilde{\rho}}(L)}{\rho_o}\right| = e^{\mathrm{Im}(\underline{\tilde{k}})} \tag{6.3.38}$$

Equation (36) can be used to obtain an algebraic expression for the imaginary part of $\underline{\tilde{k}}$.

$$\mathrm{Im}(\underline{\tilde{k}}) = -\frac{UL}{2D_t}\left(\frac{1}{\sqrt{2}}\left(1 + \left(1 + \left[\frac{4\omega D_t}{U^2}\right]^2\right)^{1/2}\right)^{1/2} - 1\right) \tag{6.3.39}$$

Equation (39) can be rewritten in terms of the time constants, τ_C and τ_D, defined in eqs. (31) and (32).

$$2\frac{\tau_C}{\tau_D}\ln(\frac{1}{\gamma}) = \frac{1}{\sqrt{2}}\left[1 + \left[1 + \left(4\omega\tau_C\frac{\tau_C}{\tau_D} \right)^2 \right]^{1/2} \right]^{1/2} - 1 \qquad (6.3.40)$$

For the purpose of relating the measured experimental results to the equivalent diffusivity with only a single plot, Fig. (11) shows the dependence of the decay coefficient upon a dimensionless variable, G.

$$G \equiv 4\omega\tau_C\frac{\tau_C}{\tau_D} \qquad (6.3.41)$$

Using this definition, eq. (40) can be rewritten.

$$\frac{\ln(\frac{1}{\gamma})}{2\omega\tau_C} = \frac{1}{G}\left[\frac{1}{\sqrt{2}}\left[1 + \left[1 + G^2 \right]^{1/2} \right]^{1/2} - 1 \right] \qquad (6.3.42)$$

In the limit of small diffusivity, so that G << 1,

$$\frac{\ln(\frac{1}{\gamma})}{2\omega\tau_C} \simeq \frac{1}{8}G \qquad (6.3.43)$$

In that case,

$$D_t \simeq \frac{U^3}{\omega^2 L}\ln(\frac{1}{\gamma}) \qquad (6.3.44)$$

Thus, for small diffusivities, eq. (44) can be used to evaluate D_t, while the plot of Fig. (11) is valid in general.

It is seen, from eq. (35), that the magnitude of the particle charge-density varies exponentially with distance downstream of the charger. Thus, the decay coefficient, γ, decays exponentially with the length of the flow interval from the charger to the point of observation of the particle charge, as is shown in eq. (38). If the charge density is measured at two points downstream of the charger, then the relative magnitude of the two observed charge-densities is also constrained by eq. (38), with the distance downstream of the charger, L, being replaced by the distance between the two points*.

---

*This distance is used in the computation of $\tilde{\underline{k}}$, in eq. (36)

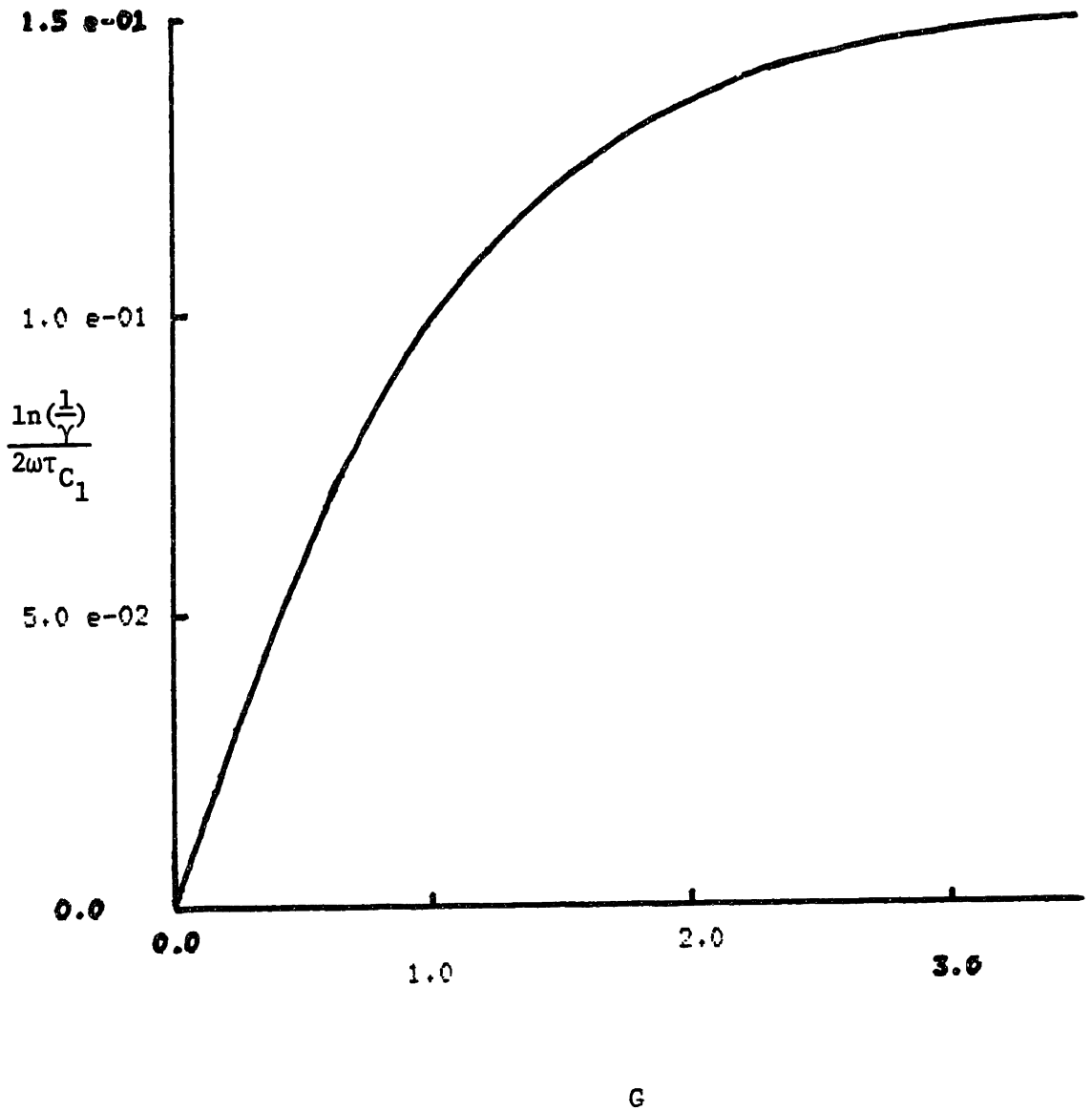

Figure 6.11. Plot of the dimensionless quantity, $\ln(1/\gamma)/2\omega\tau_C$, as a function of the dimensionless variable, $G \equiv 4\omega\tau_C^2/\tau_D$. In the limit of $G \ll 1$, the function is equal to $G/8$.

6.3.9 Interpretation of Solution in Terms of Experimental Data

The preceding theoretical development yields a prediction for the local space-averaged particle charge density as a continuous function of time at some location downstream of the charger. The experiment, however, produces a set of discrete ordered velocity/time pairs. Because of turbulent mixing (the very phenomenon that is to be observed here), the resulting velocity is anything but continuous [see Fig. (1)].

If the LDV data rate, N, is much higher than the charging frequency, $\omega/2\pi$, then the Fourier transform of the velocity vs. time function [as computed using eq. (5.1.2)] can be approximated by

$$F(f) \simeq \frac{2}{T} \sum_{n=0}^{P-1} \bar{v}_n \, e^{j 2 \pi f n T/P} \quad \frac{T}{P} \tag{6.3.45}$$

where

$$\bar{v}_n \equiv \frac{1}{M_n} \sum \quad v_i \tag{6.3.46}$$

$$n\frac{T}{P} \leq t_i < (n+1)\frac{T}{P}$$

In eq. (45), the total data time span, $0 \leq t < T$, has been divided into P intervals of equal length, where P is chosen so that

$$f \frac{T}{P} << 1 \tag{6.3.47}$$

Thus, one such interval takes up much less time than a cycle of the corona charger. The quantity, $\bar{v}_n$, defined in eq. (46), is the time-averaged vertical particle velocity for the n'th interval, and M_n is the number of individual measurements used to compute this average. If $M_n >> 1$, then it is likely that $\bar{v}_n$ will be a gradually-varying function of n, even though the individual particle velocity may vary wildly from one measurement to the next.

The approximate Fourier transform of eq. (45) is meaningful only if there exists a suitable time interval, (T/P), small enough to satisfy eq. (45), yet large enough so that $M_n >> 1$ for most intervals, $0 \leq n < P$. This constraint is similar to that of eq. (22) in that the

validity of a continuum model for the situation is at question. Given a typical charging frequency of 50 Hz and a data rate of 2 kH, it is, indeed, possible to find a time interval that is much smaller than one cycle time (20 msec), yet large enough to contain many individual particle velocity measurements.

Therefore, even though the actual velocity vs. time function is not sinusoidal, its Fourier component at the charging frequency provides a useful measure of the effects of turbulent mixing on longitudinal gradients of a scalar quantity (ie., the particle charge density).

6.4 Application of Longitudinal Mixing Model

Table 3 contains the results of application of the longitudinal mixing model of section 6.3 to the data of section 6.2. For the flow velocities, 2.5 and 4.3 m/sec, the ratio of the value for the decay coefficient, γ, obtained with the pins far from the migration plate to that obtained with the pins close to it was used to compute the effective diffusivity, D_t, corresponding to that flow velocity. Equation (6.3.44) was used, with L = 75 cm, $\omega \simeq 2\pi 20$ sec^{-1}*, U equal to the appropriate flow velocity, and the measured values of γ in table 6.1. For the 7.5 m/sec run, measurements of the relative decay coefficient, γ_r [defined in eq. (6.2.2)], were made for frequencies ranging from 20 to roughly 40 Hz. The value of $D_t = 17 \times 10^{-3}$ m^2/sec was obtained by fitting a curve of the predicted decay coefficient to the actual data. The solid curve in Fig. (8) shows the variation of γ_r with frequency that is predicted by eqs. (6.3.38) and (6.3.39), with this value of D_t. This comparison is the only actual test made of the validity of the longitudinal mixing model, as all of the other measurements made simply provided values for the diffusivity, D_t, to be used as parameters in other models.

The effective diffusivities obtained range from roughly $1 - 17 \times 10^{-3}$ m^2/sec.

Using the experimental parameters, along with the values for D_t in table 3, one can compute the magnitude of the dimensionless coefficient, G, defined in eq. (6.3.41). The values of G were ~ 0.09 and 0.22 for the 2.5 and 4.3 m/sec measurements, respectively. Thus, the use of eq. (6.3.44), valid only in the limit of small G, is justified for those computations. The exact expression of eqs. (6.3.38) and (6.3.39) was used to fit the data obtained with the 7.5 m/sec flow velocity.

---

*For the exact frequency used in each case, see table 6.1

U (m/sec)	filenames ("near")	("far")	Ratio of Decays	D_t (m^2/sec)
2.5	ld1Ø29.ØØ1	ld1112.ØØ6	Ø.432	$1.Ø9 \times 1Ø^{-3}$
4.3	ld1113.ØØ5	ld1111.ØØ7	Ø.291	$8.Ø4 \times 1Ø^{-3}$
7.5	-	-	-	$17 \times 1Ø^{-3}$

Table Reduced data from turbulent diffusivity measurements.

6.5 Corona Wind Measurement Setup and Procedures

This section describes the setup and procedures for the corona wind measurements that were made on the laboratory-scale precipitator. The experimental setup used for the corona wind measurements was essentially that described in chapter 2 [Figs. (2.1), (2.2)]. For most of the runs, however, the migration plate was removed and the corona wires extended all of the way through the active region of the precipitator [see Fig. (A1.1)]. The relationship between the velocities measured by the LDV and the actual air-flow velocities is discussed in section 6.5.1. Section 6.5.2 defines the terminology used in specification of the LDV observation volume location. A summary of the experiments performed is contained in section 6.5.3.

6.5.1 Relation Between Particle and Wind Velocities

Probably, the most important observation to be made on the experiments reported in section 6.6 is the fact that the LDV measured particle velocities, not air velocities. It is tempting to ignore this fact, and assume that the plots and figures of the following section represent measurements of the air speed. The magnitude of the measured velocities was relatively large when compared to the effective migration velocities reported in chapter 3. In addition, the velocity profiles included regions where the motion was actually directed toward the plane of the wires. It is the contention of the author that, in most cases, the particle motions accurately reflected those of the surrounding air.

6.5.2 Specification of LDV Observation Volume Location

The location of the LDV observation volume is specified by three orthogonal spatial coordinates. The first, referred to as the streamwise horizontal position, is its displacement along the main axis of the precipitator, measured relative to the center wire support bar [Fig. (A1.1)]. The term, "upstream", refers to positions nearer to the inlet and "downstream" implies that the observation volume is nearer to the

outlet. The transverse horizontal position is the horizontal displacement of the observation volume in a direction along the main axis of the LDV, measured relative to a position directly over (or under) a specified corona wire. The term, "laser side" refers to points nearer to the transmitting optics of the LDV, while points on the other side of the wire are denoted by "photomultiplier side". The vertical position is simply the vertical displacement of the observation volume, measured relative to that same corona wire. Positive values represent positions above the wire, while negative numbers are used for points below it.

The streamwise horizontal position is not considered to be a critical quantity, and thus was often measured rather casually, with a ruler placed outside of the precipitator. The two transverse displacements, however, are critical, as both the particle velocities and concentrations change rapidly in the vicinity of a corona wire. The following procedure can be used to accurately locate the observation volume. First, the observation volume is positioned exactly on the corona wire. This is accomplished by adjusting the position of the I-beam upon which the LDV rests so that both laser beams are visibly interrupted by the wire. Normally, it is simplest to do this with aerosol present in the tunnel, so that the paths of the beams are illuminated. With one beam blocked, it can easily be determined whether or not the other is interrupted by the glowing reflection from the wire. The angular positions of the threaded rods used to adjust the vertical LDV position are then noted. The distance of the transmitting optics shield from the table which supports the precipitator then provides a measure of the transverse horizontal location of the wire. The vertical and transverse horizontal positions are then reported as displacements relative to this initial location.

All of the measurements reported in this thesis were made with the LDV observation volume in the vicinity of the corona wire that was second from the receiving optics side of the tunnel. Unless otherwise specified, it should be assumed that the observation volume was 6 mm above that wire, and about 67 cm away from the upstream corona wire support bar.

6.5.3 Summary of Experiments Performed

The corona wind measurements were performed with two purposes in mind. First, it was necessary to verify that the electric field forces on current-carrying ions (transferred to the surrounding air molecules by collisions) were capable of causing a measurable change in the air-flow of the precipitator. It was important to determine whether this fluid motion was of sufficient magnitude to significantly influence the particle charging, transport, and collection processes. In addition, it was desired to measure the dependence of the induced velocity on various experimental parameters, such as the magnitude and frequency of the applied corona voltage. Such data could prove useful in modeling the mechanisms which produce the corona wind, itself.

The first experiments reported in section 6.6 were motivated by the former objective. Computer-controlled relays were used to allow observation of the vertical particle velocity transient that ensued immediately after either application or removal of the corona excitation. Of most interest were : (1) the magnitude of the change in velocity, and (2) the time over which that change took place. If it were particle migration that was being observed by the LDV, then the velocities would be expected to be on the order of those reported in chapter 5*, and the motion would be present only when the corona voltage was non-zero.

Velocity profiles, scanning in the vertical and transverse horizontal directions, are shown next. Again, the major purpose of these experiments was to verify that the observed velocity was, indeed, dominated by the air-flow. Measurements are then presented to document the variation of the induced flow velocity with positive and negative DC corona current magnitude, with RMS current for fixed-frequency AC excitation, and with frequency for fixed-magnitude AC.

Finally, the corona wind velocity at a given fixed location was measured as a function of the horizontal flow velocity for various fixed electrical excitations. The flow velocity is characterized by a

---

*The electric field strengths imposed by the migration plate were of the order of or greater than those near the ground plates in the vicinity of the corona wires

development time, τ_{dev}, equal to the ratio of the development length, ℓ_{dev} [Fig. (6.22)], to the flow velocity, U.

$$\tau_{dev} \equiv \frac{\ell_{dev}}{U} \tag{6.5.1}$$

Thus, τ_{dev} is equal to the interval of time during which a fluid element being observed by the LDV has been subjected to the corona ion body-force.

6.6 Experimental Data From Coroan Wind Measurements

Figure (12) shows a vertical particle velocity transient that resulted from the sudden application of +10 kV DC to the corona wires. The LDV observation volume was positioned immediately above a corona wire and a high-voltage relay connected the power supply to the wires at approximately 0.4 seconds after the beginning of the data acquisition step. As can be seen in Fig. (12b), the motion initially consists of a steady acceleration, at the rate of $\sim$ 5 m/sec^2, then seems to oscillate about 0.4 m/sec. With increasing time, the oscillations become less organized.

The duration of the initial transient (up to the peak velocity of $\sim$ 1 m/sec) is roughly 200 msec. The corona current waveform also underwent a transient when the relay was closed. Because of the finite power supply capacitance and impedance, the current fell from 1.4 ma initially to 1.0 ma, with a characteristic time of about 80 msec. This voltage transient could not account for the nature of the velocity function shown in Fig. (12), whether the cause of the motion was convection or migration of the particles. It is reported here only to discount the possibility that the velocity transient was due to particle migration in a slowly-rising electric field.

The plots of Figs. (13) and (14) display vertical particle velocity transients resulting from the sudden application and removal, respectively, of an 8.0 kV RMS, 50 Hz AC electrical excitation. With the AC voltage, determination of the current rise-time (to within less than a single cycle-time) is difficult. When the relay was opened, however, the current fell to zero value in less than 2.0 msec. Thus, the fact that the velocity transient in Fig. (14) was over 200 msec in duration may be taken as an indication that the particle motion was not entirely due to migration in the imposed electric field.

For the data presented in Fig. (15), the vertical particle velocity was measured at several different transverse horizontal positions. The measurements spanned an interval that extended roughly three-quarters of the distance between corona wires (the wire spacing was 3.5 cm). The peak upward velocity was seen in the vicinity of the wire, and was $\sim$ +0.80 m/sec. The maximum downward velocity was measured

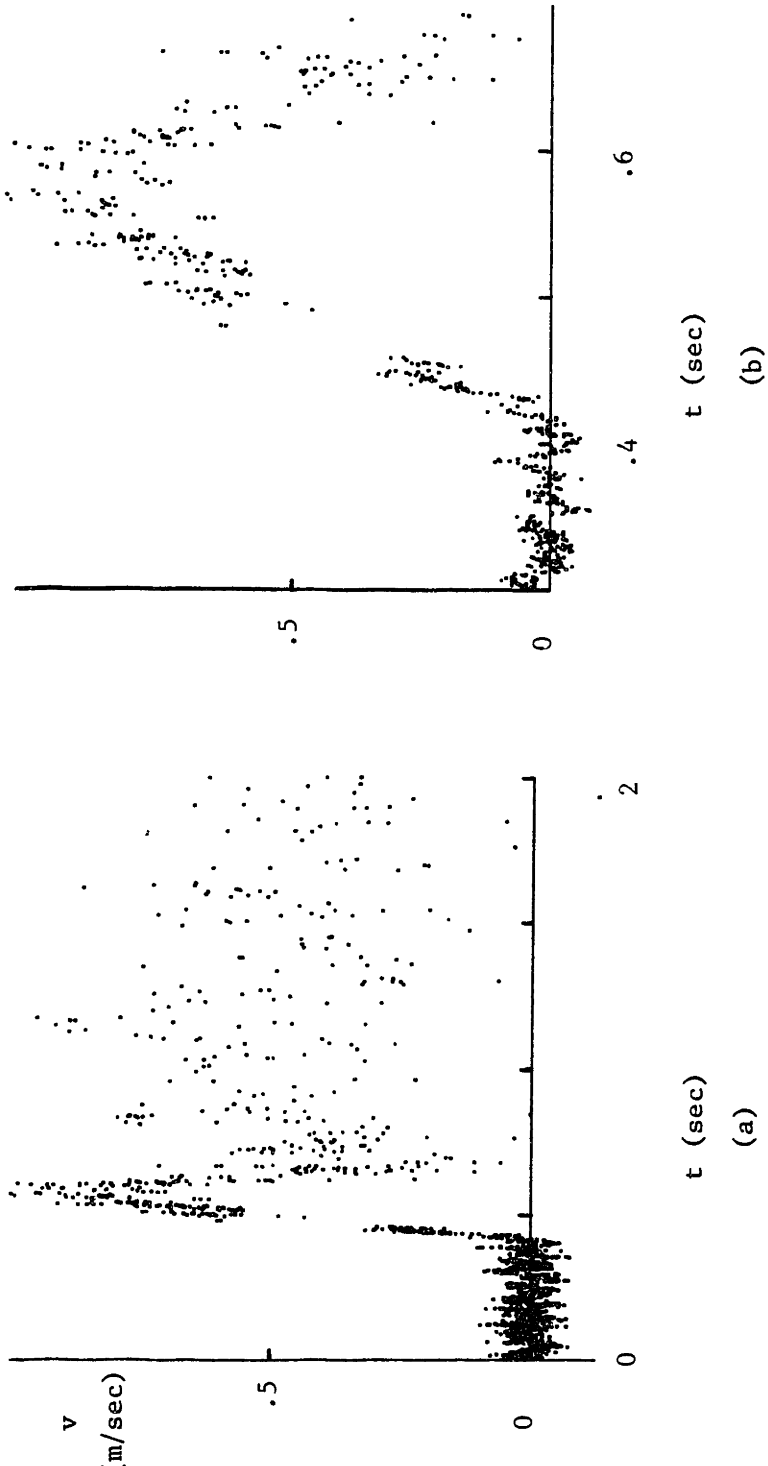

Fig. 6.12. Plot showing vertical particle velocity transient occurring immediately after application of +10 kV DC to the corona wires. LDV observation volume was 6 mm above the corona wire, 67 cm from the upstream wire support bar. The voltage was applied at t ≃ 0.4 sec. Fig. (b) is an expanded view of the initial transient.

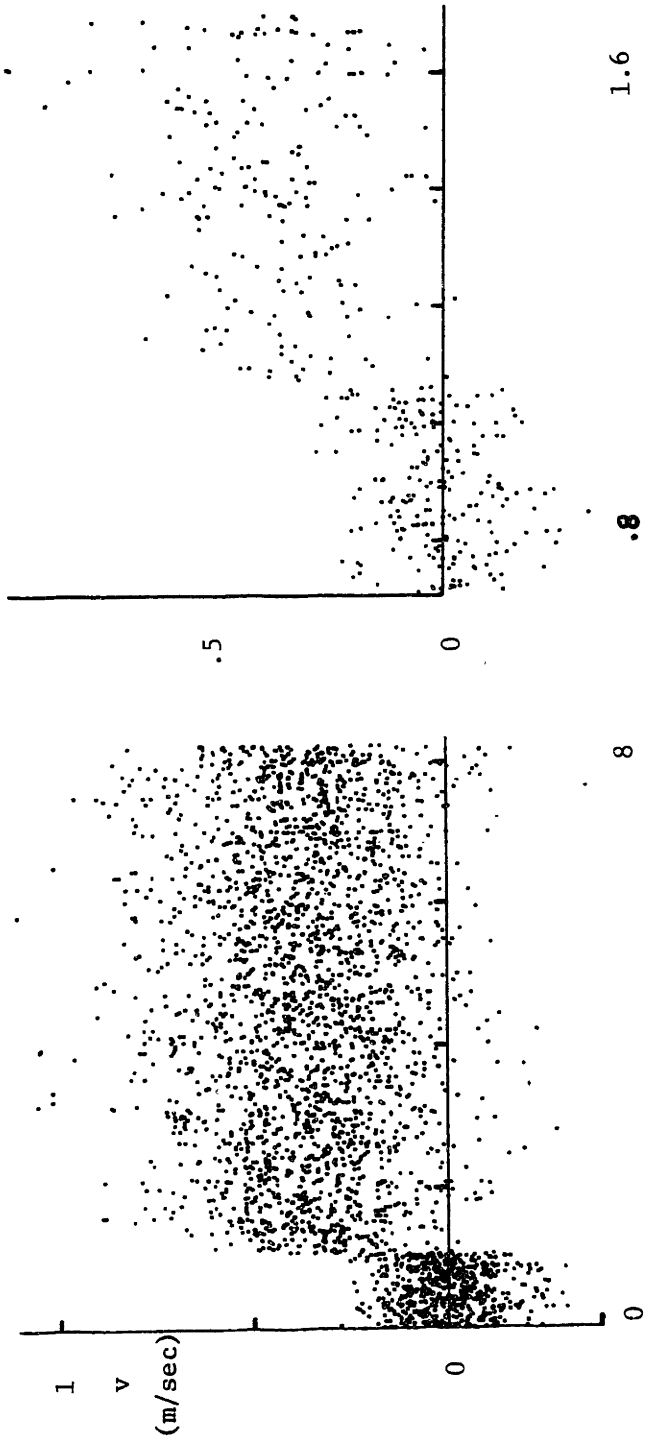

Fig. 6.13. Plot showing vertical particle velocity transient occurring immediately after application of 8.2 kV RMS, 50 Hz AC to the corona wires. LDV observation volume was 6 mm above the corona wire, 67 cm from the upstream wire support bar. The voltage was applied at t ≃ 1.0 sec. Fig. (b) is an expanded view of the initial transient.

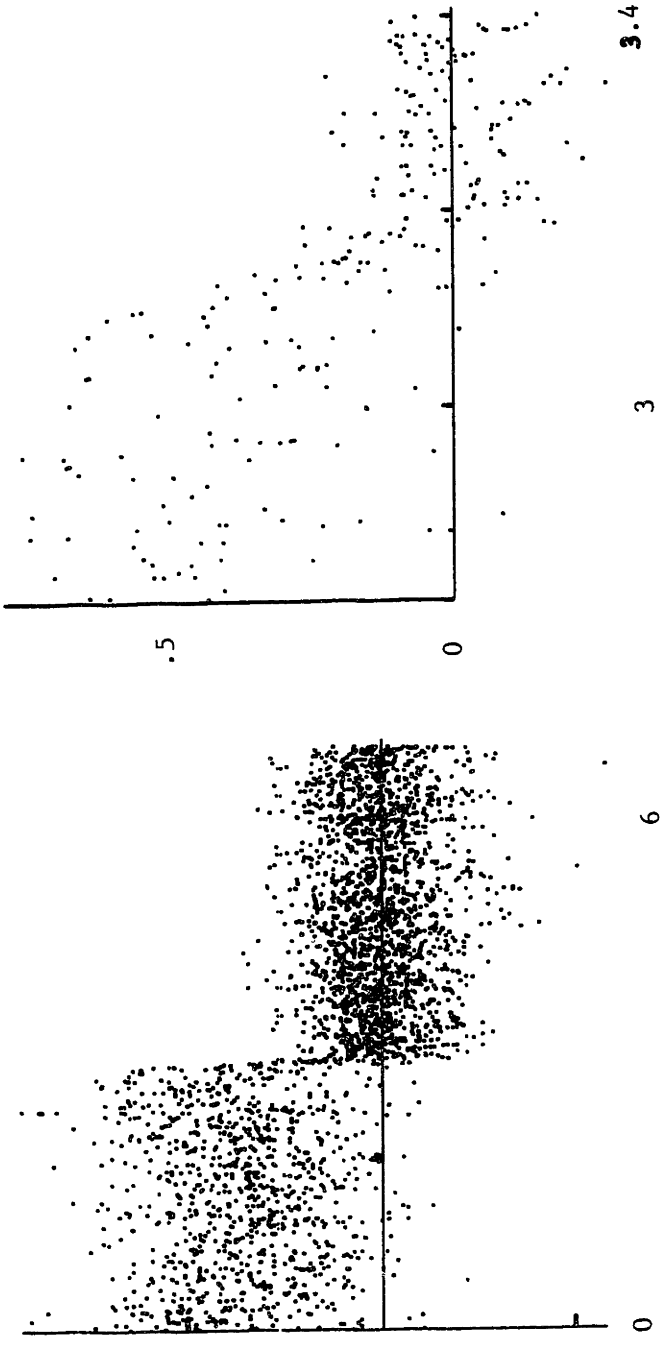

Fig. 6.14. Plot showing vertical particle velocity transient occurring immediately after removal of 8.2 kV RMS, 50 Hz AC to the corona wires. LDV observation volume was 6 mm above the corona wire, 67 cm from the upstream wire support bar. The voltage was applied at t ≃ 3.0 sec. Fig. (b) is an expanded view of the initial transient.

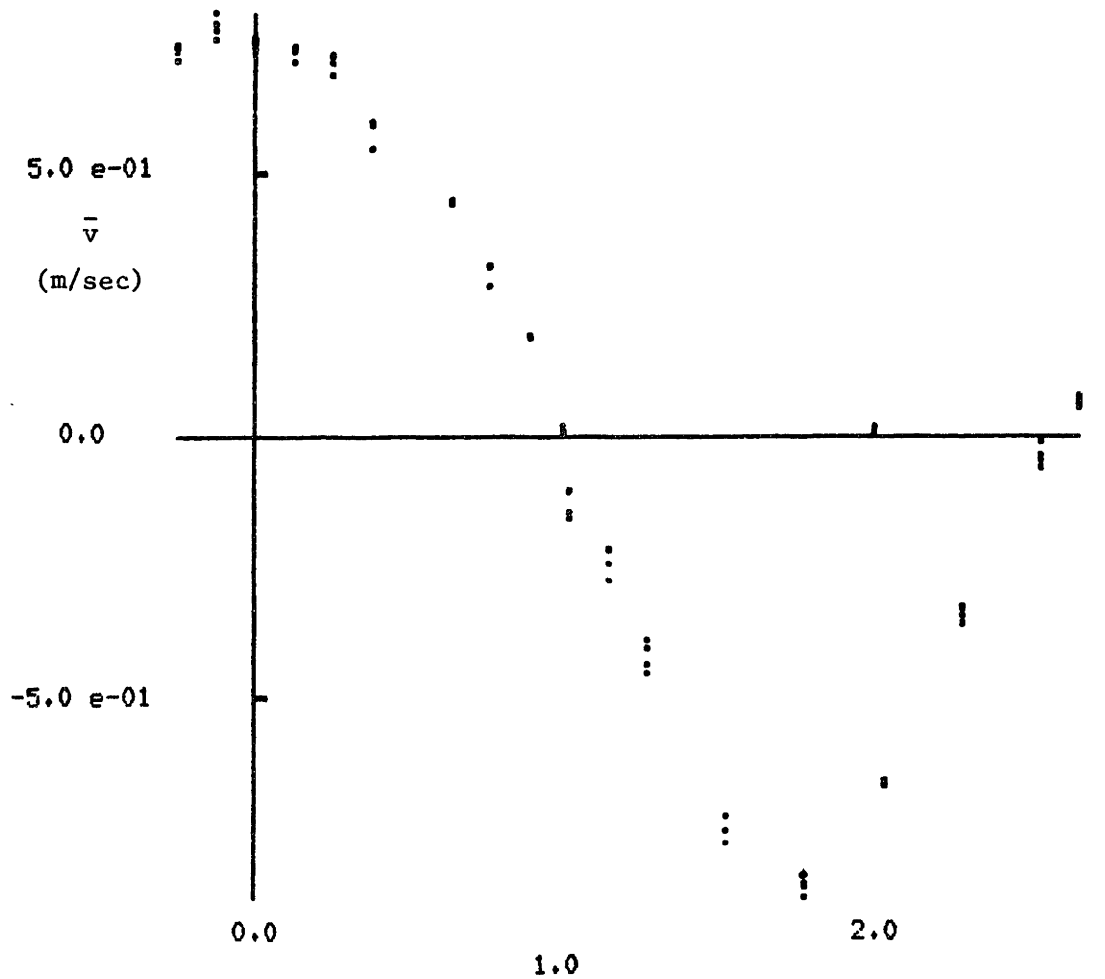

Figure 6.15. Plot of corona wind velocity vs. transverse horizontal position of the LDV observation volume. The position is measured relative to a point that is 6 mm directly above the corona wire. A 50 Hz, 8 kV RMS electrical excitation was used. The horizontal flow velocity was 4.3 m/sec (data from 8/21/83).

at about halfway between two wires, and was ∿ -0.86 m/sec. The vertical velocity, averaged over both time and space, was roughly zero, as would be expected for a contained incompressible flow.

From this data, one might predict a corona wind that has flow vectors as illustrated in Fig. (16a). The data of Fig. (17) belies this notion, however. The upper curve shown there is a plot of vertical particle velocity as a function of vertical position above/below the wire. The measured vertical velocity was positive even below the wire! Thus, the convection cells induced by the corona were most likely as pictured in Fig. (16b).

A very probable cause of this lack of symmetry in the measured velocity was the fact that the corona wires were not perfectly centered between the top and bottom ground plates. At the upstream support bar, the wires were 3 mm above the center line (ie., they were 3/4 inch from the bottom plate, 1/2 inch from the top plate). At the middle support bar, they were perfectly centered (to within 1/2 mm). With a 4.0 ma RMS 50 Hz AC corona current from the wires, the separate currents to the top and bottom plates were 2.17 ma and 1.83 ma, respectively. It is postulated that the larger current and electric field above the wires caused a non-symmetric body force on the air, resulting in the measured velocity profile of Fig. (17). The lower curve in that figure was obtained after the asymmetry was partially corrected (by rotating the upstream support bar to pull the wires somewhat lower). Apparently, the wires were still not perfectly centered. The change in the velocity profile, however, was as would be expected from the explaination given above.

For the data of Figs. (18) - (21), the LDV observation volume was held at a fixed location, 6 mm directly above the corona wire, 67 cm from the upstream support bar. Positive and negative DC coronas were applied for the tests of Figs. (18) and (19), respectively. For Fig. (20), 50 Hz AC excitations of various magnitudes were applied. Finally, for Fig. (21), the RMS corona voltage was held fixed at 8.0 kV while the frequency was varied. For reference, the velocity measured with +8.2 kV DC at the corona wires (∿ 1.5 ma) was ∿ 0.49 m/sec, while that measured with -8.0 kV DC (∿ -2.5 ma) was ∿ 0.46 m/sec. Thus, the apparent low-frequency limit of the data in Fig. (21) is much higher than the

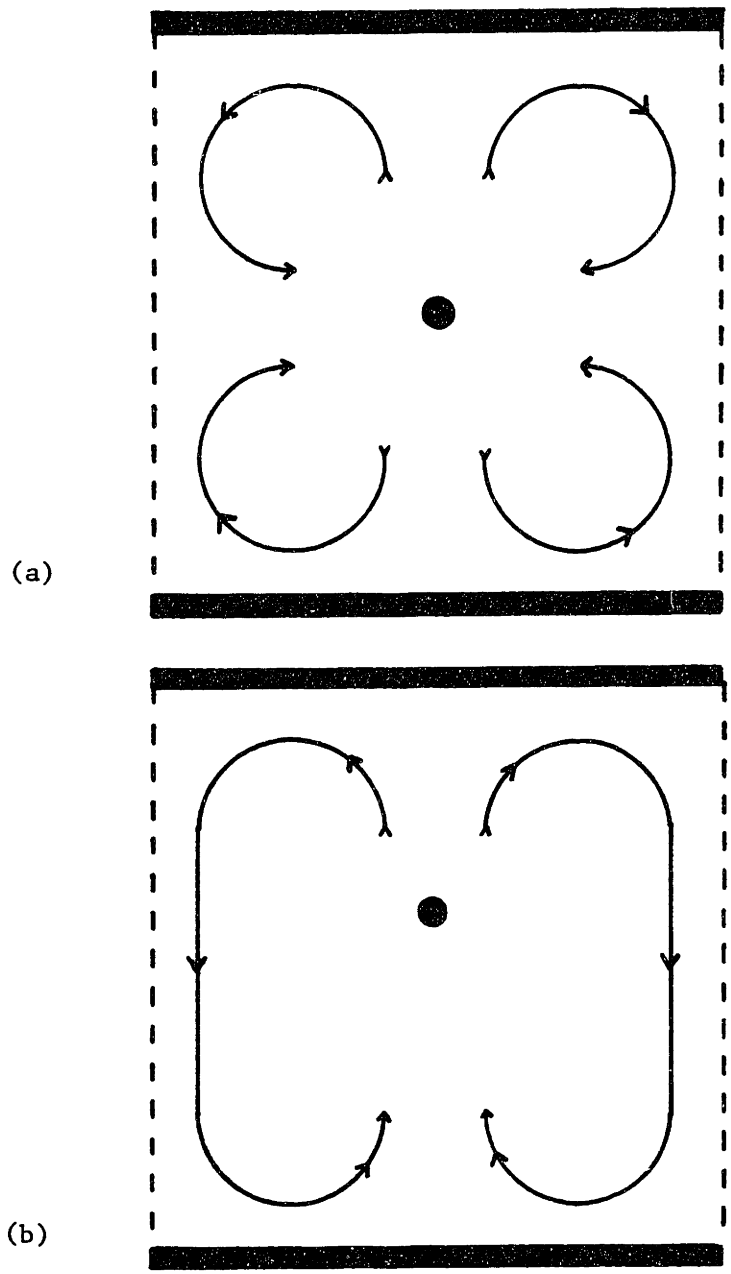

Fig. 6.16. Schematic illustration of possible flow-patterns inside the laboratory-scale precipitator. Corona wires run into the page. For (a), wire is centered between plates and pattern is symmetric. For (b), wire is off-center, and pattern is skewed. Flow about only one wire is shown in each case.

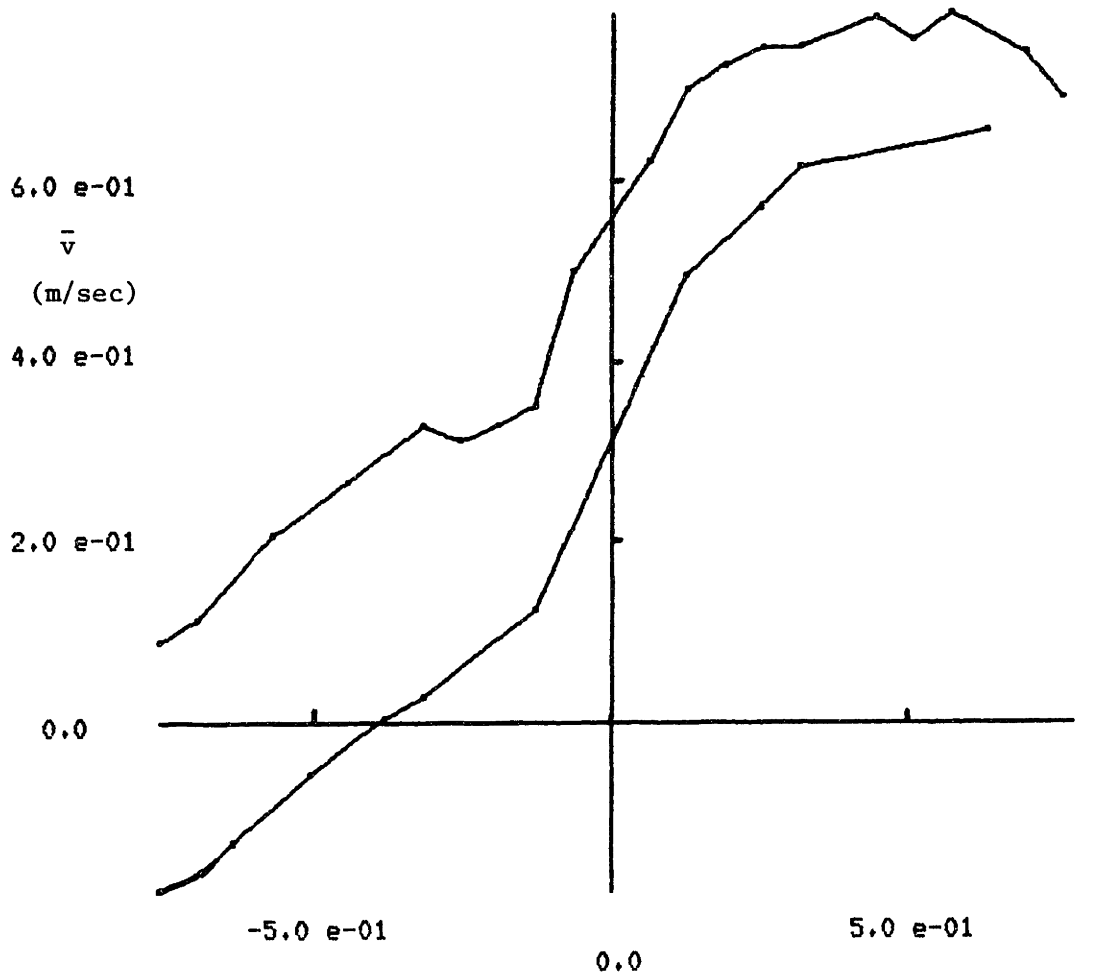

Figure 6.17. Plot of corona wind velocity vs. vertical position of the LDV observation volume. The position is measured relative to the corona wire. A 50 Hz, 8 kV RMS electrical excitation was used. The horizontal flow velocity was 4.3 m/sec (data from 8/21/83).

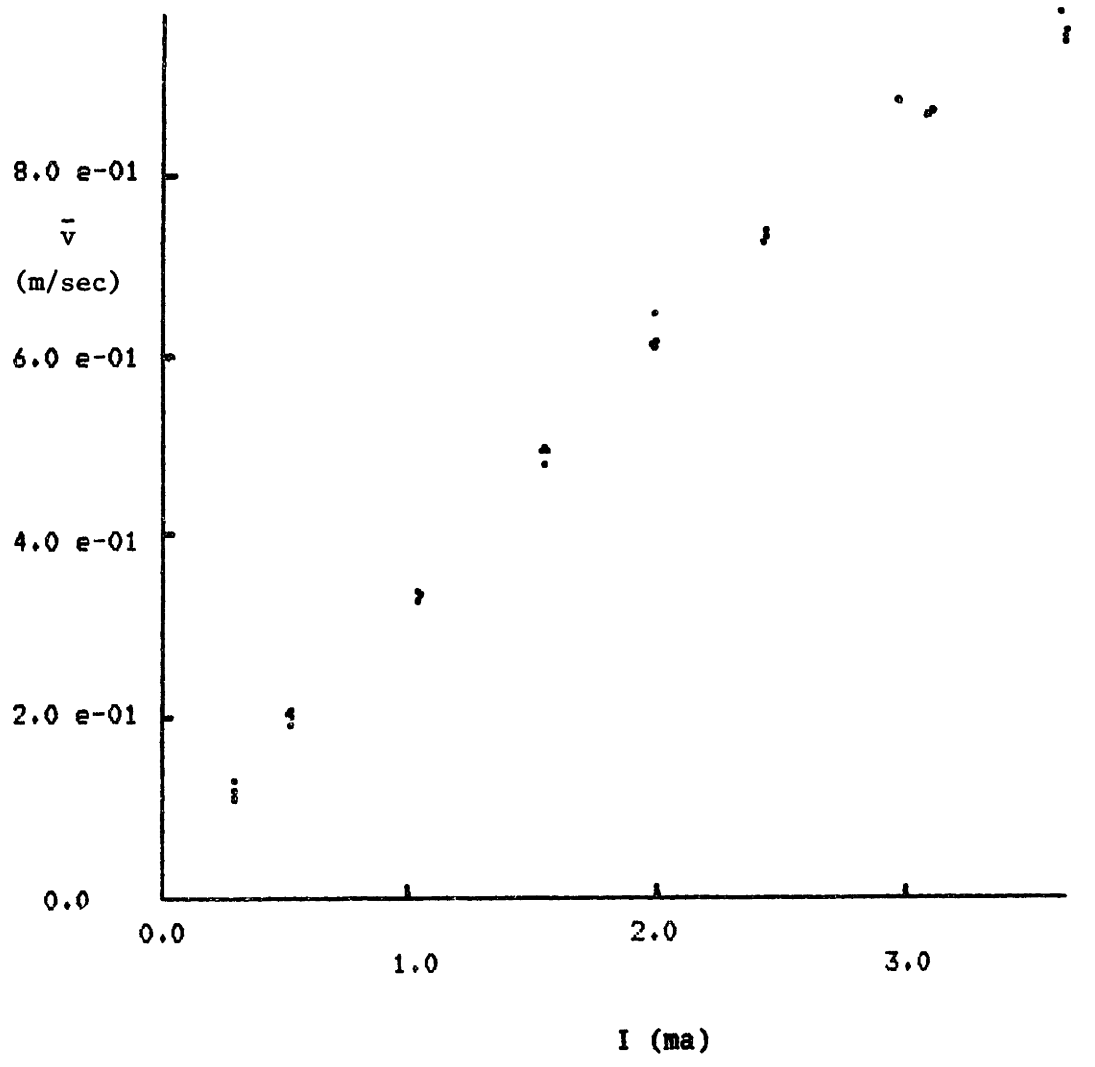

Figure 6.18. Plot of corona wind velocity vs. current magnitude for positive DC excitation. The horizontal flow velocity was 4.3 m/sec. The LDV observation volume was 6 mm above the corona wire, near to the center support bar (data from 6/14/83).

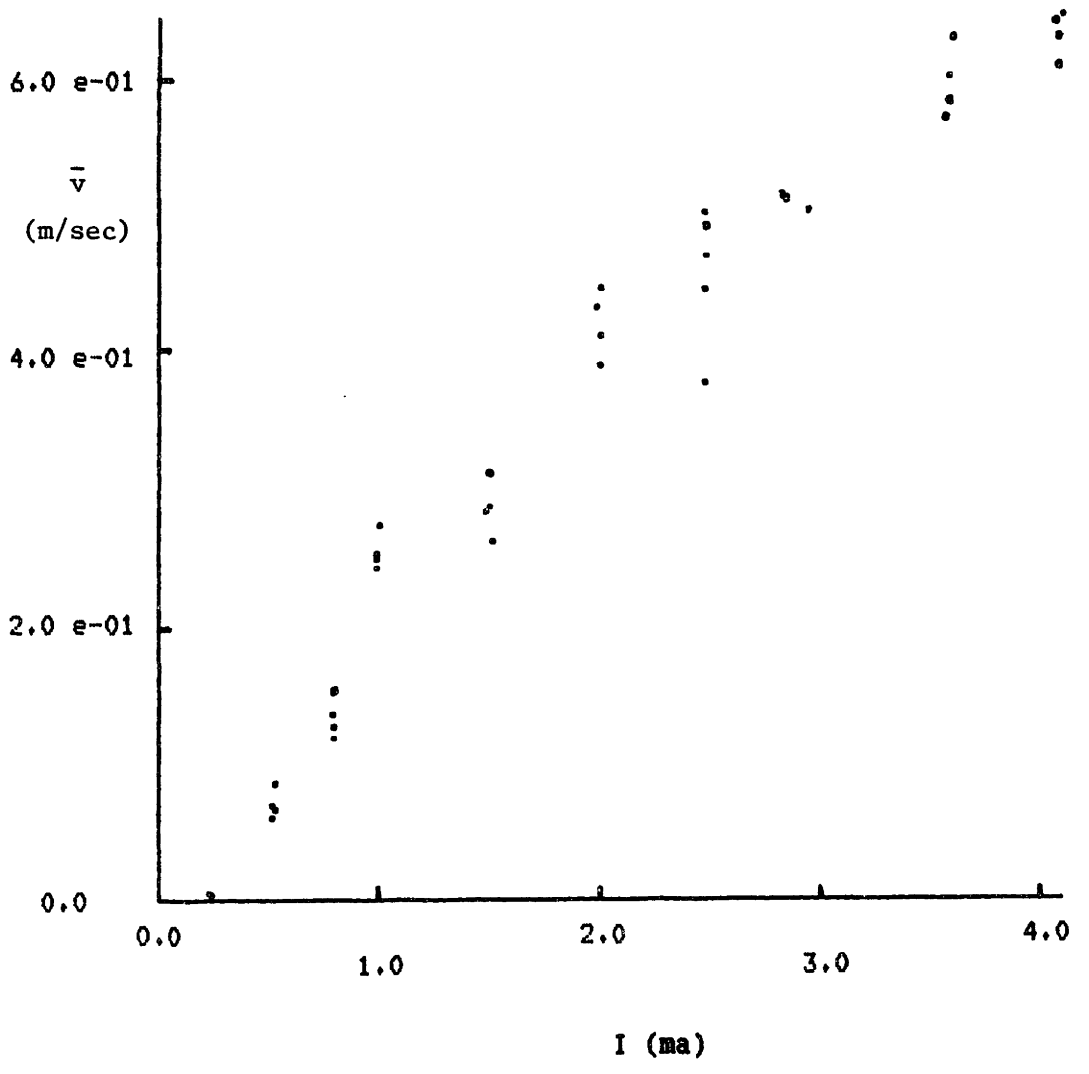

Figure 6.19. Plot of corona wind velocity vs. current magnitude for negative DC excitation. The horizontal flow velocity was 4.3 m/sec. The LDV observation volume was 6 mm above the corona wire, near to the center support bar (data from 6/14/83).

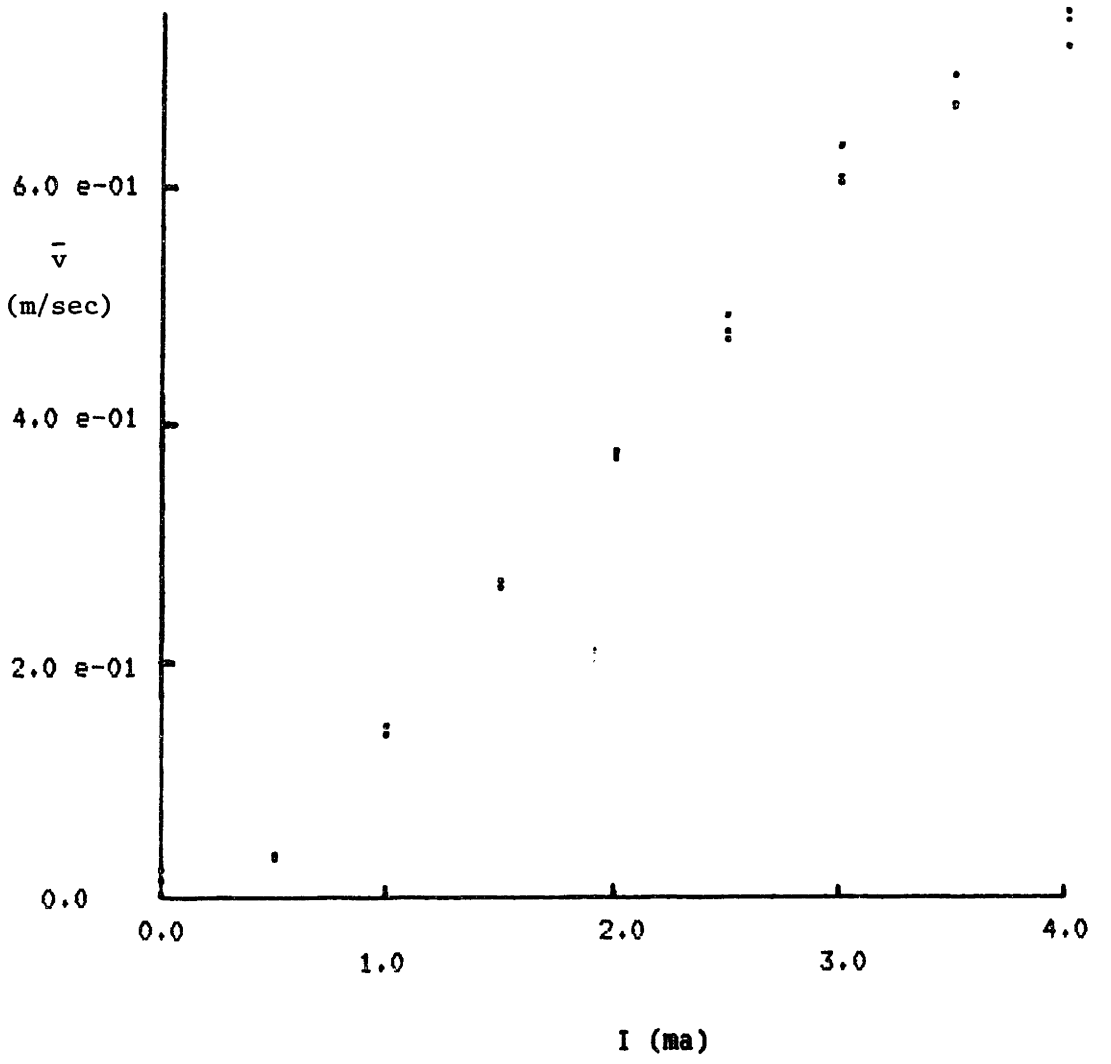

Figure 6.20. Plot of corona wind velocity vs. "RMS" current magnitude for 50 Hz AC excitation. The horizontal flow velocity was 4.3 m/sec. The LDV observation volume was 6 mm above the corona wire, near to the center support bar (data from 6/22/83).

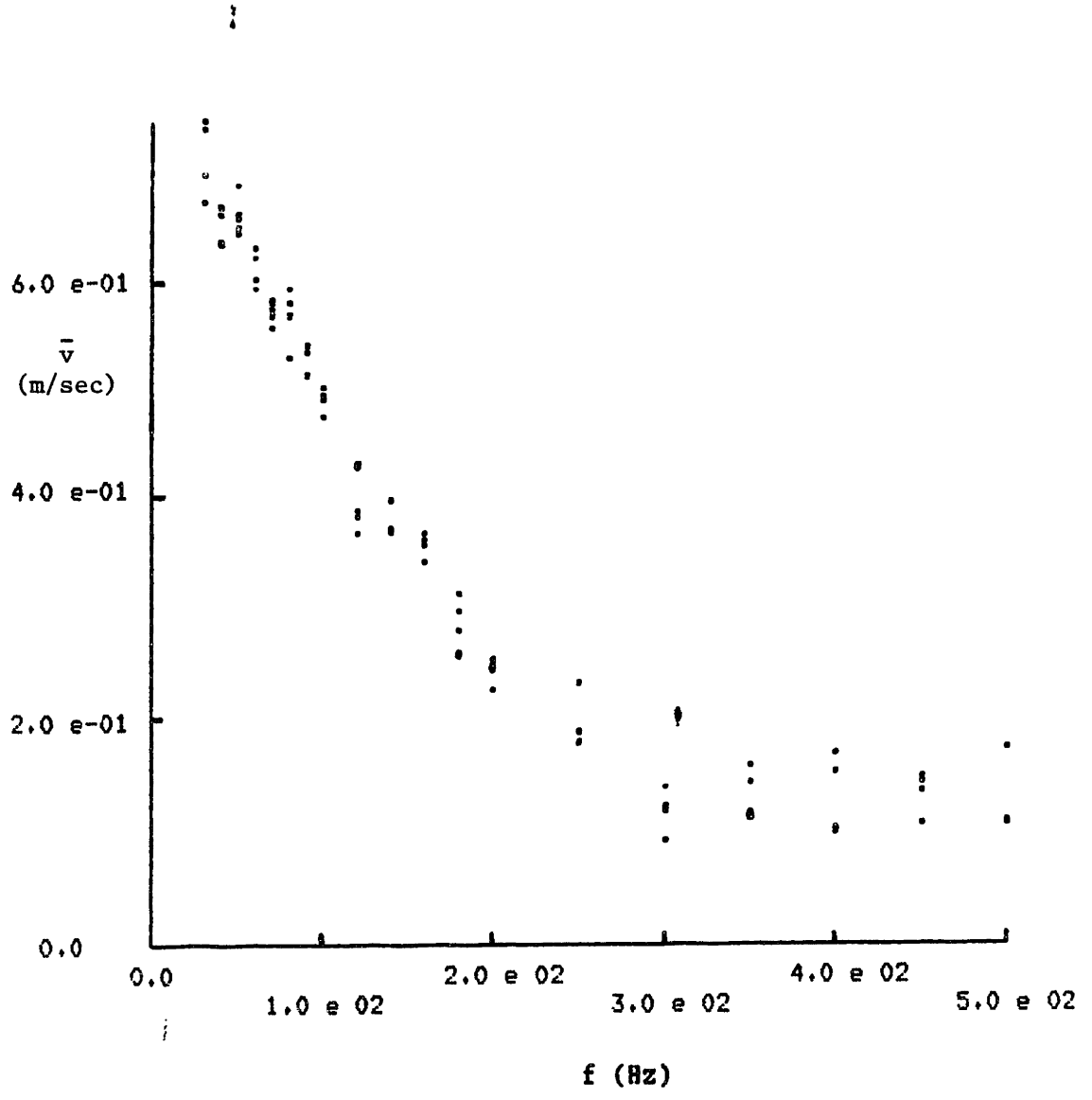

Figure 6.21. Plot of corona wind velocity vs. frequency for 8.0 kV RMS excitation. The horizontal flow velocity was 4.3 m/sec. The LDV observation volume was 6 mm above the corona wire, near to the center support bar (data from 6/15/83).

velocities reported for DC excitations at the same RMS voltage level. The frequency dependence of the corona wind [Fig. (21)] is of interest, as it gives a characteristic frequency above which the response is small. The velocity reaches a relatively low level at roughly 300 Hz, so that the characteristic half-cycle time is about 1.7 msec. The ion transit time, based on the wire-plate spacing, H = 1.5 cm, the electric field strength, $E_o = 3 \times 10^5$ v/m, ion mobility, $b_\pm = 10^{-4}$ m^2/v sec, is [see eq. (3.2.2)]

$$\tau_{m,\pm} \equiv \frac{H}{b_\pm E_o} \backsim 0.5 \text{ msec} \qquad (6.6.1)$$

This is considerably smaller than the half-cycle time at 300 Hz. The electric field strength used to calculate $\tau_{m,\pm}$ is that which exists in the steady-state (ie., with effects of a built-up ion space-charge). With high-frequency excitations, a better estimate of the electric field strength at the plate might be obtained by a solution which satisfies Laplace's equation [ie., assuming negligible space charge effects]. In that limit, the electric field strength that would accompany a voltage of $V_o \backsim 8$ kV, with a wire-plate spacing of $H \backsim 1.5$ cm, with a wire diameter of $D \backsim 0.006$ inch, is $E_o \backsim 10^5$ v/m. With such an electric field, the ion transit time becomes about 1.5 msec, much closer to the half-cycle time for a 300 Hz AC excitation. Thus, it is possible that the finite ion transit time influences the corona wind for high frequency excitations.

For the last plot presented here, both the LDV observation volume position and the electrical excitation were held fixed while the horizontal flow velocity, U, was varied. The horizontal axis in Fig. (23), however, is scaled in inverse proportion to the horizontal flow velocity, so that the plot shows the time-average vertical velocity as a function of the development time, τ_{dev}, defined in eq. (6.5.1). The shape and magnitude of the response is similar to those of the turn-on transients of Figs. (12) and (13). The transverse flow apparently "develops" as it is convected downstream by the main flow.

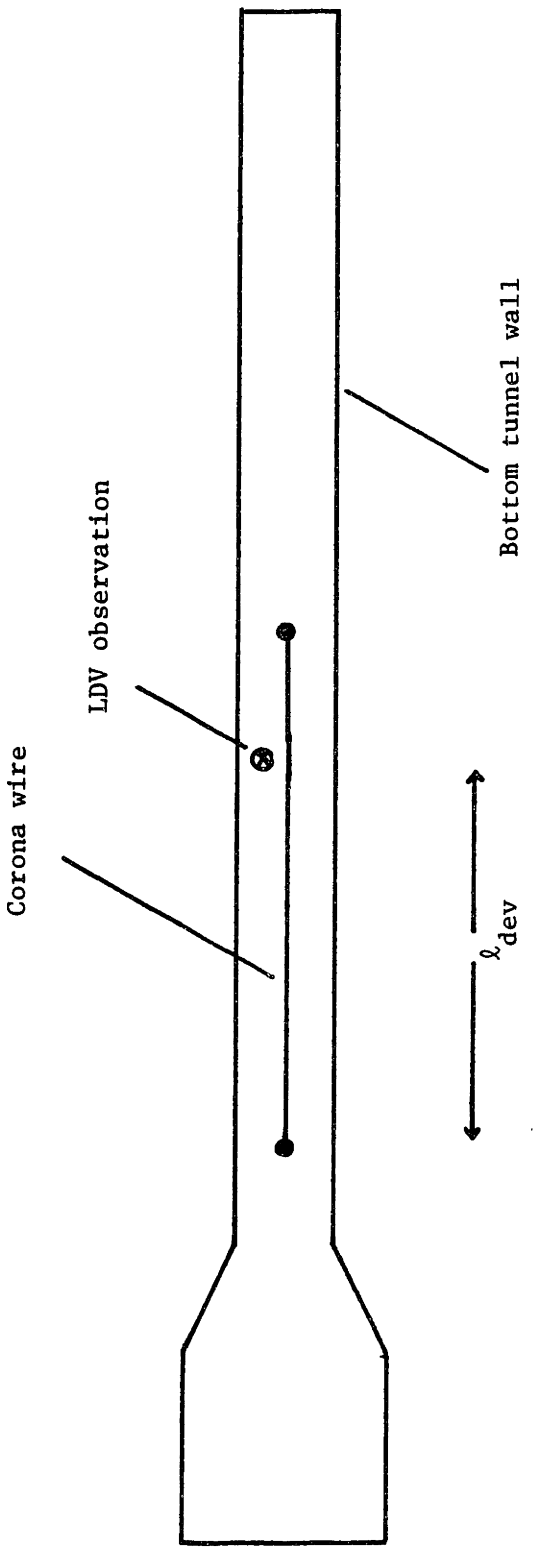

Fig. 6.22. Schematic illustration of experimental setup for corona wind measurements. LDV observation volume was $\ell_{dev} \simeq 67$ cm from upstream end of corona wires.

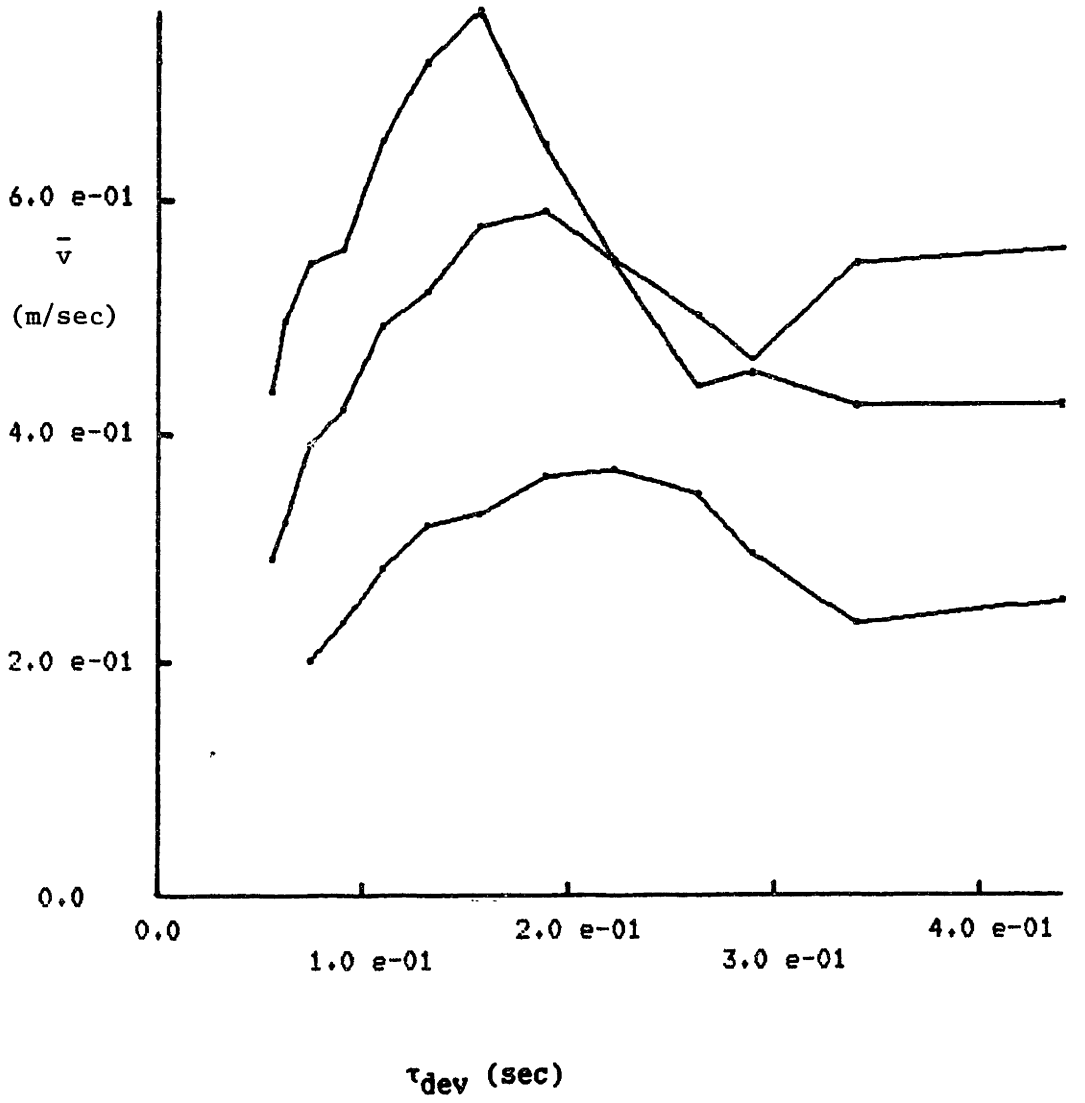

Figure 6.23. Plots of time-average corona wind velocity vs. development time, τ_{dev}, for 50 Hz AC coronas at three different current levels. For the uppermost curve, the RMS voltage was 8.2 kV, the "RMS" current was 4.0 ma. For the middle curve, the voltage and current were 7.6 kV and 3.0 ma. For the lower curve, the corresponding values were 6.9 kV and 2.0 ma. The LDV observation volume was 4 mm above the corona wire, 67 cm downstream of the upstream end of the wires (data from 8/20-22/83).

6.7 Miscellaneous Flow Measurements

Two miscellaneous measurements of the flow characteristics in the laboratory-scale precipitator are reported in this section. As both were made without any electrical excitation present, it is not appropriate to group them with any of the data presented in other sections. They serve to characterize the flow in the tunnel when it is undisturbed by effects of the corona.

Figure (24) shows the variation of the RMS spread in the streamwise velocity with the mean value of that velocity. This data was measured in the upstream (ie., charging) section of the precipitator, with the (grounded) wires present. Profiles of the mean and RMS spread in horizontal velocity vs. vertical position in the downstream (ie., migration) section of the precipitator are shown in Fig. (25). Although the measurement was made only 11 cm downstream of the leading edge of the plate, it is seen that boundary layers of significant thickness exist at each surface of the flow region.

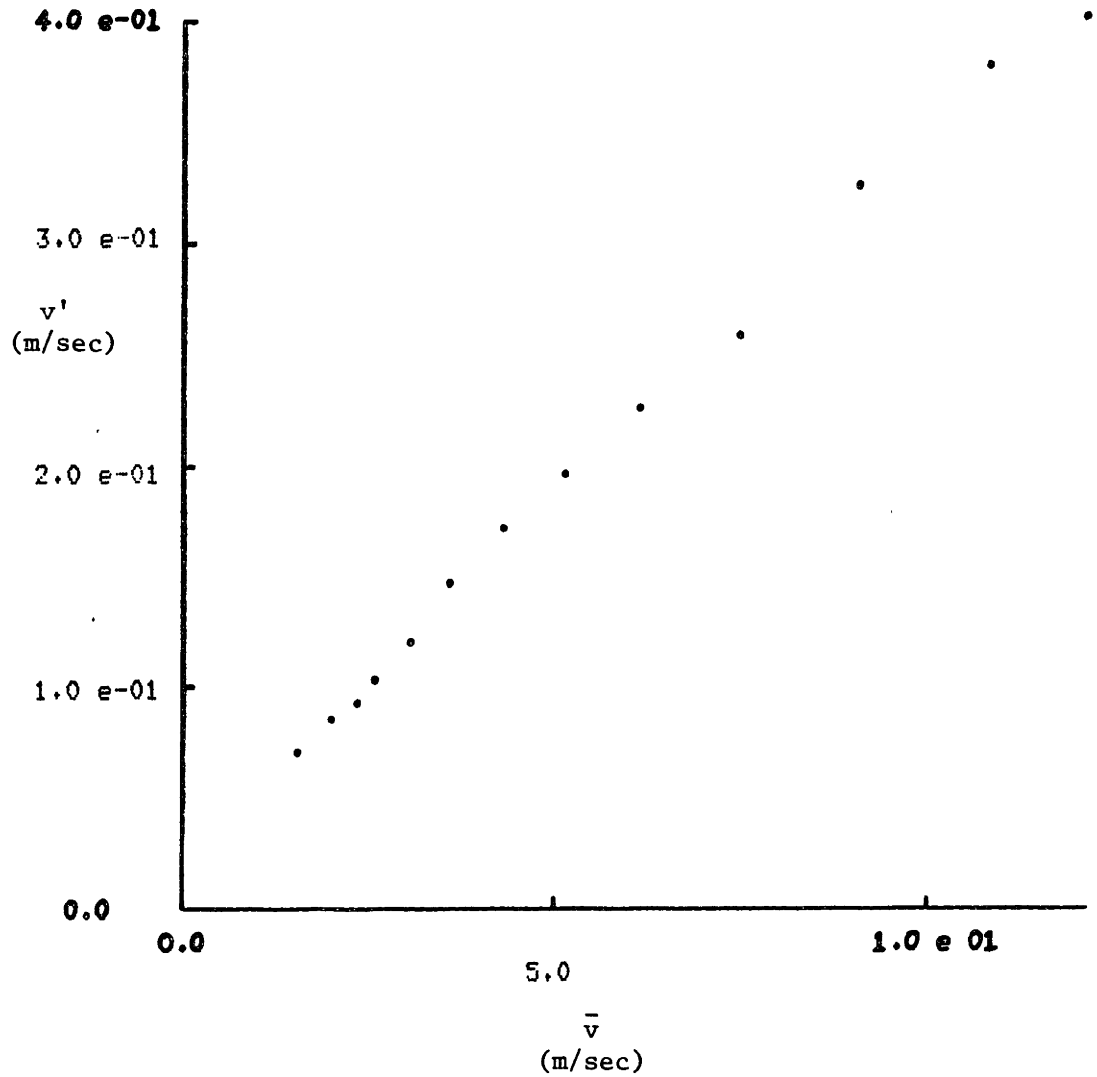

Fig. 6.24. Plot showing variation of RMS spread in horizontal flow velocity with mean horizontal flow velocity. LDV observation volume was in charging section of precipitator, but the corona wires were grounded. (Data from 8/20/83)

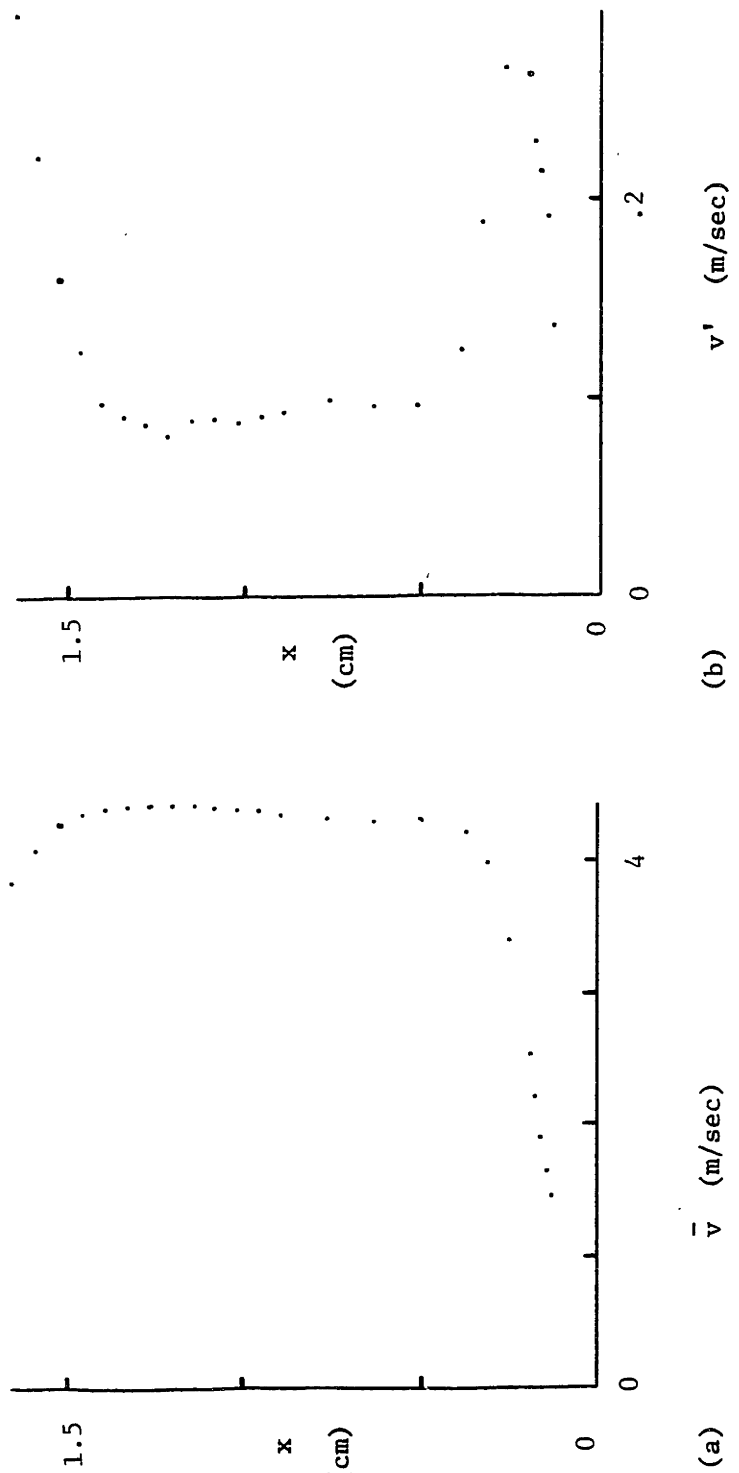

Fig. 6.25. Plots showing mean (a) and RMS spread (b) of horizontal flow velocity vs. distance above migration plate (no voltages applied). LDV observation volume was scanned vertically. Streamwise horizontal position was ~ 11 cm downstream of leading edge of plate.

6.8 Conclusions

In a typical application of laser-doppler velocimetry to air-flow measurements, seed particles are added to the gas stream to scatter light from the directed laser beams. The mechanical properties of the particles [ie., the size, shape, and density] are normally chosen so as to make the particle inertia negligible. Thus, they follow the flow, serving as little more than passive markers of the fluid velocity field.

The experiments of chapter 5 are unusual, in that the most important quantity being measured by the LDV involves the motion of charged particles relative to that of the air surrounding them*. Rather than being passive flow markers, the particles are an integral part of the process under study [ie., AC corona charging]. Fluid mechanical effects, such as the flow turbulence, are considered there to be unwanted noise.

The opposite is true of the data and models reported in this chapter. The corona wind and turbulent mixing are both fluid mechanical phenomena, and do not require the presence of particles. For the corona wind experiments, the particle migration is considered to be "noise", while the greater part of the measured velocity is that due to an induced air flow. Even though particle mobilities are measured in the turbulent mixing experiments, the mobility is viewed only as a sinusoidally-varying passive scalar contaminant which decays with increasing axial coordinate, due to the turbulence. Observation of the migration velocity of particles simply provides a convenient measure of the particle charge density in the flow. In principle, any other passive scalar contaminant could have been used#.

The main purposes of the experiments described in this chapter were : (1) to document the flow conditions in the laboratory-scale

---

*The particle mobility is defined as the ratio of the particle migration velocity, relative to its surrounding medium, to the imposed electric field strength

#For example, a sinusoidally-varying point-source of heat, coupled with a sensitive thermocouple further downstream, could have given a measure of the diffusion of heat by the flow turbulence

precipitator, and : (2) to provide values for parameters such as the effective turbulent diffusivity and typical corona wind velocities, for use by models developed elsewhere. The results of these experiments are summarized below.

The turbulent diffusivity measurements produced values for D_t that agree, to within an order of magnitude, with those reported by other researchers*. The longitudinal turbulent diffusion model of section 6.3 was able to match the results of diffusivity measurements made over a range of frequencies reasonably well [see Fig. (8)]. The inferred flow diffusivities were of the order of 10^{-3} - 10^{-2} m^2/sec.

Evidence was presented that the particle velocities measured in the corona wind experiments were due, for the most part, to induced motions of the air in the tunnel, as opposed to particle migration effects. The time-average particle migration velocity is seen, both in the models of chapter 3 and in the experiments of chapter 4, to decrease with increasing electrical excitation frequency. Thus, it may be that the experiments run with AC coronas gave more accurate measurements of the corona wind velocity, itself.

The value of the characteristic velocity, U_E, defined by Yamamoto [eq. (1.5.3)], can be determined roughly for the situation examined here. Using the approximate formula of eq. (1.5.7), with $i \simeq 2$ ma, $\ell \simeq 3$ m, $b_i \backsim 10^{-4}$ $m^2/v \cdot sec$, and $\rho \backsim 1$ Kg/m^3,

$$U_E \backsim 2.6 \text{ m/sec} \qquad (6.8.2)$$

The measured velocities, on the order of 1 m/sec, are within an order of magnitude of this value.

---

*A review of research on turbulent mixing is to be found in section 1.5.2

Chapter 7

Conclusions and Suggestions for Future Work

7.1 Introduction

In chapter 1, the motivations for this thesis work were stated in terms of both practical and scientific goals. The practical goal was to determine the feasibility of AC electrostatic precipitation as a means of collecting highly resistive particulate. From a scientific viewpoint, the experiments and models described in chapters 2 - 6 were intended to offer insight into the charging, transport, and collection processes that occur in an electrostatic precipitator.

This chapter summarizes the most important experimental and theoretical results of the previous six chapters. Section 2 summarizes the major experiments performed and the results that were reported in the last three chapters. The various models proposed there, and in chapter 3, are then reviewed in light of these results in section 3. An evaluation of the practical application of AC electrostatic precipitation is presented in section 4. Finally, section 5 contains suggestions for future work.

7.2 Summary of Experiments

The experiments performed for this thesis provide a quantitative evaluation of the overall performance of a laboratory-scale electrostatic precipitator, as well as an examination of the individual mechanisms that together comprise the collection process. Although the major goal of the research was to investigate AC precipitation, the data that was obtained using DC excitations, for purposes of comparison, stands in its own right.

7.2.1 Particle Mobility Measurements

Measurements were made of the mobility spectra of particles leaving corona chargers with various electrode configurations and excitation schemes. The technique of determining mobility statistics of charged particles by direct measurement of their migration velocity in response to a known electric field has been used in the past[1]. The experiments presented in chapter 5 are, though, to the author's knowledge, the first to use a laser-Doppler velocimeter to clearly show the effects of a non-uniform electric field and corona current on the DC charging of particles*. No previous reports on AC particle charging measurements of any kind were found in the literature.

With low-frequency AC excitations of a given RMS voltage applied to the corona wires, the migration velocity distributions obtained are roughly approximated by a superposition of those distributions which correspond to positive and negative DC coronas of similar magnitude. The RMS spread in measured velocity decreases gradually as the frequency is increased. A bias in the particle charge exists which generally increases with frequency. The sign of the charge bias is highly dependent upon the electrode geometry.

7.2.2 Corona Wind Measurements

Measurements were made of the velocities of particles under the influence of the corona wind in the laboratory-scale precipitator. Evidence was presented that the observed velocities were, for the most part, due to the corona wind, itself. With electric field strengths typical of those in a commercial device, and corona current densities within an order of magnitude of those used normally#, The measured wind

---

*Although some of the increased spread in particle velocities shown in Fig. (5.5) can be attributed to variations in the particle size, from one particle to another, the differences in the distributions obtained with positive and negative DC coronas cannot be explained by such an argument.

#The levels used here were $\sim$ 0.5 - 1 $\mu A/cm^2$, typical levels are of the order of 100 nA/cm^2

velocities were of the order of 1 m/sec. The time-average flow velocity induced by AC excitations of a fixed RMS voltage decreased with increasing frequency, falling to a low level for frequencies above about 300 Hz. For reference, the ion transit time from wires to plates, with DC excitations, was about 0.5 msec. As was noted in section 6.8, this transit time is based upon the electric fields which exist near the plates in the presence of a steady-state corona ion charge distribution. In the absence of ion space-charge effects[#], the electric field strengths could be considerably lower, resulting in ion transit times that are of the order of the half-cycle time with 300 Hz.

7.2.3 Turbulent Diffusivity Measurements

Measurements of the Effective diffusivity of the flow in the laboratory-scale precipitator were performed, using a new approach which exploited the AC charging of flow-entrained particles. The measurements yielded values that were of the order of 10^{-3} - 10^{-2} m^2/sec. One unique feature of the technique used was that it could, in principle, determine the effective diffusivity of a flow from measurements made at a single point in space. Particles were charged using one of the electrode configurations that was under study in the experiments of chapter 5. The Fourier component of measured particle migration velocity at the AC charging frequency was compared to the RMS velocity spread. The ratio between the two gave an indication of the decay in coherence of the particle charge density function, which was assumed to be purely sinusoidal at the charger.

7.2.4 Precipitation Efficiency Measurements

The collection efficiency of the laboratory-scale precipitator was determined by the use of a mass-monitor. The aerosol mass-loading of the air-stream leaving the tunnel was measured while electrical excitations that varied in frequency and peak voltage were applied to the corona

---

[#]With high-frequency AC voltages, the ion space-charge distribution may not reach a steady-state during a half-cycle of the excitation

wires. These experiments provided quantitative measurements of the overall performance of the device with both DC and AC excitations. The data from these experiments was found to be consistent with the charging measurements reported in chapter 5*. This, in itself, is reassuring, given the fact that two entirely different diagnostic instruments were used in these experiments. With low-frequency AC excitations of a given RMS voltage, the collection efficiency approached that obtained with positive DC voltages of similar magnitude. The effective precipitation velocity of the particles decreased with increasing excitation frequency (as the voltage magnitude was held fixed), apparently approaching zero velocity for very high frequencies. The collection efficiency measured with negative DC coronas of either the same voltage or current (as was used with the positive DC corona) was significantly higher.

*The same models which predict the RMS spread in particle charge can also be used to predict the overall precipitation efficiency. These models are discussed in section 7.3.

7.3 Review of Models for Particle Charging and Precipitation

7.3.1 Particle Charging

The uniform-field charging model of chapter 3 approximates the corona charging process in an electrostatic precipitator as one which occurs in a spatially-uniform electric field and corona ion flux. The values of electric field and corona current density used are normally those that exist in the vicinity of the collection plates in the actual precipitator. In Chapter 5, this simplified model is seen to predict successfully both the order of magnitude of particle mobilities and the variation of the mean mobility with excitation voltage* for DC charging experiments performed on the laboratory-scale precipitator with a wire-plate electrode configuration.

With AC wire-charging at frequencies below about 100 Hz, the model is able to predict some of the mobility statistics, such as the RMS spread in particle mobility, accurately. The measured frequency dependence of the mean particle mobility, however, cannot be explained. At higher frequencies, the measured and predicted charging statistics differ greatly.

The most likely reasons for the inability of the uniform-field charging model to match the experimental results of AC charging experiments involve violations of its basic assumption; that of spatially uniform electric field and corona current density. These reasons are : (1) The negative corona current is not uniformly distributed over the length of the corona wire, while the positive is, and (2) the finite ion migration velocity results in moving "fronts" of ion charge, rather than quasi-stationary corona currents, in the charging region of the precipitator. The importance of the first is demonstrated by the barbed-wire charging experiments of section 5.3.5, in which the sign of the particle charge bias was reversed by restricting the positive and negative coronas to similar geometries. The crude charging model of section 5.4.6 suggests one way in which such

---

*It can predict the variation of mean mobility with voltage for voltages above the corona onset level.

differences in the spatial distribution of corona currents could affect the particle charge statistics.

It is likely that the second factor becomes important at frequencies of $\sim$ 300 Hz, as it is then that the ion transit time, from wire to plate, is of the order of the half cycle time of the excitation*. The corona wind measurements of chapter 6 [Fig. (6.21)] show that the induced flow velocity falls off at about that frequency.

7.3.2 Particle Transport and Precipitation

The results of application of the uniform-field charging model are embedded into the turbulent diffusion model of chapter 4, and used to predict the precipitation efficiency with AC excitations in terms of the measured performance with positive DC coronas. This model accounts for effects of the flow turbulence by means of an effective turbulent diffusivity, whose value is obtained from the mixing measurements and analysis of chapter 6. The results match measured precipitation data to within experimental error over the entire observed frequency range (20 $\rightarrow$ 500 Hz).

The large difference between the measured performance with positive and negative DC coronas cannot be explained by the model. This discrepancy is especially perplexing in view of the similarity between the results of charging experiments in the two cases. It is likely that the cause of the difference lies in the disparate distributions of corona current density.

In chapter 1, it was stated that two distinct collection processes can occur in a two-stage AC electrostatic precipitator; one being due to the oscillatory particle migrations, the other resulting from their time-average motion. The discussion of section 4.5 was concluded with the idea that only the latter collection mechanism contributed significantly to the measured efficiency of the laboratory-scale precipitator. The particle oscillations were seen to be unable to aid in

---

*See comments in section 6.8

the precipitation process because the flow turbulence could not transport particles to within a short enough distance of the plates.

One of the scientific motivations given in chapter 1 for the study of AC electrostatic precipitation was the possibility that the process could be made to be very sensitive to the turbulence characteristics in the core region and in the boundary layer flows of a precipitator. It is seen in chapter 4 that the linear regions* of the boundary layers in the laboratory-scale precipitator are thick enough that the oscillatory particle migrations are unimportant in determining the collection rate, and that the device acts much as a DC precipitator, with the effective migration velocity being replaced by the time-average velocity of the particles. Thus, the laboratory-scale precipitator is no more sensitive to the turbulence conditions in the flow than is a DC device.

A two-stage AC precipitator, excited by an unbiased collection electric field, could give particles a zero time-average migration velocity, so that the only possible mechanism of collection would be that due the combination of turbulent transport and particle oscillatory motions. Such a device would allow investigation of the turbulent transport processes in an electrostatic precipitator.

---

*The linear region of the boundary layer is one in which little turbulent transport takes place, as is discussed in section 4.5.

7.4 Practical Application of AC Electrostatic Precipitation

The most obvious question that one might ask about AC electrostatic precipitation is "Does it work?". The answer to that question is most certainly yes. An AC precipitator can be made to collect significant amounts of particulate, as is demonstrated by the experimental results of chapter 4. Perhaps a more relevant question is " How well does AC electrostatic precipitation work, in relation to DC precipitation with highly resistive particulate and with moderately resistive particulate?". This section addresses the second question.

7.4.1 Comparison of AC and DC Performance with Highly Resistive Ashes

In the laboratory-scale precipitator, the effective particle migration velocity with a 60 Hz AC excitation of a given RMS voltage magnitude [8 kV RMS] is about 28 % that obtained with a negative DC excitation at that same voltage level. If this were assumed to hold true for a commercial precipitator, then under ideal conditions [ie., when the DC device was not constrained by a highly resistive particulate], an AC precipitator would have to be about 4 times as big as its DC counterpart in order to achieve the same collection efficiency. Of course, as the particulate resistivity rose, the performance of the DC device would be degraded, while the AC precipitator would presumably continue to operate at roughly the same levels of efficiency. Thus, a parameter of some importance is the particulate resistivity at which the size required of a DC precipitator is the same as that of an AC device which has the same collection efficiency.

Figure (1.3) shows the variation of the effective precipitation rate, w_{eff}, with the particulate resistivity, ρ_ℓ, for a typical commercial device. According to the data presented there, the precipitation rate falls by a factor of about 4 as the resistivity rises from 3×10^9 Ω-cm to 7×10^{11} Ω-cm. Thus, if issues of the power supply cost are to be neglected*, then one would do better to use an AC

---

*An AC precipitator running with a 60 Hz excitation would require no rectifiers to obtain its power from an AC line.

precipitator to collect particulate whose resistivity was above $\sim 10^{12}$ Ω-cm.

7.4.2 Avoidance of Back Corona in AC Electrostatic Precipitation

It is seen in section 1.4.2 that, in the limit of infinitely resistive particulate, the AC precipitator is tightly constrained in its operating regime. The excitation frequency must be high enough to avoid large accumulations of ion charge on the collected particulate layer, yet low enough that the particles are charged to a significant fraction of the appropriate saturation charge. These limits are expressed mathematically in eq. (1.4.7), in terms of an interval over which the excitation cycle time may vary. It is also seen in section 1.4 that the corona current density must be higher than values commonly used in precipitators [$\sim$ 0.5 - 1 $\mu m/cm^2$], in order that the range of allowable frequencies include 60 Hz. Smaller current densities can be used, at the expense of lower particle charging levels.

No experiments were performed to verify the immunity of the laboratory-scale precipitator to back corona problems, as the particles used in the experiments were not highly resistive. Its collection efficiency was measured under conditions which crudely simulated the presence of a highly resistive particulate layer. High-voltage insulating tape was placed over the collecting plates, preventing the conduction of any time-average current. As would be expected, the precipitator was unable to collect any particulate using DC excitations[#]. With AC excitations, the precipitator functioned essentially as it had with the uncovered electrodes.

7.4.3 Scaling

All of the experimental results presented in this thesis were obtained from the laboratory-scale precipitator, whose dimensions are roughly 1/8 of those of a typical commercial device. It is of interest

---

[#]There was no corona current, as the entire applied voltage appeared across the insulating tape.

to determine whether these results are applicable to a full-size precipitator.

Many of the dynamic processes that occur within an electrostatic precipitator have characteristic times which depend upon the wire-plate spacing, H. Among them are : (1) the particle migration time, $\tau_{mig} \equiv H/w_{net}$ [see eq. (4.4.5)], (2) the turbulent diffusion time, $\tau_d \equiv H^2/D_t$ [see eq. (4.4.4)], and (3) the ion transit time, $\tau_{m,\pm} \equiv H/b_{\pm}E_o$ [see eq. (3.2.2)]. All three of these times are seen to rise with increasing lateral dimension of the precipitator.

In a comparison of the performance of AC precipitation to that obtained with DC excitations, the first two are unimportant. Given a fixed time-average particle migration rate, both suffer (or benefit) equally from increased migration or diffusion times*. Changes in the ion transit time, however, are likely to have much more effect on the AC precipitation process than they do on the DC.

Adding to the wire-plate spacing increases the time that ions must spend enroute from the wires to the collection plates, thus allowing the air flow to convect them further downstream. This is unlikely to have much effect upon the distribution of corona ions in a DC precipitator, as the ion migration velocity, v_i, is normally much greater than the flow velocity, U#. If the ion transit time in an AC device becomes of the order of or greater than the half-cycle time of the excitation, however, then the ions may not even reach all points within the precipitator. In the limit of a very high excitation frequency, so that $\tau_{m,\pm} \gg T$, the excitation cycle time, then only a very small volume immediately about the corona wires will contain significant concentrations of corona ions.

The corona wind velocity induced by AC excitations in the laboratory-scale precipitator fell off at a frequency of roughly 300 Hz.

---

*This is true only because the time-average particle motions dominate the precipitation process with AC collection. If the particle oscillatory motions were significant in determining the precipitation efficiency of the AC precipitator, then the flow turbulence would affect the DC and AC devices differently, as is pointed out in Appendix 3.

#The ion migration velocity, v_i, is of the order of 10 - 50 m/sec, while the flow velocity, $U \sim 1 - 2$ m/sec.

It is likely that effects of the finite ion migration velocity were responsible for this fall-off. For a fixed electric field strength, the ion transit time [eq. (3.2.2)] is proportional to the plate spacing. Thus, the effect of a larger plate spacing would be to lower the critical excitation frequency above which the ion charge distribution was no longer quasi-stationary. If the plate spacing were 8 times bigger, with no change in either the ion mobility of electric field strength, then this critical frequency could become as low as 40 Hz. Thus, with the field strengths used in the laboratory-scale precipitator, ions might not reach all points in a full-scale device during the time of a half-cycle of a 60 Hz applied excitation. Even those particles that are near to the corona wires might spend a considerable fraction of the time subjected to a bipolar flux of ions [one moving away from the wires, the other consisting of ions from the previous half-cycle, being attracted back toward the wires].

7.5 Suggestions for Future Work

The first four chapters of this thesis seem to form almost a complete investigation of AC electrostatic precipitation. The uniform-field charging model of chapter 3 is embedded into the turbulent diffusion model of chapter 4 to make accurate predictions of the AC precipitation efficiency in terms of that obtained with positive DC voltages. The only apparent disrepency is the unexplained difference between the efficiencies measured with positive and negative DC voltages of the same magnitude. The experimental evidence presented in chapter 5, however, shows that several factors that are unaccounted for by these simple models can be important in determining the mobility statistics of particles charged by an AC corona. Rigorous models that incorporate such factors have yet to be developed.

This section contains suggestions for future work that may lead to a better understanding of the charging, transport, and collection mechanisms in an AC electrostatic precipitator. Section 1 outlines a set of experiments whose results should be well-modeled by the uniform-field charging model of chapter 3. Two-stage AC precipitation experiments, which promise to allow sensitive investigation of the turbulence characteristics of the flow in an electrostatic precipitator, are proposed in section 2. In section 3, reference is made to an earlier work on the charging of particles in turbulent air streams, which could be applied to those experimental results already obtained from the laboratory-scale precipitator. Experiments which investigate scaling issues are covered in section 4. Finally, section 5 recommends experiments which can verify the immunity of AC precipitators to back corona problems.

7.5.1 Corona Triode Charging and Precipitation Experiments

It would be useful to study particle charging and migration under conditions for which the assumptions of the uniform-field charging model of chapter 3 are valid. Figure (1) illustrates schematically such an experiment, which uses a corona triode to charge and precipitate particles. The triode consists of three electrodes, referred to here as the pin, grid, and ground electrodes, to produce a uniform, controlled flux of ions in the charging region, while minimizing effects of the corona wind there.

Ions are produced at the pins by a large voltage imposed between the pin and grid electrodes. The grid electrode is constrained to a potential that is partway between that of the pin and ground electrodes. Thus, some of the ions produced at the pins will follow electric field lines through the grid toward the ground plate. If effects of the ion space-charge and finite migration velocity are negligible, then both the imposed electric field strength and corona current density will be nearly uniform in the lower region.

Those particle which pass below the grid should thus charge and migrate according to the equations of the uniform-field charging model. The LDV could then be used to study the process in any of three different modes : (1) The mobility statistics of particles leaving the charger could be measured in much the same way as with the experiments reported in chapter 5, (2) The particle migrations in the charging region could be observed directly, or (3) the LDV could be used as a particle counter, providing measurements of the particle concentration in the charging/precipitation region of the triode.

It is expected that the positive and negative charging characteristics will be similar when equal magnitude imposed electric fields and current densities are used*. In addition, the AC charging should behave as predicted in chapter 3.

---

*Of course, if one were sure of the outcome of an experiment, then the actual performance would be unnecessary.

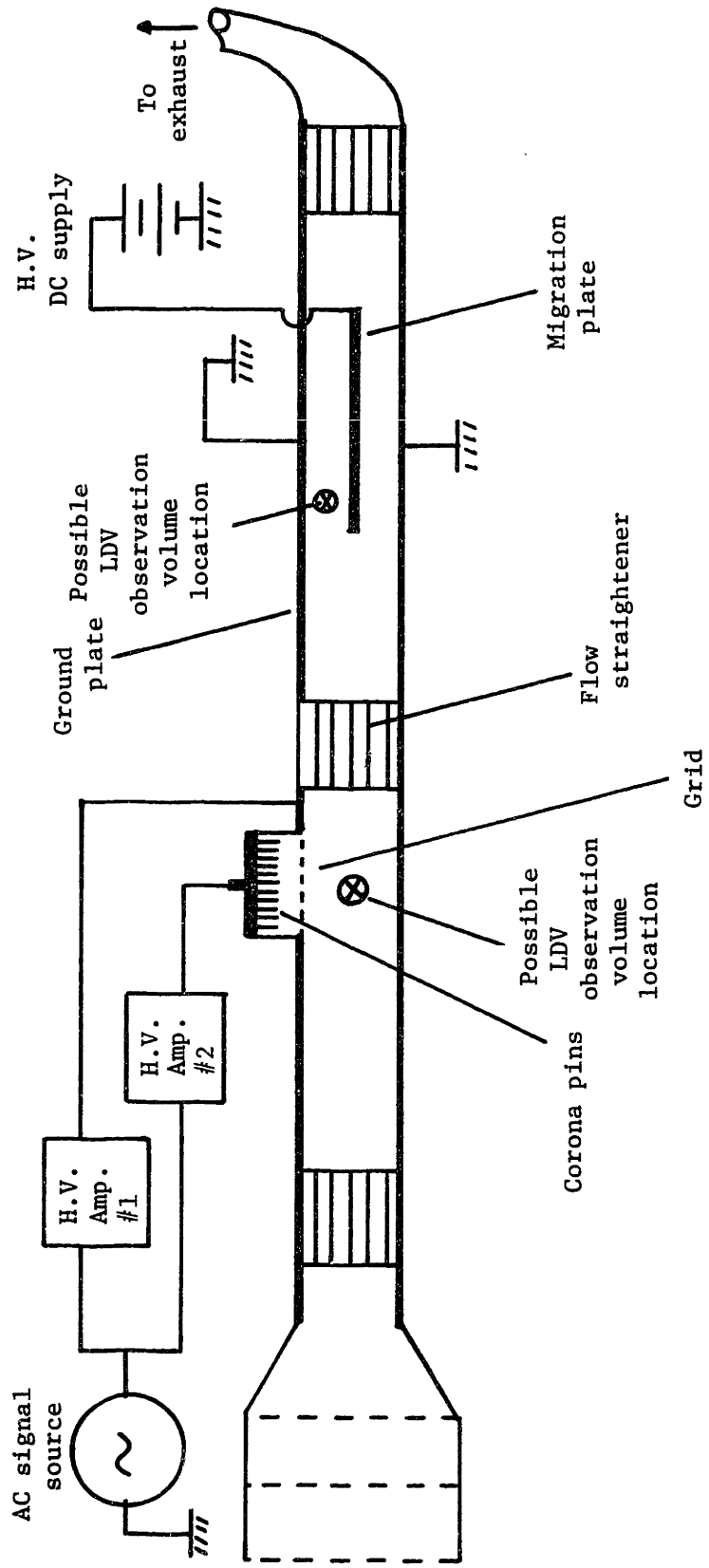

Fig. 7.1. Possible configuration for corona triode AC charging and precipitation experiments. Particles are charged and some precipitate below the triode grid. Those that do not precipitate are convected by the air flow to the migration plate. Measurements of particle charging statistics can be made at the migration plate. Particle net precipitation velocity in the AC corona can be measured below the grid.

7.5.2 Two-Stage AC Electrostatic Precipitation Experiments

The corona triode charger described in the previous section could be used with a DC excitation to supply particles of a uniform mobility[#]. These particles could then be subjected to an unbiased AC collection field, to study the two-stage precipitation of pre-charged particles. The major purpose of such a study would be to obtain a precipitator whose efficiency is a sensitive function of the turbulence conditions both in the main flow and in the boundary layers adjoining the collection surfaces.

For initial experiments, the migration plate used for the charging measurements of chapter 5 could serve as the high-voltage electrode in such an experiment. The LDV could be used to measure the collection efficiency by observation of the axial decay in particle concentration.

7.5.3 Modeling of Charging and Precipitation from Turbulent Flows in Non-Uniform Fields

No attempt was made in this thesis to incorporate the results of Radun [see section 1.5.1] for the charging, transport, and precipitation of particles from turbulent flows, in the presence of non-uniform but steady electric fields and corona current densities. His equations were complicated enough to preclude analytic solutions in any but the simplest cases. It is still of interest to apply the model that he derived to the situation of steady-state AC charging and precipitation of particles. Even if a numerical solution is required, such a solution should still be used to verify the validity of the model. Simplifications of the general model could then be made, on the basis of an understanding of those effects that are of most importance to the problem at hand.

[#]This assumes that the particles produced by the aerosol generator are of uniform size

7.5.4 Scaling Studies

It would be difficult to construct a full-scale model of even one pair of plates of a commercial precipitator. However, studies of charging and precipitation processes over a range of plate spacings could be used to determine what trends, if any, exist as the length-scales are increased. It would be useful to at least double the transverse dimensions of the laboratory-scale precipitator. Of additional interest would be observation of the AC charging and precipitation processes which occur when the corona wires are transverse to the main flow, as they are in a conventional device.

7.5.5 Studies of Back Corona Prevention in AC Electrostatic Precipitators

In section 1.4, two questions concerning AC electrostatic precipitation were raised. They were : (1) Under what conditions would an AC precipitator be able to operate without any effects of back corona, regardless of the particle resistivity?, and (2) would operation under those conditions result in appreciable particulate collection? The first question was addressed theoretically in that section, while the second formed the basis for all of the experimental work of this thesis. As the practical motivation behind the study of AC electrostatic precipitation is the desire to obtain a precipitator that is immune to effects of the resistivity of the precipitated particulate, it is of great interest to verify, experimentally, the results of the analysis of section 1.4. Two possible experimental programs are outlined below.

The most direct approach involves simply substituting a highly-resistive particulate for the DOP aerosol used in experiments on the laboratory-scale precipitator. It is not feasible to use low-sulfur fly ash, as its resistivity at room temperatures is not high enough to cause back corona problems with typical DC excitations. It should be possible, however, to obtain dusts of the toners used in electrophotography. These dusts have been developed to be of fairly uniform size, as well as very high resistivity [so as to retain a charge], and thus should be ideal for this application.

A very convincing (and reassuring) demonstration of the practical

application of AC electrostatic precipitation might consist of the following two experiments performed in rapid succession. One would attempt to precipitate a very highly-resistive particulate in the laboratory-scale precipitator, using a DC excitation at the corona wires. Because of problems with back corona, the precipitation efficiency would be very low, as could be verified in "real time" by use of the LDV as a particle density counter at the outlet of the precipitator. The DC excitation would then be replaced by an appropriately chosen AC voltage, at which point the collection efficiency would jump to a satisfactory level.

The experiments described above could take a long time to complete, as they require the buildup of a layer of resistive particulate on the collection plates. This buildup time could be eliminated if a way were found to permanently coat the collection surfaces with a material that simulates the presence of a highly-resistive particulate layer. The experiment could be run in a fashion similar to that described above, except that the initial transient (during which a particulate layer of sufficient extent was collected) would be unnecessary. This simulated highly-resistive layer might be as simple as a layer of insulating tape covering the electrodes, with pin-holes located periodically over the surface.

References for Chapter 7

[1]Mazumder, M.K., Renninger R.G., Chang T.H., Raible R.W., Hood W.G., Ware R.E., Sims R.A., "Simultaneous Measurements of Aerodynamic Size and Electric Charge of Aerosol Particles in Real Time on a Single Particle Basis", Third Symposium on the Transfer and Utilization of Particulate Control Technology: Volume II (Electrostatic Precipitators), p. 160 (July, 1982).

Appendix 1

Detailed Descriptions of Experimental Hardware and Software

A1.1 Wind-Tunnel

The precipitator is housed in a wind-tunnel, 3.18 cm high, 13.97 cm wide, and 2.44 m long (1-1/4 inch by 5-1/2 inch by 8 ft). The side walls are made of 0.64 cm thick glass (1/4 inch), and permanently epoxyed to sheet of aluminum which forms the bottom surface. Two different removable tops exist for the tunnel. One is simply another aluminum sheet, backed by a plywood board. The other consists of two separate, electrically isolated aluminum sheets attached to another plywood board (Fig. 1). In the latter case, the upstream aluminum sheet, which extends through the charging region, is grounded along with the bottom sheet. The downstream sheet is held at a high potential to provide a field with which particle mobilities can be measured. With this arrangement, it is not necessary to suspend the thin plate (described in section 2.2) between the top and bottom walls. All of the particle charging experiments reported in this thesis, however, were performed using the single aluminum sheet on top, along with the center plate.

During experiments, the top section is clamped to the glass side walls by four wooden struts, held down themselves by wing-nuts on threaded rods attached to the supporting table. In earlier experiments, the edge between the top and side walls was sealed by placing a bead of putty ("DAP" window-glaze) along the top of the glass. For later runs, strips of neoprene, 0.16 cm thick (1/16 inch) were glued to the top sections to provide the seal. The purpose of the change was simply to make opening and closing of the tunnel more convenient.

An entrance section, constructed of plexiglas, is placed upstream of the precipitator, in order to aid in mixing of the injected aerosol and to isolate the tunnel flow from effects of room air movements. Its inlet is covered by a plexiglas sheet through which 77 0.676 cm (0.266 inch) diameter holes were drilled in a rectangular array (11 wide by 7 high). The cross-section of the inlet is 9.53 cm by 13.97 cm (3-3/4 by 5-1/2 inch), the vertical and horizontal hole spacing is 1.27 cm (1/2

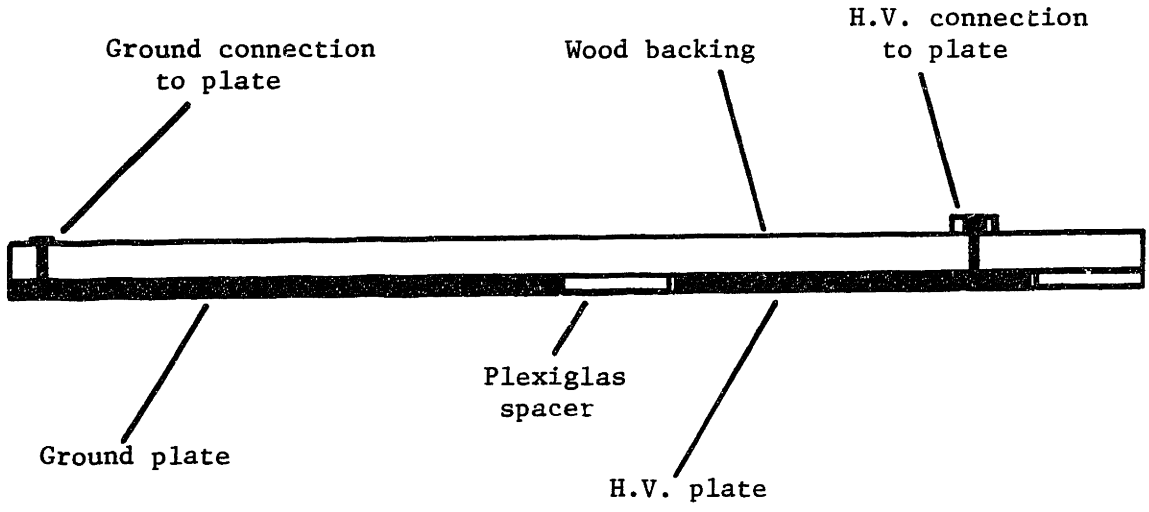

Fig. A1.1 Alternate top for precipitator.
The two aluminum plates are electrically isolated so that one can be grounded (through a small resistance) while the other is held at a high potential.

inch). About 5 cm downstream from the inlet are three 0.64 cm (1/4 inch) polyflow tubes which pass through the side walls of the section. Aerosol is injected into the section through small holes drilled in the tubes (about 20 per tube). Turbulence caused by jets of air passing through the inlet plexiglas sheet mixes the aerosol with the incoming air. Two more perforated metal plates, placed at 15.24 cm and 27.94 cm downstream of the inlet (5 and 11 inch, respectively) and a copper screen, at 41.91 cm (16-1/2 inches), allow further mixing before a contraction to the tunnel dimensions.

At the tunnel outlet is a short contraction section to a 6.35 cm diameter (2.5 inch) corrugated rubber tube. The tube is connected, via various air ducts, to a roof fan which provides suction to drive the flow. One section of the ducting, 60.96 cm (2 ft) in length, is perforated by 9 rows of 2.54 cm (1 inch) diameter holes, 6 holes per row. The holes can be covered by tape to increase the flow-rate, or left open to slow it down. In addition, a metal plate can be slid in or out to partially block the flow. Use of these crude controls allows experimentation with mean horizontal flow velocities that vary from roughly 1.5 to 12.0 m/sec.

A1.2 Aerosol Generator

The aerosol of particles used both for fluid-flow observation and for precipitation studies is produced by a Sinclair-LaMer evaporation-condensation aerosol generator. The system, pictured in Fig. 2, can provide a fairly monodisperse aerosol with average particle diameter anywhere from 0.01 to 1.5 μm. The particle size is determined by the proportions of alcohol and dioctyl-phthalate (DOP) mixed together in the atomizing chamber. Although references exist which thoroughly document its construction and operation [1,2], a brief description of the device is given below. The diagnostic instruments used to measure the performance of the generator are treated in the next section.

A fog is created in the main chamber (a glass jar, roughly 20 cm high, 10 cm diameter) by a pressurized air stream which entrains and atomizes the DOP/alcohol mixture. This fog leaves the chamber via a copper pipe which leads to a glass tube. An electrical resistance strip,

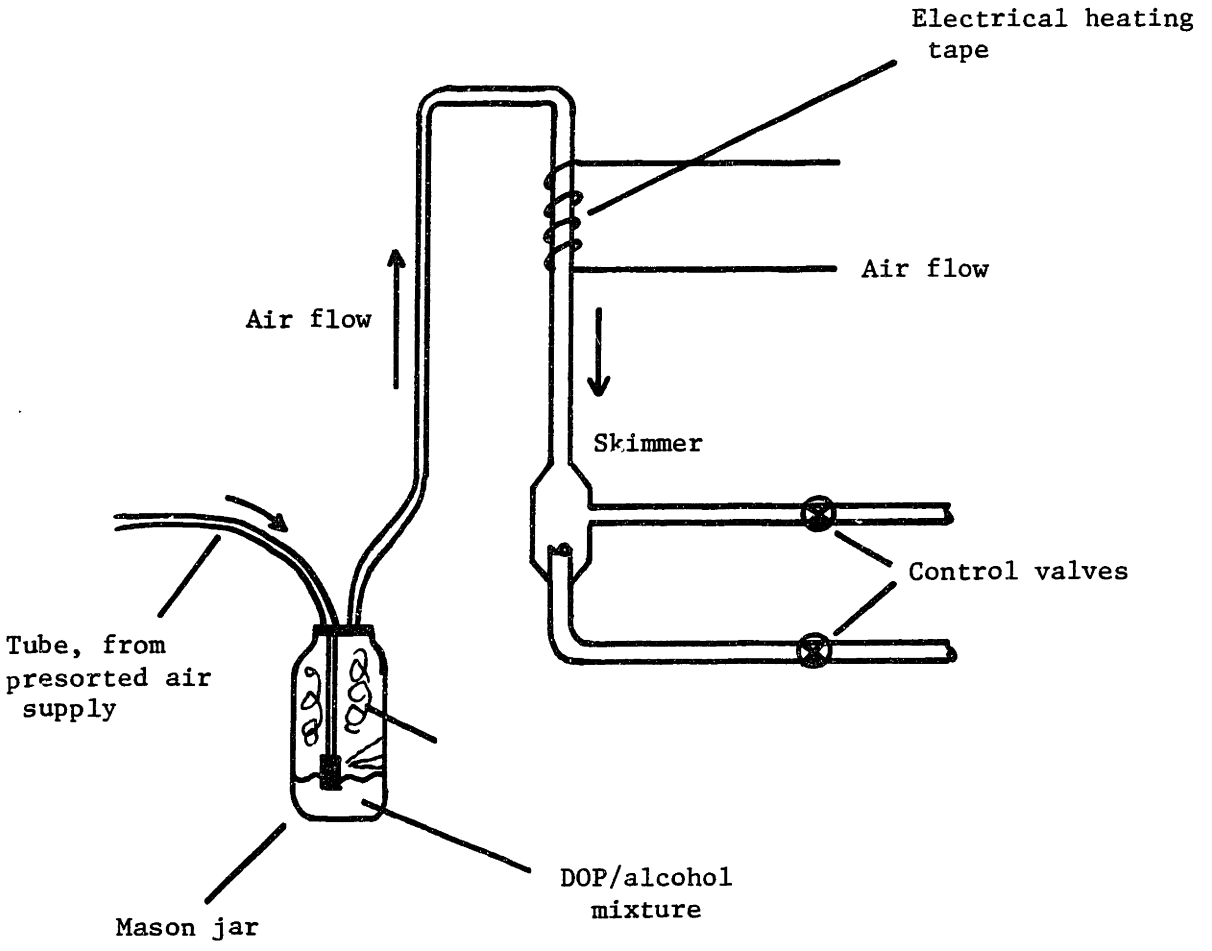

Fig. A1.2 Schematic illustration of Aerosol Generator. Pressurized air enters mason jar from left. Aerosol for experiment, and that which is discarded as well, exits on right.

wrapped around the glass tube, heats the air, vaporizing the fog. As the flow passes on to cooler sections of the tube, DOP particles recondense, nucleating on dust in the air. Aerosol particles near the center of the tube, where radial thermal gradients are at a minimum, are of relatively uniform size. Particles created near the tube walls are "skimmed off" by the arrangement shown in Fig. 3. The relative settings of the two constricting valves pictured there determine the amount of aerosol that is rejected. The aerosol that passes through valve (a) is then sent to the experiment.

The user has four major degrees of freedom in running the generator. They are: (1) the feed pressure at the inlet of the atomizer [The settings used for experiments run here ranged from 15 psig to 25 psig], (2) the voltage applied to the electrical heating tape [ranging from 45 to 70 volts RMS here], (3) the proportions of DOP and alcohol used in the atomizing chamber [the lowest concentration used was 10% DOP, the highest was 35% DOP], and (4) the settings of the two valves at the generator output. The pressure, voltage, and DOP/alcohol proportions used must be matched so as to allow for complete vaporization of the fog particles and recondensation to the desired size. In practice, settings are adjusted by use of the diagnostic instruments described in the following section.

A1.3 Aerosol Diagnostics

The two instruments used to size the aerosol particles used in experiments are : (1) an impacter which mechanically separates particles of different diameters by constraining the air flow in which they are suspended to follow tightly-curved paths, and (2) an optical sizer with which one determines the mean particle size by shining polychromatic (white) light through the fog and measuring the angles at which peaks of intensity are observed for red and green scattered light. Both devices are described in more detail below. Further information on the impacter may be found in the user's manual [3], and the optical scattering sizer is documented in theses by Sacher [1] and Zahedi [4].

The impacter, a commercial unit manufactured by Anderson (Atlanta, Georgia), separates sampled particulate into several different size

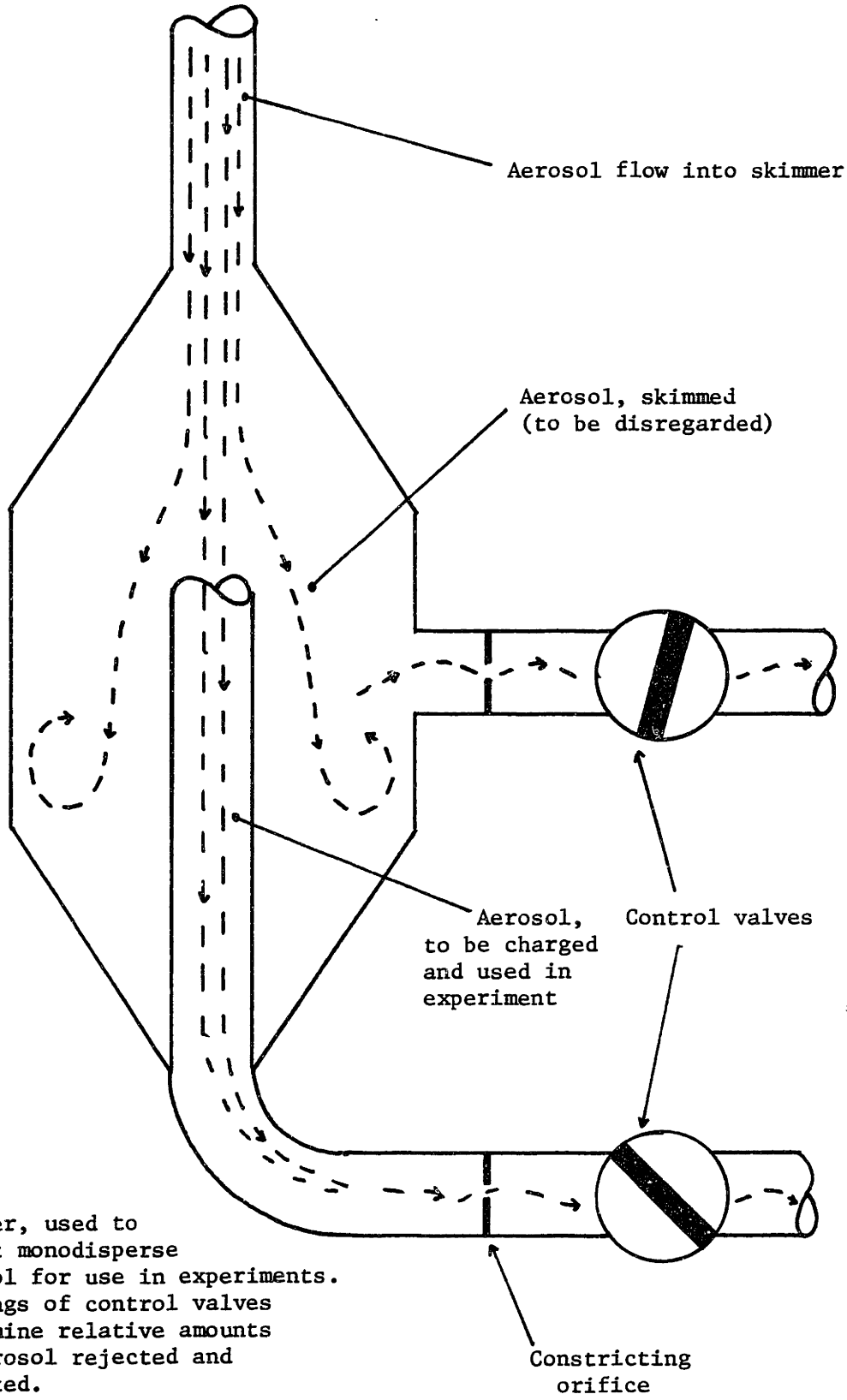

Fig. A1.3 Skimmer, used to select monodisperse aerosol for use in experiments. Settings of control valves determine relative amounts of aerosol rejected and accepted.

ranges. The device actually measures the aerodynamic diameter of particles (The aerodynamic diameter of a particle is defined as the diameter of a sphere of density 1 g/cm^3 with a settling velocity in air at standard temperature, pressure, and gravity, equal to that of the particle in question), and discriminates between 9 ranges, from $\geq$ 11 μm to $\leq$ 0.43 μm.

The impacter consists of 8 perforated disks stacked on top of one another and spaced by outer cylindrical shells, with a thin metal dish between each pair of disks. A ninth outer shell houses a piece of filter paper. Figure (4) shows, schematically, both the fully assembled impacter and an "exploded" view of two stages. The sampled air-stream enters above the top shell and exits after the bottom one. The perforations are largest at the top and decrease in size for each succeeding disk.

At each stage, the air-flow is forced through the perforations in a disk, and forms jets of roughly the diameter of those holes. The jets are turned radially outward by the dish below. Since the dishes are of slightly smaller diameter than the outer cylindrical shells, the air then leaks around the dish to the next stage. Due to their finite inertia, some particles are unable to follow the jets as they turn radially outward above a dish, and impact upon the dish. The succession of smaller jets (with accompanying higher velocities) results in impaction of smaller particles on each dish, with the smallest particulate collecting on the filter paper in the final stage. The dishes are weighed before and after a timed run to determine the mass of particulate sampled from each size range.

The manufacturer s specifications consist simply of an aerodynamic diameter corresponding to each stage, for which 50% of the particles passing through the perforated disk will impact upon the dish below. A higher fraction of those particles with larger aerodynamic diameters will be collected, and less of those with diameters smaller than that specified are impacted on the dish. Thus, as a crude approximation, the first dish will collect most particles larger than its corresponding 50% impaction diameter, the next dish stops those particles with diameters between its own critical size and that of the previous dish, and so on. If the standard flowrate of 1 ft^3 per minute is used, then the size

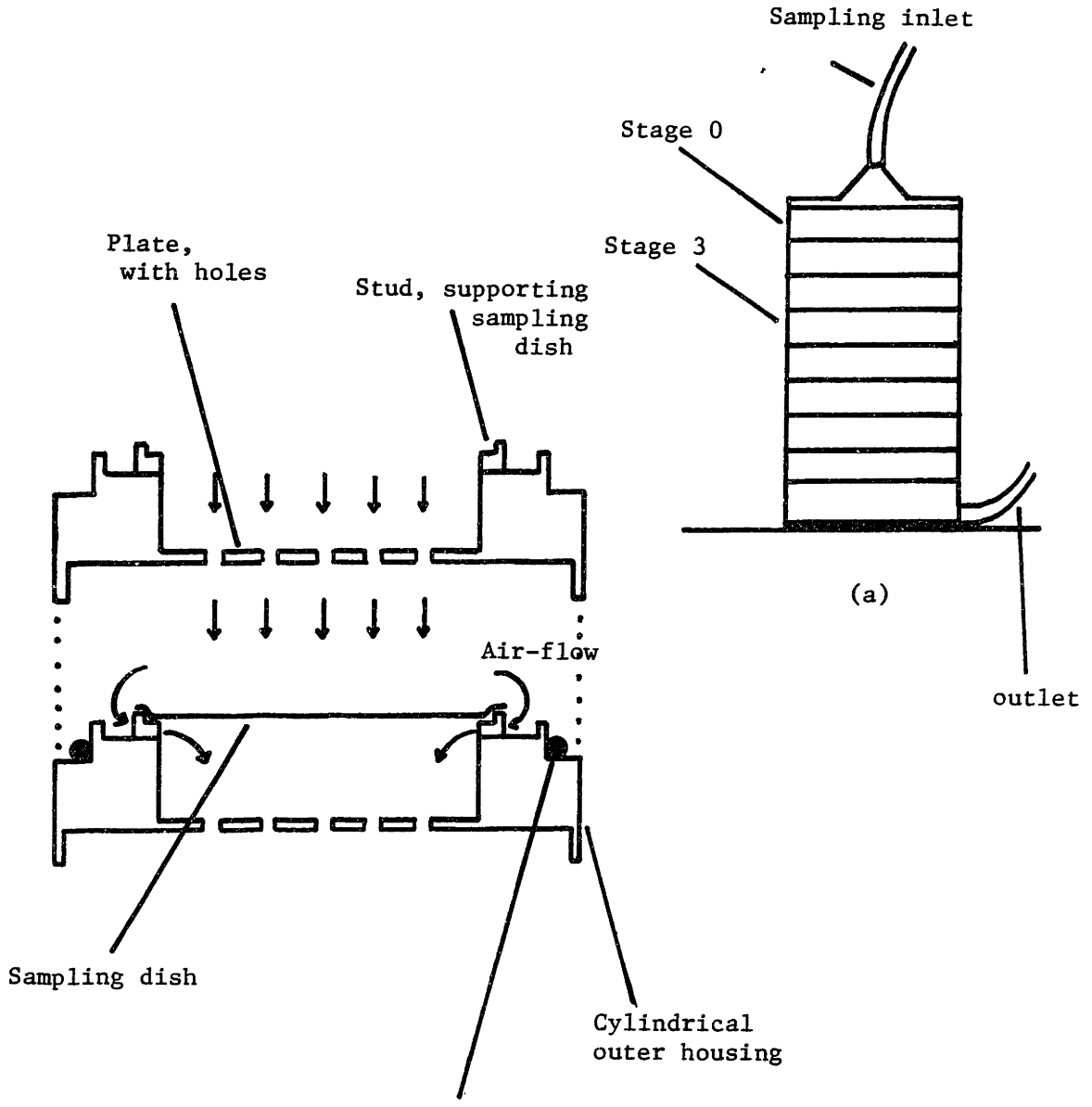

Fig. A1.4 Schematic illustration of Anderson Impactor.

(a) Fully assembled impactor.
(b) "Exploded" view of two stages.
Air flows through holes in plate,
around edges of dish, to next plate.

ranges sampled by each dish are as given in table 1.

The optical particle sizer is shown schematically in Fig. 5. Aerosol is admitted through the tube at the top of the chamber and exits through another at the bottom. A movable light source shines polychromatic (ie., white) light in a columnar beam incident upon the aerosol. A long copper tube allows the user to view light scattered from the particles along a narrow range of angles ($< 3^{\circ}$).

For those components of light with wavelengths on the order of the mean particle size, the intensity of radiation scattered from the particles will have a strong dependence on the viewing angle (relative to the direction of propagation of the incident beam), and the particle size (relative to the wavelength). With a given particle size and electrical properties, the Mie solution for the scattering of a plane-wave of electromagnetic radiation incident upon a spherical particle, can be used to predict the intensity of light as a function of the wavelength and angle. Thus, if the particles are of uniform size, one can in principle determine that size by measurement of the intensity of scattered light, of a given wavelength, as a function of the viewing angle. The requirement of a relatively uniform particle size insures that the peaks of scattering intensity are not "blurred" by the responses of different particles.

Red and green light, with wavelengths 0.6328 μm and .4579 μm, respectively, not only satisfy the criterion of a wavelength on the order of the 1 μm particle size, but can be distinguished by the human eye as well. Thus, one can size particles using the device simply by observing the peaks of red or green light scattered by them. In practice, the red peaks are used, as they are sharper than the green (ie., each one is visible over a narrower range of angles).

Figure 6 contains a chart showing the angular location of the peaks in intensity of scattered light as a function of the normalized particle diameter, α. The normalized diameter is simply the ratio of the particle diameter to the wavelength of the scattered light. The computations required for the chart were performed by Zahedi[4]. As is apparent in Fig. 6, a single particle diameter can result in several red peaks. It is the combination of all observed peaks in the scattered red light that characterizes the particle size.

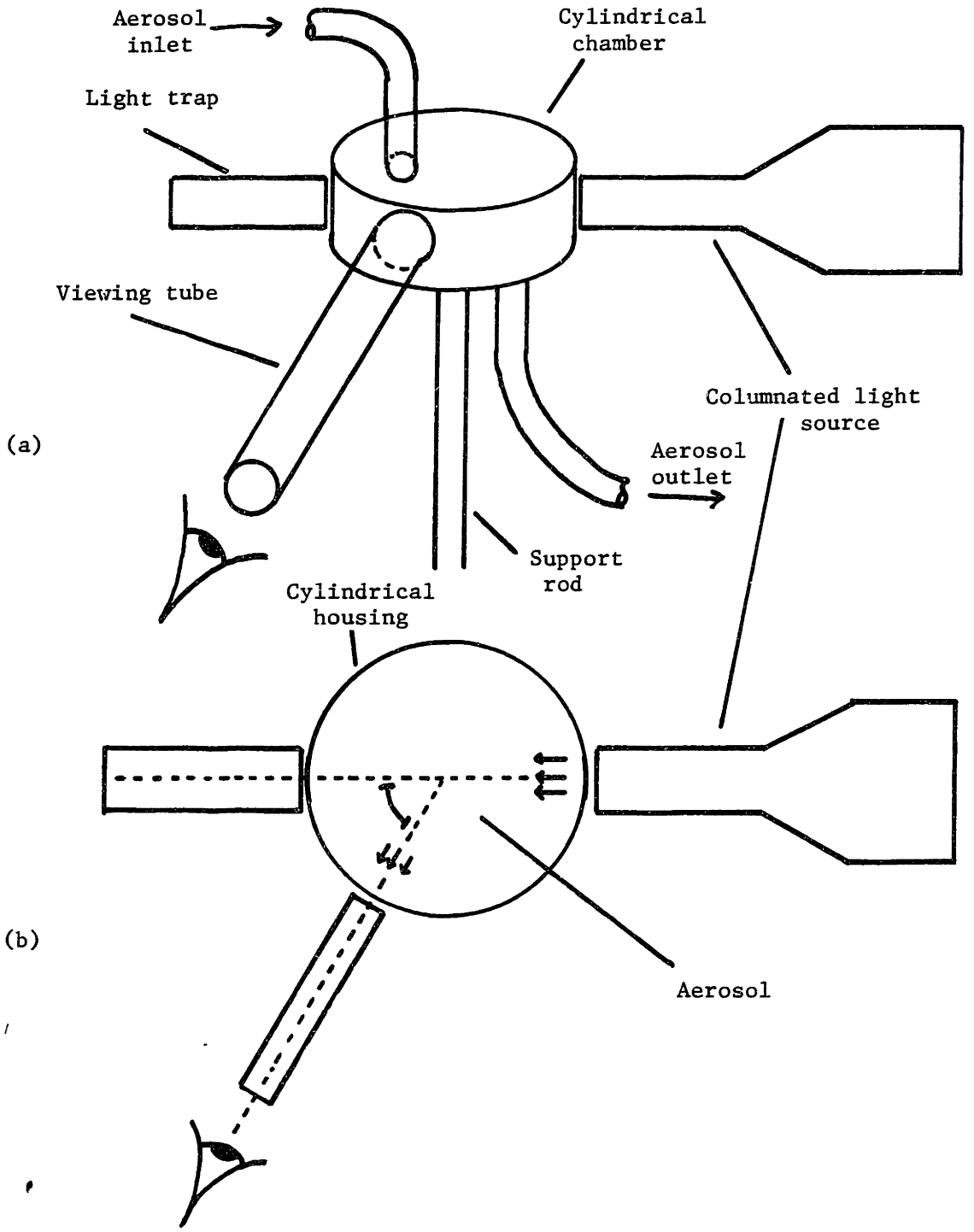

Fig. A1.5 Schematic illustration of optical particle sizer.
(a) Side view
(b) Top view

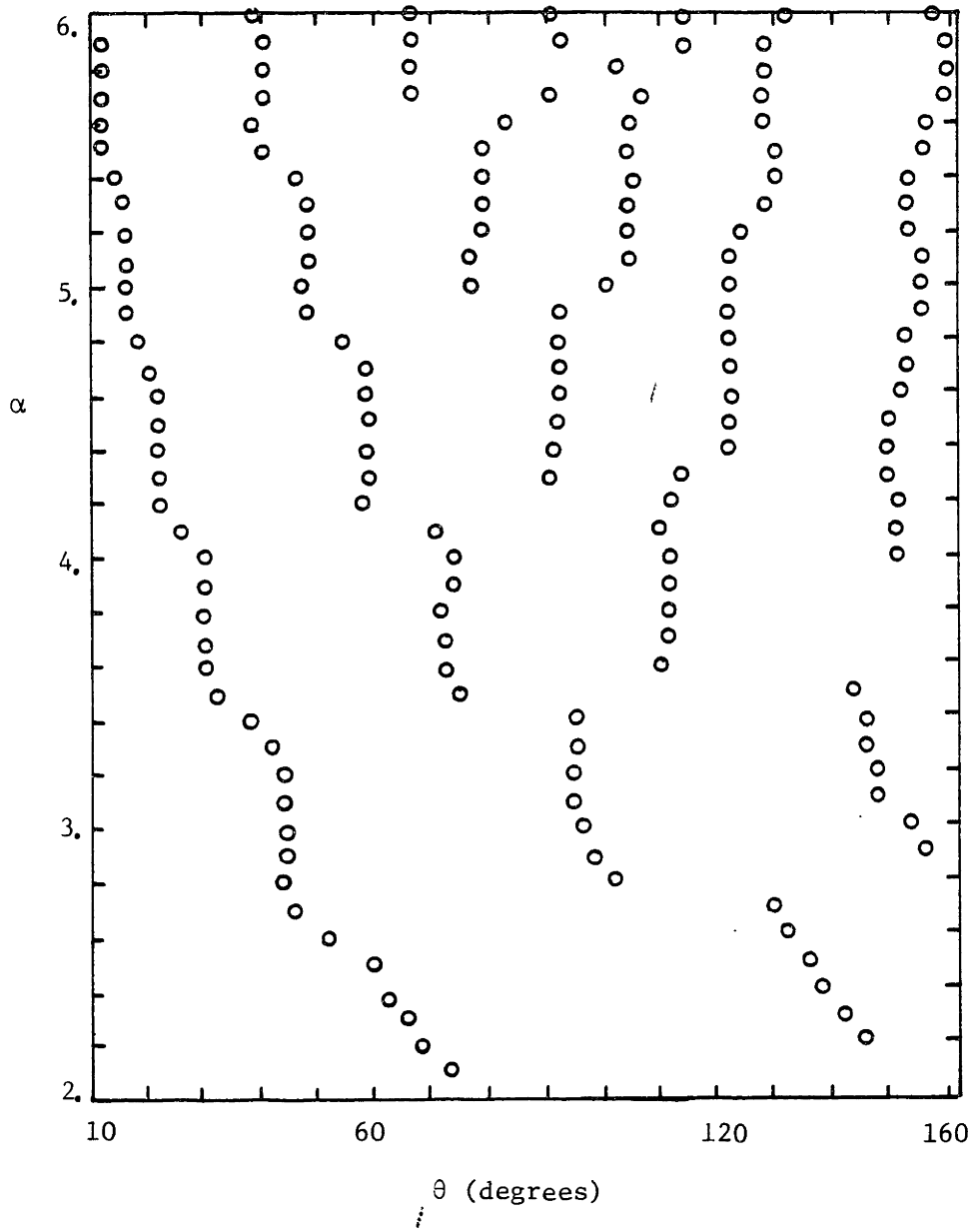

Fig. A1.6. Plot showing predicted angular locations of relative maxima in intensity of scattered light, as a function of particle diameter, normalized to wavelength of the light. The horizontal axis is, θ, the scattering angle (in degrees). The vertical axis is $\alpha \equiv 2\pi R/\lambda$ where 2R is the particle diameter and λ is the wavelength of the light.

A1.4 High-Voltage Electrical Supplies

Both the charging and collecting sections of the precipitator are driven by high-voltage power supplies, either DC or AC. Although the voltage requirements of the two are roughly the same ($\pm$10 kV DC, $\sim$8 kV RMS AC),the currents differ greatly. While the collecting section supply need drive virtually no current (less than 10 μA), the corona current in the charger can be as high as 10 mA.

Two high-voltage $\pm$DC power supplies and a single AC supply are available to the facility. Thus, both sections can simultaneously apply a DC voltage of desired polarity and magnitude. The DC source that is normally connected to the migration plate in the collector is a $\pm$30 kV, $\pm$2 mA supply (NJE Corporation, Kenilworth, NJ). The other source (also manufactured by NJE) is rated at $\pm$30 kV, $\pm$35 mA maximum, and thus, was used to drive the corona wires.

The AC corona drive is provided by a signal generator (Hewlett Packard model 202A), followed by a low-voltage solid-state amplifier in series with a 1000:1 transformer. The voltage/current ratings of the amplifier ($\sim$25 V RMS, $\sim$5 A RMS) are matched to the corona requirements by the transformation. A circuit diagram for the AC excitation system is shown in the general setup illustration of Fig. (2.1). Two series coupling capacitors are shown there; one on each side of the transformer. The input capacitor (actually, a parallel combination of several motor-starting capacitors, totaling $\sim$ 4000 μf capacitance) is necessitated by an offset voltage at the amplifier output which would otherwise cause saturation of the transformer core. The output capacitor is a 40 kV, 2000 pf ceramic capacitor. Its purpose is to bias the corona voltage so as to allow no time-average corona current. Most AC experiments were performed using this series capacitor (although it was easily removed), because the principle advantage of AC precipitation over DC is its ability to collect particles without passing a net (time-average) current through the particulate layer.

The 1000:1 transformer, itself, is actually composed of three transformers in series. The first is a 5:1 step-up transformer, with a rating of 550 V RMS output (at 60 Hz). The second has a 2:1 turns-ratio, and a rating at 60 Hz of 220 V RMS. The third transformer, with a 100:1 ratio, is immersed in oil to prevent breakdown, and has a 60 Hz rating

of 30 kV.

The AC system is capable of driving the corona wires to 8 kV RMS at frequencies ranging from 20-500 Hz. The limit at low frequencies is saturation of the transformer and high impedance of the series capacitors. At high frequencies, transformer losses and amplifier current-limiting are the most important factors.

A1.5 Laser-Doppler Velocimeter System

The laser-Doppler anemometer (LDV) system, consisting of a laser, optical components, photomultiplier tube, along with digital and analog data processing circuitry, is detailed in this section. The "front end" of this system, up to the analog signal processor which provides a digital output specifying individual particle velocities, is a commercial unit, purchased from TSI, Inc.. Data is received in parallel form by a microprocessor-based buffer circuit, which transmits it serially to a remote computer (a Motorola 68000-based multi-user system) for permanent recording and digital processing. The description below begins with the laser and continues "along the signal path" to the computer, itself.

The laser, manufactured by Spectra Physics, Inc., produces a 15 mw linearly polarized coherent beam of light of approximately 0.8 mm diameter and 0.6328 μm wavelength. The orientation of the polarized beam is such that the electric field is vertically directed. Under certain conditions (described below), a horizontally polarized beam is desired. In such cases, a half-wave retardation plate is inserted in the optical path to rotate the beam polarization by 90°. A beamsplitter, consisting of two accurately machined prisms mounted in an aluminum frame, divides the laser beam into two parallel beams of roughly the same diameter as the original one, each 25 mm from the main optical axis. The relative intensities of the two beams depends upon the orientation of the incoming beam polarization, relative to the prisms. Let the primary axis be defined as being parallel to a line joining the two beams, but perpendicular to the main optical axis. If the incoming beam is polarized perpendicular to the primary axis, then the split beams will be of equal intensity. If it is polarized along the primary axis,

however, the beam intensities will differ by a factor of about 50. This allows flexibility in choosing the mode of operation of the LDV, as some techniques require asymmetric beams to sense particle velocities. However, the former mode (equal intensity beams) is desired for all measurements made in this thesis. For horizontal velocity measurements, the beams are split in a horizontal plane, so that the vertically polarized output from the laser results in equally intense beams. For vertical velocity measurements, a horizontally polarized incoming beam is needed to obtain the same result, as the beamsplitter is rotated by 90° from its position in the previous situation. For this case, the retardation plate is inserted to rotate the beam polarization.

A lens following the beamsplitter focuses the two beams to a crossing 350 mm away. The standing wave interference pattern created at this crossing comprises the LDV observation volume, an ellipsoid of diameter approximately 0.25 mm and length 2 mm. Particles that pass through the observation volume scatter light in all directions. The intensity of the scattered light oscillates at a frequency that is proportional to the rate at which the particle crosses nodes of the interference pattern (i.e., proportional to the particle velocity component in the plane of the beams and perpendicular to the main optical axis).

An acoustically-excited Bragg cell, placed between the beamsplitter and transmitting lens, is capable of shifting the frequency of one of the laser beams slightly (by 40 MHz). This shift can serve two major purposes: First, it can bias the apparent measured velocity so that (once the bias is removed) the system can recognize reversals in the flow direction. It should be noted here that, without the bias, the signal from a particle moving at a given speed in one direction cannot be distinguished from that due to the same particle moving just as quickly in the opposite direction.

Secondly, when the system is used to measure a small transverse velocity that is superimposed upon a large streamwise component, particles may enter and leave the observation volume in less time than it takes to cross the distance between two nodes of the interference pattern. The effect of a frequency shift of one of the beams may be thought of as causing the nodes to move at a velocity equal to the

product of the shifting frequency and the node spacing. Thus, with a sufficiently high frequency shift of a beam, one can measure transverse velocities approaching zero, even in the face of large streamwise velocities. This is precisely what must be done to measure the small migration velocity of particles being convected horizontally between vertically-separated plates.

There are other reasons for making frequency-shifted velocity measurements (having to do with directional biases in data rejection), but they are of secondary importance here.

The same amplifier that drives the 40 MHz Bragg cell also contains a downmixer which can be used to lower the apparent frequency shift to anywhere from 1 kHz to 10 MHz (at discrete intervals). In practice, the apparent shift frequency used is the lowest for which the velocity bias is "sufficient" in some sense.

Light scattered from the particles is focussed on the surface of a photomultiplier tube by a set of lenses and prisms. The receiving system can be placed anywhere, as long as an optical path exists between it and the observation volume. The two most common arrangements have the photomultiplier system aligned with the main optical axis, either on the same side of the observation volume as the transmitting optics (backscatter), or on the opposite side (forward scatter). The backscatter mode has the advantage of ease of alignment, as both transmitting and receiving optics can be mounted together, while the forward scatter mode affords a much higher signal strength, due to the physics of the light scattering process (Mie scattering). This signal strength advantage can be up to two orders of magnitude. One other advantage of backscatter operation is that the observation volume need be optically accessible from only one direction. Forward scatter requires a clear optical path through the experimental section from both sides. For most measurements made in this project, the forward scatter mode will be used, in order to get the best signal-to-noise ratio possible.

The laser and transmitting optics are mounted on a 150 cm long base and the receiving apparatus is on another, 25 cm in length. Both of these bases are secured to a 9 ft aluminum I-beam, so that the entire system can be moved to change the observation volume location without

requiring realignment of the optics [Fig. (2.3)]. The I-beam rests on a movable support which allows positioning along all three axes. Vertical positioning is controlled by turning four threaded rods (one full turn alters the vertical position by 0.127 cm, or 0.05 inch). Horizontal movement in the streamwise direction of the tunnel is controlled by rolling the entire apparatus (on wheels) along a track on the floor. The transverse horizontal position is changed by sliding the I-beam across its supporting structure.

The analog signal processor, which receives the photomultiplier output voltage, is a part of the commercial system sold by TSI. Its output is a 24-bit parallel word, specifying, for each particle counted: (1) the total number of fringes (peaks in the interference standing light wave) through which the particle traveled, and (2) the time that it took for the particle to pass through a specified number of fringes. This number, N, can be set equal to 2, 4, 8, 16, or 32 fringes. In order to aid rejection of spurious signals, the processor determines the particle transit time for N/2 fringes as well as for N fringes, and compares the two. If the ratio is not equal to two, within a user-set fraction, f, no data is outputted. The allowable values of f are approximately 0.20, 0.15, 0.10, 0.07, 0.05, 0.02, 0.01, and 0.00, the last of these signifying no comparison (i.e., all data is outputted).

Parallel data from the LDV signal processor is buffered and converted to serial form by a digital circuit, based on a Zilog Z-80A microprocessor. The circuit, constructed on vectorboard using wire-wrap [Fig. (7)], is a stand-alone microcomputer with six 8-bit parallel I/O channels (Z-80A PIO), two serial ports (Z-80A DART) and a set of six 7-segment LED display chips. The system is controlled in any of three ways: (1) a 20 key input pad that is connected via one of the 8-bit parallel I/O channels, coupled with the LED display (both of which are mounted on the board), (2) a separate video terminal, connected through an RS-232 serial port, or (3) a remote terminal (or computer), connected through an EIA-level serial port. The EIA port is capable of communications at baud rates of 300, 600, 1200, 2400, or 4800, and can transmit and receive along a 200 ft length of twisted pair wires. Thus, it can be used to communicate with the remote computer. The 16 K-byte address space is divided between 4 K-bytes of ROM (Intel 2732 EPROM) and

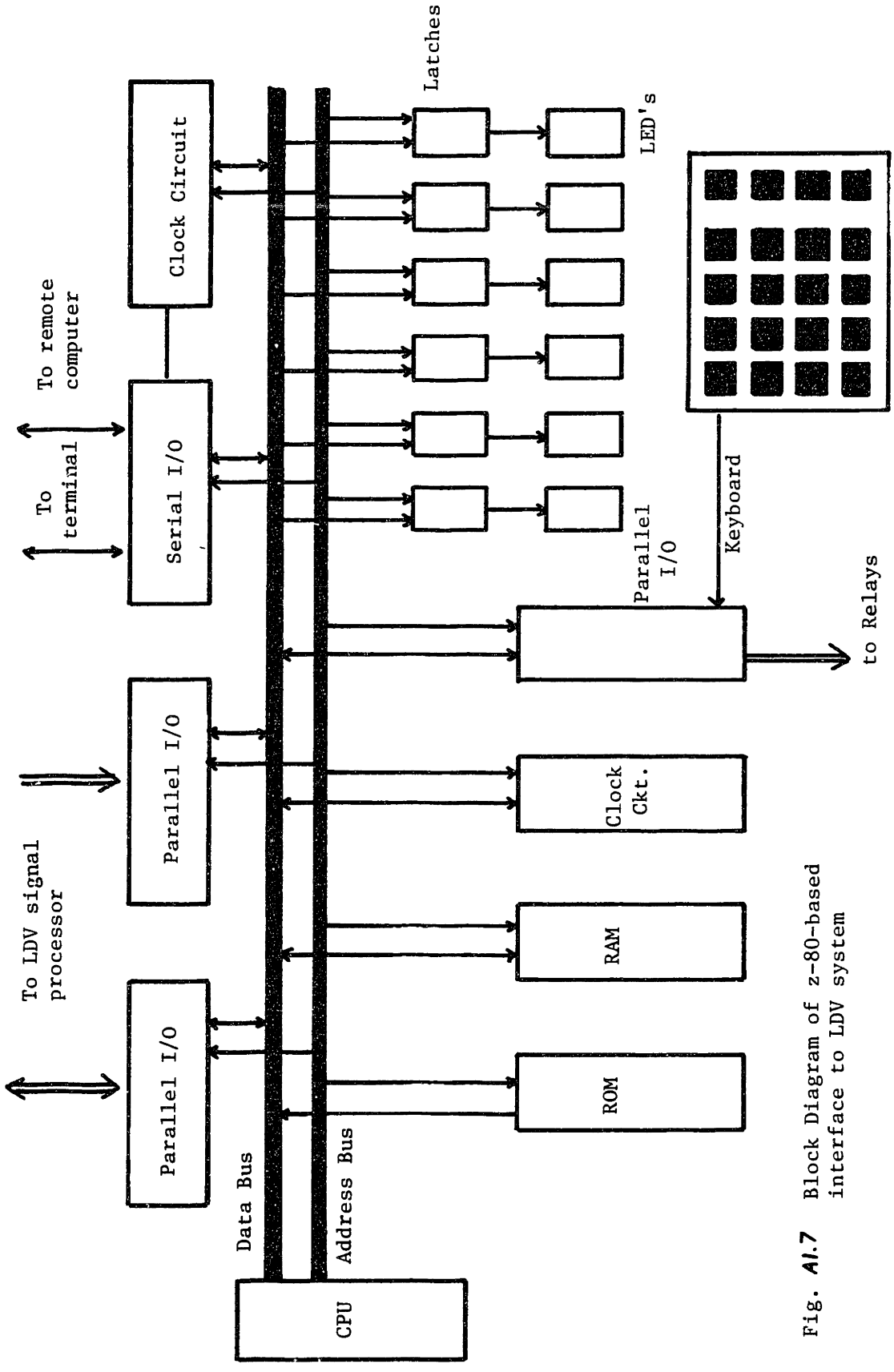

Fig. A1.7 Block Diagram of z-80-based interface to LDV system

12 K-bytes of RAM (Intel 2114-L3 RAM). Two clock/timer chips (Z-80A CTC) are included, one for control of the serial ports, and the other for timing information to accompany LDV data points.

With presently-implemented software, the following procedure is used to obtain and process data with the LDV: First, the system is set up to record a specified number of data points in a given format. Up to seven bytes of information can be stored for each particle counted; three bytes of parallel data from the LDV, and four bytes from the clock chip, to specify the time of arrival of the data. If all seven bytes are stored, then the microcomputer can buffer the data from about 1600 particles. If only four bytes are stored per data point (two bytes of LDV data and the two low-order system clock bytes), the RAM memory is sufficient for storage of up to 2941 measurements.

Next, the LDV is turned on, positioned, and enabled. As particles are counted, outputs from the LDV and clock chip are recorded in RAM. At the same time, the data is converted to serial form and transmitted to the remote computer as quickly as possible. Depending upon how much data is recorded for each particle, the buffer circuit can accept anywhere from 1000 to 5000 points per second. At the 2400 baud rate, the serial line can transmit the data from 15 to 75 points per second. After the pre-set number of particles have been observed, the LDV is automatically disabled, and the system "waits" until the buffer circuit has transmitted all of its data to the remote computer.

The remote computer accepts the particle velocity and timing information and performs some preliminary data processing on it. Basic results, such as the mean particle velocity and RMS turbulence intensity, are transmitted back through the microprocessor to the terminal, along with a signal that confirms receipt of the raw data. Upon command, the remote computer can store the data on the system disk, for later re-processing. The facility is then ready to begin taking data at another location in space or time.

The microprocessor has control of three relays, to allow coordination of data-acquisition with timed changes of their settings. Two of the relays are high-voltage (25 kV, 1 A) relays, while the third is a signal switch (100 v, 100 mA). Presently, one of the high-voltage relays switches DC voltages and can control excitation to either the

corona electrodes or the plate, while the low-voltage relay switches the input signal to the AC amplifiers. The second high-voltage relay is not presently used. The user can alter the settings of these relays between data runs, or at a controlled time during one. In the latter case, the interface circuit is set up to begin taking LDV data at a specified time up to 8 seconds before or after a change in the relay settings, and continues collecting data until the desired number of points have been obtained.

The 68000 is programmed using higher-level languages (i.e., FORTRAN, C, etc.) allowing involved processing of the recorded data at a later time. This processing can include autocorrelations or Fourier transforms of the particle velocity data, or tasks as simple as plotting of the velocity distribution or velocity vs. time.

A1.6 Mass-Monitor System

The most direct method of evaluating the overall performance of the laboratory-scale precipitator involves measurement of the mass-loading of its outlet stream. The mass-monitor system allows a user to simultaneously sample both the inlet and outlet streams of the precipitator, and to measure the mass-loading of each. Since the mass-monitors (along with their associated plumbing and computer interfaces) are identical, only one is described below. The description begins with the sampling tube, and follows, first, the path of the aerosol, then the path of information to the remote computer.

The sampling tube is a 0.635 (1/4 inch) copper tube with a 0.102 cm (0.040 inch) wall, pointed upstream and centered in the cross-section of the flow region. The copper tube is grounded, to avoid any buildup of charge due to self-precipitation of charged particles that may be sampled. A vacuum pump in the mass-monitor draws air out through the tube at the controlled rate of one liter per minute. The air, laden with aerosol, goes from the tube to a neutralizing cylinder (supplied by TSI, Inc., the manufacturer of the mass-monitors) in which any net charge in the aerosol is removed by emission of charged particles from a radioactive source. This neutralizer serves two purposes. First, it reduces the loss of sampled particles due to self-precipitation effects.

More importantly, though, the design of the mass-monitor requires that the sampled particles be uncharged to avoid large errors in the mass-loading measurement. The air stream that leaves the neutralizer goes directly to the mass-monitor.

The mass-monitor, itself, is a commercial unit supplied by TSI (Thermo-Systems, Inc., St Paul, Minnesota). It determines the total particulate mass-loading of a sampled air stream by electrostatically precipitating the particles onto the surface of an oscillating piezoelectric crystal and comparing its resonant frequency with that of a matched, uncoated crystal [Fig. (8)]. The difference in resonant frequencies is approximately proportional to the total mass of particulate deposited on the first crystal. Thus, the rate of change of this differential frequency gives a measure of the mass-loading of the sampled stream.

As supplied by the manufacturer, the mass-monitor outputs information in the form of six-digit numbers printed on a narrow paper strip. Each number represents the difference in resonant frequency between the two crystals, either in Hertz (averaged over the previous second), or in tenths of Hertz (averaged over the previous ten seconds). The printing module, however, is easily removed, and can be replaced by a circuit card with a standard edge connector (0.1 inch pad spacing), to allow transfer of the digital frequency difference information to a microcomputer. Both mass-monitors in the facility have been interfaced with a single 6800-based microcomputer in this manner.

The interface consists of 24 data lines (4 lines for each BCD [binary-coded-decimal] digit), two handshake lines, (+5 v) power, ground, and one control line. The control line is used to turn on and off the voltage at the precipitator needle which deposits aerosol particles onto the sampling crystal. Proper use of this control line maximizes the allowable time of use of the resonant crystals between cleaning operations.

The 6800-based microcomputer consists of a 6800 microprocessor, 12 8-bit parallel ports (M6820, M6821 PIA), and two serial ports (M6850). The configuration is similar to that shown for the Z-80-based system illustrated in Fig. 7. One serial port is to be connected to a 300-baud terminal, the other to a remote computer which normally communicates at

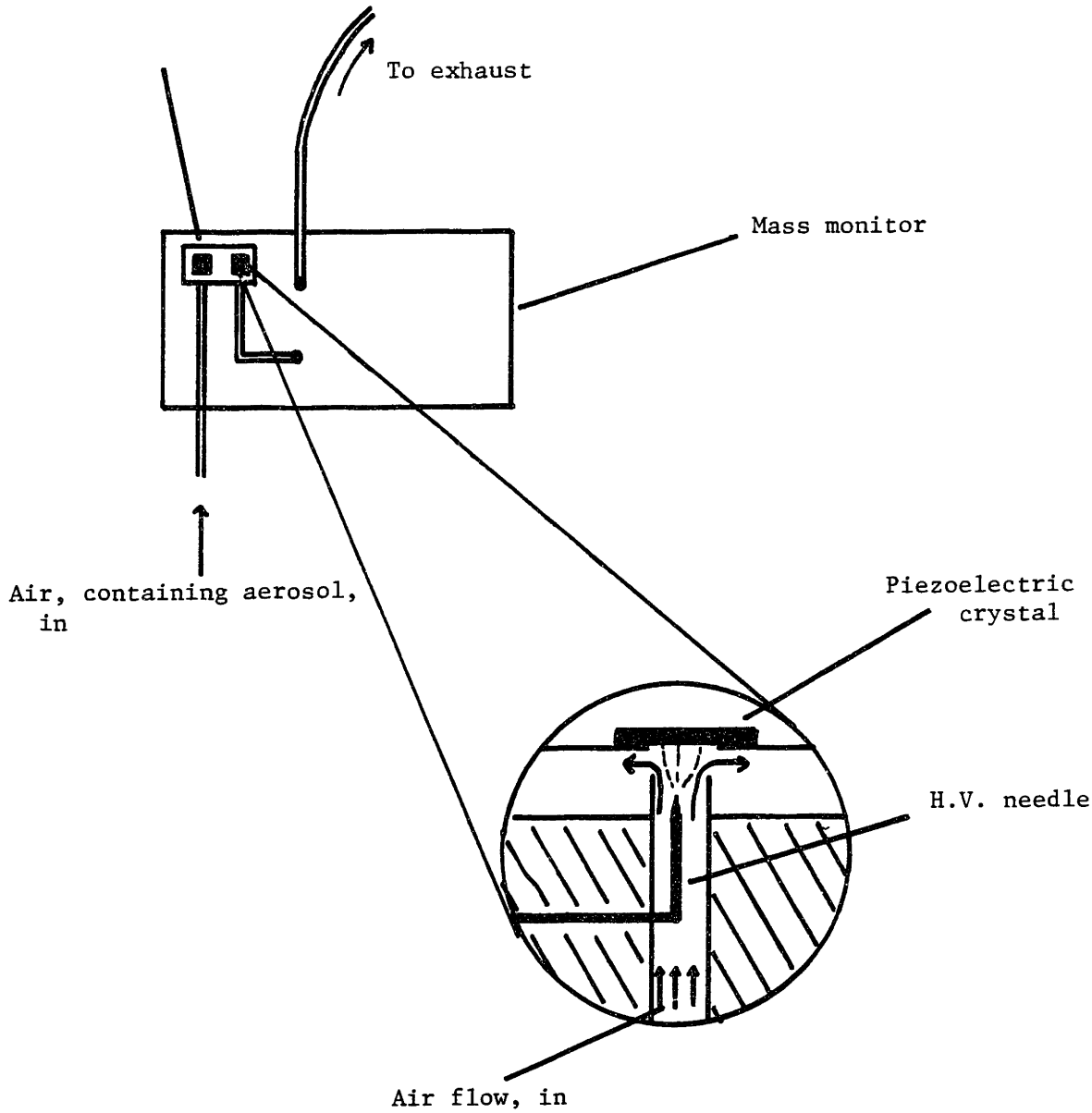

Fig. A1.8 Schematic illustration of mass-monitor. Air, laden with particulate flows by both crystals. Particles are deposited only on one.

a 4800-baud rate. The connection to the remote computer is actually made through the LDV interface circuit, which is to be described in the next section. The lower 32 K-bytes of the address space are occupied by RAM (2102), while the upper 4 K-bytes are available for ROM (2708 EPROM°s), which contains the monitor.

With presently-implemented software, the following procedure is used to acquire data from the mass-monitor system: First, the remote computer is informed of the number of intervals over which the crystal resonant frequency differences are to be measured, and whether one or both of the mass-monitors should activated. Then, when the user actually requests a measurement, the microcomputer enables the precipitator voltage for the appropriate mass monitor(s), allowing aerosol particles to be deposited on the corresponding crystal(s). As data becomes available from the mass-monitor(s), it is immediately transmitted to the remote computer, with appropriate identification as to its origin (ie., which mass-monitor is reporting). After the desired number of measurements have been taken, all mass-monitor precipitator voltages are turned off, and the remote computer returns preliminary information about the mean value and standard deviation of the rate of change of frequency differences for the mass-monitor(s). In addition, the raw data can be written into disk files of the remote computer, for later processing.

A1.7 Mass-Monitor System Software

A single program, named **"swt.c"** (swt, for small wind-tunnel), is responsible for data acquisition from the mass-monitors. When called, the program first prompts the user for experimental parameters such as the operating configuration (ie., using only inlet, only outlet, or both mass-monitors), the desired number of measurement intervals to constitute a run, and an output file name to which raw data is to be written. Then, the user has the option of starting a measurement run immediately, or setting the system up to begin a run after a specified delay interval.

The procedure most commonly used for this thesis research included washing the crystals in a soap solution after each run, rinsing them in water, then letting them dry for two minutes before re-mounting in the

mass-monitors. The system was then given five minutes to come to thermal equilibrium after mounting of the crystals before another run was started. The delayed running mode is tailored to fit this operating procedure. The user starts the delayed run after rinsing the crystals, and is given a prompt after 100 seconds to re-mount them. Then after a five minute delay, the measurement run begins automatically.

In addition to acquiring and recording the raw data, the program reports the mean value of the rate-of-change of crystal frequency difference and the RMS deviation from that mean after every run. Other processing steps, such as efficiency calculations from several mass-loading measurements, can be performed upon request from the user.

Little processing of the raw mass-monitor data is necessary, beyond that already done by the data acquisition software. Only one other program was created to deal with mass-monitor data files. The program, "mm_cal_plot.c" (mm_cal_plot, for mass-monitor calibration plot), can be used to create calibration curves for a set of crystals, usually immediately before a set of measurement runs is to be made. Such a curve is useful in determining the difference frequency at which a set of crystals saturates (ie., the level above which the change in resonant frequency is no longer proportional to the mass deposited on the sampling crystal). It can also be used to detect abrupt changes in the behavior of a crystal, such as those resulting from a chip or crack in the substrate.

A1.8 LDV System Software

Data acquisition operations for the LDV system are controlled by two programs, named "lda.c" and "time_runs.c". The first is a general-purpose program which acquires and stores velocity data, performing only minimal analysis, itself. The second uses the anemometer as a particle counter, observing only its data rate, for the purpose of making particle concentration measurements. Brief descriptions of these two programs, along with those that process data recorded by the first, are given in this section.

When called, the general purpose program (lda.c) initializes the relays and sets up the microcomputer interface to take the maximum

allowable number of data points (2941 points, 4 bytes recorded per point). The default relay setting leaves all three open, but different initializations can be used. From the main level of the program, the user can request changes in the number of data points taken or the relay settings.

The user has two options in actually taking data, referred to here as the "immediate" and the "delayed" modes of operation. Upon entering the immediate mode, the user is prompted for the value of the shift frequency used and the number of nodes over which particle transits are to be timed (Both of these values are set by switches on the instruments and cannot be read through the digital interface). After that, the system simply starts a data-taking operation as soon as it is requested by the user, continuing until the desired number of data points has been accumulated. With the delayed mode, data acquisition begins at a controlled interval of time either before or after a change in the relay settings (up to $\pm$ 8 seconds). The alternate setting is determined by the user before entering this mode.

From the main level of the program, the user can request that the last set of data points taken be stored in a disk file with a given file name. The main purpose of the program is to generate these files, allowing more involved processing of the velocity/time data by other programs.

As its name might imply, the program, "time_runs.c" is used to time data-acquisition steps. For each timing run, the microcomputer interface is actually set up to record velocity/time information for each particle that is tracked by the LDV system, but the only data that is transmitted to the remote computer is the time of the last measurement (ie, the length of time required to acquire the desired number of data points). The program initially prompts the user for the number of data points to be acquired each run, and for the number of runs to be used in determining the average data rate. There are two reasons for taking data over several runs, rather than a single one. First, the maximum allowable number of data points (2941) may not give a sufficiently large sample to avoid errors due to statistical fluctuations in the data rate. In addition, with several runs, the user can get a mean value and standard deviation for the data rate, allowing

determination of a level of confidence in the results.

The program is capable of interleaving two sets of runs, keeping track of the mean and standard deviation for each separately. If requested, it can alternate between runs, automatically switching one of the relays between each. The most common measurement made in this way is that of relative particle concentration with and without electric field excitation applied to either the corona wires or the migration plate. With automatic switching between the two states, errors due to drift in the aerosol generator output are minimized, as long as the time scales are much longer than the interval between two runs.

A number of programs exist to process data files written by the program, "lda.c", the most important of which are described below. The basic format of each is the same: The program is given the name of a file containing LDV data, opens the file, reads in the raw velocity/time data, and converts it to a format that is more convenient for mathematical manipulation. The data is then processed in some way to yield some desired output.

The program, **"process.c"** , performs a number of analyses of the data. First, it computes a mean value and RMS deviation from that value for the measured fluid velocity. Although the "lda.c" program gives the user values for these quantities, this program makes more accurate estimates of them. Rather than simply averaging the particle velocity measurements to obtain the mean flow velocity, the "process.c" program divides the total measurement time into a number of evenly-spaced intervals, and uses interpolation between measured velocities to determine appropriate values for the velocity in each interval. It is this evenly-spaced interpolated velocity function that is used to determine the mean value and standard deviation of the flow velocity. If the particle volume density is assumed to be constant, then the average of all particle velocity measurements made will generally be higher than the mean velocity, simply because a larger number of measurements are made during intervals of higher velocity. The evenly-spaced, interpolated velocity function is used to avoid this problem, known as "velocity bias". The "lda.c" program does not normally correct for velocity bias, and when it does, it uses a smaller number of interpolation points than does the "process.c" program (in the interest

of execution speed in real time). The "process.c" program can also compute an autocorrelation function for the measured velocity (again, using the interpolated data). As this computation is long and involved, the program is usually executed in a background mode, outputting its results into another file. The autocorrelation function values can then be plotted at a later time by the program, "proc7.c" .

The program, "proc9.c" is used to plot measured velocity data as a function of time (actual data, not interpolated), over the entire interval corresponding to a given data file, or any sub-set of that interval. Velocity distribution functions, plotting the number of particles within a specified range of a given velocity as a function of that velocity, are plotted by "proc10.c" . The latter program allows the user to superimpose several distributions, to allow comparison, for example, of velocity distributions with and without an applied electrical excitation.

As it is sometimes of interest to examine the spectral composition of a measured velocity function, the program, "proc11.c" , computes the Fourier transform of the velocity/time data in a file recorded by "lda.c". Because the computation is lengthy, this program is normally run in a background mode (as with "process.c"), and outputs its results into a file.

References for Appendix 1

1
Sachar K.S., "Charged Drop Scrubbing of Submicron Particles", PhD Thesis, MIT (May 1974).

2
Liu B.Y.H., Whitby K.T., Yu H.H.S., "Condensation Aerosol Generator for Producing Monodispersed Aerosols in the Size Range 0.036 to 1.3 μ", J. Recherches Atmospheriques 2, 397-406 (1966).

3
"Instruction Manual for Anderson Non-Viable Sampler", Anderson 2000 Inc., P.O. Box 20769, Atlanta, Georgia.

4
Zahedi K., "Measurement of Particle Size By Higher Order Tyndall Spectra", BS Thesis, MIT (October 1973).

Appendix 2

Setup, Procedures, and Data For AC Precipitation Experiments

A2.1 Introduction

This appendix presents details about the AC precipitation efficiency measurements of chapter 4 that are important enough to warrant inclusion in this thesis, but are not necessary to the development of that chapter. The experimental setup and procedures are described in section 2. Section 3 contains plots of the experimental data that supplement those of Figs. (4.1) - (4.7).

A2.2 Experimental Setup and Procedures

The setup used in the precipitation efficiency measurements was similar to the general setup described in chapter 2, with two minor differences. First, the corona wires extended through the entire active region of the tunnel (154.2 cm) rather than half of it, as shown in Fig. 2.1. The wires were attached to a 0.64 cm (1/4 inch) brass rod at the downstream end by springs, passed through small holes in a similar rod at their midpoint, and were threaded through holes in a third rod at the upstream end (Fig. 1). The spring tension was adjusted to reduce vibration of the rods during corona excitation. The purpose of the center rod was also to minimize wire vibration.

Only one of the two mass-monitors was used in these experiments (the one at the outlet of the tunnel). By measuring precipitation efficiency through comparison of the outlet mass loading with and without electrical excitation, one can avoid problems associated with calibration differences between mass-monitors. In addition, the measurements made are more conservative, in that any collection due to inertial impaction in the normal tunnel flow is ignored.

The aerosol generator described in section 2 of appendix 1 was used only for those experiments run after 7/27/83. For experiments performed before that date (which includes all results reported in chapter 4), a larger atomizing chamber was used. Besides containing more

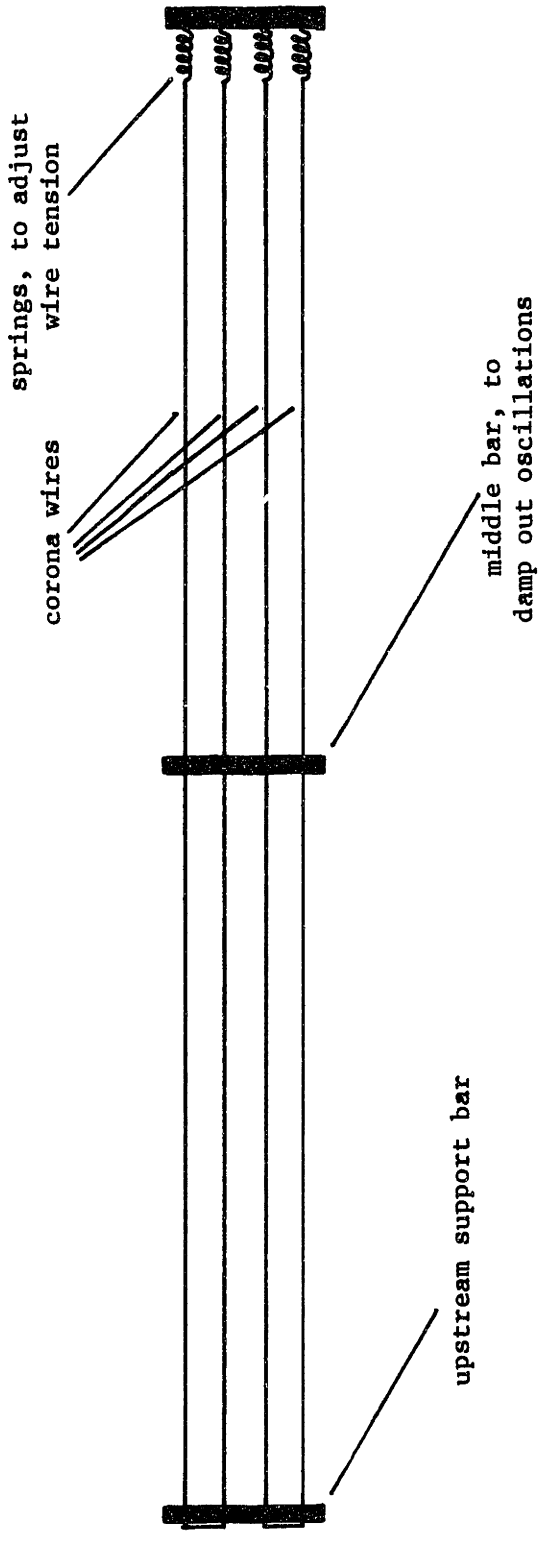

Figure A2.1 Supporting structure for corona wires in precipitation efficiency measurements.

DOP/alcohol mixture, the chamber allowed the addition of fluid during operation (through a two-valve system). In addition, the brass atomizing tube, through which air was passed to entrain the liquid, had three nozzles instead of the single nozzle used later.

The obvious advantages of this earlier setup were: (1) a larger aerosol generation rate, and (2) the capability to run for indefinite periods of time without shutting down for refills. Unfortunately, these same factors proved to liabilities as well. As was discovered after the first set of runs, the relative proportions of atomized alcohol and DOP in the fog that left the chamber were not the same as those of the added fluid. Thus, the concentration of DOP in the liquid contained within the chamber rose gradually during the set, as is reported with the data in section 3.3. The concentration has some effect on the mean particle size (the particle diameter varies roughly as the cube root of the DOP concentration).

In addition, with the pressure and heating-tape settings used for the first set, the optical particle sizer yielded no diffraction bands. This indicates that the particle size distribution was not narrow enough to give distinguishable peaks in the intensity of scattered red or green light.

These problems were corrected by two changes in the experiment. First, the large chamber was replaced by the mason jar setup described in appendix 1 with a single atomizing nozzle. In addition, the feed pressure and heating tape temperature were adjusted so that distinct scattering bands were obtained with the optical particle sizer. Although the angular locations of the bands did not always correspond to a given particle size in Fig. A1.6, their existence implied a relatively uniform particle size.

Each data point consisted of three measurements of the outlet mass-loading. The first and third were performed with no applied electrical excitation. For the second run of each series, a specified voltage (either $\pm$DC or AC) was applied to the corona wires. The electrical response of the system (ie., the corona current) was recorded, along with the three mass-loadings. For DC excitations, the current was characterized simply by its mean value. For AC coronas, the positive and negative peak currents were observed, along with the "RMS"

measurement from a multimeter (not a "true RMS" measurement, though).

The third mass-loading measurement corresponding to one data point served as the first one of the next data point. Thus, only (2n+1) measurements were required to obtain (n) data points in any single run.

The deposition crystal was cleaned regularly to remove all precipitated DOP aerosol particles. An alcohol rinse was used for all experiments performed before 7/11/83, and a soap-solution rinse replaced it thereafter. For the alcohol rinse procedure, the deposition crystal was removed from its fixture in the mass-monitor and rinsed with denatured alcohol from a plastic squeeze bottle (for about 5 seconds). It was dried in a pressurized air-stream for roughly 10 seconds, then returned to the mass-monitor. About five minutes was allowed for the crystal to come to thermal equilibrium with its surroundings. As the electrical conditions in the tunnel were changed at roughly the same time as the crystal mounting, those same five minutes allowed the mass-loading of the aerosol stream exiting the neutralizer to approach that of its inlet stream.

This procedure was sufficient to remove all particulate from the crystal (as evidenced by the relatively uniform initial frequency difference for consecutive runs), but repeated washings caused deterioration of the substrate. In order to preserve the crystals, a soap-water solution was used for the rinse in later experiments. The solution was a mixture of soap in distilled water, 1 part soap to 5 parts water (micro cleaning solution, Cole-Parmer catalog No., K8790-20). After the crystal was removed from the mass-monitor, it was placed in the soap solution for 1 minute, then rinsed in distilled water (from a squeeze bottle) for about 10 seconds. It was blown dry by a pressurized air stream for roughly 15 seconds, then allowed to dry further for 2 minutes before mounting. A five minute thermal equalization interval followed, after which the next measurement began. In later experiments (after 6/7/83), the crystal was washed after every run, to improve the repeatability of measurements.

Before a set of runs, the tunnel, aerosol generator, and mass-monitor were run for at least 30 minutes, to reduce effects of any warm-up transients. Each measurement consisted of 12 readings of the crystal frequency differences, spaced by 10 seconds, each. The first

reading was normally discarded, as it tended to yield anomalous results. This left 10 frequency differences (between the 11 readings), from which a mean value and standard deviation were derived.

A2.3 Experimental Data

This section contains two groups of figures. In the first group are plots of data from experiments already reported in chapter 4. These plots show the dependence of the measured effective particle migration velocity, w_{eff}, on corona current levels, instead of on the corona voltage, as was the case for figures in that chapter. Figures (2) - (6) correspond to Figs. (4.1), (4.2), (4.5), (4.6), and (4.7), respectively. Together, these figures show both the voltage and current dependence of the effective migration velocity for positive and negative DC excitations, for 30, 60, and 100 Hz AC excitations, all with a 4.3 m/sec horizontal flow velocity. Figures (4.3) and (4.4) give the frequency dependence of w_{eff} for AC excitations of fixed magnitude (8.0 kV RMS) with both 4.3 m/sec and 8.9 m/sec flow velocities.

The second group of figures presented here report data from the remaining 6 sets of efficiency measurements (out of a total of 13) that were performed on the laboratory-scale precipitator. Figure (7) shows the frequency dependence of w_{eff} for a fixed magnitude AC corona voltage of 6.0 kV RMS. The rest of the group report data from experiments run with the high-speed horizontal flow ($U \simeq 8.9$ m/sec). Figures (8) and (9) are plots of w_{eff} vs. excitation voltage and current, respectively, for positive DC excitations. The corresponding plots for negative DC voltages are in Figs. (10) and (11). Figures (12) - (17) contain similar data for the fixed-frequency experiments, run with 30, 60, and 100 Hz excitations.

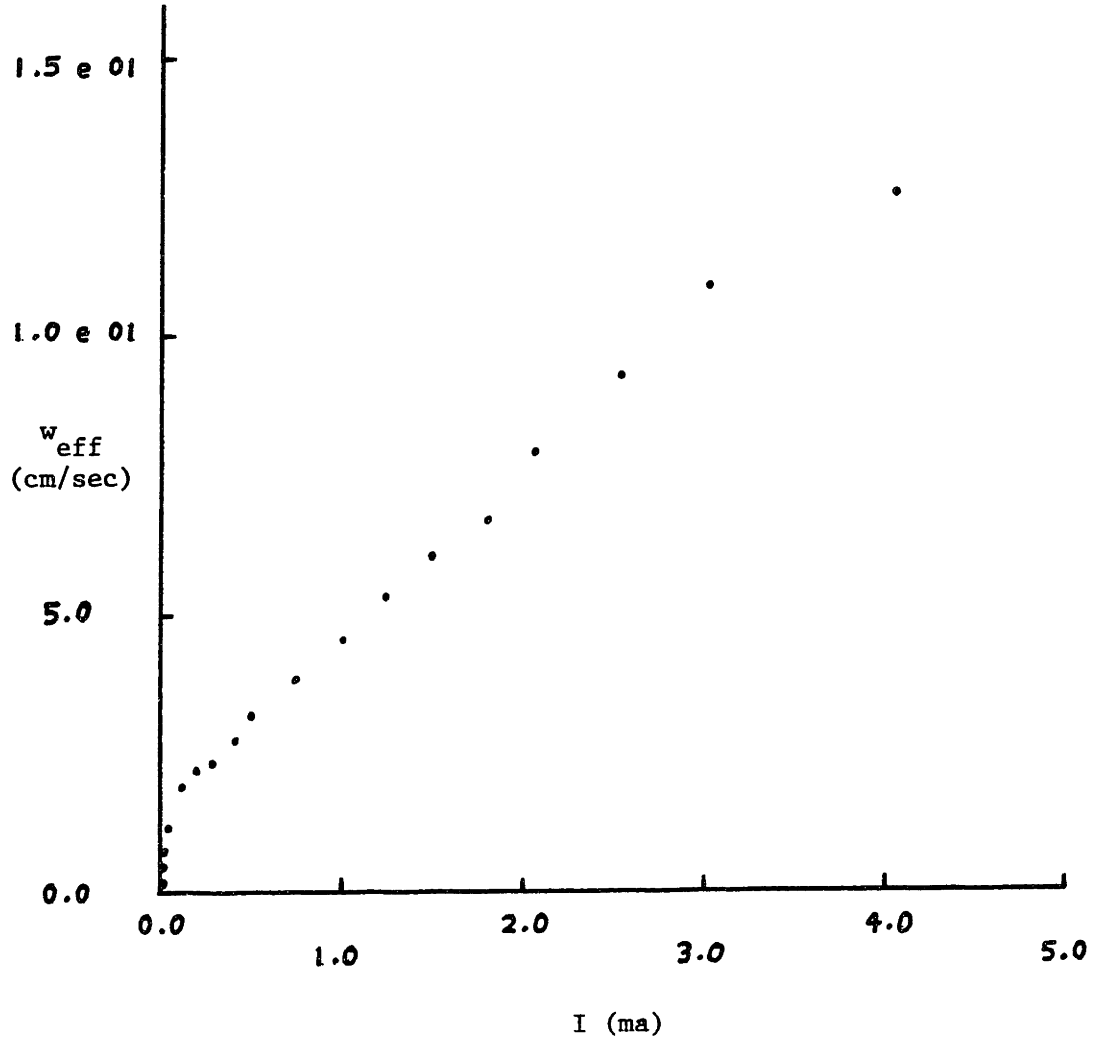

Figure A2.2. Plot of effective particle migration velocity vs. (positive) DC corona excitation current magnitude. Horizontal flow velocity was 4.3 m/sec (6/10/83).

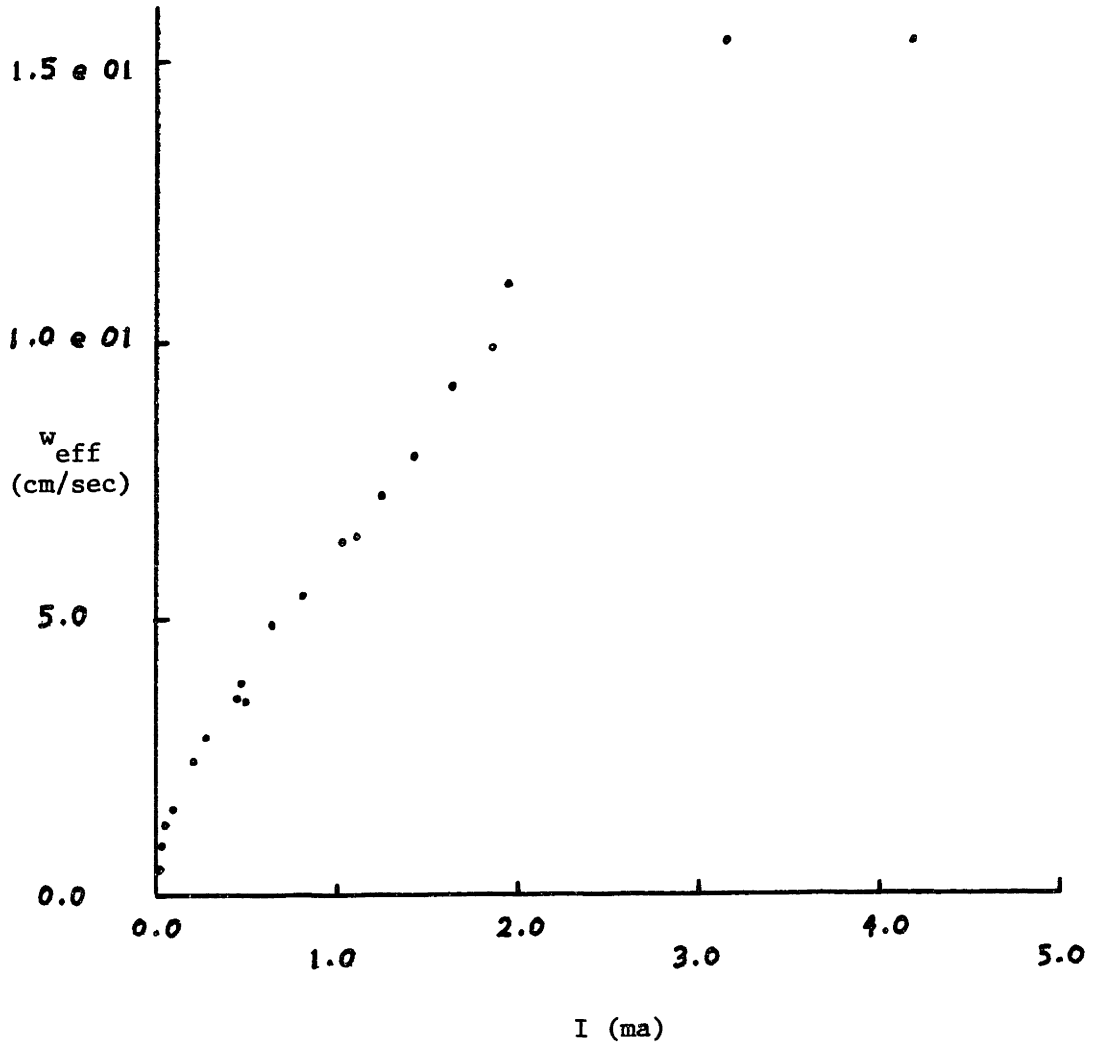

Figure A2.3. Plot of effective particle migration velocity vs. (negative) DC corona excitation current magnitude. Horizontal flow velocity was 4.3 m/sec (6/8/83).

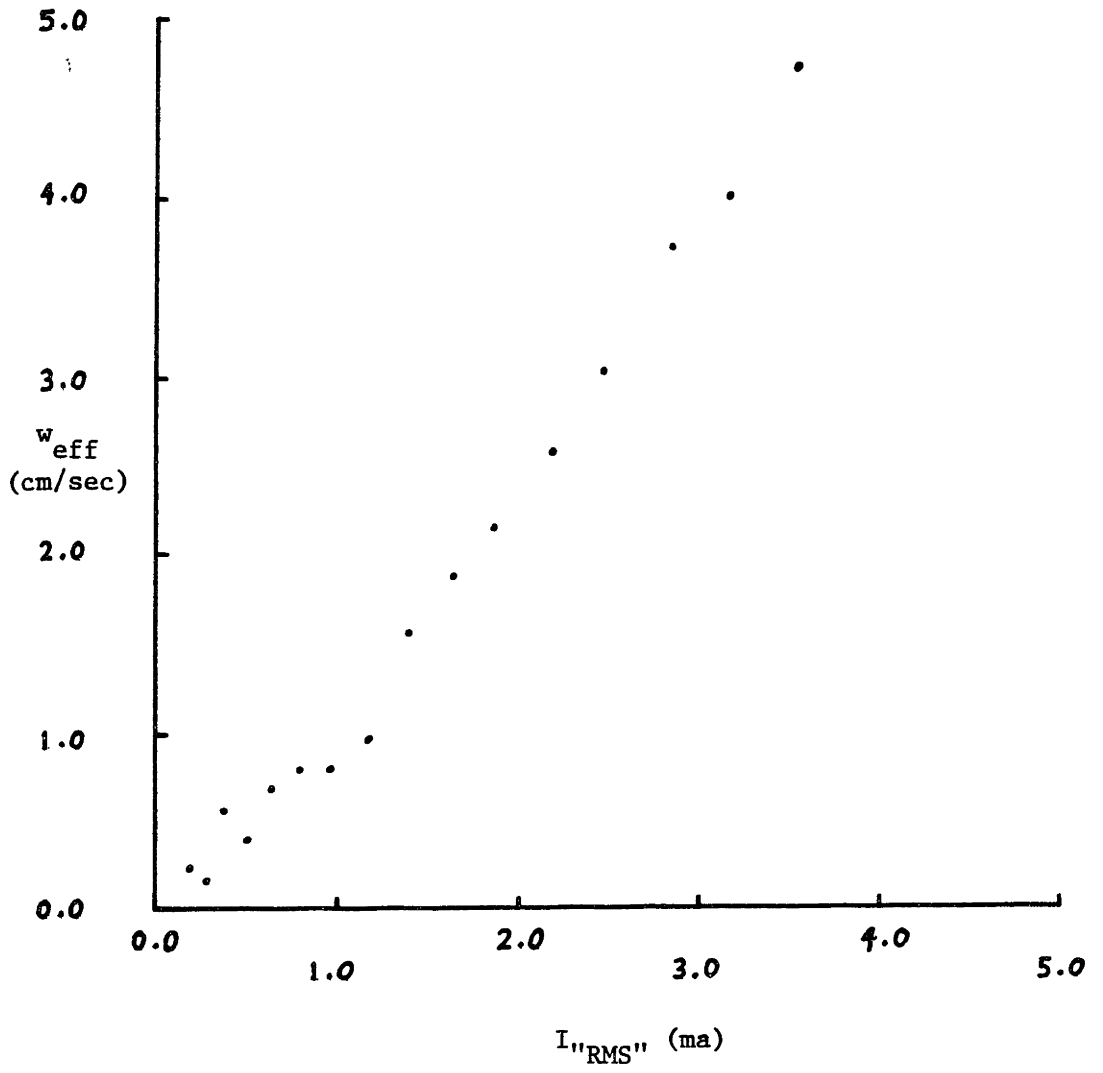

Figure A2.4. Plot of effective particle migration velocity vs. "RMS" corona excitation current magnitude. Horizontal flow velocity was 4.3 m/sec. 30 Hz AC excitation was used (6/11/83).

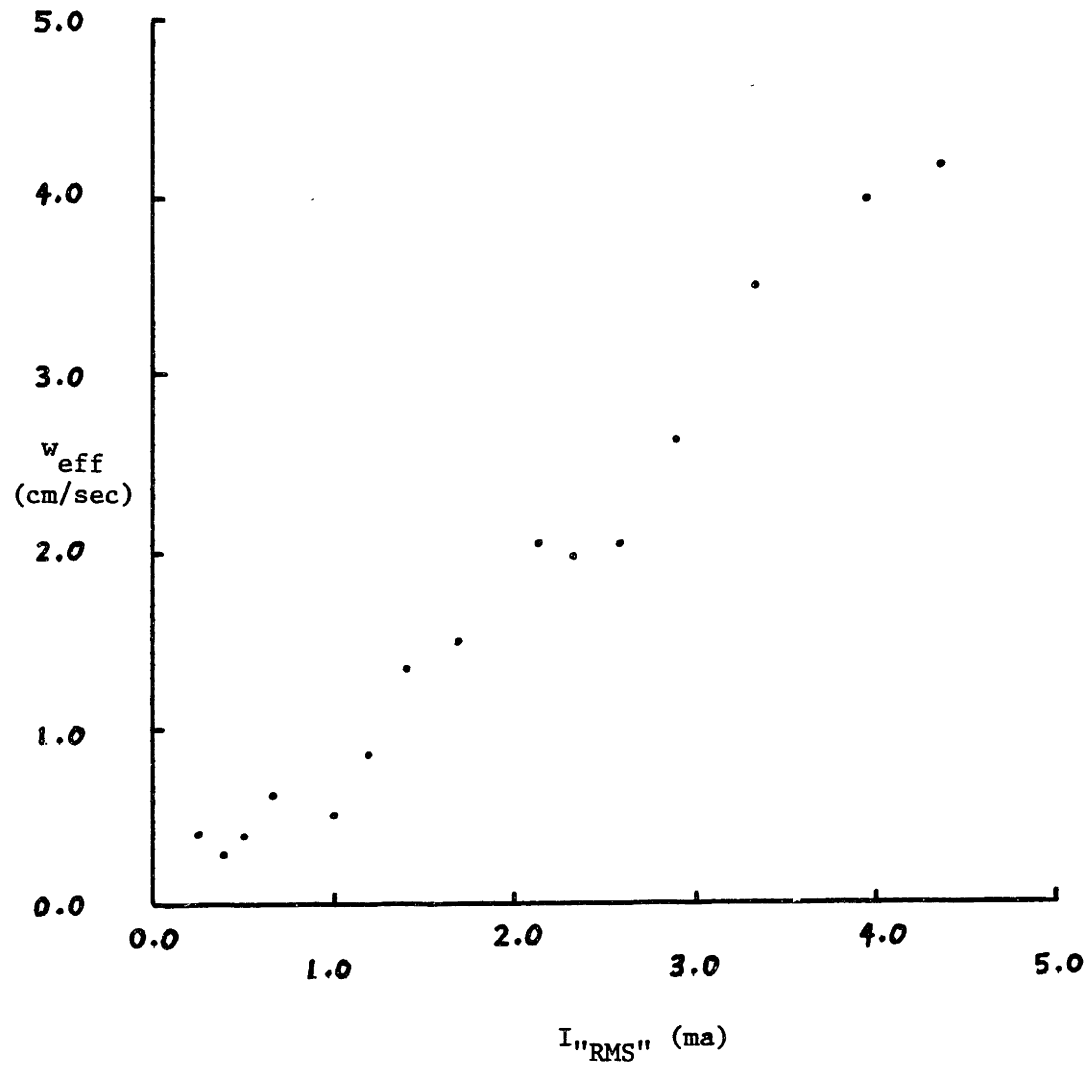

Figure A2.5. Plot of effective particle migration velocity vs. "RMS" corona excitation current magnitude. Horizontal flow velocity was 4.3 m/sec. 60 Hz AC excitation was used (6/13/83).

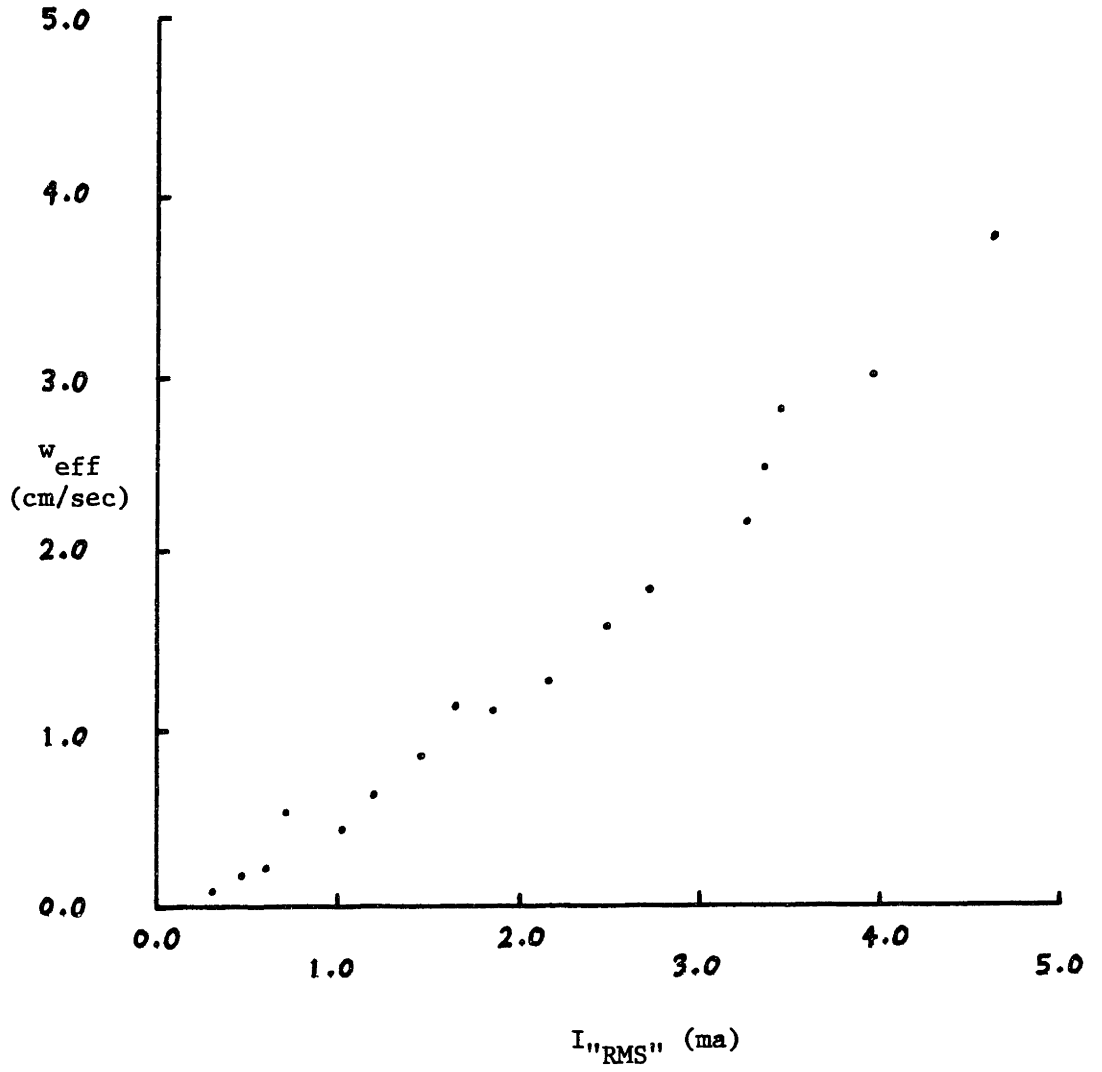

Figure A2.6. Plot of effective particle migration velocity vs. "RMS" corona excitation current magnitude. Horizontal flow velocity was 4.3 m/sec. 100 Hz AC excitation was used (6/12/83).

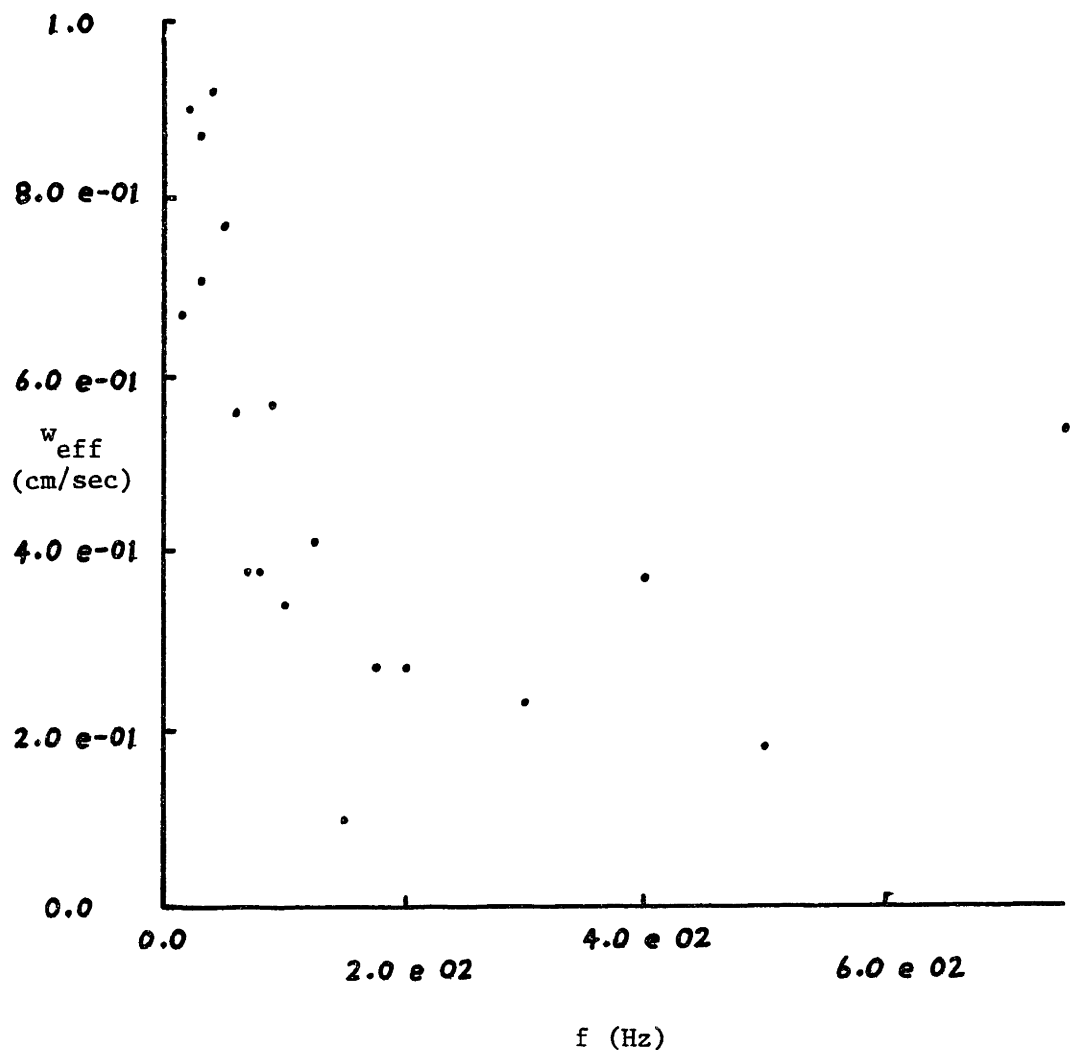

Figure A2.7. Plot of effective particle migration velocity vs. corona excitation frequency. Horizontal flow velocity was 4.3 m/sec, applied voltage magnitude was 6 kV RMS (6/7/83).

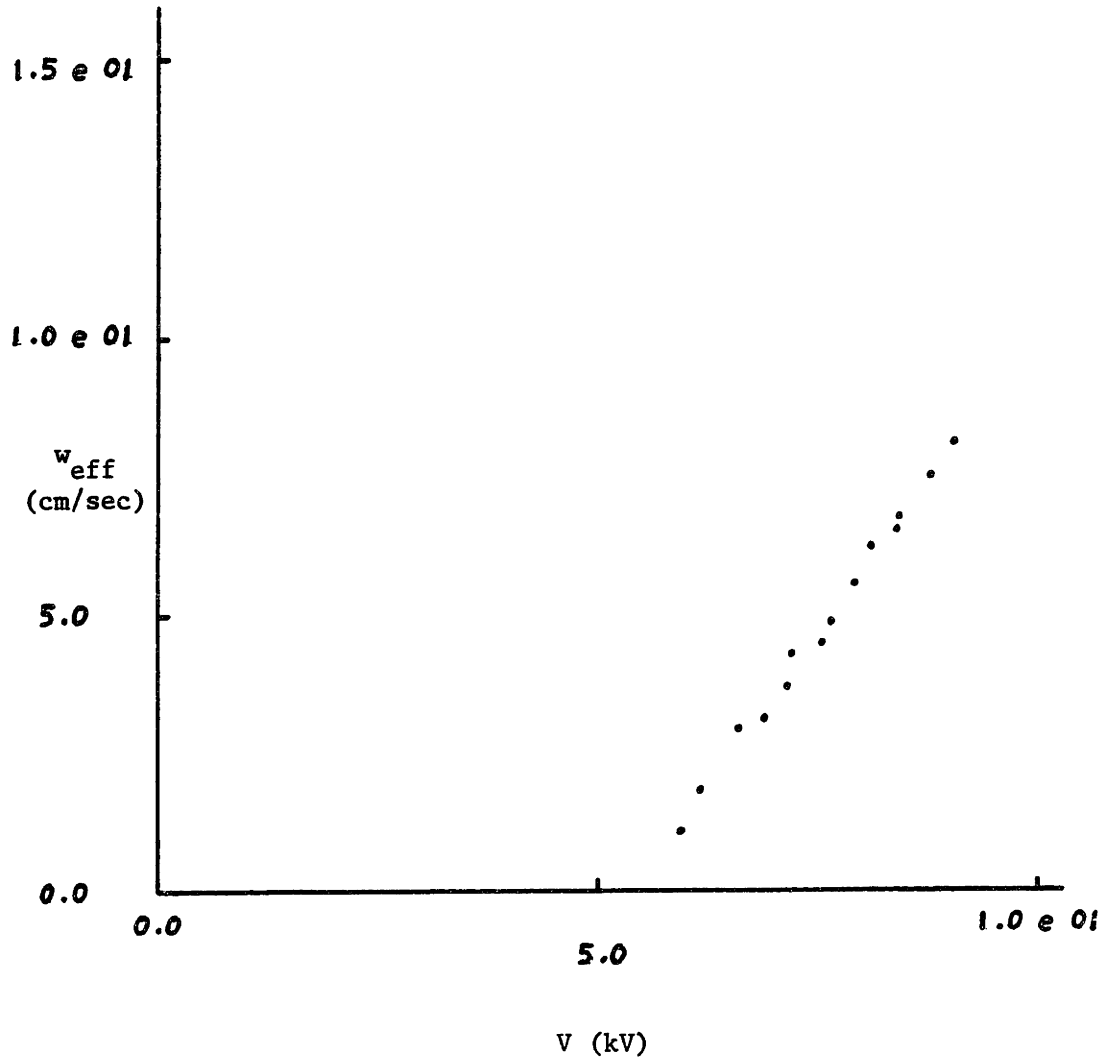

Figure A2.8. Plot of effective particle migration velocity vs. (positive) DC corona excitation voltage magnitude. Horizontal flow velocity was 8.9 m/sec (7/13/83).

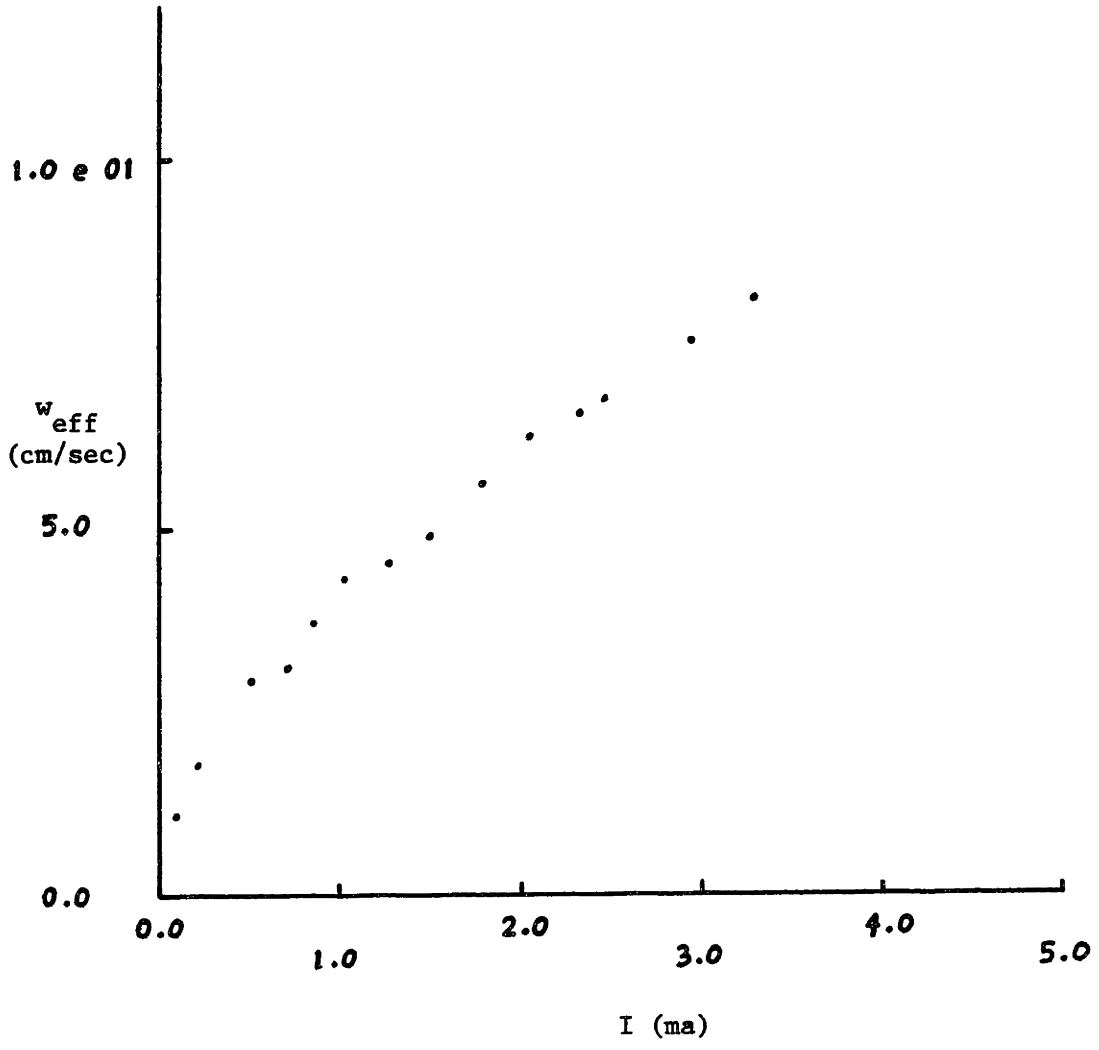

Figure A2.9. Plot of effective particle migration velocity vs. (positive) DC corona excitation current magnitude. Horizontal flow velocity was 8.9 m/sec (7/13/83).

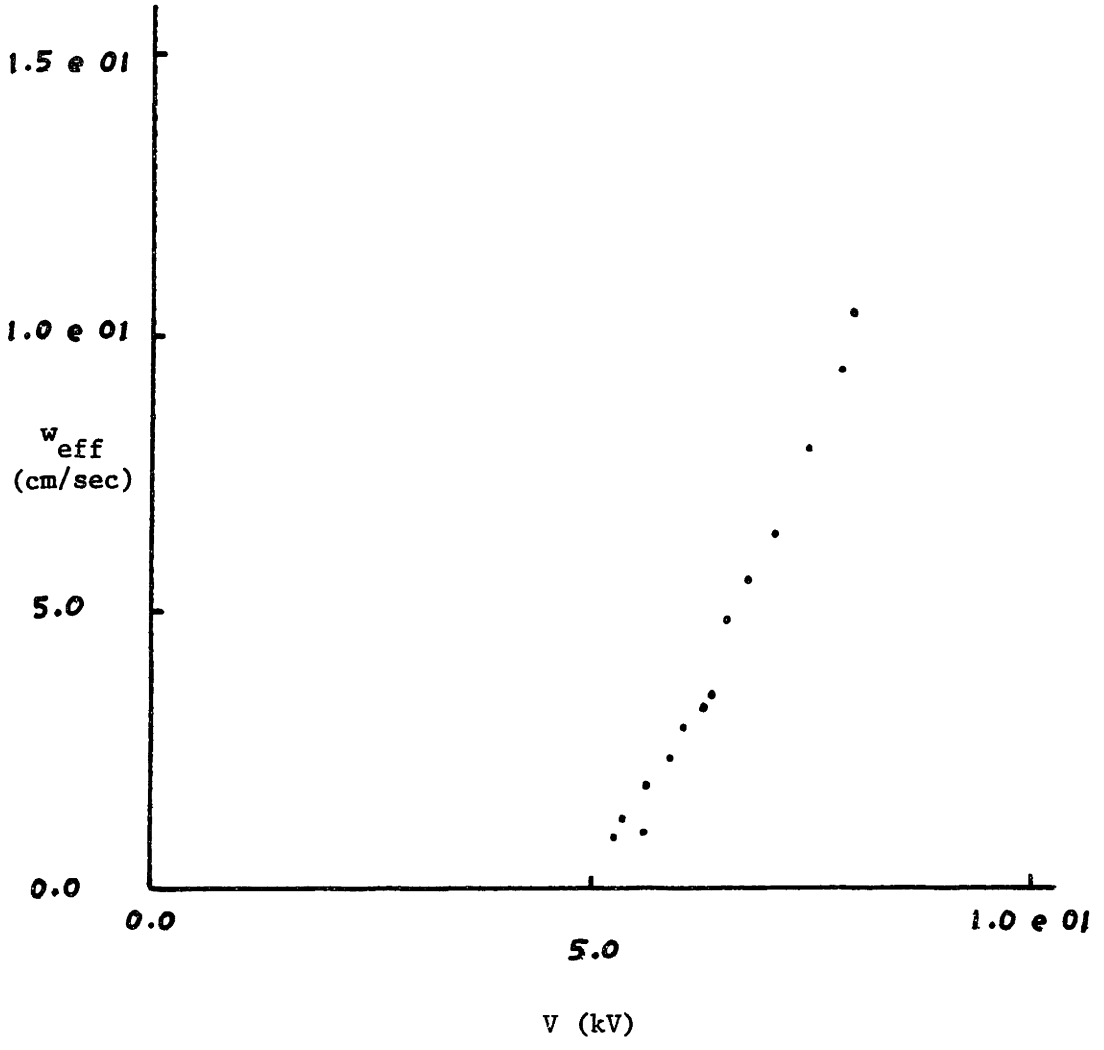

Figure A2.10. Plot of effective particle migration velocity vs. (negative) DC corona excitation voltage magnitude. Horizontal flow velocity was 8.9 m/sec (7/13/83).

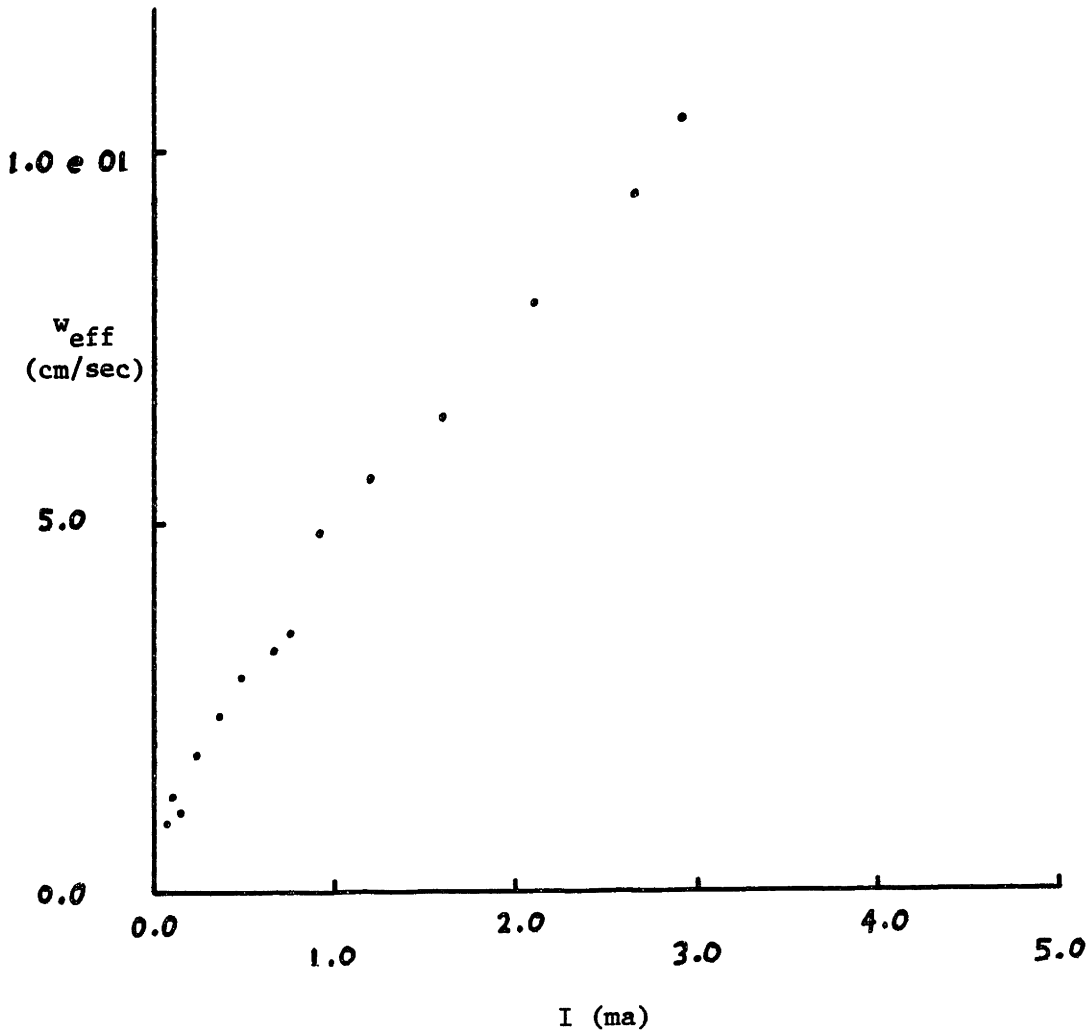

Figure A2.11. Plot of effective particle migration velocity vs. (negative) DC corona excitation current magnitude. Horizontal flow velocity was 8.9 m/sec (7/13/83).

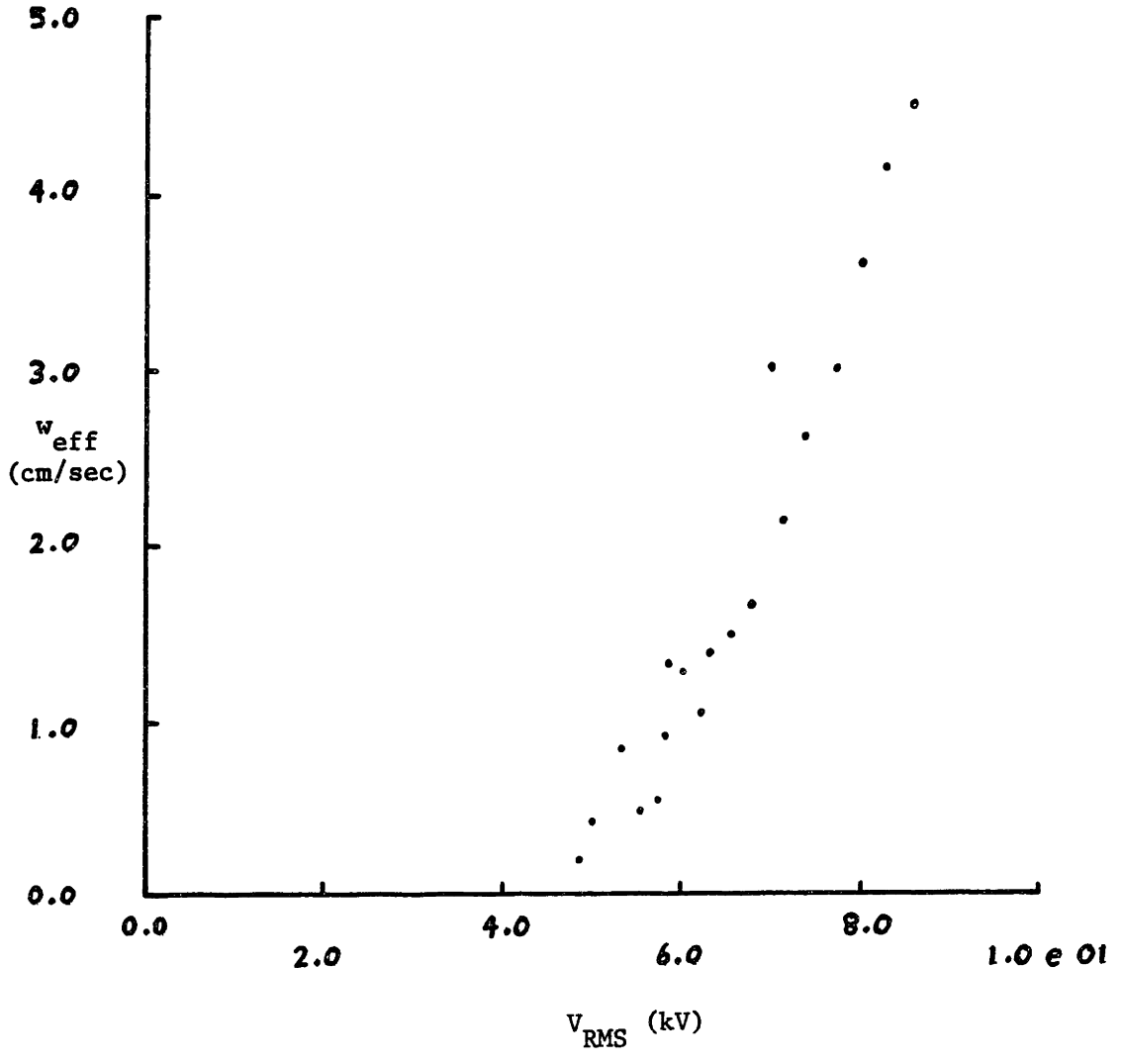

Figure A2.12. Plot of effective particle migration velocity vs. RMS corona excitation voltage magnitude. Horizontal flow velocity was 8.9 m/sec. 30 Hz AC excitation was used (7/18/83 - 7/19/83).

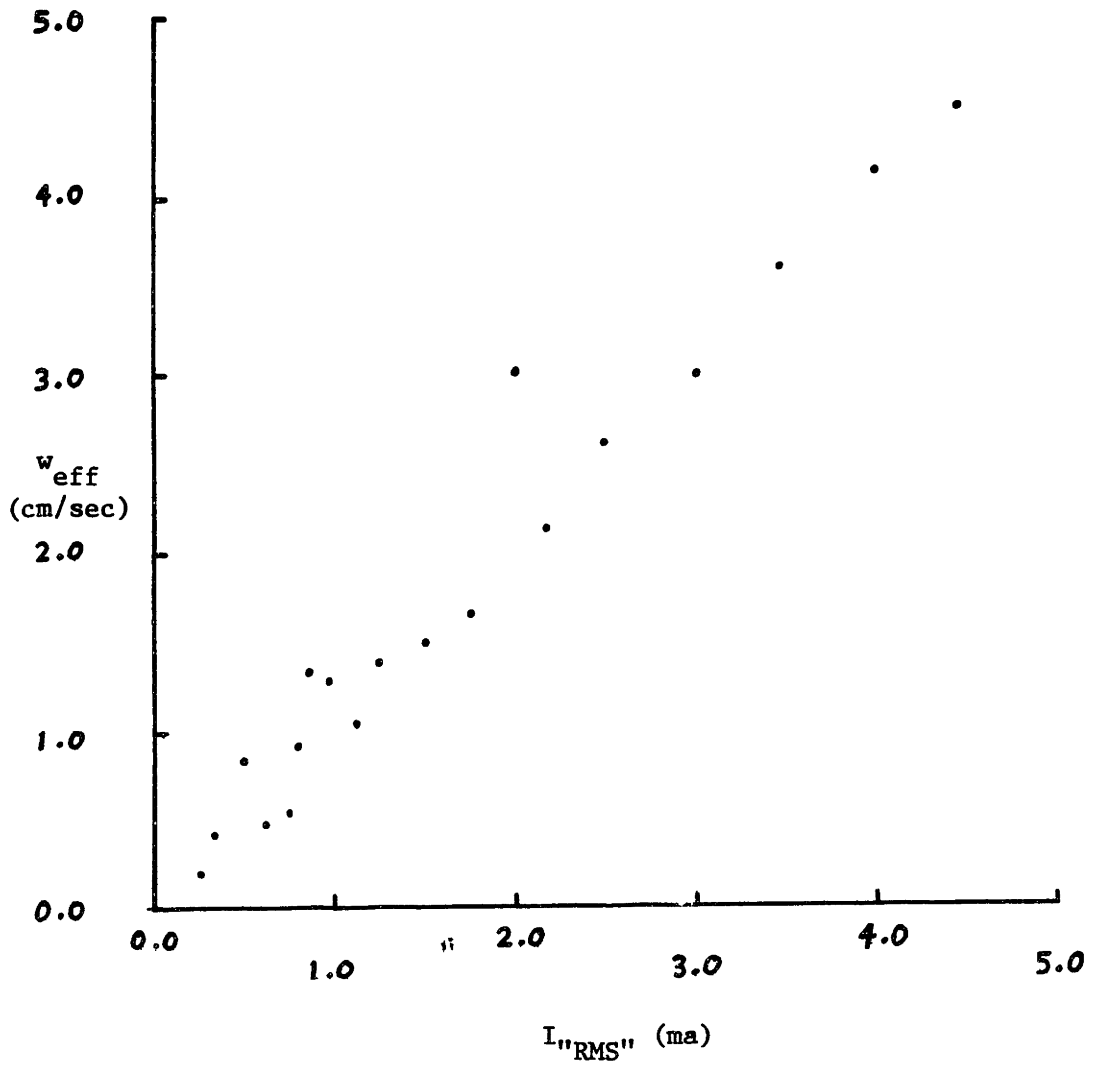

Figure A2.13. Plot of effective particle migration velocity vs. RMS corona excitation current magnitude. Horizontal flow velocity was 8.9 m/sec. 30 Hz AC excitation was used (7/20/83).

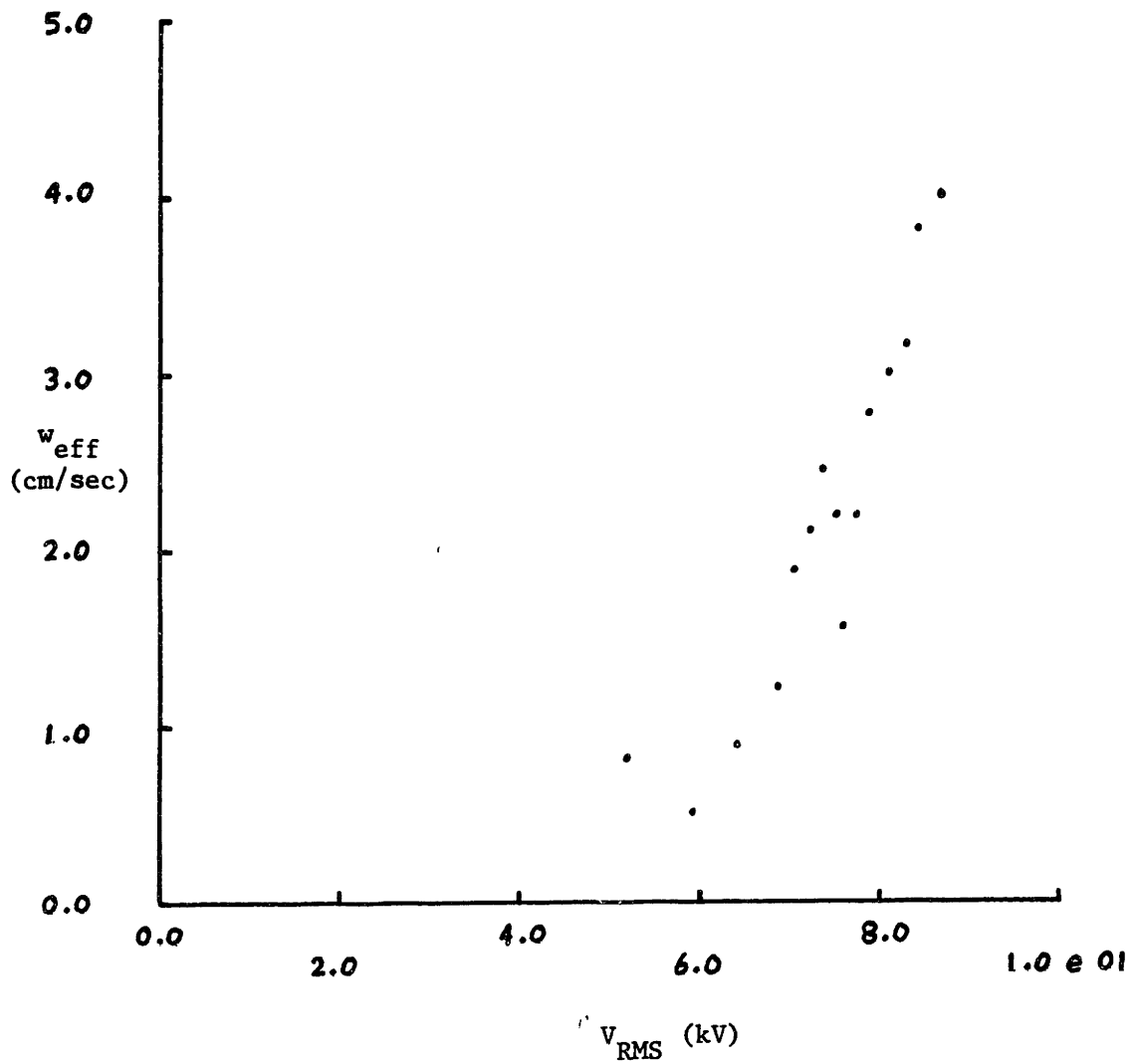

Figure A2.14. Plot of effective particle migration velocity vs. RMS corona excitation voltage magnitude. Horizontal flow velocity was 8.9 m/sec. 60 Hz AC excitation was used (7/21/83).

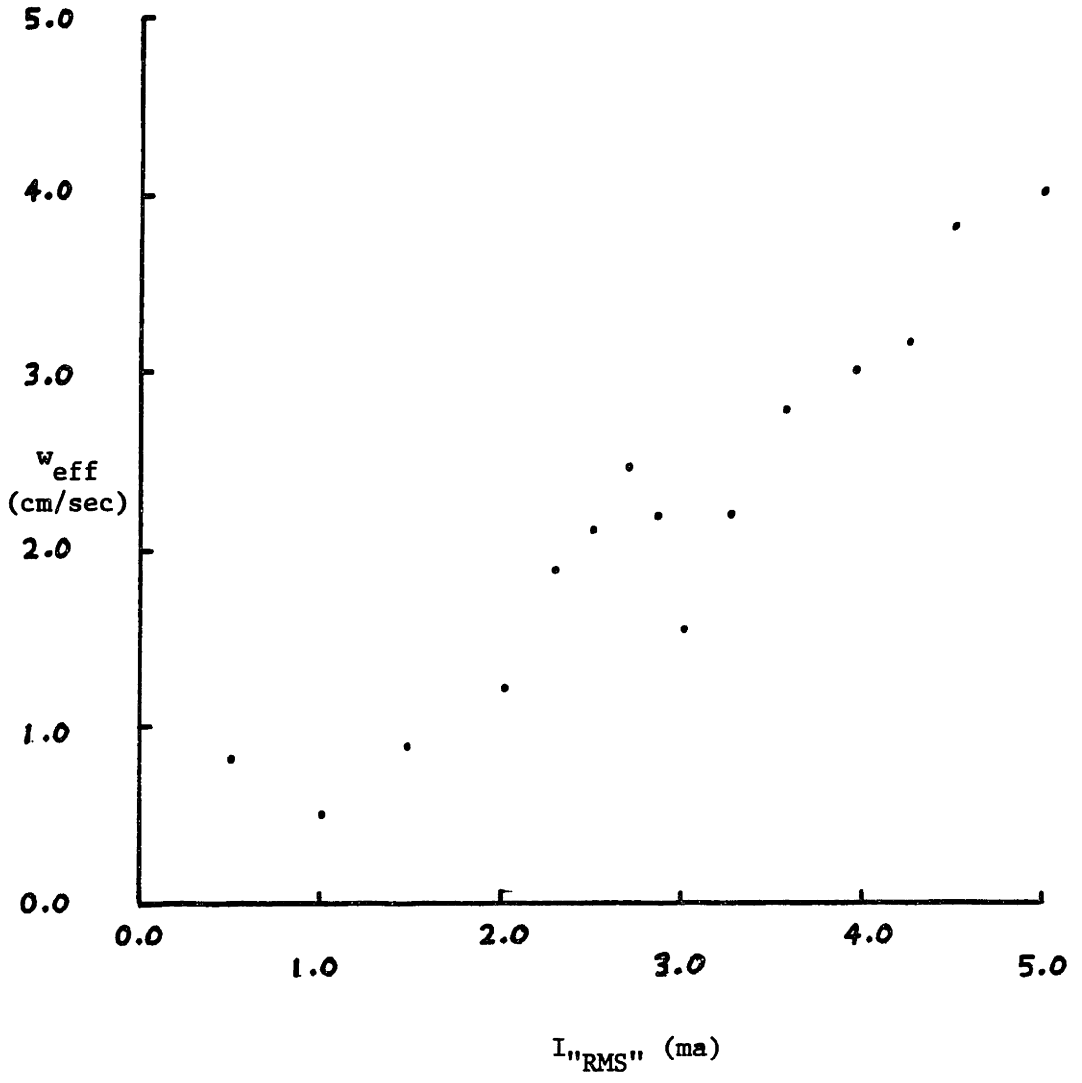

Figure A2.15. Plot of effective particle migration velocity vs. RMS corona excitation current magnitude. Horizontal flow velocity was 8.9 m/sec. 60 Hz AC excitation was used (7/21/83).

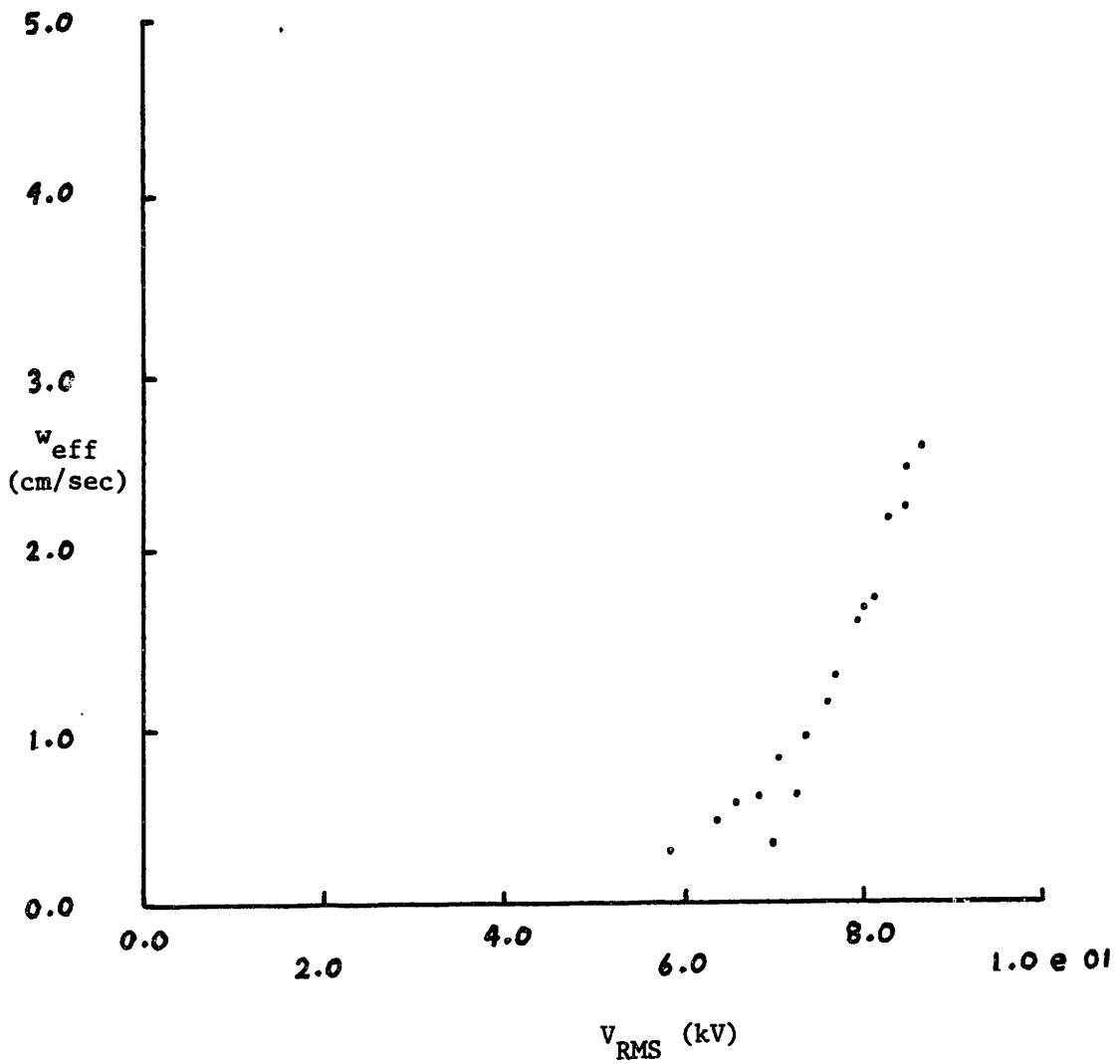

Figure A2.16. Plot of effective particle migration velocity vs. RMS corona excitation voltage magnitude. Horizontal flow velocity was 8.9 m/sec. 100 Hz AC excitation was used (7/20/83).

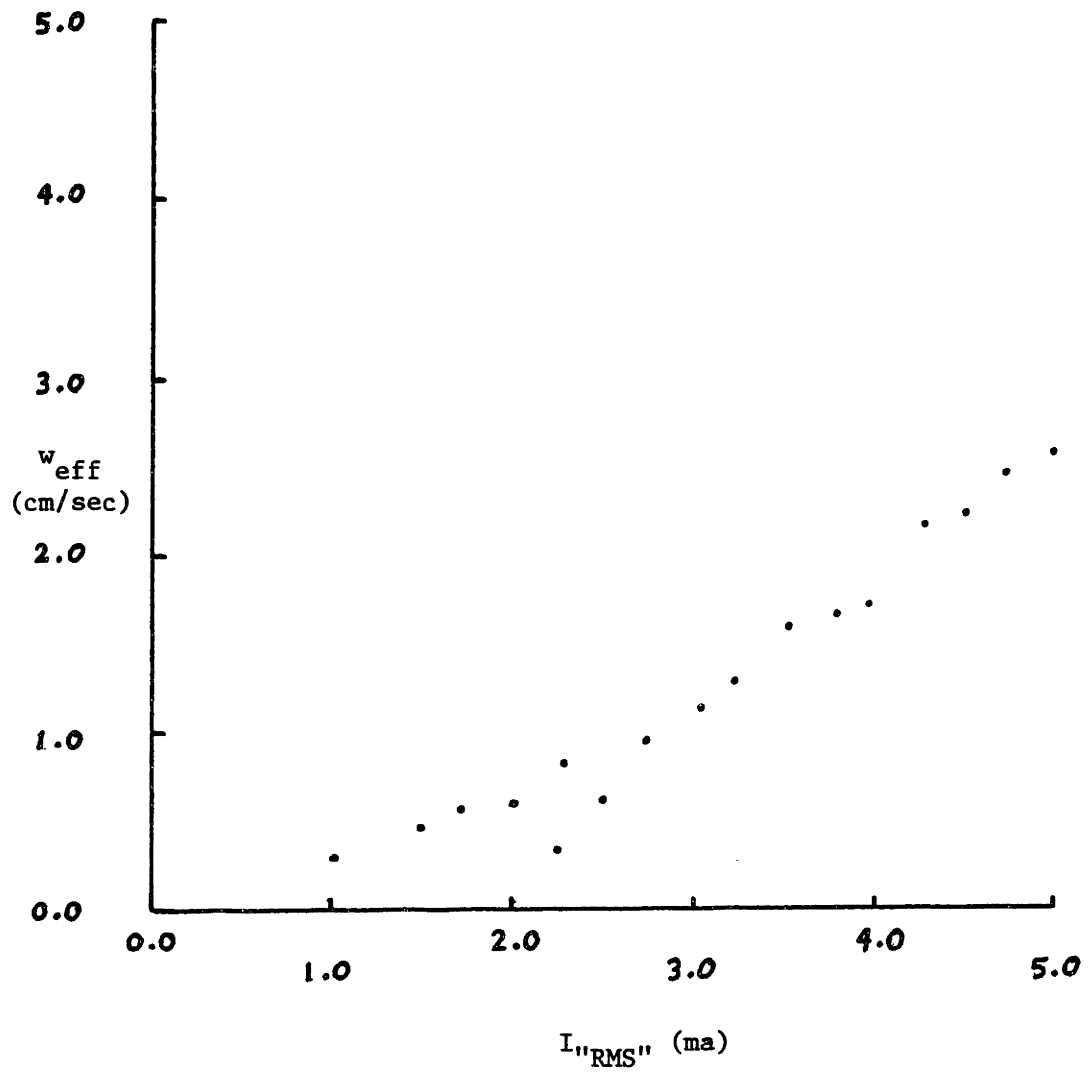

Figure A2.17. Plot of effective particle migration velocity vs. RMS corona excitation current magnitude. Horizontal flow velocity was 8.9 m/sec. 100 Hz AC excitation was used (7/20/83).

Appendix 3

Detailed Turbulent Diffusion Model

A3.1 Introduction

This appendix contains a detailed analysis of the turbulent diffusion model, introduced in chapter 4, for single-stage AC electrostatic precipitation of particles from turbulent flows*. As presented here, the model accounts both for the effects of a finite turbulent diffusivity, D_t, and for the possibility that the oscillatory particle migrations can significantly affect the precipitation rate at the collection plates. The situation proposed in chapter 4 is included as a special limiting case, in which the bulk diffusivity is infinite, but the turbulent mixing does not bring particles close enough to the plates for their oscillatory migrations to precipitate them.

The generalized situation is described in section 2. The differential equation which constrains the particle concentration in the volume is derived in section 3, and the discussion of section 4 results in an approximate boundary condition. A quasi-one-dimensional approximation is introduced in section 5, to simplify the volume equation, and 6 presents a normalization which allows solution of the problem in terms of dimensionless variables. The actual solution of the problem is presented in section 7. The solution for the steady-state particle concentration as a function of position in the precipitator is then used in section 8 to determine the collection efficiency of the device. Section 9 includes a discussion of the general predicted behavior of the precipitator.

The model presented here is a generalization of Leonard's model for DC precipitation in the presence of a finite turbulent diffusivity[1].

---

*It is assumed that the reader is already familiar with the treatment of the model that is presented in section 4 of chapter 4

A3.2 Problem Description

The situation is as pictured schematically in Fig. (1), and described previously in chapter 4. Air, laden with particles, flows between two parallel plates of length, L, width, D, and separation, H. The mean flow velocity, U, is assumed to be uniform in the core flow, decreasing rapidly to zero across thin boundary layers at each plate. The particle concentration, n(x,z,t), is taken as uniform at the inlet.

$$n(x,0,t) = n_o \tag{A3.2.1}$$

As in the simplified situation of chapter 4, the particles experience both a time-average migration toward the lower plate and an oscillatory motion. In this generalized case, the particle migration will be characterized by four lengths and the cycle time of the motion. These four length, defined below, are illustrated in Fig. (2) The lengths, $\ell_{max,+}$ and $\ell_{max,-}$ are the maximum displacement of a particle during two consecutive half-cycles, referred to hereafter as the positive and negative half-cycles, respectively (As the nomenclature might imply, they correspond to the positive and negative half-cycles of an applied electrical excitation). The distance, ℓ_{net}, the net displacement of the particle during one cycle of the particle motion, is now the sum of the net displacements during these same two consecutive half-cycles, $\ell_{net,+}$, and $\ell_{net,-}$, respectively. Normally, only the sum, ℓ_{net}, is of importance. It is possible for ℓ_{net} to be much smaller than the sum of $\ell_{max,+}$ and $\ell_{max,-}$, because particles can undergo nearly equal backward and forward displacements each half-cycle, as is the case for very high frequency charging. It is assumed that ℓ_{net}, $\ell_{max,+}$, and $\ell_{max,-}$ are all much smaller than any other physical dimensions of the system described thus far.

The effects of turbulent mixing on particle transport in the precipitator will be modeled by assignment of a uniform equivalent diffusivity, D_t, in the bulk flow. A zone of thickness, $\delta << H$, in which no turbulent transport takes place, is assumed to exist immediately adjacent to the plates at x = 0, H, respectively. The only way that particles can reach the plates from the edge of the core flow is to migrate across this zone.

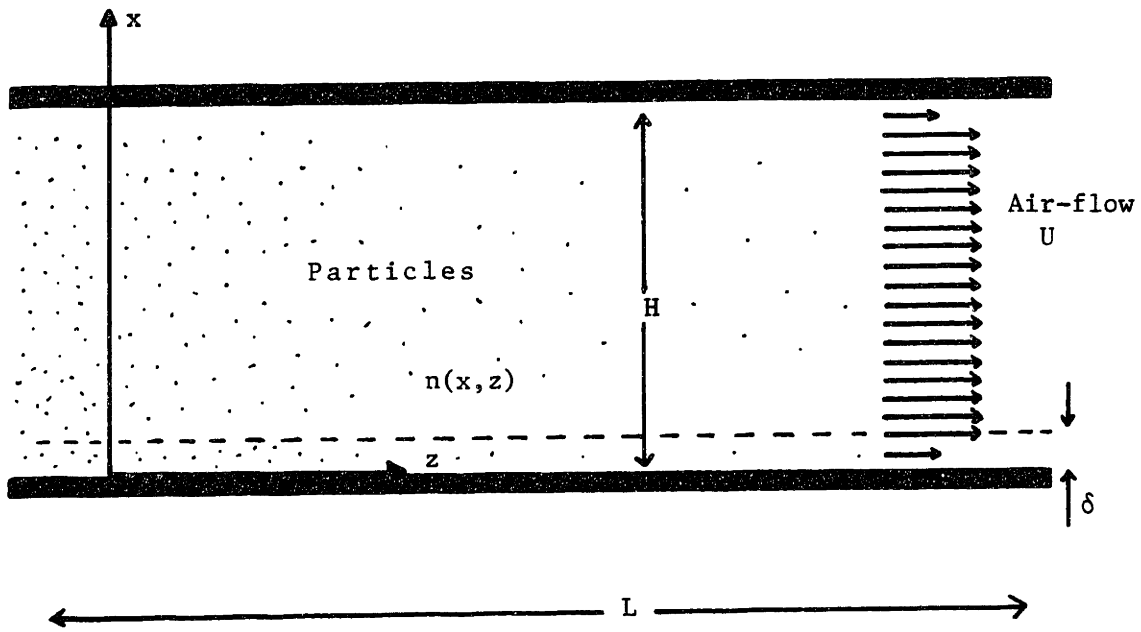

Fig. A3.1. Schematic illustration of situation for detailed turbulent diffusion model. Particles enter at left, convected by air-flow. Particle density decreases with increasing axial coordinate, due to precipitation onto lower plate.

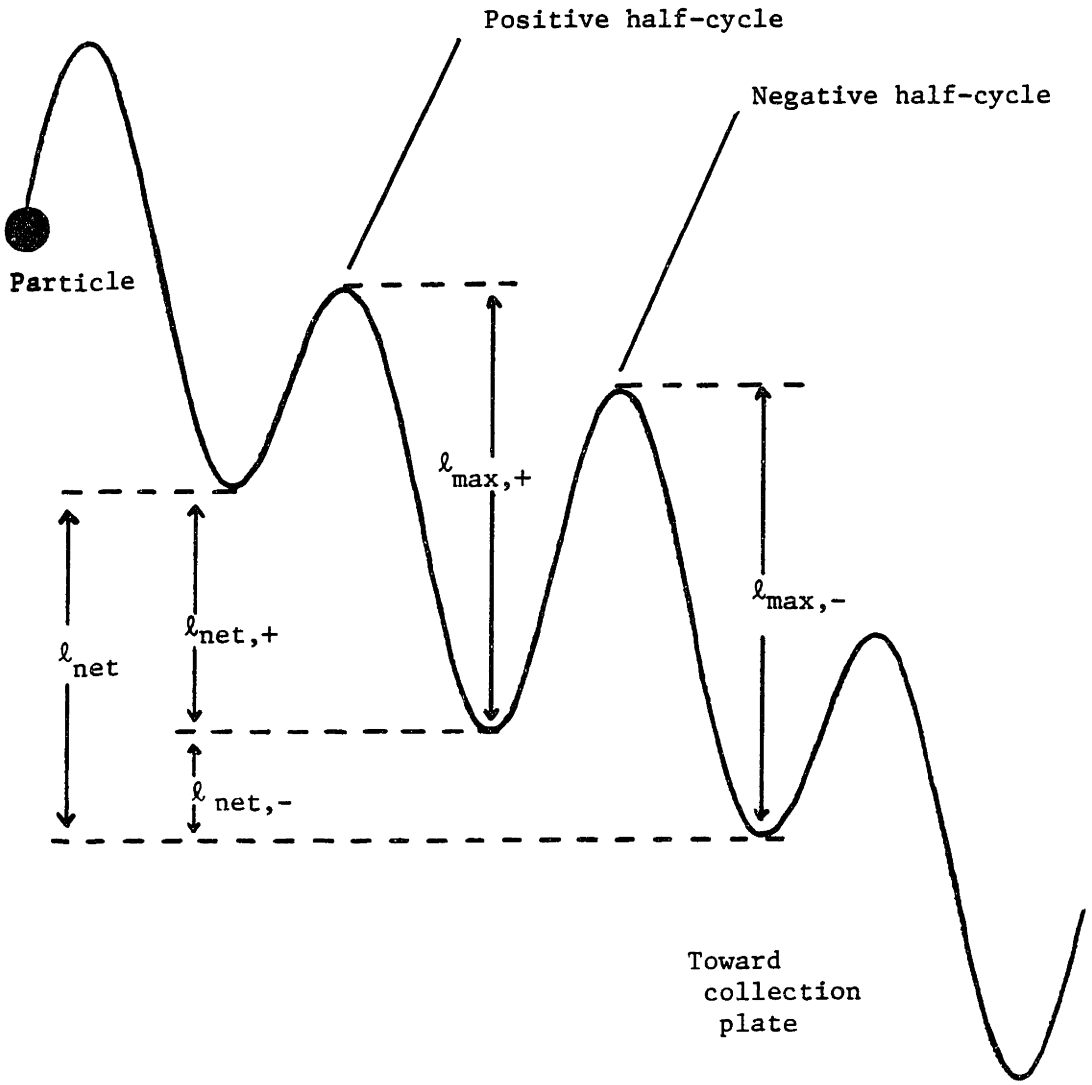

Fig. A3.2. Path of particle undergoing universal precipitation. In the general case, the motion during positive and negative half-cycles of the electrical excitation can be different.

It will be assumed that the device has been in operation for a sufficiently long time that it has reached a steady-state (except that the amount of particulate accumulated on the wall increases steadily with time. Thus, for time-scales that are long compared to the cycle time of the particle motion, the concentration profile is unchanging with time.

It is desired to determine the overall precipitation efficiency of the device. Since, in this case, the particle concentration, $n(x,z,t)$ can depend upon the transverse coordinate, x, the definition of the efficiency given in eqs. (4.4.6) and (4.4.7) cannot be applied here. The time-average particle concentration, $\langle n(x,z)\rangle$, is defined

$$\langle n(x,z)\rangle \equiv \frac{1}{T} \int_{t}^{t+T} n(x,z,t')\, dt' \tag{A3.2.2}$$

The efficiency, η, is

$$\eta \equiv 1 - \frac{1}{n_o} \int_{0}^{H} \langle n(x,L)\rangle\, dx \tag{A3.2.3}$$

Thus, as before, the collection efficiency is simply the fraction of particulate entering the device that is precipitated before it reaches the exit at $z = L$.

A3.3 Derivation of Volume Equation

Application of the law of conservation of mass to the particle concentration, $n(\bar{r},t)$, yields

$$\frac{\partial n(\bar{r},t)}{\partial t} = - \nabla \cdot \Gamma_n(\bar{r},t) \tag{A3.3.1}$$

where

$$\Gamma_n(\bar{r},t) = \bar{I}_z\, Un(\bar{r},t) - \bar{I}_x w(t) \cdot n(\bar{r},t) - D_t \nabla n(\bar{r},t) \tag{A3.3.2}$$

is the particle flux-density. The quantity, $w(t)$, is the total particle migration velocity, which is a periodic function of time. It is defined as

$$w(t) = w_{net} + w'(t) \tag{A3.3.3}$$

where $w'(t)$ is the oscillatory part of the migration velocity and has

zero net value.

$$\int_{t}^{t+T} w'(t) = 0 \tag{A3.3.4}$$

A simple substitution of variables can be used to show that if $n(\bar{\xi},t)$ satisfies the differential equation

$$\frac{\partial n(\bar{\xi},t)}{\partial t} = - \nabla \cdot \Gamma_n(\bar{\xi},t) \tag{A3.3.5}$$

where

$$\Gamma_n(\bar{\xi},t) = U n(\bar{\xi},t) + w_{net} n(\bar{\xi},t) - D_t \nabla n(\bar{\xi},t) \tag{A3.3.6}$$

then $n(\bar{r},t)$ will satisfy equations (1) and (2) if

$$\bar{\xi} = \bar{x} - \bar{i}_x \int^t w'(\tau)\, d\tau \tag{A3.3.7}$$

To be precise, the Del-operator in eqs. (5) and (6) should perform spatial differentiation with respect to the coordinate, $\bar{\xi}$, not $\bar{r}$. However, as can be seen from eq. (7), the same value is obtained from differentiation with respect to either coordinate, as long as the time, t, is held constant.

Equation (6) can be used to substitute for $\Gamma_n(\bar{\xi},t)$ in eq. (8), yielding a constant-coefficient partial differential equation for $n(\bar{\xi},t)$. The most significant difference between such an equation and the one which would result from eqs. (1) and (2) is the lack of time dependence in the coefficients of the former. If the appropriate boundary conditions for this transformed problem are also time-independent, then a steady-state solution will exist that has no time dependence at all. Under such circumstances, $n(\bar{\xi},t)$, will satisfy the equation

$$D_t \nabla^2 n(\bar{\xi}) - (\bar{i}_z U - \bar{i}_x w_{net}) \cdot \nabla n(\bar{\xi}) = 0 \tag{A3.3.8}$$

Once a solution to eq. (8) is determined (satisfying, as of yet, undetermined boundary conditions), it will be a solution to eqs. (1) and

(2) as well if $\bar{\xi}$ is related to $\bar{r}$ as specified in eq. (7). A physical interpretation of such a solution would be that the steady-state particle distribution "wiggles" up and down with a cycle time equal to that of the particle migration. This oscillation is superimposed upon the steady diffusion and convection modeled by eq. (8). The maximum excursion of these "wiggles" is bounded by the sum of $\ell_{max,+}$ and $\ell_{max,-}$, as the integral of eq. (7) can never exceed that value. If there are no significant variations of $n(\bar{\xi})$ over such small distances, then the oscillations of $\bar{\xi}$ about $\bar{r}$ specified in that equation can be neglected. In fact, one could then simply replace $\bar{\xi}$ by $\bar{r}$ in eq. (8) to obtain an approximate differential equation constraining $n(\bar{r})$ in the core flow. The only location where such an approximation may not be valid is near the plates, where the concentration may change very rapidly in the thin boundary layer. If it is the overall efficiency that is of interest, then errors in the actual time-varying concentration over such small distances are unimportant, as they will not contribute significant error in the evaluation of eq. (A3.2.3).

A3.4 Derivation of Boundary Conditions

There exist four significant boundaries to the system, one each at x=0, H, and one each at z=0, L. Equation (1) states the constraint on n(x,z) at z=0. For the condition at the outlet, it will be assumed that the collection region actually extends far beyond z=L [even though the precipitation efficiency is still to be calculated by eq. (A3.2.3)], and that the particle concentration tends toward zero as $z \to \infty$.

$$n(x,z) \Big|_{z \to \infty} \to 0 \qquad \text{(A3.4.1)}$$

Thus, the boundary conditions imposed at the inlet and outlet of the precipitator are relatively straightforward. Derivation of the corresponding conditions at the plates is more involved.

In the previous section, an equation was derived to constrain the particle distribution in the core flow. This equation had no significant dependence on the oscillatory particle migration velocity, w'(t). Those oscillations, which have zero time-average value, do not affect the particle transport processes in the volume because their maximum amplitude of displacement is much smaller than any other physical dimensions of the core flow. This may not be the case near the collection plates, due to both the existence of a thin boundary layer there, and the non-linear nature of the boundary condition imposed by the collection plate.

In the simplified derivation of chapter 4, it was assumed that the positive and negative corona half-cycles produced identical particle migrations, so that $\ell_{max,+} = \ell_{max,-} \equiv \ell_{max}$, and $\ell_{net,+} = \ell_{net,-} \equiv \ell_{net}$. It was shown there that the flux of particles during a half-cycle would be determined entirely by the time-average particle migration velocity during that half-cycle if

$$\ell_{max} - \ell_{net} < \delta \qquad \text{(A3.4.2)}$$

where δ is the thickness of the zone of no turbulent transport adjacent to each plate. If the corresponding inequalities hold true in this more general case,

$$\ell_{max,+} - \ell_{net,+} < \delta \qquad \text{(A3.4.3)}$$

$$\ell_{max,-} - \ell_{net,-} < \delta \qquad (A3.4.4)$$

then the arguments of that chapter can be applied here also, and the effective rate at which particles precipitate onto the plate at x=0 is simply equal to the time-average migration velocity, w_{net}.

In the argument below, it will be assumed that this is not the case, and that

$$\ell_{max,+} - \ell_{net,+} > \delta \qquad (A3.4.5)$$

so that the boundary condition derived in chapter 4 does not apply. Physically, the implication of eq. (5) is that, at some time during each positive half-cycle, the zone of no turbulent transport is entirely cleared of particles*.

Figure (4.11a) shows a portion of the collection region in the vicinity of the zone, immediately before a positive half-cycle of the particle motion. Outside of the zone, the turbulent transport time, based on the oscillating migration lengths, $\ell_{max,+}$ and $\ell_{max,-}$, is assumed to be very short. Significant gradients in the particle concentration cannot exist on such length scales, even for times on the order of the cycle time, T. Particles initially move away from the collection plate, as was the case in the simplified model of chapter 4. Those particles that are initially in the zone travel out of it. Outside, however, the concentration remains relatively constant, even after the zone has been cleared of particles. Turbulent diffusion is able to overcome the migration away from the plate. The difference between the situation here and that of chapter 4 is that, at some time, the entire zone of no turbulent mixing is cleared of particles.

Once the particles begin to migrate toward the collection plate, the outer edge of the zone acts as a source, supplying particles at the concentration, n(0,z). The number of particles per unit area that actually reach the plate is given by

$$\bar{i}_x \cdot \int_{t_1}^{t_2} \bar{\Gamma}_n \, d\tau = \int_{t_1}^{t_2} n(0,z)\, w(t)\, dt - \delta\, n(0,z) \qquad (A3.4.6)$$

---

*The particles must, at some time, have moved backwards [up, in Fig. (2)] the distance, $\ell_{max,+} - \ell_{net,+}$, or else the maximum and net displacements could not possibly be $\ell_{max,+}$ and $\ell_{net,+}$, respectively.

The only transport mechanism that can move particle through the zone in the $\bar{i}_x$ direction is migration. The term in eq. (6) involving δ accounts for the fact that those particles that are left in the zone at the end of the half-cycle will be swept out of it at the beginning of the next half-cycle. The time when the particles begin moving towards the plate and the time of ending of the positive half-cycle are denoted by t_1 and t_2, respectively. By the definition of $\ell_{max,+}$,

$$\int_{t_1}^{t_2} w(t)\, dt \equiv \ell_{max,+} \tag{A3.4.7}$$

Thus, the number of particles collected per unit collection area during the positive half-cycle can be expressed as

$$\bar{i}_x \cdot \int_{t_1}^{t_2} \bar{\Gamma}_n\, d\tau = n(0,z) \cdot [\ell_{max,+} - \delta] \tag{A3.4.8}$$

A similar argument applies to the negative half-cycle of the particle motion. If an effective precipitation velocity is defined so that

$$-\bar{i}_x \cdot \frac{1}{T} \int_{t}^{t+T} \bar{\Gamma}_n\, d\tau = n(0,z)\, w_p \tag{A3.4.9}$$

then the above reasoning can be used to determine an expression for w_p.

$$w_p = \frac{1}{T} \left(\max[\ell_{max,+} - \delta, \ell_{net,+}] + \max[\ell_{max,-} - \delta, \ell_{net,-}] \right) \tag{A3.4.10}$$

The function, max(a,b), selects the larger of its arguments. In the case where the inequality of eq. (5) is satisfied (along with that corresponding to the negative half-cycle), eq. (10) becomes

$$w_p = \frac{1}{T} [\ell_{max,+} - \ell_{max,-} - 2\delta] \tag{A3.4.11}$$

It is seen that w_p is the effective time-average velocity at which particles leave the core flow and precipitate out at the collecting plate. For time-scales that are much longer than the cycle time of the microscopic particle motion, only this mean flux is important. Thus, an appropriate boundary condition for the time-independent volume equation, eq. (A3.3.8), is

$$\bar{i}_x \cdot \Gamma_n(\bar{r})\Big|_{x=0} = \left(D_t \frac{\partial n(\bar{r})}{\partial x} + w_{net} n(\bar{r}) \right)\Big|_{x=0} = w_p n(\bar{r})\Big|_{x=0} \tag{A3.4.12}$$

or

$$D_t \frac{\partial n(\bar{r})}{\partial x} \Bigg|_{x=0} = [w_p - w_{net}]\, n(\bar{r}) \Bigg|_{x=0} \qquad \text{(A3.4.13)}$$

As was the case with the model of chapter 4, it will be assumed that the particle flux at the upper plate is zero.

$$-\bar{i}_x \cdot \bar{\Gamma}_n(\bar{r}) \Big|_{x=0} = \left(D_t \frac{\partial n(\bar{r})}{\partial x} + w_{net} n(\bar{r}) \right) \Bigg|_{x=0} = 0 \qquad \text{(A3.4.14)}$$

A3.5 Quasi-One-Dimensional Approximation

Although eqs. (A3.2.1), (A3.3.8), (A3.4.1), (A3.4.13), and (A3.4.14) form a well-posed boundary-value problem, it is desired to further simplify the problem. Diffusion in the flow direction ($\bar{i}_z$) will be neglected in comparison with convection. This approximation is acceptable if the characteristic diffusion time, based on the length of the precipitator, L, is long compared to the transit time, τ_c, defined in eq. (4.4.3).

$$\tau_{d,L} \equiv \frac{L^2}{D_t} >> \tau_c \tag{A3.5.1}$$

In this case, the Laplacian operator in eq. (A3.3.8) can be replaced by a second derivative with respect to the transverse coordinate, x [$\bar{\xi}$ is replaced by $\bar{r}$, as discussed at the end of section A3.3].

$$U\frac{\partial n(x,z)}{\partial z} = w_{net}\frac{\partial n(x,z)}{\partial x} + D_t\frac{\partial^2 n(x,z)}{\partial x^2} \tag{A3.5.2}$$

Note that, with the removal of streamwise diffusion, the downstream boundary condition, eq. (A3.4.1) is no longer necessary. The problem is now specified by eqs. (A3.2.1), (A3.4.13), (A3.4.14), and (2).

A3.6 Normalization

The following normalization is applied to the problem posed by eqs. (A3.2.1), (A3.4.13), (A3.4.14), and (2), in order to allow easier interpretation of its results. With the understanding that "→" means "is normalized to",

$$\begin{aligned} x &\to H \\ z &\to L \\ n &\to n_o \end{aligned} \tag{A3.6.1}$$

Equation (A3.5.2) becomes

$$\frac{\tau_d}{\tau_c}\frac{\partial \underline{n}}{\partial \underline{z}} = \frac{\partial^2 \underline{n}}{\partial \underline{x}^2} + \frac{\tau_d}{\tau_m}\frac{\partial \underline{n}}{\partial \underline{x}} \tag{A3.6.2}$$

The normalized values of n, x, and z, are represented by $\underline{n}$, $\underline{x}$, and $\underline{z}$, respectively. The boundary conditions become

$$\underline{n}\Big|_{\underline{z}=0} = 1 \tag{A3.6.3}$$

$$\frac{\partial \underline{n}}{\partial \underline{x}}\Big|_{\underline{x}=0} = \frac{\tau_d}{\tau_m}\left(\frac{w_p}{w_{net}} - 1\right) \underline{n}\Big|_{\underline{x}=0} \tag{A3.6.4}$$

$$\frac{\partial \underline{n}}{\partial \underline{x}}\Big|_{\underline{x}=1} = -\frac{\tau_d}{\tau_m} \underline{n}\Big|_{\underline{x}=1} \tag{A3.6.5}$$

It is seen that, in its present (simplified) form, the problem is specified by three dimensionless quantities. The ratio of τ_d to τ_c represents the competition between diffusion and convection of the particulate. If $\tau_d >> \tau_c$, then no significant diffusion occurs during residence time of the gas. The ratio of τ_d to τ_m represents the competition between migration and diffusion of particles. The last ratio, w_p/w_{net}, is important in determining whether turbulent diffusion is a help or a hindrance to the precipitation process. Note that, by the definitions of w_p and w_{net}, this ratio cannot be less than unity. If $w_p = w_{net}$, as it would in the case of DC precipitation, then the effect of turbulent diffusion is to reduce the concentration buildup of particulate near the collection plate, and thus, to impair collection. If $w_p >> w_{net}$, then the particle oscillations are able to remove them from the edge of the flow region much faster than their net migration can get them there. In that case, the effect of the turbulent diffusion is to reduce a particle <u>deficit</u> near the wall, and thus, to improve the collection.

A3.7 Problem Solution

For the sake of convenience, the following dimensionless parameters are defined.

$$\beta \equiv \frac{1}{2}\frac{\tau_d}{\tau_m} \tag{A3.7.1}$$

$$k \equiv \frac{\tau_c}{\tau_m} \tag{A3.7.2}$$

$$g \equiv 2\frac{w_p}{w_{net}} - 1 \tag{A3.7.3}$$

Because all quantities to be dealt with in this section are normalized, the underbars will be dropped [This is done simply for the sake of convenience]. Thus, eqs. (A3.6.2) - (A3.6.5) become

$$2\frac{\beta}{k}\frac{\partial n}{\partial z} = \frac{\partial^2 n}{\partial x^2} + 2\beta\frac{\partial n}{\partial x} \tag{A3.7.4}$$

$$\left.\frac{\partial n}{\partial x}\right|_{x=0} = \beta(g-1)\,n\Big|_{x=0} \tag{A3.7.5}$$

$$\left.\frac{\partial n}{\partial x}\right|_{x=1} = -2\beta n\Big|_{x=1} \tag{A3.7.6}$$

$$n\Big|_{z=0} = 1 \tag{A3.7.7}$$

This section contains a synopsis of the technique of solution of the boundary-value problem specified by eqs. (4) - (7). Briefly, the method of seperation of variables is applied to eq. (4), yielding two ordinary linear differential equations, one constraining the z-dependance of n(x,z), the other constraining its x-dependance. The former is a linear, first-order, constant-coefficient, ordinary differential equation, and is easily solved. The second, in conjunction with eqs. (5) and (6), forms a Sturm-Liouville problem[1], whose solution involves a transendental eigenvalue equation. A summation of orthogonal modes of the solution is used to satisfy the inlet boundary condition,

eq. (7). The resulting expression for $n(x,z)$ is then used to evaluate eq. (A3.2.3), determining the collection efficiency of the device in terms of the dimensionless parameters, β, k, and g [which are, themselves defined in terms of τ_d/τ_m, τ_c/τ_m, and w_p/w_{net}, in eqs. (1) - (3)].

A3.7.1 Application of the Method of Seperation of Variables

The particulate concentration, $n(x,z)$, is expressed as the product of two functions, each dependent upon only one spatial coordinate.

$$n(x,z) = N_x(x)\,N_z(z) \tag{A3.7.8}$$

Substitution of this form for $n(x,z)$ into eq. (4) yields two ordinary differential equations.

$$2\frac{\beta}{k}\frac{1}{N_z}\frac{dN_z}{dz} = \frac{1}{N_x}\left(\frac{d^2N_x}{dx^2} + 2\beta\frac{dN_x}{dx}\right) = -(1+\zeta^2)\beta^2 \tag{A3.7.9}$$

Since the quantity to the left of the first equal sign is independent of x, and the quantity between the equal signs is independent of z, both must be equal to a value that does not depend on either coordinate. The particular form of the seperation constant in eq. (9) is chosen for convenience of solution of the resulting ordinary differential equations, as is shown below. For real values of the arbitrary constant, ζ, the seperation constant, $-(1+\zeta^2)\beta^2$, varies within the range, $-\beta \to -\infty$.

The constraint that eq. (9) places on the z-dependence of $n(x,z)$ is

$$\frac{dN_z}{dz} = -\frac{1}{2}(k\beta)\,(1+\zeta^2)\,N_z \tag{A3.7.10}$$

The solution of eq. (10) is

$$N_z(z) = e^{-\frac{1}{2}(k\beta)(1+\zeta^2)z} \tag{A3.7.11}$$

The equation that constrains $N_x(x)$ is more complicated.

$$\frac{d^2 N_x}{dx^2} + 2\beta\frac{dN_x}{dx} + (1 + \zeta^2)\beta^2 N_x = 0 \qquad \text{(A3.7.12)}$$

Solutions to eq. (12) are of the form,

$$N_x(x) = A\, e^{\alpha x} \qquad \text{(A3.7.13)}$$

where A is an arbitrary constant, and α satisfies the equation,

$$\alpha^2 + 2\beta\alpha + (1 + \zeta^2)\beta^2 = 0 \qquad \text{(A3.7.14)}$$

Application of the quadratic equation solution to eq. (14) yields two possible values for α.

$$\alpha_{\pm} = -\beta \pm j\beta\zeta \qquad \text{(A3.7.15)}$$

where it is understood that the upper sign on the right in eq. (15) is taken to obtain α_+, and the lower sign is taken for α_-. Thus, the form of a solution for $N_x(x)$ is

$$N_x(x) = e^{-\beta x}\left(A_+ e^{j\beta\zeta x} + A_- e^{-j\beta\zeta x} \right) \qquad \text{(A3.7.16)}$$

where A_+ and A_- are both arbitrary constants.

A3.7.2 Derivation and Solution of Eigenvalue Equation

The boundary conditions, eqs. (5) and (6) constrain $N_x(x)$ as follows.

$$\left.\frac{dN_x}{dx}\right|_{x=0} = \beta(g - 1)N_x\Big|_{x=0} \qquad \text{(A3.7.17)}$$

$$\left.\frac{dN_x}{dx}\right|_{x=1} = -2\beta N_x\Big|_{x=1} \qquad \text{(A3.7.18)}$$

Substitution of eq. (16) into eqs. (17) and (18) yields a set of constraints on the "arbitrary" constants, A_+ and A_-.

$$(g - j\zeta)A_+ + (g + j\zeta)A_- = 0 \qquad \text{(A3.7.19)}$$

$$(1 + j\zeta)\, e^{j\beta\zeta} A_+ + (1 - j\zeta)\, e^{-j\beta\zeta} A_- = 0 \qquad \text{(A3.7.20)}$$

Equations (19) and (20) form a set of simultaneous, homogeneous, linear equations which determine A_+ and A_-. Non-trivial solutions to these equations exist only if the corresponding determinant is equal to zero. This condition will be met if and only if

$$e^{j2\beta\zeta} = \frac{(g - j\zeta)(1 - j\zeta)}{(g + j\zeta)(1 + j\zeta)} \qquad \text{(A3.7.21)}$$

For purely real values of ζ, it is more convenient to express the constraint of eq. (21) in terms of real quantities.

$$\tan(\beta\zeta) = -\frac{(g + 1)\zeta}{g - \zeta^2} \qquad \text{(A3.7.22)}$$

It can be verified that eqs. (21) and (22) represent identical constraints for purely real values of ζ by the following procedure. Euler's formula* can be used to express the complex exponential of eq. (21) in terms of the trigonometric functions, $\sin(2\beta\zeta)$ and $\cos(2\beta\zeta)$. Setting the real and imaginary parts of the resulting equation equal#, one obtains two constraints, each involving one of those trigonometric functions. The use of half-angle formulae allows expression of these constraints in terms of $\sin(\beta\zeta)$ and $\cos(\beta\zeta)$. It will be seen that the two equations that are obtained are both satisfied under the conditions of eq. (22). Fig. (3) gives a graphic illustration of the constraint of eq. (22) on the permissible values of ζ. An infinite number of eigenvalues exist. The n'th root of eq. (22), which will be referred to as ζ_n, for n = 1 to ∞, may be specified by the two equations

$$(n - 1)\frac{\pi}{\beta} < \zeta_n < n\frac{\pi}{\beta} \qquad \text{(A3.7.23)}$$

and

$$\tan(\beta\zeta_n) = -\frac{(g + 1)\zeta_n}{g - \zeta_n^2} \qquad \text{(A3.7.24)}$$

A trivial root, $\zeta = 0$, exists in addition to those specified above.

---

*$e^{j\theta} = \cos(\theta) + j\sin(\theta)$

#It is assumed, here, that ζ is real

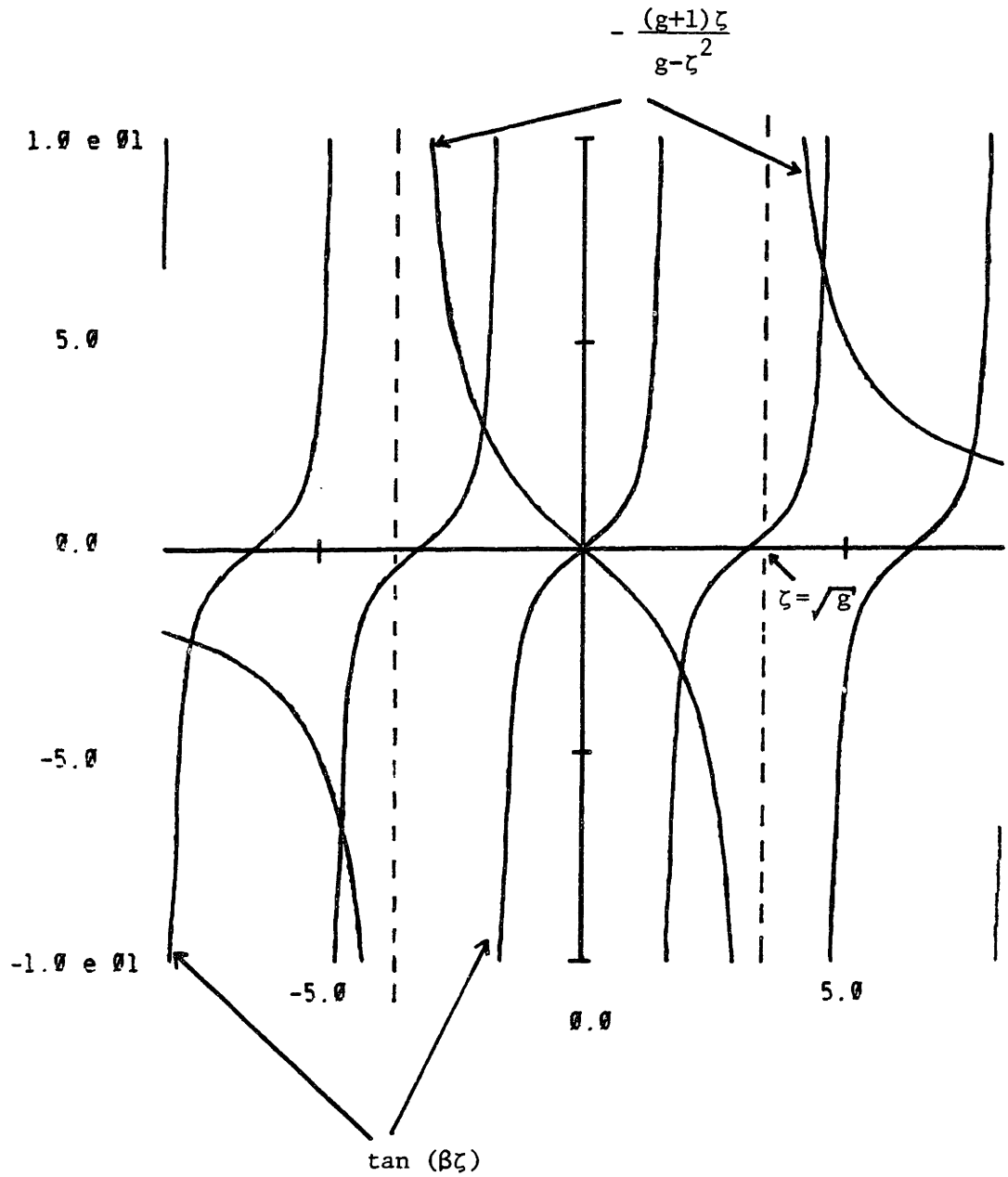

Fig. A3.3. Graphic solution to eigenvalue equation, eq. (A3.7.22). Points of intersection of the plots of tan ($\beta\zeta$) and $(g+1)\zeta/(g-\zeta^2)$ correspond to eigenvalues, ζ_n for n=1, ∞. Plots drawn above are for β=1, g=3.5.

A3.7.3 Determination of Modes of Solution

For values of ζ that satisfy the eigenvalue equation, eq. (22), the two constraints of eqs. (19) and (20) are identical, and thus do not uniquely determine A_+ and A_-. Either one can be used to express A_- in terms of A_+.

$$g(A_{n,+} + A_{n,-}) = j\zeta_n(A_{n,+} - A_{n,-}) \tag{A3.7.25}$$

where $A_{n,+}$ is the value of A_+ that is associated with the n'th eigenvalue, ζ_n, and $A_{n,-}$ is the corresponding value for A_-. Expansion of eq. (16), using eq. (25) yields an expression for $N_{n,x}(x)$, the n'th eigenfunction for $N_x(x)$ that has only one arbitrary multiplicative constant.

$$N_{n,x}(x) = A_n e^{-\beta x}\cos(\beta\zeta_n x - \Omega_n) \tag{A3.7.26}$$

where

$$\Omega_n \equiv \cos^{-1}\frac{\zeta_n}{\sqrt{\zeta_n^2 + g^2}} \tag{A3.7.27}$$

$$A_n \equiv j(A_{n,+} - A_{n,-})\sqrt{1 + (\zeta_n/g)^2} \tag{A3.7.28}$$

Equation (28) is included only for completeness; the coefficient, A_n, is entirely arbitrary and its dependence on the coefficients, $A_{n,+}$ and $A_{n,-}$ is thus unimportant.

Equations (11) and (26) can be combined and summed over all possible modes to give a general solution to the problem posed by eqs. (4) - (6).

$$n(x,z) = \sum_{n=1}^{\infty} f_n(x,z) \tag{A3.7.29}$$

where

$$f_n(x,z) = A_n e^{-\beta x}\cos(\beta\zeta_n x - \Omega_n)\, e^{-\frac{1}{2}(k\beta)(1+\zeta^2)z} \tag{A3.7.30}$$

The values of the coefficients, A_n, are chosen so as to satisfy the remaining constraint, eq. (7).

$$n(x,0) = \sum_{n=1}^{\infty} f_n(x,0) = \sum_{n=1}^{\infty} A_n e^{-\beta x} \cos(\beta \zeta_n x - \Omega_n) = 1 \qquad \text{(A3.7.31)}$$

A3.7.4 Orthogonality of Solution Modes

The problem posed by eqs. (12), (17), and (18) falls into a category of problems known as Sturm-Liouville problems[1]. The most general statement of such a problem is of the form

$$\frac{d}{dx}\left[p(x)\frac{dy(x)}{dx} \right] + \left[q(x) + \lambda r(x) \right] y(x) = 0 \qquad \text{(A3.7.32)}$$

with boundary conditions

$$\left[\frac{dy(x)}{dx} + a\,y(x) \right] \Bigg|_{x=0} = 0 \qquad \text{(A3.7.33)}$$

$$\left[\frac{dy(x)}{dx} + b\,y(x) \right] \Bigg|_{x=1} = 0 \qquad \text{(A3.7.34)}$$

The function, $y(x)$, is the dependent variable constrained by the differential equation, eq. (32), and boundary conditions, eqs. (33) and (34). The functions, $p(x)$, $q(x)$, and $r(x)$ are specified functions of the independent variable, x. The constants, a and b, are given as well. The variable, λ, is an eigenvalue, in that solutions to the problem specified by eqs. (32) - (34) exist only for certain descrete values of λ. If $y_1(x)$ is a valid solution to the set for $\lambda=\lambda_1$, and $y_2(x)$ is valid for $\lambda=\lambda_2$, then it must be that

$$(\lambda_1 - \lambda_2) \int_0^1 r(x)\, y_1(x)\, y_2(x)\, dx = 0 \qquad \text{(A3.7.35)}$$

If the two eigenvalues are distinct (ie., $\lambda_1 \neq \lambda_2$), then the integral of eq. (35) must be equal to zero. For the problem under consideration,

$$p(x) = e^{2\beta x} \qquad \text{(A3.7.36)}$$

$$q(x) = 0 \qquad \text{(A3.7.37)}$$

$$r(x) = e^{2\beta x} \qquad \text{(A3.7.38)}$$

$$a = -\beta(g - 1) \qquad \text{(A3.7.39)}$$

$$b = 2\beta \qquad \text{(A3.7.40)}$$

and the function, $y(x)$, is, of course, replaced by $N_x(x)$.

Each side of eq. (31) can be multiplied by the quantity,

$$e^{2\beta x} N_{m,x}(x) = e^{2\beta x} A_m e^{-\beta x} \cos(\beta \zeta_m x - \Omega_m) \qquad (A3.7.41)$$

and integrated between the limits, 0 and 1. Due to the orthogonality of the modes, the integrals corresponding to those terms on the left of eq. (31) for which $n \neq m$ will all be equal to zero. The resulting equation is

$$\int_0^1 A_m^2 \cos^2(\beta \zeta_m x - \Omega_m)\, dx = A_m^2 \left[\frac{1}{2} + \frac{(g + \zeta_m^2)(g + 1)}{2\beta (g^2 + \zeta_m^2)(1 + \zeta_m^2)} \right] =$$

$$A_m \frac{\zeta_m}{(1 + \zeta_m^2)^{3/2}} \frac{1}{\beta} \left[(-1)^{m+1} 2 e^{\beta} + (g-1) \left(\frac{1+\zeta_m^2}{g^2+\zeta_m^2} \right)^{1/2} \right] \qquad (A3.7.42)$$

[A considerable amount of algebraic manipulation was omitted in obtaining the last result]. Equation (42) is solved for A_n.

$$A_n = 2 \zeta_n \left(\frac{g^2+\zeta_n^2}{1+\zeta_n^2} \right)^{1/2} \left[\frac{(-1)^{n+1} 2 e^{\beta} \sqrt{g^2+\zeta_n^2} + (g-1)\sqrt{1+\zeta_n^2}}{\beta (1+\zeta_n^2)(g^2+\zeta_n^2) + (g+\zeta_n^2)(g+1)} \right] \qquad (A3.7.43)$$

Thus, the particle concentration is given by eqs. (29) and (30), with A_n specified by eq. (43)*.

*The reader who wishes to actually evaluate $n(x,z)$ needs to use eqs. (23), (24), (27), (29), (30), and (43).

3.8 Determination of Collection Efficiency

The efficiency of collection of the precipitator of Fig. (1), defined in eq. (A3.2.3), can be expressed in terms of the normalized solution of the previous section.

$$\eta = 1 - \int_0^1 \underline{\underline{n}}(x,1)\,\underline{dx} \tag{A3.8.1}$$

Equation (1) can be evaluated explicitly, using eqs. (A3.7.29), (A3.7.30), and (A3.7.43).

$$\eta = 1 - \sum_{n=1}^{\infty} \frac{2(g+1)\zeta_n^2}{\beta(1+\zeta_n^2)^{3/2}} \left[\frac{(-1)^{n+1} 2 e^{\beta\sqrt{g^2+\zeta_n^2}} + (g-1)\sqrt{1+\zeta_n^2}}{\beta(1+\zeta_n^2)(g^2+\zeta_n^2) + (g+\zeta_n^2)(g+1)} \right] e^{-\frac{1}{2}(k\beta)(1+\zeta_n^2)} \tag{A3.8.2}$$

Equations (A3.7.27), (A3.7.23), (A3.7.24), (A3.7.1), (A3.7.2), and (A3.7.3) are repeated below, for convenience.

$$(n-1)\frac{\pi}{\beta} < \zeta_n < n\frac{\pi}{\beta} \tag{A3.8.3}$$

$$\tan(\beta\zeta_n) = -\frac{(g+1)\zeta_n}{g-\zeta_n^2} \tag{A3.8.4}$$

$$\beta \equiv \frac{1}{2}\frac{\tau_d}{\tau_m} \tag{A3.8.5}$$

$$k \equiv \frac{\tau_c}{\tau_m} \tag{A3.8.6}$$

$$g \equiv 2\frac{w_p}{w_{net}} - 1 \tag{A3.8.7}$$

A3.9 Discussion of Solution

Figures (4) - (7) show the dependence of the collection efficiency predicted by the turbulent diffusion model on the three independent parameters, $B \equiv \tau_d/2\tau_m$, $k \equiv \tau_c/\tau_m$, and $g \equiv 2(w_p/w_{net} - 1$. In Fig. (4), the precipitation velocity, w_p, is equal to the time-average migration velocity, w_{net}. Thus, for that figure, the situation is much like that of a conventional (DC) precipitator*, as the collection efficiency is determined solely by the time-average particle migrations. Several curves, corresponding to various values of the parameter, β, are plotted. Increasing values of β imply less turbulent mixing. It is seen in this case that, with other parameters held fixed, higher turbulence levels result in lower collection efficiencies. Physically, the turbulence drives particles away from the collection plate while the net particle migrations tend to "pile them up" there.

Similar sets of plots are shown in Figs. (5) - (7), for successively higher values of w_p, relative to w_{net}. When $w_p > w_{net}$, the oscillatory particle migrations contribute to the rate of particle precipitation at the plate. For small values of k, it is seen that the collection efficiency actually improves with increasing turbulence levels (ie., lower values of β). Physically, this occurs because the turbulence aids in transporting particles to the vicinity of the collection plate. Since $w_p > w_{net}$, the particles precipitate more quickly than their time-average migrations can bring them to the vicinity of the collection plate. In the limit, $w_p >> w_{net}$, portrayed in Fig. (7), the collection efficiency is strongly dependent upon the level of turbulent mixing in the precipitator. For values of β that are on the order of or less than unity, turbulent mixing is the major mechanism of particle transport in the bulk flow.

Regardless of the value of w_p relative to w_{net}, the collection efficiency with completely laminar flow (ie., $\beta \to \infty$) reaches 100% for $k = 1$, while with finite turbulent mixing, it can only approach that value. Thus, for any given value of w_p/w_{net}, and a high enough fixed

---

*The situation is also like that predicted for the AC precipitator in chapter 4.

value for k, the collection efficiency with laminar flow will exceed that with turbulent mixing present.

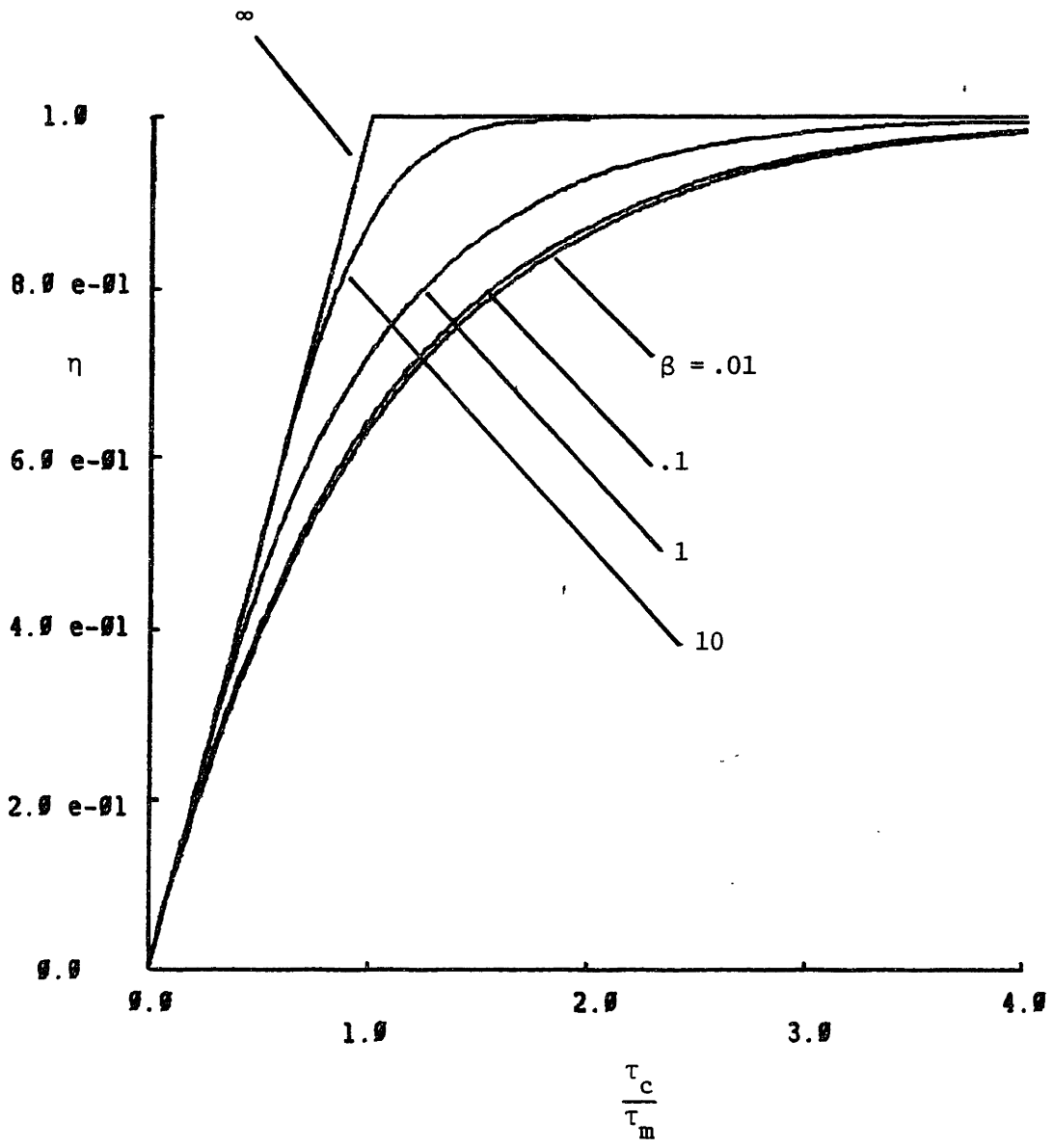

Fig. A3.4. Plot showing variation of collection efficiency, predicted by the turbulent diffusion model, with the parameter, $k \equiv \tau_c/\tau_m$, for various values of $\beta \equiv 1/2\ \tau_d/\tau_m$. For this plot, $g \equiv 2(w_p/w_{net})-1 = 1$, so that $w_p = w_{net}$.

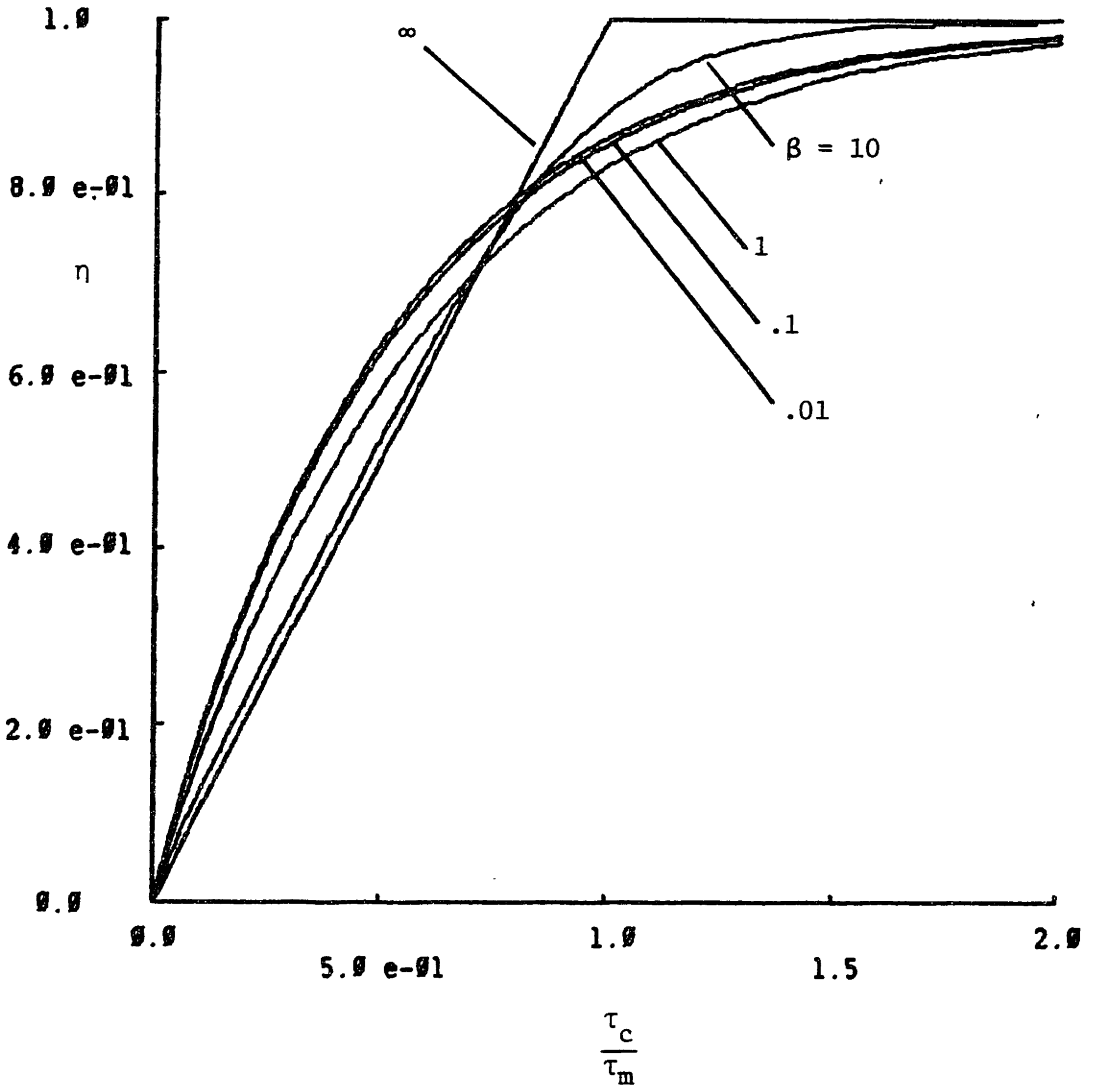

Fig. A3.5. Plot showing variation of collection efficiency, predicted by the turbulent diffusion model, with the parameter, $k \equiv \tau_c/\tau_m$, for various values of $\beta \equiv 1/2\ \tau_d/\tau_m$. For this plot, $g \equiv 2\ (w_p/w_{net})-1 = 3$, so that $w_p = 2\ w_{net}$.

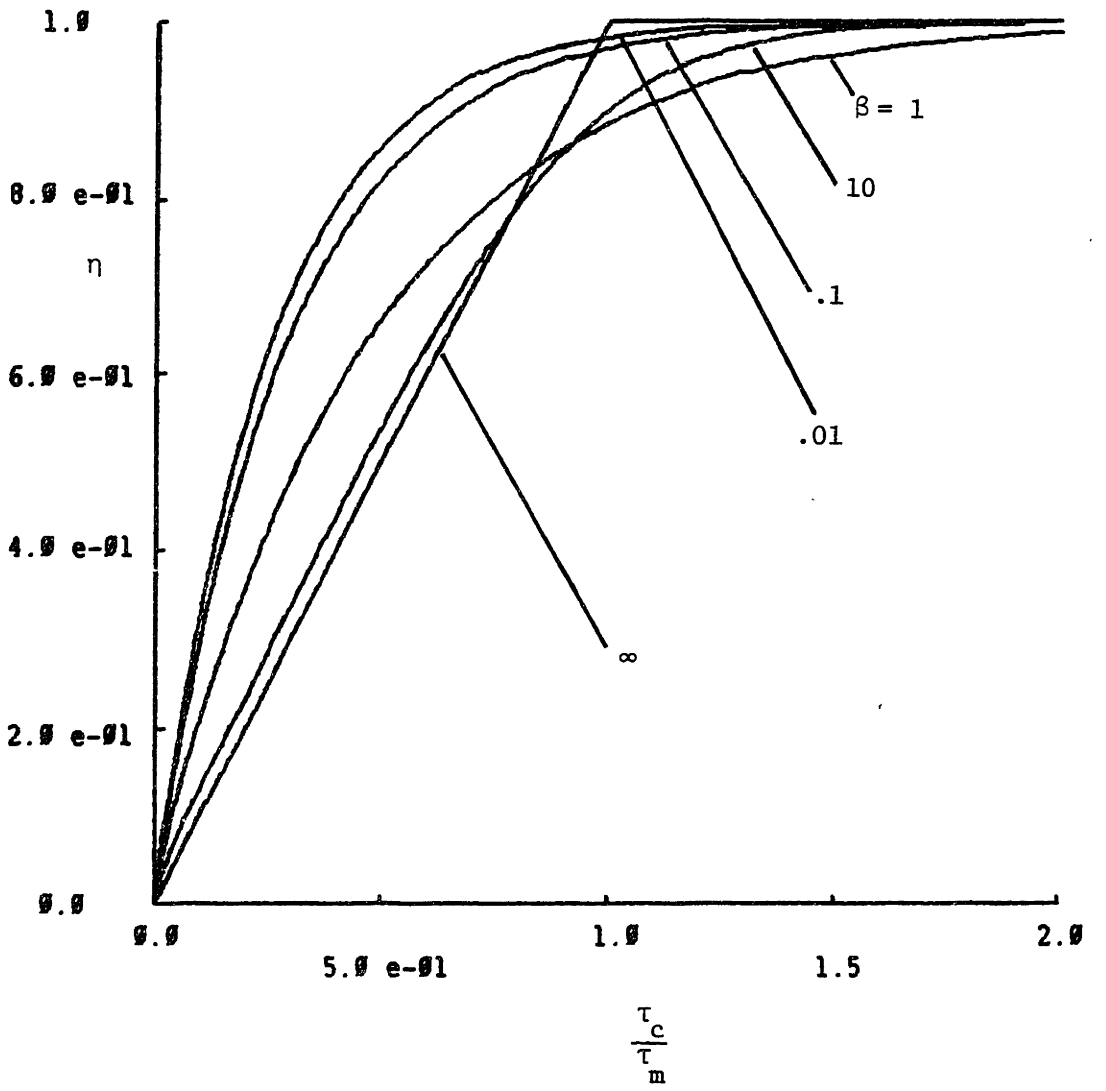

Fig. A3.6. Plot showing variation of collection efficiency, predicted by the turbulent diffusion model, with the parameter, $k \equiv \tau_c/\tau_m$, for various values of $\beta \equiv 1/2\ \tau_d/\tau_m$. For this plot, $g \equiv 2\ (w_p/w_{net})-1 = 7$, so that $w_p = 4\ w_{net}$.

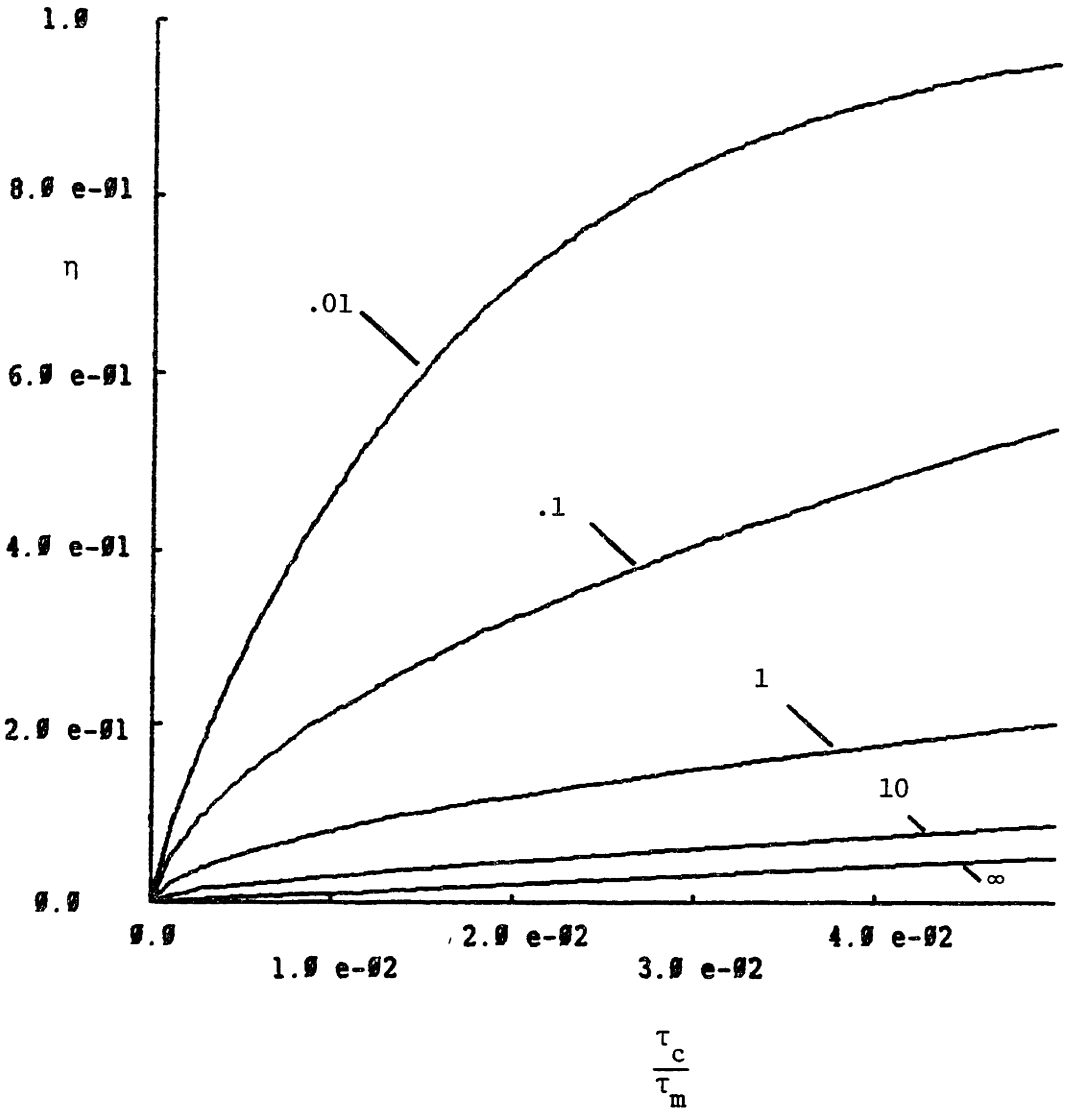

Fig. A3.7. Plot showing variation of collection efficiency, predicted by the turbulent diffusion model, with the parameter, $k \equiv \tau_c/\tau_m$, for various values of $\beta \equiv 1/2\ \tau_d/\tau_m$. For this plot, $g \equiv 2(w_p/w_{net})-1 = 199$, so that $w_p = 100\ w_{net}$.

References for Appendix 3

1
Leonard G., Mitchner M., Self S.A., "Particle Transport in Electrostatic Precipitators", Atmospheric Environment Vol. 14, pp. 1289 - 1299 (1980).

2
Hildebrand F.B., Advanced Calculus for Applications, Prentice-Hall Inc., Englewood Cliffs, N.J. (1976).

Appendix 4

Electric Field Solution for Unipolar Ion Conduction Between Concentric Cylinders

A4.1 Introduction

This appendix presents an electric field solution for the problem of unipolar ion conduction between two concentric cylinders. The results are used in the analyses of chapter 5, to roughly estimate the electric field strength in the vicinity of the ground plates of the laboratory-scale precipitator in terms of the imposed voltage and measured current. The idealized situation is described in section 2. In section 3, Gauss' law, and the law of conservation of charge are used to determine the radial dependence of the electric field strength in terms of its magnitude at the outer cylindrical surface, $E_r(R_o)$. The value of $E_r(R_o)$ is determined in section 4, by integrating the electric field strength from the inner to outer cylindrical surfaces, and requiring that the integral be equal to the imposed voltage, V_o. The behavior of the field solution in the limit of a very thin inner cylinder is examined in section 5

A4.2 Problem Statement

The situation is as pictured in Fig. (1). A voltage, V_o, is imposed between two concentric, perfectly conducting, infinitely long cylinders. The radii are R_i and R_o, for the inner and outer cylinders, respectively. The inner cylinder emits positive ions uniformly from its surface at such a rate that the emitted current per unit length is I_o/ℓ. The imposed voltage causes the ions to migrate from the inner to the outer cylindrical surfaces. The system is assumed to be in the steady-state. It is desired to determine the electric field strength and ion charge density in the volume between the electrodes [ie., for $R_i < r < R_o$].

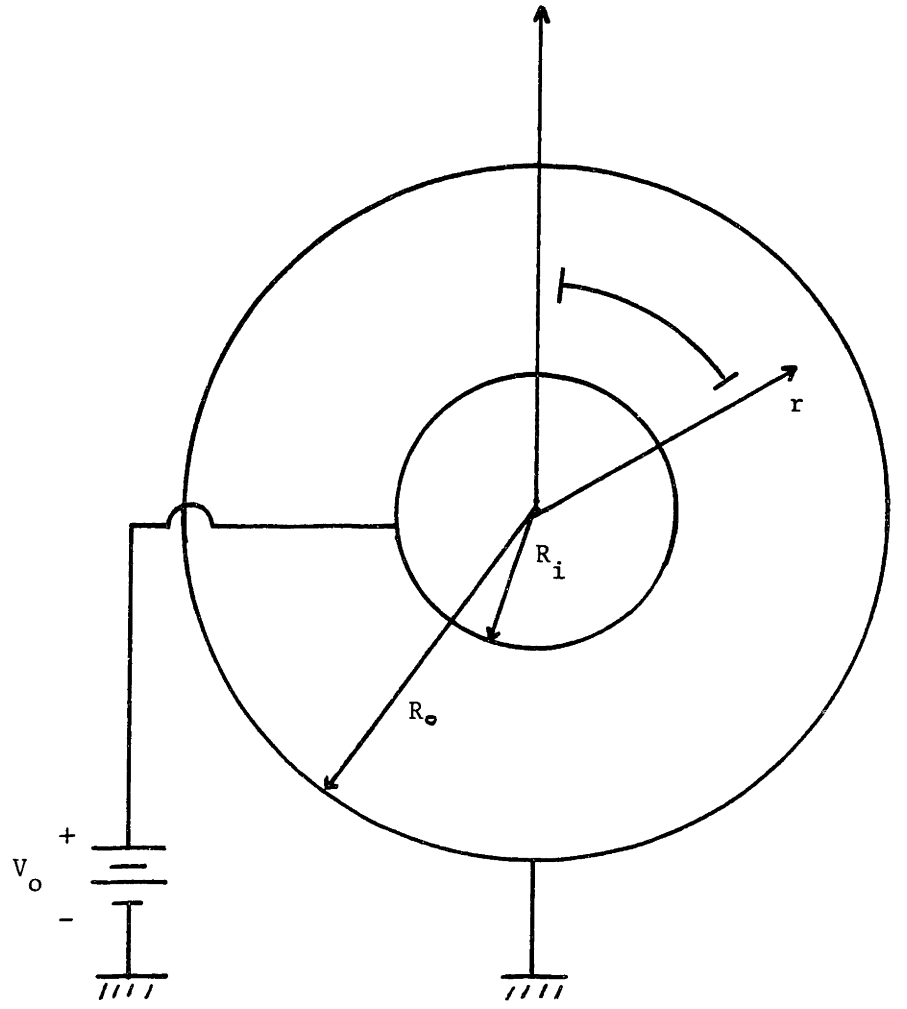

Fig. A4.1. Schematic illustration of electric field problem. Ions are emitted uniformly from inner cylindrical surface at $r=R_i$. They migrate to the outer surface at $r=R_o$, under the influence of the applied electric potential, V_o.

A4.3 Determination of Radial Dependence of Electric Field Strength

Because neither the ion emission nor the boundary conditions on the imposed potential depend upon the azimuthal or axial coordinates*, it will be assumed that the electric field and ion charge density are functions of the radial coordinate, r, only. By symmetry, the electric field must have only a radial component. Thus,

$$\bar{E}(r,\theta,z,t) = \bar{i}_r E_r(r) \tag{A4.3.1}$$

and

$$\rho(r,\theta,z,t) = \rho(r) \tag{A4.3.2}$$

where $E_r(r)$ is the radial electric field strength at the radial position, r, and $\rho(r)$ is the charge density there.

The statement of conservation of charge for the ions becomes

$$2\pi r \rho(r) b_i E_r(r) = I_o/\ell \tag{A4.3.3}$$

where b_i is the ion mobility. Because the electric field strength has only a radial component, Gauss' law takes on a particularly simple form.

$$\frac{1}{r}\frac{d}{dr}[r E_r(r)] = \frac{\rho(r)}{\varepsilon_o} \tag{A4.3.4}$$

Equations (3) and (4) can be combined to determine the radial electric field strength, $E_r(r)$, in terms of its magnitude at the outer cylindrical surface, $E_r(R_o)$.

$$E_r(r) = \left(\frac{I_o/\ell}{2\pi\varepsilon_o b_i} \right)^{1/2} \left[1 + (\kappa^2 - 1)\left(\frac{R_o}{r}\right)^2 \right]^{1/2} \tag{A4.3.5}$$

where

$$\kappa \equiv \frac{E_r(R_o)}{\left(\frac{I_o/\ell}{2\pi\varepsilon_o b_i} \right)^{1/2}} \tag{A4.3.6}$$

---

* The azimuthal coordinate is the angular position, θ, and the axial coordinate is z.

It is interesting to note that if $\kappa = 1$ exactly, then the electric field strength is of uniform magnitude throughout the region between the electrodes.

A4.4 Determination of the Electric Field Strength at the Outer Cylindrical Surface

The applied voltage, V_o, must be equal to the integral of the electric field strength, taken between the two electrodes.

$$V_o = \int_{R_i}^{R_o} E_r(r)\, dr \qquad (A4.4.1)$$

Equation (1) can be used to constrain the value of the dimensionless constant, κ [and thus, the value of $E_r(R_o)$].

$$\frac{V_o/R_o}{\left(\frac{I_o/\ell}{2\pi\varepsilon_o b_i}\right)^{1/2}} = \kappa - \sqrt{\kappa^2 - 1 + \left(\frac{R_i}{R_o}\right)^2} + \sqrt{\kappa^2 - 1}\ \ln\left[\frac{R_o}{R_i}\,\frac{\sqrt{\kappa^2-1} + \sqrt{\kappa^2 - 1 + \left(\frac{R_i}{R_o}\right)^2}}{\sqrt{\kappa^2-1} + \kappa}\right] \qquad (A4.4.2)$$

A considerable amount of integration and algebraic manipulation was omitted in deriving eq. (2) from eqs. (1) and (A4.3.5). The quantity on the left in that equation is a dimensionless parameter that characterizes the competition between effects of the imposed voltage and those of the ion space charge in determining the variation of the electric field strength in the region. It will be defined as

$$Y^{-1/2} \equiv \frac{V_o/R_o}{\left(\frac{I_o/\ell}{2\pi\varepsilon_o b_i}\right)^{1/2}} \qquad (A4.4.3)$$

Thus, according to the definition of eq. (3), the parameter, Y, is equal to the quantity on the left in eq. (2), taken to the power of -2. This definition of Y is close to that used by Yabe[1] in his numerical solution for the electric field with a wire-plate corona electrode geometry [see

section 1.5.3 for a review of his work]. Given values of V_o, R_o, R_i, I_o/ℓ, and b_i, eq. (2) can be iteratively solved for the proper value of κ. The solution is convenient only for the case in which $\kappa > 1$, so that the third term involves the natural logarithm of a positive real number. Examination of eq. (2) reveals that a value, $\kappa > 1$, can be found if $\gamma^{-1/2} > 1$.

A4.5 Discussion of Solution

One limit of this field solution is of interest here. If

$$\frac{R_i}{R_o} \ll 1 \tag{A4.5.1}$$

and

$$\gamma^{-1/2} \backsim 1 \tag{A4.5.2}$$

then it can be argued that $\kappa \backsim 1$ as well*. Thus, the electric field strength at the outer cylindrical surface is

$$E_r(R_o) \backsim \left(\frac{I_o/\ell}{2\pi\varepsilon_o b_i} \right)^{1/2} \tag{A4.5.3}$$

In the limiting situation described by eqs. (1) and (2), eq. (A4.4.2) is approximated by

$$\gamma^{-1/2} \backsim 1 + \sqrt{\kappa^2 - 1}\, \ln\left(\frac{R_o}{R_i}\right) \tag{A4.5.4}$$

so that

$$\sqrt{\kappa^2 - 1} \backsim \frac{\gamma^{-1/2} - 1}{\ln\left(\frac{R_o}{R_i}\right)} \tag{A4.5.5}$$

The electric field strength at the inner electrode surface can be estimated by using eq. (5) to compute $\kappa^2 - 1$, and substituting this value into eq. (A4.3.5).

---

*If $\kappa >> 1$, then the third term of eq. (A4.4.2) would be very large, so that that equation could not possibly be satisfied.

References for Appendix 4

[1] Yabe A., Mori Y., Hijikata K., "EHD Study of the Corona Wind Between Wire and Plate Electrodes", AIAA Journal, Vol. 16, No. 4 (April, 1978).